POLYTHECNIC OF TURIN

Department of Mechanical and Aerospace Engineering

Master of Science in AUTOMOTIVE ENGINEERING

Thesis Project

Design and Validation of the Unsprung Masses of a Formula SAE vehicle

Supervisor

Prof. Andrea Tonoli

Candidate

Luis Daniel Medina Querecuto

April 2020

SQUADRA | CORSE
POLITO

ABSTRACT

This work describes the development process of the unsprung components of a formula-styled race car that participated in the 2018 Formula SAE Italy and Formula Student Spain competitions representing the Politecnico di Torino.

The report is mostly focused on the mechanical design of structural elements, considering performance and packaging constraints and the ease of manufacturing and assembling (DFMA). A comprehensive description of the design process is included, highlighting the integration between the different disciplines and technical divisions of the PoliTo Racing Team (*Squadra Corse Polito*), with a focus on the wheel uprights as the element in which converge the transmission, cooling, suspension and brake systems. Detailed 3D CAD models were used to achieve the integration between parts and as input for structural FEM analyses before the definitive technical specification. Next, the production and validation of the designed parts are addressed. The whole process is compared to the standard V-model approach for complex project development including practical considerations.

Particular attention is paid to the study of the wheel uprights using Altair OptiStruct to realize linear static structural analyses. The radial stiffness data of the wheel bearings was used to implement the constraints for the stress analyses, avoiding the use of rigid elements for eliminating the motion of the bearing seats. This allowed obtaining a more accurate assessment of the stresses and compliance compared to the traditionally used boundary conditions that artificially stiffen the analyzed parts.

In the case of the braking system, an analytical model was used to calculate the braking forces and estimate the brake rotor temperatures in exercise. This was followed by a thermo-mechanical study to define the final geometry of the brake rotors. Track tests on both the 2017 and 2018 formula student cars allowed to collect data about the temperatures experienced by the rotors and calipers to correct the initial models for future development.

In the end, the manufacturing and assembly processes are described, followed by an assessment of the performance achieved. A failure of the brake discs after the first competition starting from one of the laser-cut holes revealed that this process should be avoided if high precision and good surface finishes are not guaranteed. Finally, some recommendations for future development are done based on the observations.

Para Ana Valentina. Porque realicé muchas simulaciones con FEA durante el desarrollo de este proyecto oxidado.

ACKNOWLEDGEMENTS

I would like to express my gratitude to Prof. Andrea Tonoli, supervisor of this thesis and faculty advisor of PoliTo Racing, for allowing me to participate in the Formula Student team and giving me the opportunity to write this thesis about the project in which I put all my dedication and passion during 2018.

The conclusion of this work represents a final step to complete my double degree in Mechanical and Automotive Engineering. It has been a long journey since 2011 and I would have not been able to complete it without all the love and support of my family. I thank you all, especially my grandparents, my parents and my sisters, for making me who I am and for loving me unconditionally, even from afar.

I am also grateful to my friends, either the ones I have known for a long time and the ones I found when I came to Turin. Thank you, for all the moments and the memories that make this journey unforgettable.

A special acknowledgement goes to the PoliTo Racing team and all the great people making part of it. We grew together as individuals and professionals, and I thank you all for making me feel part of the family. The things I learned while developing Desy are probably the most important skills for my future life as an Engineer and I am glad of having worked alongside incredible people as you all are.

I also have to thank the glorious "Team Fórmula SAE UCV". I would not be here today if it was not because we struggled together to design and build race cars and learned how to solve problems and think in practical terms in the process.

Finally, I want to express my infinite gratitude to Uribí. You have been and you are my happy place and my calm. Thank you for always believing in me as I have always believed in you.

Contents

TABLE OF FIGURES

LIST OF TABLES

INTRODUCTION

i. Context and motivation

In 2017 the Formula Student team of the Polytechnic of Turin (*Squadra Corse Polito*) competed for the 12th time in the European Formula Student [1] / Formula SAE [2] Electric season. The results obtained during the competition showed an overall improvement with respect to the previous seasons. The advancements were mainly in terms of the increased reliability and competitiveness of the 2017 car with respect to its predecessors and this was reflected in the competition results. The history of world ranking positions and individual competition places reached by PoliTo racing team is shown in Figure 1. Right after the 2017 Formula Student Czech Republic Event, PoliTo racing team was placed in the 14th place in the World Ranking, amongst nearly 170 teams from different universities worldwide [3].

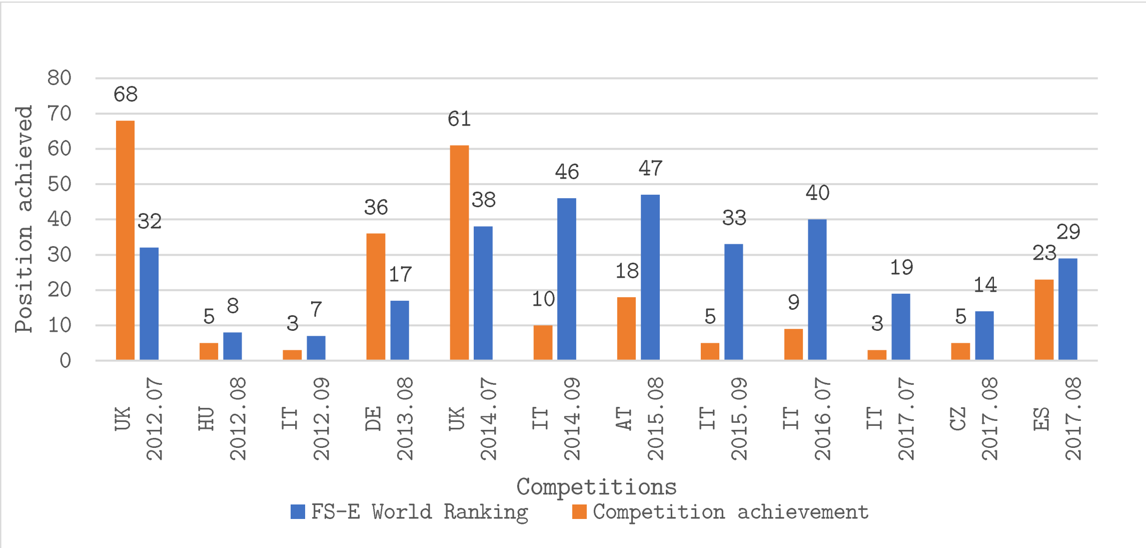

Figure 1: FS Electric World Ranking history of PoliTo racing team [3].

The 2017 PoliTo racing prototype (SC17) is an open-wheeled, single-seat, electric-drive (EV) race car, shown in Figure 2. It was designed and built by the voluntary students of the Team according to the regulations of the Formula SAE and Formula Student competitions [1, 2]. Its main technical characteristics are listed in Table 1. The main components were an evolution from the previous prototypes and the overall mechanical design was largely based on the Team's experience and know-how. Between 2016 and 2017, a total weight reduction of nearly 40 kg was achieved.

Table 1: SC17 prototype's main technical characteristics

Total weight	223 kg
Chassis	Carbon fiber monocoque
Tractive system	4 in-wheel 35 kW (peak) motors
Geartrain	Wheel-mounted planetary transmissions. Ratio 16:1
Battery	7.4 kWh battery pack. LiPo[1] cells
Controls	Torque vectoring strategy
Aerodynamics	Front and Rear wings. Ultra-light aerodynamic package.
New	Active telemetry

Figure 2: SC17- “Furiosa”

However, although the Team achieved overall good results with the SC17 prototype, the performance of the car was still not considered fully competitive against the best teams in the same category.

In most motorsports’ competitions, there is a minimum car weight that must be respected by the car designers. Conversely, the Formula SAE/Student Electric rules do not impose a minimum car weight and limit the maximum power that can be drawn from the accumulator to 80 kW [1, 2]. For this reason, the car weight is one of the most important parameters used by the student teams to optimize their vehicles.

[1] Abbreviated from for *Lithium Polymer*.

Table 2 shows a comparison between some of the prototypes that were at the top of the Formula Student World Ranking [3] at the end of the 2017 season and the SC17. The PoliTo Racing car had a lower power-to-weight ratio compared with the main competitors. This factor has a great impact on the performance of a racing vehicle and is also an indicator of how optimized the design is.

Table 2: Comparison between PoliTo racing team and the best Formula Student Electric competitors in 2017.

	Karlsruhe Institute of Technology [4]	Technical University Delft [5]	University. of Stuttgart [6]	RMIT University [7]	University of Pennsylvania [8]	Polytechnic of Turin
Car	KIT17e	DUT17	E0711-8	R17e	REV3	SC17
Traction	4WD, outboard motors	4WD, outboard motors	4WD, Outboard motors	RWD, single onboard motor	RW, single onboard motor	4WD, Outboard motors
Weight [kg]	188	171	172	184	181	223
Motor Peak Power [kW]	-	139	138	75	80	140
Battery Capacity [kWh]	6.5	-	6.8	6.4	5.6	7.4

In Mechanical Engineering a component or system is said to be “oversized” when its size and mass are greater than it requires to function safely under the expected loads [9]. In motorsports, oversized parts and systems are said to provide poor performance [10]. On the other hand, an increased mass sometimes could be needed to increase the reliability of structural parts. Hence, an appropriate trade-off between reliability and vehicle weight is a primary requisite to achieve a high-performance race car [10].

Because of this, one of the main goals of the design for the 2018 Formula Student/SAE season was to optimize the design of the new car to achieve a more competitive prototype in terms of power-to-weight ratio. One of the key areas for optimization was the unsprung mass.

ii. Problem Statement

To compete in the 2018 Formula Student/SAE Electric season, the PoliTo Racing team needs to design a new race car with a reduced mass and yaw moment of inertia compared to the SC17. The lighter a racing car is, the more effectively it can use the available power to accelerate in all directions at the maximum possible rate [10, 11]. At the same time, it must be reliable and comply with the requirements imposed by the competition.

The vehicle mass is divided between sprung and unsprung components, and the second one has a large influence in the total yaw moment of inertia and the road-holding capabilities [10, 11]. For the PoliTo Racing team, the unsprung mass includes part of the suspensions, brakes, transmissions, steering and cooling systems.

In terms of the suspension system, the structural components must be stiff enough to withstand the forces transmitted from the tires. At the same time, the need for lightweight parts limits how stiff can the unsprung elements be. The use of in-wheel electric motors determines other important design constraints for the unsprung masses, requiring integrated planetary transmissions in the wheel assemblies.

With regard to the braking system, wheel brakes must provide the maximum amount of deceleration possible while being lightweight and operating at the desired temperature range. The outboard brakes used by the Team in recent years have been based on commercial components that are heavier than necessary for the Formula Student application. Custom, lightweight braking components can be designed, but an excessive reduction in mass could lead to temperature rises beyond the adequate range. Thus, designing the outboard brakes requires a good compromise between low weight and reliability.

For these reasons, to reach the weight-reduction goals for 2018, it is necessary to design lightweight unsprung components that offer structural integrity, considering the thermal conditions when dimensioning the braking system.

Additionally, documenting the development process and validating the analytical and numerical models used for developing the brake rotors would allow further improvements in the following competition seasons.

iii. Aim and Objectives

The aim of this work is to describe the development process of the unsprung components for the 2018 PoliTo Racing car (SC18) complying with the Formula Student Electric and Formula SAE Electric rules, and to validate the design tools used for developing the braking system using experimental measurements to assess their accuracy.

The following objectives have been established:

1. Unsprung components:
    a. To design the wheel uprights according to the requirements from the PoliTo Racing Team.
    b. Produce a detailed CAD assembly to verify the overall packaging of the unsprung masses and compliance with the Formula Student Electric regulations, considering manufacturability and ease of assembly (DFMA[2]).
    c. Verify the structural integrity of the unsprung components through finite-element stress analyses.
2. Braking System:
    a. Design and develop the SC18 brakes system to comply with the weight reduction target for the 2018 Formula Student season while obtaining a braking performance superior to that of SC17.
    b. Determine the adequate work temperatures of the brake rotors through analytic calculations and analyzing the telemetry data from SC17.
    c. Develop finite element analyses to decide the final geometry of the brake rotors based on the work temperatures and the thermal and mechanical stresses.
    d. Validate through experimental (track) tests the analytical and numerical analysis tools used to develop the system.
3. To describe the workflow followed by the PoliTo Racing Team for the design, production and validation processes, for further improvement in the following years.

[2] Design for Manufacturing and Assembly

iv. Delimitation

Developing a Formula Student vehicle is a complex, multidisciplinary project. Hence, the tasks are distributed among several technical divisions that focus on different areas or systems of the car. The Unsprung Masses division manages some components that do not fall under the “unsprung” category. For example, overseeing the design of the brakes system, the division is responsible for designing, sizing and selecting onboard elements such as pedals, master cylinders, tubes, fittings and valves. This was decided in previous years for practical and organizational convenience. Since a dedicated group takes care of the complete development of each vehicle system, it is easier to obtain good results in terms of consistency and integration among the different parts.

The same applies to other systems such as the suspension, where the suspension mounts, anti-roll bars, drop links and bell cranks are developed by the Unsprung masses sub-team, even though those are chassis-mounted elements. Another example of this is the steering system, including the steering wheel, steering column and rack-pinion mechanism.

Similarly, the transmission mechanisms and the motors cooling system are developed by the Powertrain division of the PoliTo Racing team [12], even though most of the pieces that are part of those systems are unsprung.

For a better understanding of the scope of this work, the vehicle architecture and the organization of the PoliTo Racing Team, Figure 3 shows the physical vehicle systems containing unsprung components. It should be noted that some components are only partly unsprung while others are developed by the Powertrain division. Hence, the content of this work regards only the elements shown in the bottom left quadrant (in purple color). The ones at the boundaries will only be briefly addressed.

Moreover, this work does not contain detailed design procedures and analyses regarding vehicle dynamic studies and design choices in terms of suspension geometry, tire selection and chassis loads estimations. Those tasks were thoroughly done by the Vehicle Dynamics division and provided as input information for designing the unsprung components.

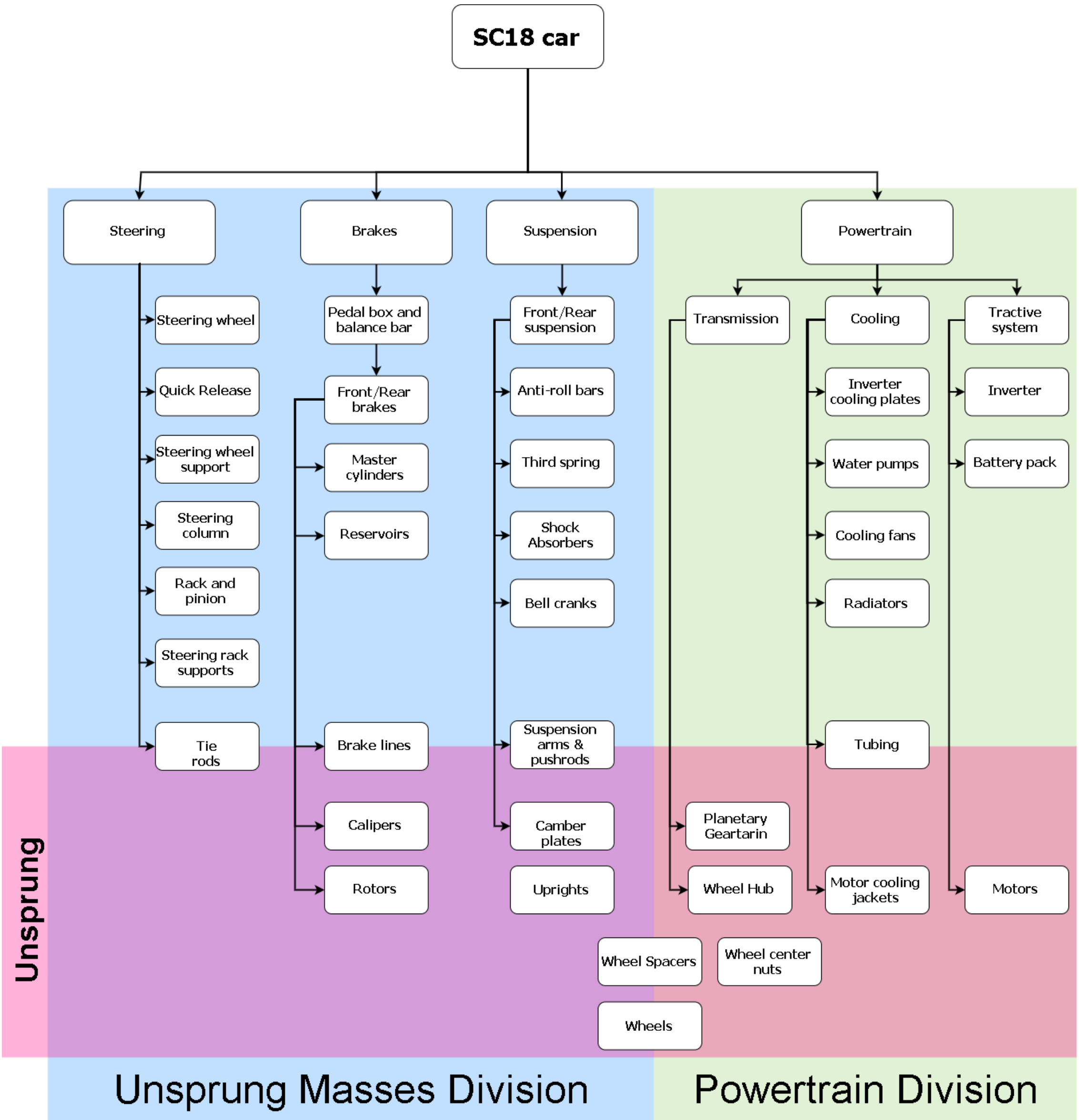

Figure 3: Vehicle systems including unsprung components and distribution of the responsibilities between the technical divisions of the PoliTo Racing Team in 2018. This work will address the design of the components in the bottom left zone.

v. Method and processes

The unsprung masses components were developed following a process like the so-called "*V method*" or "*Vee model*" [13]. This methodology is implemented in several industries for developing complex systems, to organize in a logical and functional manner the different phases of a project. The method allows proceeding in a coherent sequence and ensuring the achievement of the desired results by validating and verifying the performance against the design requirements in an iterative way [14, 15, 13].

The V method can be represented by a diagram like the one shown in Figure 4. It exemplifies what would be an ideal cycle for the development of the Formula Student vehicle, with a shape that represents two main branches or macro-phases of the system development process.

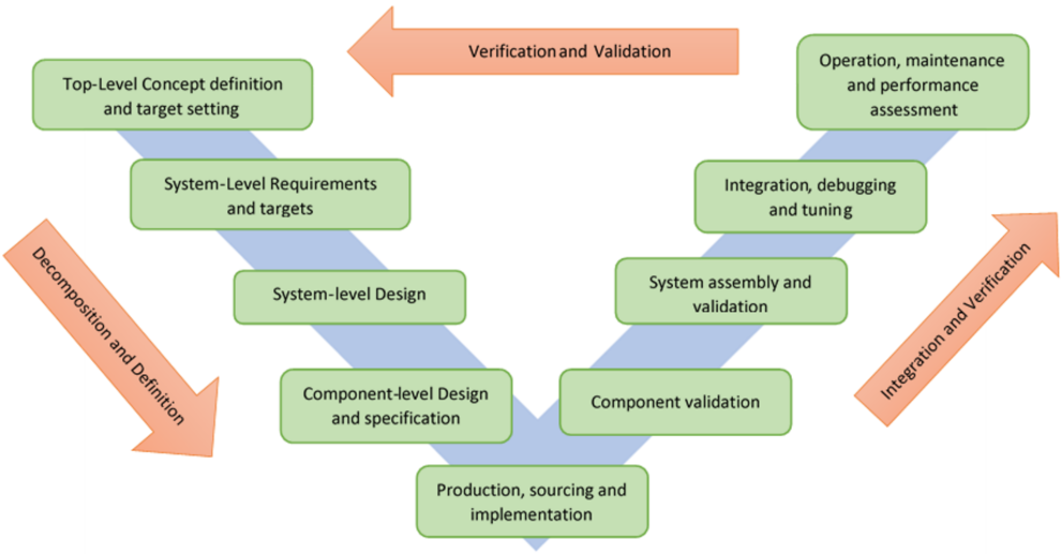

Figure 4: V model diagram of a complex system development process.

The left side corresponds to the process of defining the requirements and specifications of the system, following a Top-Down approach. This means that higher level analyses are done, and the "macro" requirements are well defined before proceeding to the detailed design of a system and then its specific components. The outputs from this project definition and design process contain technical specifications that allow to proceed to the production, sourcing and implementation of the designs.

On the other hand, the right side of the "V" represents the testing, integration and validation of the produced parts. In this case, the method follows a Bottom-Up approach.

Thus, tests and validations are made first on the individual parts, which are then integrated to an assembly and then to a system. This way, all levels are verified against the design and manufacturing specifications.

However, the V model does not exactly represent the actual process followed by the Formula Student team, as it is a rather sequential or “linearized” scheme. In fact, the development of the Formula Student project is highly “non-linear” because most of the project phases occur either in parallel or in an iterative way. Figure 5 shows a Gantt chart of the 2018 PoliTo Racing Team project.

An important consideration regarding the development of the Formula Student car is the fact that the PoliTo Racing Team is composed of volunteer undergraduate students that participate during an average of 2 years in the organization. For this reason, it is subjected to a highly dynamic transfer of knowledge and responsibilities between the new and the old members of the team, every year.

Designing a race car requires engineering knowledge to be applied through a series of technical skills that range from using CAD modelling software and analysis tools to manufacturing processes and many other abilities that are specific to the different areas of the car. For instance, designing the monocoque requires knowledge about how composite structures are manufactured. Much of this knowledge is built up on the experience of the previous generations of the team. The rest must be acquired through technical training or in some cases self-learning and researching the existing bibliography.

Another aspect to be considered when designing a Formula Student race car is the availability of resources (i.e. time, budget, manufacturing processes and workshop availability, materials, tools, software licenses, etc.). This limits in many cases the design choices. For instance, a given design of a specific part would require a very expensive machining process which is not available for the team; therefore, it is replaced by another solution. In the same way, the planning of the production process is often done according to the availability of the technical partners to collaborate in the manufacturing of the parts that need special machinery or tools to achieve complex geometries or precise tolerances, and the deadlines imposed by the Formula Student events.

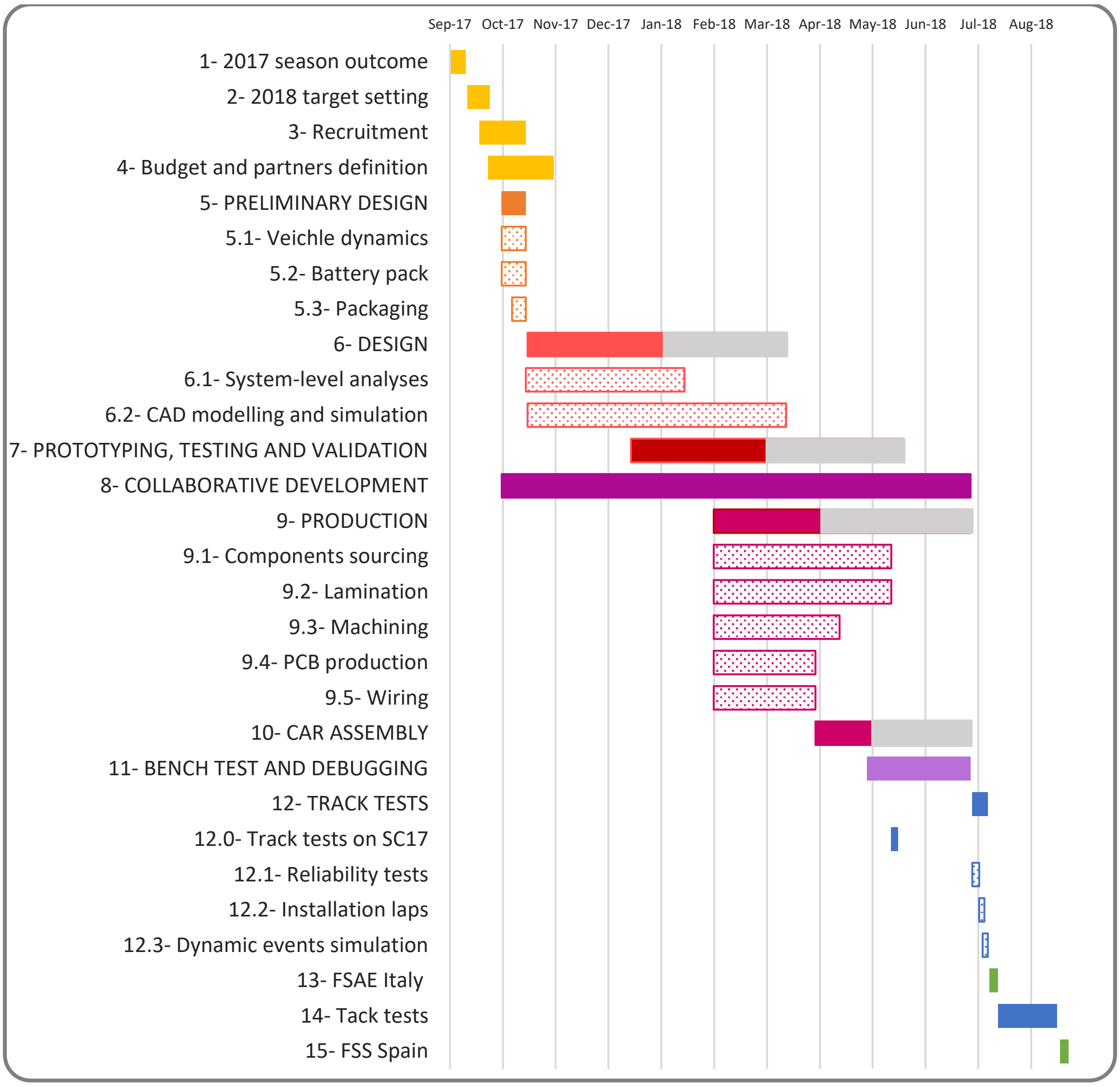

Figure 5: 2018 PoliTo Racing Team project. Grayed bars represent delays with respect to the planned dates.

vi. Background and literature review

A racing car must be capable of traveling a defined circuit in the lowest amount of time. To do so, it has to possess a great performance in terms of power delivered to the ground and in terms of handling [10, 16]. This enables it to accelerate and decelerate at the maximum possible rates. In addition to that, there is a specific set of rules that must be respected to be allowed to enter the competition of interest (in this case Formula SAE/Formula Student).

The performance of a vehicle depends largely on the characteristics of the most fundamental component in the vehicle-road interaction: the pneumatic tire.

The tires are complex compliant elements that generate the forces that allow the vehicle to move and follow a determined path. With respect to the reference system shown in Figure 6, these forces can be longitudinal (braking or driving, along the X' axis) or lateral (cornering forces, along the Y' axis) or, in most situations, a combination of the two. They are originated by the effects of physical adhesion between the tire rubber and the ground, the elasticity of the tire structure, and local deformations on the external thread in contact with the asphalt [17].

These phenomena determine the total friction between the tire compound and a paved road and are affected by the vertical force applied on the tire (force along the Z' axis in the tire reference frame). The longitudinal and lateral friction coefficients are defined, respectively, as the ratios

$$\mu_x = \frac{F_x}{F_z} \tag{1}$$

$$\mu_y = \frac{F_y}{F_z} \tag{2}$$

which are also known as force coefficients. For racing tires working on a proper surface, the coefficients given by equations (1)and (2) can be greater than 1. This means that under a given set of conditions, the tire is able to generate a lateral or longitudinal force that is greater in magnitude than the vertical force applied to it.

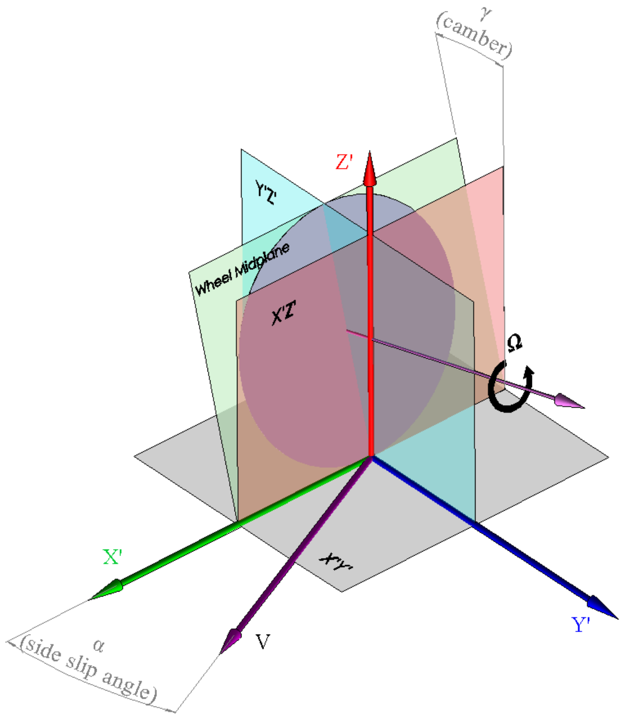

Figure 6: Reference frame used in the study of tire - road interaction [17].

The generation of the tire forces occurs when the rotation of the tire gives rise to a certain amount of slip between the rubber and the asphalt at the tire contact patch. SAE J670 standard defines the longitudinal slip ratio as

$$SR = \frac{\Omega - \Omega_0}{\Omega_0} \tag{3}$$

where Ω is the wheel angular speed and Ω_0 is the angular speed corresponding to free-rolling conditions. The slip ratio has a positive value when a driving torque is applied to the wheel and a negative one when the wheel is braking [17]. Figure 7 shows the typical characteristic of the longitudinal tire force with respect to the longitudinal slip ratio, for different values of vertical force.

In the case of the lateral forces, they are generated when there is a difference between the X' axis shown in Figure 6, and the travel direction of the tire. Such difference is called slip angle, denoted as α in Figure 6. Like the longitudinal tire forces, the lateral ones also depend on the vertical load applied to the tire, the inclination angle with respect to the vertical plane and the inflating pressure, among other parameters. An example of the lateral tire force characteristic is shown in Figure 8.

Tire forces present a nonlinear dependence with respect to several parameters, among which the vertical load has a large influence. For this reason, one of the primary roles of the suspension system is to maximize the contact between the tires and the ground and thus the tire forces.

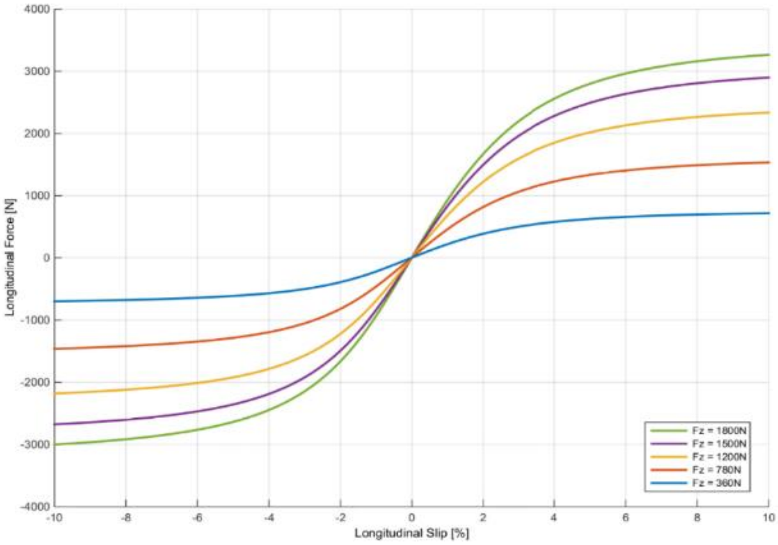

Figure 7: Pure longitudinal tire force. Variation with respect to the longitudinal slip.

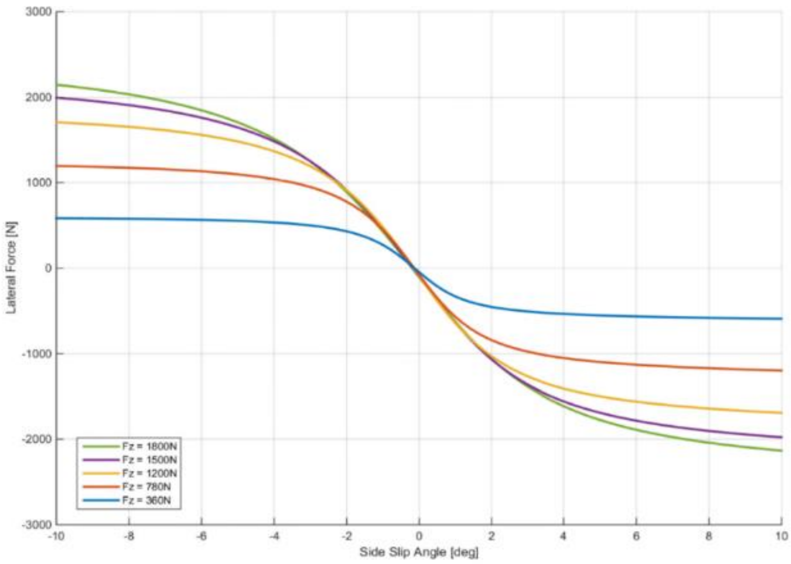

Figure 8: Pure lateral tire force. Variation with respect to the side slip angle.

vii. Unsprung Mass

The SAE J670-Standard defines the unsprung mass of a motor vehicle as:

"All weight that is not carried by the suspension but is supported directly by the tires. The unsprung weight includes the weight of the tires and wheels and all parts that move directly with the tires and wheels, plus a portion of the weight of the suspension linkages, ride springs, and driveshafts"

Another definition is [18]:

"*That part of the mass that does not change its position – with respect to the ground- is called the unsprung mass. Some suspension components contribute partly to sprung mass, partly to unsprung mass. To evaluate the two contributions, the mass of these elements must be divided into two parts, concentrated ideally in the suspension joints, in such a way as to conserve the moment of inertia and the center of gravity position"*

Thus, the main unsprung elements of a traditional vehicle are the wheels and tires, uprights, wheel hubs and bearings, and the outboard components of the braking system. In the case of the Formula Student Electric vehicles made by PoliTo racing team, the driving traction is provided by electric motors mounted on the uprights and connected to the wheel hub through a planetary transmission. This configuration is also known as In-Wheel Motors or *IWMs*. It can be seen in Figure 9, which depicts the front right wheel assembly of the SC17 car.

The electric motors are equipped with concentric cooling jackets, which are also an additional part of the unsprung mass, along with the water flowing inside them. Additionally, a fraction of the mass of the power and control cables connecting the motors to the power inverters is also unsprung.

The unsprung assemblies of the SC17 vehicle were developed with a focus on good mechanical reliability and flexible setup possibilities. As discussed in the Thesis work by Carboneri [19], they accomplished the design goals for that season, achieving "*a good mechanical behavior under load, no reliability problems and guaranteeing safety in every racing condition*". This result was obtained thanks to the application of design and optimization methods known by the Team from previous years, and the use of suitable materials and fabrication processes thanks to a successful collaboration with technical sponsors. In the case of the braking system, the unsprung elements (mainly brake rotors and calipers) were sized conservatively, using commercially available parts from motorcycling applications.

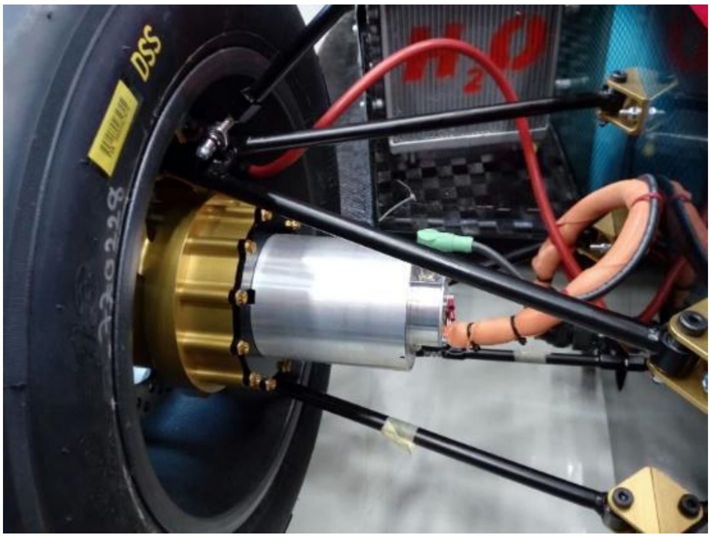

Figure 9: Front wheel assembly, SC17 prototype.

viii. Role of the unsprung mass in vehicle performance

There are two basic design requirements for designing any race car [10]:

> *"The provision of the largest vehicle "g-g[3]" maneuvering areas throughout the range of operating conditions.*
>
> *The provision of vehicle control and stability characteristics that enable a skilled driver to operate at or near these acceleration limits."*

The impact of the unsprung mass in fulfilling those can be studied in terms of the road-holding ability and the characteristics of the suspension geometry.

Road holding

The impact of the unsprung mass in vehicle performance can be studied in terms of the road-holding ability by analyzing simple quarter-car models with 2 degrees of freedom, like

[3] The term "g-g diagram" refers to a plot in which the longitudinal and lateral accelerations of a vehicle recorded while it travels along a particular circuit are plotted in the abscissas and ordinates, respectively. This is often used as an analysis tool to evaluate the performance of a car [10].

the one shown in Figure 10. This schematic representation can be used to study the behavior of a suspension system.

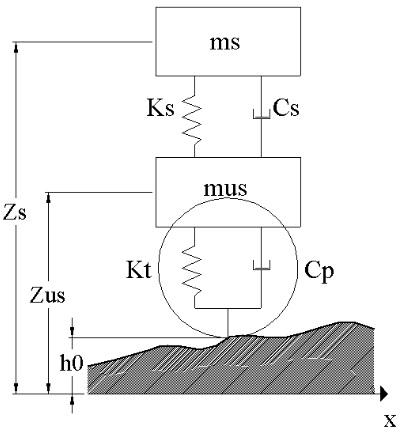

Figure 10: Quarter-car model with 2 degrees of freedom.

As was mentioned in the previous section, the tire forces vary with the vertical load applied to the tire. Thus, the undesired variations in the contact force between the tire and the ground should be minimized to provide better handling. The quarter car model allows obtaining insights about such variations, as well as the acceleration of the sprung and unsprung masses.

This type of study is usually done to investigate the values of stiffness and damping to obtain the desired frequency response, but it also allows assessing the influence of the unsprung masses in the tire-road interaction. Figure 11 shows the ratio between the amplitude of the dynamic component of tire-road contact force and the displacement of the ground contact point multiplied by the vertical stifness of the tire [18]. A reduction in unsprung reduces the maximum variation of contact force.

Additionally, the unsprung mass determines the second natural frequency of the suspension. When excited at such frequency, the amplitude of the system response tends to have a resonant peak that worsens the ability of the suspension to maintain the tire in contact with the ground. The natural frequency of the unsprung mass can be determined by [10]

$$\omega_{us} = \sqrt{\frac{K_s+K_t}{m_{us}}} \tag{4}$$

Thus, reducing the unsprung mass will increase the frequency at which the wheel response will have an amplitude peak.

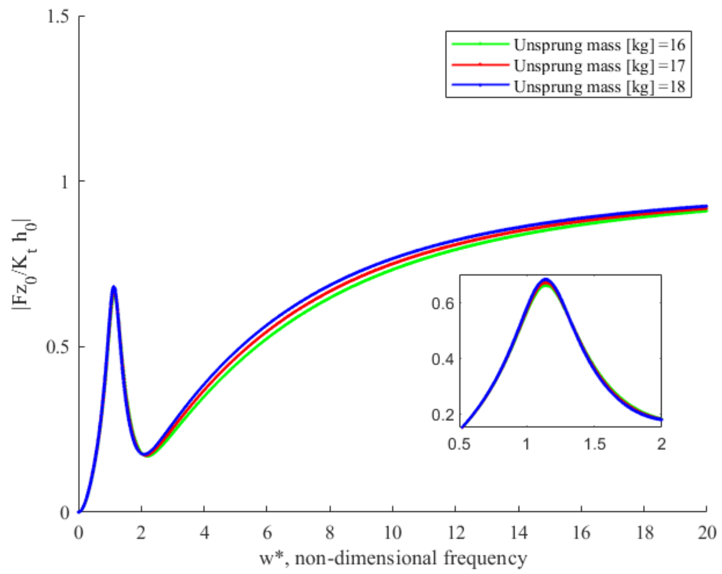

Figure 11: Ratio between the dynamic component of tire-road contact force and the displacement of the supporting point.

This is especially important in the case of PoliTo racing team. The major drawback of the IWMs used by in the SC17 car is the additional mass and polar moment of inertia added to the vehicle compared to EVs with onboard motors. The work by Watts et al. [20], as well as that from Anderson and Harty [21], assessed experimentally the possibilities for integrating IWMs into road vehicles. Their results showed that the opportunities provided by the independent IWMs for achieving an improved control of the vehicle dynamics outweigh the possible decrease in handling performance due to the increased unsprung weight. The disadvantages can be minimized by implementing suitable considerations during the development of EVs featuring IWMs.

In terms of racing applications, the work by Yu, Deli and Castelli-Dezza [22] assessed analytically the influence of unsprung mass and unsprung rotational inertia in lap time. They found that the most influencing parameter is the rotational inertia of the wheel assembly; lower rotational inertia values resulted in reduced lap times, for the same values of unsprung and sprung mass. However, although it is theoretically possible to change the rotational inertia of the wheel components while maintaining the same values of unsprung mass, this is often very difficult in practice, due to packaging and manufacturing constraints. Thus, in practice, reducing the unsprung mass, the rotational inertia is also reduced in most cases, and vice-versa. Hence, reducing the unsprung mass of race cars is of paramount importance.

Suspension geometry

Another role of the unsprung masses in vehicle performance is related to the kinematic behavior of the suspension. The relative motion between the wheel and the vehicle body is characterized by the so-called “wheel path”, which depends on how the unsprung mass is linked to the sprung mass. The set of geometric parameters that define this is called *suspension geometry* and the unsprung components play an important role in determining it by accommodating the outer (wheel – side) joints of the suspension mechanism. Figure 12 shows the most relevant parameters defined by the location of the outer ball joints of the suspension linkages.

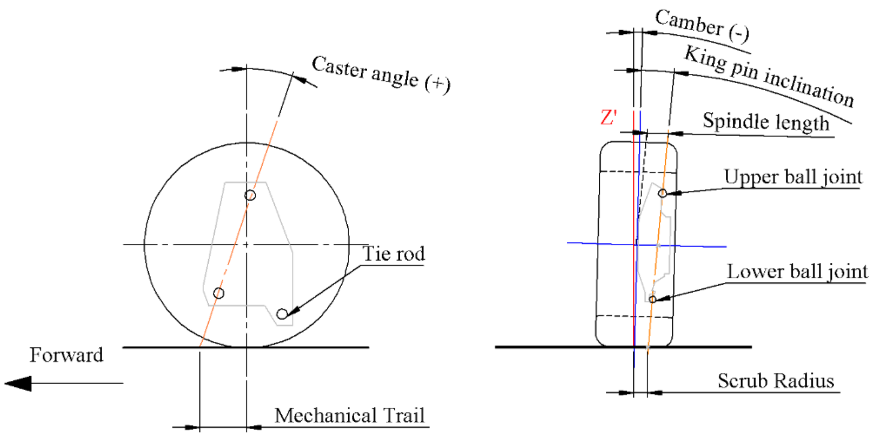

Figure 12: Front suspension packaging [10].

The suspension elements transfer the forces exchanged between the tires and the road to the vehicle body. Hence, the unsprung components must be rigid enough to withstand these loads and prevent any relevant deformations from altering the kinematic behavior of the suspension, as this would negatively influence the handling characteristics of the car.

Ideally, a car suspension would allow only a vertical translation of the wheels relative to the car body, so that the position of the tire with respect to the ground remains constant. This way, the contact area between the rubber and the road would be always maximized. In reality, the wheels change their position relative to the ground as they follow the path imposed by the suspension geometry. For an independent suspension in front view, this motion is a rotation about the instant center depicted in Figure 13.

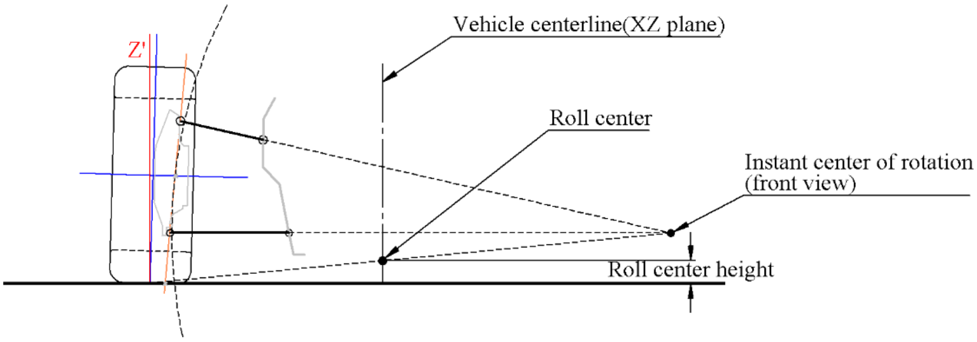

Figure 13: Wheel path about the front view instant center.

There are several types of suspension systems that offer different advantages and disadvantages. The Short-Long Arm suspension (SLA) is the type used by the PoliTo Racing team. It suspension offers a series of advantages in terms of elasto-kinematic properties and for this reason it has been widely adopted for racing applications [10, 16]. Figure 14 shows an example of a typical SLA suspension used in Formula SAE competitions. The load path from the wheel to the car body is achieved by using two controls arms ("A-Arms" or "wishbones") connected to the car body and the unsprung components through spherical joints. This allows to design the position of the arms so that these are only subjected to axial forces (compression-extension). Moreover, the shock absorber does not play a structural role (i.e. it is not subjected to non-axial forces). Thus, the wheel path depends only on the suspension geometry.

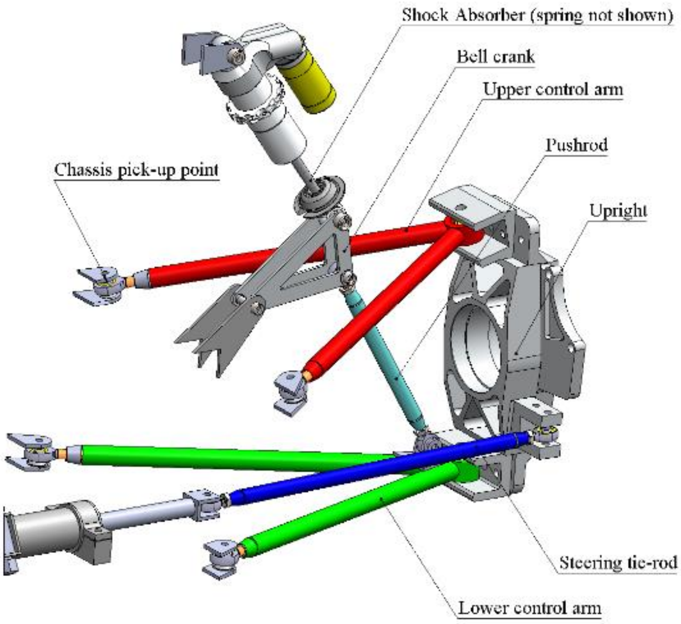

Figure 14: Example of an SLA suspension geometry. Team Formula SAE UCV 2013.

The stiffness requirement for the structural elements of the suspension is in contrast with the need for minimizing the unsprung mass. In general, a rigid component is likely to be heavier than a less stiff one, if both are made of the same material. However, this is not necessarily always true.

ix. Yaw inertia

The importance of reducing the yaw inertia for improving the performance of a race car is related to the vehicle's ability to change direction, i.e. to follow the driver's commands.

To analyze this problem, it is necessary to use a defined reference frame. The one used by the Squadra Corse Polito is based on the vehicle axis system presented by G. Genta and L. Morello [18] depicted in Figure 15. In this reference system, the positive X-axis points in the vehicle's forward direction of motion, and the positive Z-axis points upwards. The rotation of the vehicle body about the Z-axis is called *yawing* motion. It is caused by a component of the external moment vector acting on the vehicle, the so-called Yawing moment [10].

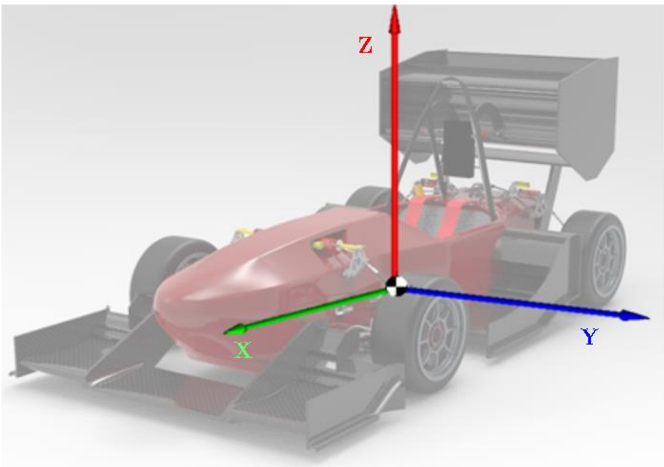

Figure 15: Vehicle-centered reference frame.

The yaw inertia is the moment of inertia of the car about the Z-axis. For a given vehicle component having a mass m and moment of inertia Izz about an axis z passing through its center of gravity, parallel to the vehicle's Z-axis, the contribution to the total Yaw inertia is given by

$$I_{ZZ} = I_{zz} + m\, d^2 \tag{5}$$

where d is the distance from the center of mass of the part and that of the whole car (Huygens – Steiner Theorem). Figure 16 shows an insightful representation of the moment of inertia and the yaw inertia for a generic vehicle

.

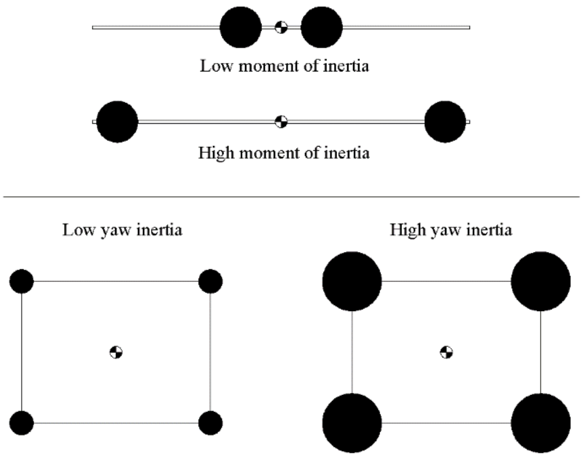

Figure 16: Moment of inertia.

With reference to Figure 17, we can write the following equations to describe the Yaw equilibrium in a very simplified way:

$$M_z = J_z\ddot{\psi} = F_{y_f}a - F_{y_r}b + \frac{1}{2}C_{M_z}S\rho V^2 \tag{6}$$

where Mz is the yawing moment. From (6), we can see that for a given set of geometrical parameters and side force values, smaller values of the barycentric yaw moment of inertia of the whole vehicle, Jz, produce higher yaw accelerations $\ddot{\psi}$. This has an impact on the cornering capabilities for the vehicle. An understeering car has a deficit of yaw moment and an oversteering car has an excess of yaw moment [23].

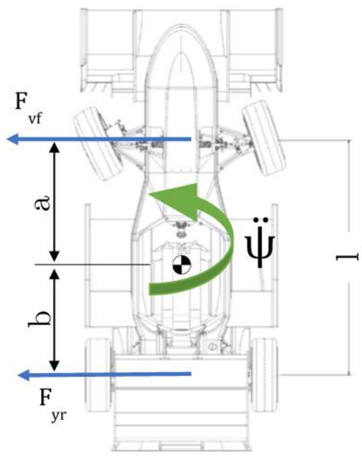

Figure 17: Yaw moment diagram. Aerodynamic forces not shown.

A more formal way to analyze this is by considering a high-speed cornering model of a rigid vehicle [18]. Under the assumptions of small slip angles of the vehicle (β) and the wheels (α_i), small yaw angular velocity (r) and neglecting pitch, roll and ride motions due to the suspension's compliance, the final expressions of the linearized equations of motion for a vehicle can be written as [18]:

$$mV(\dot{\beta} + r) + m\dot{V}\beta = Y_\beta \beta + Y_r r + Y_\delta \delta + F_{ye} \tag{7}$$

$$J_z \dot{r} = N_\beta \beta + N_r r + N_\delta \delta + M_{ze} \tag{8}$$

Equations (7) and (8) are linearized based on the assumptions of small angular quantities and considering the longitudinal motion as decoupled from the lateral one. The terms Y_β, Y_r, Y_δ, N_β, N_r and N_δ are the so-called derivatives of stability[4] and the terms F_{ye} and M_{ze} are external disturbances [18]. Each derivative is associated with a physical effect on the vehicle stability and control. These linearized equations of motion can be used to make a formal analogy between the dynamic behavior or a motor vehicle and a mass-spring-damper system [10] [18]. A schematic representation of this is shown in Figure 18.

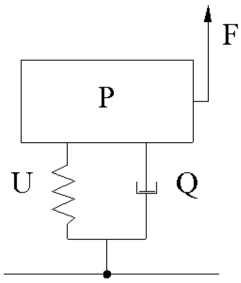

Figure 18: Mass-spring-damper system formal analogy for studying the lateral stability of a motor vehicle [18].

This is helpful in studying the stability of the vehicle at constant speed. The equation

$$P\ddot{r} + Q\dot{r} + Ur = S''\delta + T''^{\dot{\delta}} + N_\beta F_{ye} - Y_\beta M_{ze} + mV\dot{M}_{ze} \tag{9}$$

is enough to study the dynamic behavior of the vehicle [18]. In this analogy, the mass P, stiffness U and damper Q correspond to the expressions:

$$P = J_z mV \qquad S'' = Y_\delta N_\beta - N_\delta Y_\beta$$
$$Q = -J_z Y_b - mVN_r \qquad T'' = mVaC_1$$
$$U = N_\beta(mV - Y_r) + N_r Y_\beta$$

4 These expressions are only applicable under the set of assumptions already described. The complete derivation of this high-speed cornering model for a rigid vehicle can be found on [18].

Therefore, it is possible to see the influence of vehicle mass and yaw inertia in lateral stability by looking at the response from such system. However, the models described so far are only simplified methods, applicable only under the described assumptions and for specific situations. They can be used as preliminary design tools to gain insights about the influence of different parameters. In general, the results from such analyses show the benefits of a reduced mass and yaw inertia for achieving better handling capabilities and lower lap times. Figure 19 shows an example of the yaw rate response of a race car with different values of yaw moment of inertia (on the left) and unsprung mass (right) during a step-steer maneuver. These curves were obtained through a vehicle dynamics simulation software [24]. The different values of Yaw moment of inertia and unsprung mass have been exaggerated to highlight the differences. The car with reduced Yaw moment of inertia shows a faster stabilization compared to the other 2 cases. Similarly, the one with less unsprung mass stabilizes faster than the baseline model. Changing these two parameters is not possible in real life, but it can be done in simulation environments to demonstrate the influence of each one.

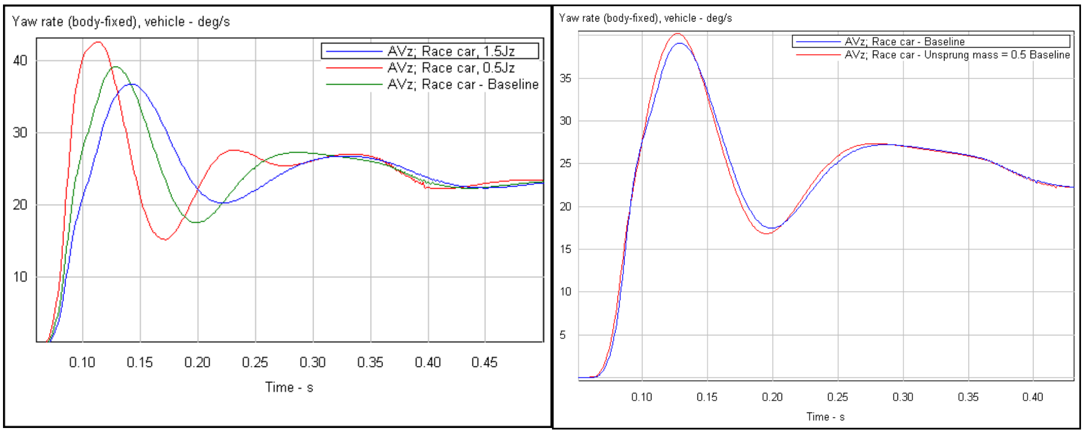

Figure 19: Time response of the Yaw rate during a step-steer maneuver.

x. Thermal capacity of brake rotors and calipers

The braking system of a race car is used to modulate the vehicle speed by converting kinetic energy into thermal energy through the friction between the brake pads and rotors. During a braking maneuver on a level surface, the amount of energy that the brakes system must convert into heat is given by [25]

$$\Delta E_b = \frac{m}{2}(V_1^2 - V_2^2) + \frac{I}{2}(\omega_1^2 - \omega_2^2) - F_{drag} d_{brake} \qquad (10)$$

where m is the vehicle mass, I is the mass moment of inertia of the rotating parts. V is the vehicle speed and ω is the angular speed of the wheels. The subscripts 1 and two refer to the conditions before and after braking, respectively. The last term accounts for the aerodynamic drag energy over the distance covered during braking.

Because of this process the temperature of the rotors and calipers is increased, and the temperature rise is inversely proportional to their mass (unsprung mass). For a brake disc, the corresponding temperature rise during a braking maneuver is given in a simplified way by [25]

$$\Delta T = \frac{E_{b_i} p}{m_{disc} C_p} \tag{11}$$

where E_{b_i} is the portion of the total energy that must be dissipated by a single disc in the axle i, m_{disc} is the mass of the brake disc and C_p is specific heat of the material it is made of. The factor p is a partition coefficient that determines the proportion of the total heat that is transferred to the rotor [25]. For a single braking maneuver, it depends only on the thermophysical properties of the materials used for the construction of the disc and the brake linings, and the surface areas through which the heat is transferred. During continuous or repetitive braking operation, the effects of convection and radiation heat transfer have a more relevant role in the overall thermal balance [25].

When the thickness of a brake disc is small compared to its surface area, its internal resistance to conduction heat transfer can be neglected. Thus, it is reasonable to consider a uniform temperature distribution on the disc. This condition is verified if [26]

$$Bi = \frac{hL_c}{k} \ll 0.1 \tag{12}$$

where Bi is the Biot number, a dimensionless parameter that indicates the proportion between the temperature gradient in a solid (the brake disc) and the temperature difference between its surface and the fluid around it (the air) [26]. The letter h represents the convection heat transfer coefficient, k is the thermal conductivity of the solid material, and L_c is the characteristic length of the rotor body, defined as the ratio between its total volume and surface area.

If the condition (12) is verified, the conduction heat transfer problem is characterized by the Fourier number,

$$Fo = \frac{\alpha t}{L_c^2} \tag{13}$$

where α is the thermal diffusivity and t is time. Thus, the temperature response of the brake rotor can be analyzed considering a uniform temperature distribution, using the so-called lumped formulation [26]

$$\frac{T - T_\infty}{T_i - T_\infty} = e^{-Bi \cdot Fo} \tag{14}$$

T represents the rotor temperature at a given instant of time. The subscripts i correspond to the initial thermal conditions and ∞ refers to the temperature of the air surrounding the disc. An example of the theoretical variation in time of the brake rotor temperature during a stop is shown in Figure 20.

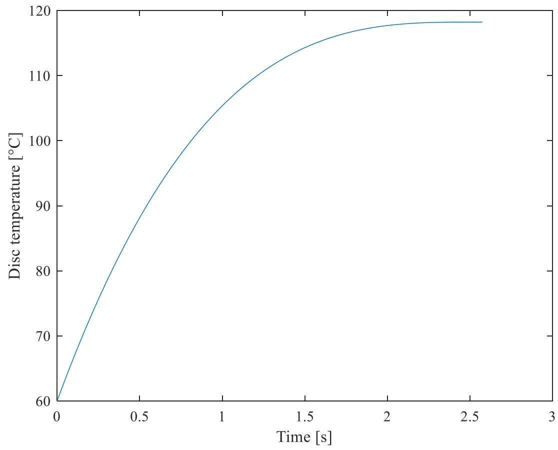

Figure 20: Theoretical brake rotor temperature during a single braking maneuver.

By combining (11) and (14), it is possible to determine the temperature of the brake rotor after a given number of brake maneuvers [25]. The ideal brake rotor design would work at the optimal temperature of the brake linings compound. From (11), it is evident that the greater the mass of the disc, the lower the temperature rise for a given amount of dissipated heat. Conversely, the lighter parts will generally cool down faster that heavier ones.

xi. PoliTo Racing 2018

The Formula Student/SAE Electric endurance and autocross tracks are complicated layouts requiring intense use of brakes and high acceleration capabilities [1, 2]. For this reason, weight saving, and inertia reduction constitute primary concerns when designing the race cars prototypes. Good handling performance is even more important considering that the race cars are driven by students, with little testing time available (a couple of weeks during the summer).

To achieve an important reduction of the mass and inertia of SC18 with respect to SC17, important packaging changes were implemented. The most relevant one was the adoption of a split-up power inverters layout on the sides of the cockpit. A comparison between the SC17 and the SC18 inverter and battery pack layout can be seen in Figure 21. The power inverter and battery pack of SC17 were installed on the rear end of the monocoque. For 2018 the team managed to split up the inverters, placing them on the sides of the cockpit, allowing to move the battery pack toward the center of the car. This resulted in a lower moment of inertia about the Z-axis.

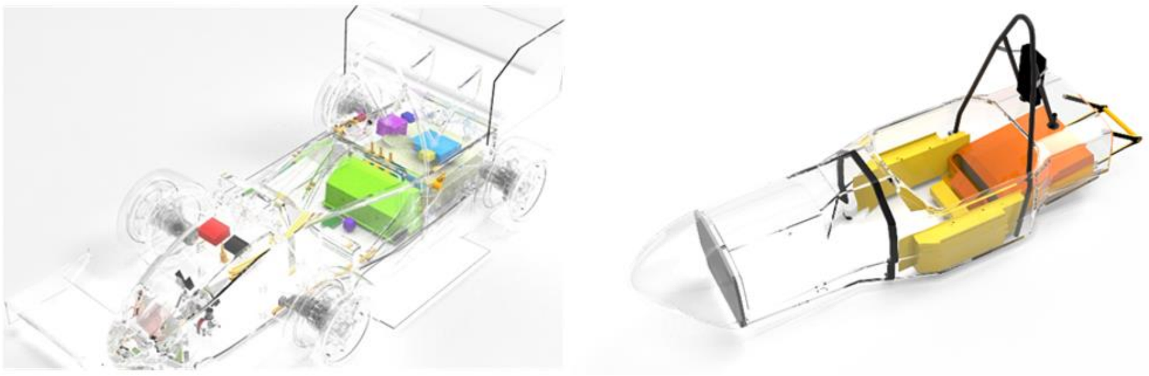

Figure 21: Comparison between SC17 (left) and SC18 (right) inverters and battery pack layout.

Another important measure to reduce the mass and inertia was to optimize the design of the unsprung masses. The main driving factor for achieving this was the reduction of the module of the double stage planetary transmission spur gears [12], which opened new possibilities for packaging the final drive into the uprights. Another key factor was the change of the outboard brake components used, as will be discussed in the following.

CHAPTER 1. PROJECT DEFINITION

This chapter illustrates the process followed when designing the unsprung mass components of the SC18 formula student prototype.

The design phase followed a *top-down* design approach, as shown in Figure 22. Top-down design refers to a development process in which the more general ("Top") aspects are defined first, so that the smaller details ("down") can be designed according to the established parameters. The advantage of the top-down method is that *"it breaks down a project's goals into smaller problems that are more easily solved"* [27].

To effectively use the top-down design approach, it is necessary to establish the requirements that the complex system must fulfill (this is also referred to as "specification" [10]). In Systems Engineering, project requirements are a set of parameters that "*define what the system must do and how well it must perform*" [14]. In race car design, the specification summarizes the objectives of the design in detail [10]. These must be expressed in clear, unambiguous, comprehensive and concise terms, and they must account for the design constraints (i.e., the factors that restrict design possibilities).

For a race car, the design requirements and constraints are determined by the regulations of the competition in which the vehicle participates. In the case of the Formula SAE and Formula Student events, there is a specific set of rules that must be fulfilled, and a comprehensive definition of the boundaries imposed by the competition organizers to the car designers, e.g., the minimum allowed dimensions for the car.

Other characteristics, such as the vehicle mass or the acceleration capabilities, are set according to the goals of the car designers for the competition season. The following sections describe how the goals for 2018 were set and then translated into more specific system specifications that drove the design of the different components. At the end of this chapter, the specifications for the unsprung components are listed, and the results from the evaluation of the SC17 systems is summarized, to define the starting point for SC18.

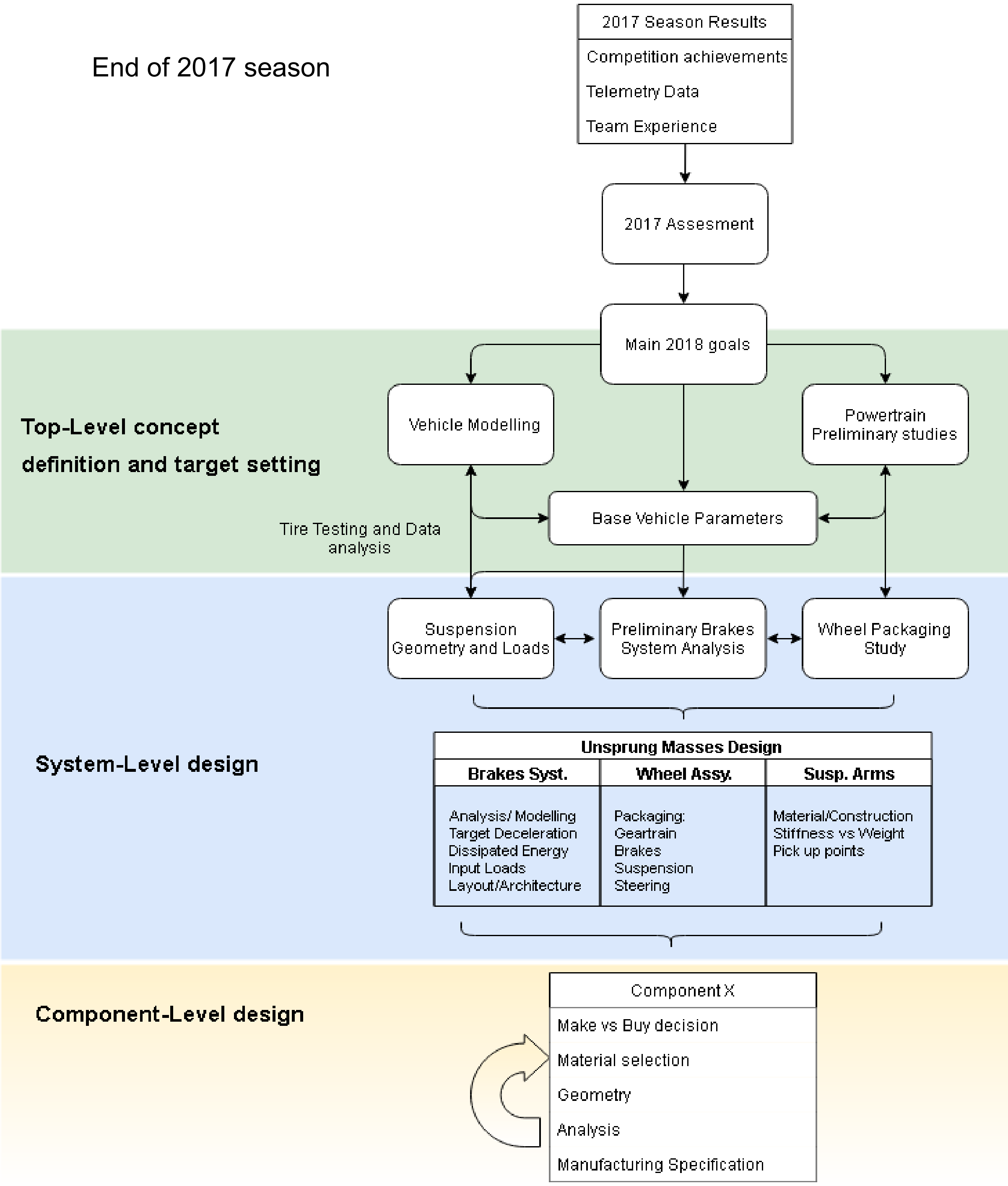

Figure 22: Design phase workflow.

1.1 Evaluation of the 2017 season

In autumn 2017, the PoliTo Racing Team realized an evaluation of the overall performance during the Formula Student/SAE Electric competitions of that year. The competition results were analyzed, along with the telemetry information and the experience from the team members. The feedback from the drivers was also an important source of information for assessing the performance of SC17.

As introduced in section i, the SC17 car was heavier than best competitors in the Formula Student events. At the beginning of the 2018 season, the Vehicle Dynamics division of PoliTo racing analyzed how the mass of the SC17 prototype was distributed among the different parts and sub-systems. The aim was to determine which components contributed the most to the total mass and decide in which areas to focus to improve the compromise between performance and reliability on SC18.

Figure 23 shows a Pareto diagram with the results of the mass survey. The battery pack and the composite monocoque represented 23% and 14% of the mass of SC17, respectively. Nevertheless, the combined contribution of the unsprung components was 72.8 kg, nearly 33% of the total.

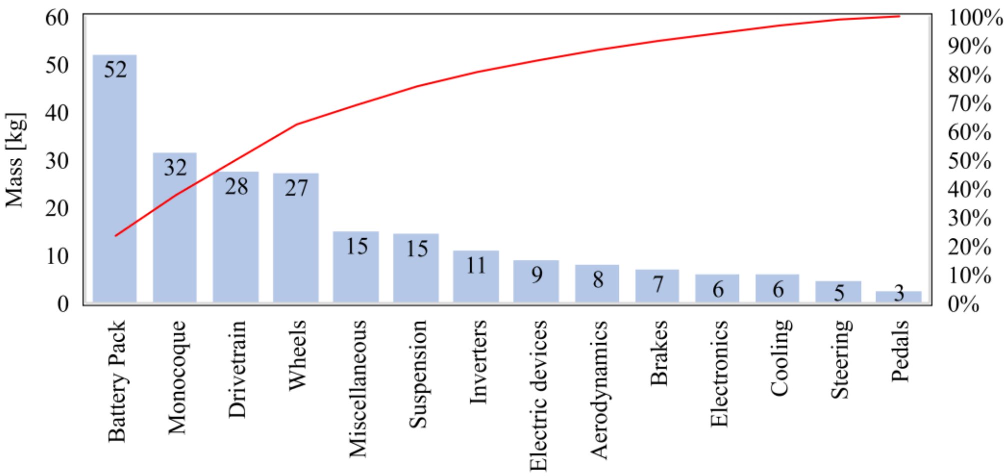

Figure 23: Pareto analysis of the mass contribution of the main systems of SC17. This done by the Vehicle Dynamics division of the PoliTo racing Team during the 2018 season.

Additionally, the Vehicle Dynamics division studied the contribution of each component of the SC17 to the moments of inertia about the center of gravity of the car. This was done by carefully measuring the distance between the center of gravity of each part and the car center of gravity, both on a CAD model and on the actual SC17.

The results are summarized in Figure 24. Only the yaw inertia is reported because of its direct interest in this work. The unsprung components represented about 42%.

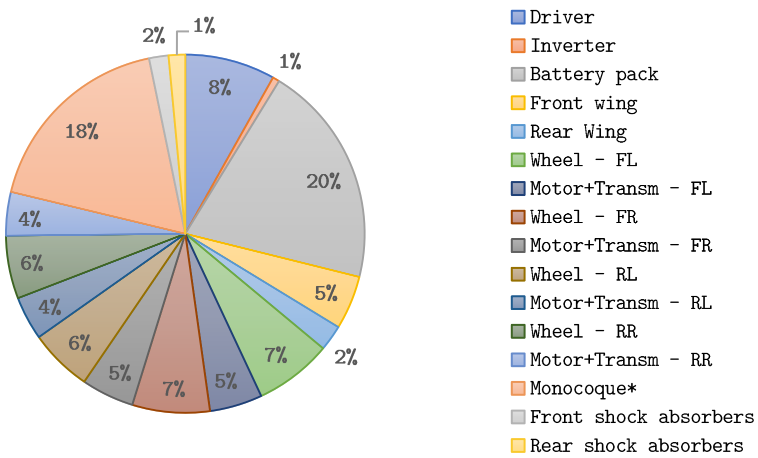

Figure 24: Contribution of the main vehicle components to the total yaw inertia about the vehicle's center of gravity. This analysis was done by the Vehicle Dynamics division of PoliTo racing team during the 2018 season. [5]

Other analyses were done using the telemetry data collected during 2017. The results confirmed that the car performance was limited by the total weight and yaw inertia, but there was also room for improvement in terms of vehicle dynamics and the reliability of the electric systems. This would allow a better use of the energy stored in the battery pack, which was one of the strengths of the SC17. Table 3 summarizes some of the conclusions from the analysis of the 2017 car.

Table 3 Positive and negative aspects of the SC17.

PROS	CONS
Good mechanical reliability	Excessive weight and inertia
Adequate battery pack capacity	Sub-optimal use of the tire forces
Flexibility in suspension configuration	Low downforce compared to competitors
Adjustable aerodynamic package	Excessive steering compliance
	Difficult maintenance

[5] Throughout this work, the abbreviations FL, FR, RL and RR are used for referring to the front left, front right, rear left and rear right wheels of the car, respectively.

1.2 Top-Level Concept definition and target setting

The design of SC18 started with the definition of the Team goals and the top-level concept. The goals are established based on the analyses of the previous seasons, the competition regulations and team experience. They should guide the development of every aspect of the new vehicle so that each technical division of the team can work in the same direction. This ensures consistency throughout the different sub-systems and facilitates integration between them.

Based on the results of the analyses of the 2017 season, the Team established the following goals for 2018:

a) Reduce the car mass and moments of inertia to obtain a more competitive vehicle for the Formula Student Electric events.
b) Use the 2017 data to develop better control systems and develop a car with enhanced handling performance (greater lateral and longitudinal accelerations).
c) Select a new type of tires based on track tests with different compounds.
d) Upgrade the aerodynamic package to obtain more downforce without a significant increase in drag.
e) Redesign the electric and electronic systems to increase the reliability and serviceability and improve energy efficiency.
f) Re-define the car packaging and systems integration to achieve the weight-saving and inertia-reduction targets.
g) Develop a complete and detailed CAD model of the vehicle to improve the integration of the different systems during the design phase.

Once the goals have been established, they have to be translated into numerical targets to drive the design decisions. This is done through initial studies of the vehicle dynamics, the powertrain and the aerodynamic package, aimed to determine what improvements can be made from the previous car to achieve the established goals within the competition requirements. Experts in race car designing also refer to this stage as the Preliminary Design phase [10]. It has the objective of determining the overall packaging and estimating components size, weight and location for obtaining the desired center of gravity location. From there, target values for the new vehicle are established, as well as the overall dimensions and types of architectures used for the main systems. The available resources are also considered to assess whether the changes are feasible or not. The resources may include budget, time, available facilities, technical partners, previous experience, know-how, software licenses, etc. Table 4 contains a summary of the 2018 targets.

Table 4: Some of the main targets for the SC18 vehicle

Total Vehicle Mass	200 kg (12% reduction compared to SC17)
Yaw inertia	20% reduction compared to SC17
Center of gravity height	15 mm lower than SC17.
Car dimensions	1525 mm wheelbase, 1200 mm track width.
Body	CFRP[6] monocoque (125 000 $\frac{Nm}{rad}$ torsional stiffness)
Suspension	Push-rod SLA front and rear.
Aerodynamic Downforce	700 N at 60 km/h.
Tractive system voltage	600 V
Traction	4 IWMs with max. output power of 32 kW each.
Battery capacity	7.8 kWh
Battery energy density	10% increase with respect to SC17.

This established a baseline to start with the design of the vehicle systems of SC18. However, the initial targets and estimates can be modified during the design process depending on the results from more detailed analyses.

Among the results from the preliminary design phase, the ones directly related to the design of the unsprung components are summarized in the following sections.

1.2.1 Requirements and targets for systems involving unsprung components

The requirements for the unsprung masses are divided among the suspension, steering, braking, transmission and cooling systems. The system-level limitations and requisites for those systems that directly influence the design of the unsprung components are listed in this section. Additionally, the applicable competition restrictions are further discussed.

To begin with, the main stiffness and geometry constraints for the unsprung parts are determined by the suspension geometry and kinematics. These define the shape of the suspension arms, as well as their attachment points on both the body and the uprights.

[6] CFRP stands for *Carbon Fiber Reinforced Polymer.*

Lastly the wheel size defines the boundary within which the uprights can be developed. Table 5 summarizes the requirements and constraints for the suspension system in 2018.

Table 5: Suspensions system requirements and targets for 2018.

Requirement/ target type	Description
Competition rules [1]	*1. "The vehicle must be equipped with fully operational front and rear suspension systems including shock absorbers and a usable wheel travel of at least 50mm with driver seated (25mm jounce and 25mm rebound)"* *2. "The minimum static ground clearance of any portion of the vehicle, other than the tires, including a driver, must be a minimum of 30 mm"* *3. "All suspension mounting points must be visible at technical inspection, either by direct view or by removing any covers"*
Team targets	1. The maximum camber variation due to the compliance of the suspension elements must be lower than 0.1 deg. 2. The maximum rear toe angle variation due to the compliance of the suspension elements must be lower than 0.1 deg.
Requirements	1. The system must offer different possibilities for adjusting the pushrods length, static toe and camber angles. 2. The unsprung masses must fit within the envelope of a 13" wheel rim without interferences. 3. There must be a precise fit on each of the spherical joints. The radial and axial play must be minimized with respect to SC17.

Similar to the suspension system, the steering system dictates the location of the attachment points of the tie-rods in the front axle. In addition to that, it poses kinematic requirements related to the steering motion and stiffness requisites to limit the variations in the steering response originated from compliance. The steering system constraints affecting the unsprung mass are listed in Table 6.

Table 6: Steering system constraints and targets.

Requirement/ target type	Description
Competition rules [1]	1. *"All steerable wheels must have stops placed on the rack to prevent linkage lock up or tires from contacting any part of the vehicle"* 2. *"Allowable steering system free play is limited to a total of 7° measured at the steering wheel"*
Team targets	1. Target weight reduction: 30% 2. Steering ratio:3.46:1 3. Maximum steering angle variation due to tie rods and upright compliance: 0.1 deg. 4. The design must guarantee a maximum steering angle of the inner wheel equal to 27.2° with no interferences. 5. The assembly and maintenance operations must be simplified compared to the SC17. Possibility of adjusting the Ackerman angle.

Next, the unsprung parts of the powertrain system must be integrated into the uprights. This implies several specific considerations for the different interfaces. Table 7 summarizes the main requirements associated with this.

Table 7: Powertrain systems requirements and targets influencing the unsprung masses.

Requirement/ target type	Description
Competition rules [1]	1. *"Any cooling or lubrication system must be sealed to prevent leakage"* 2. *"The lowest point of any lubrication system can only be lower than the line between the lowest point of the main hoop and the lowest chassis member behind the lubrication system if it is protected from hitting the ground by a structure mounted directly to the chassis"*
Team targets	1. Transmission weight reduction: 25% 2. Final gear ratio= 14.8:1

Table 7: Powertrain systems requirements and targets influencing the unsprung masses (continued).

Requirements	1. Double stage planetary transmissions integrated on the wheel uprights. Optimization of the number of components compared to SC17. 2. Each motor will be equipped with cooling jackets produced through additive manufacturing. 3. The wheel bearings must be installed according to the technical specifications from the manufacturer. The bearing seats must have the appropriate sizes and tolerances to guarantee the proper functioning. 4. The bearing seats and motor flanges must have adequate stiffness to prevent any deformation that would compromise the correct operation of the transmissions. 5. The transmission system must be provided with filling, draining and venting holes to allow for oil changes. There must be a magnetic plug to collect the metallic particles produced by the normal wear of the gears. 6. The assembly and maintenance operations must be simplified compared to the SC17.

Finally, the Formula SAE/Student competitions impose several regulations on the braking system, because it is considered a safety critical area. Table 8 contains those rules that are directly related to the outboard part of the brakes, i.e., the components that are part of the unsprung masses.

Table 8: Braking System requirements affecting the unsprung masses.

Requirement/ target type	**Description**
Competition rules [1]	*1. "The vehicle must be equipped with a braking system that acts on all four wheels and is operated by a single control"* *2. "The brake system must have two independent hydraulic circuits (…) Each hydraulic circuit must have its own fluid reserve, either by the use of separate reservoirs or by the use of a dammed reservoir"* *3. "The braking systems must be protected from failure of the drivetrain (see T6.4.2) and from minor collisions"*

Table 8: Braking System requirements affecting the unsprung masses (continued).

Competition rules [1]	*4.*	*"In side view, any portion of the brake system that is mounted on the sprung part of the vehicle must not project below the lower surface of the chassis"*
	5.	*"The first 90% of the brake pedal travel may be used to regenerate brake energy without actuating the hydraulic brake system. The remaining brake pedal travel must directly actuate the hydraulic brake system, but brake energy regeneration may remain active."*
	6.	*"Regenerating energy is allowed and unrestricted but only when the vehicle speed is >5 km=h".*
Team targets	1.	Target weight reduction: 30%
	2.	Maximum deceleration: 1.8g[7]
	3.	The average temperature of the brake rotors in operation must be greater than that of the SC17 brakes, provided that it remains below 400°C.
	4.	The assembly and maintenance operations must be simplified compared to the SC17.

Additional competition regulations

In addition to the regulations that apply to different areas of the vehicles, the Formula SAE competitions have specific rules for the so-called "*critical fasteners"* [1]:

> *"Critical fasteners are defined as bolts, nuts, and other fasteners utilized in the primary structure, the steering, braking, driver's harness, suspension systems and those specifically designated as critical fasteners in the respective rule."*

According to this, the fasteners used in the unsprung masses are considered critical. Thus, they must meet or exceed the characteristics of ISO grade 8.8 [1] [2]. Additionally, all of them must be either hexagon head bolts according to DIN 933 or DIN 931 standards,

[7] This notation, commonly used in automotive engineering, expresses the acceleration values as multiples of the gravitational acceleration g=9.81 m/s^2. Thus, 1.75g means 1.75 x 9.81 m/s^2 = 17.18 m/s^2.

or socket head cap screws as specified by DIN 912 or DIN 7984. Moreover, all the threaded connections in critical locations must have at least two full threads exposed from the securing nut and must have a positive locking mechanism to prevent any loosening from vibrations. Nylon lock nuts cannot be used in high temperature locations.

All the competition rules mentioned so far are checked during the scrutineering, i.e., the first part of the technical inspection, before the car is allowed to enter the competition. Once the scrutineering is passed, the vehicle is required to pass other tests to be allowed to compete on any of the dynamic events of the competitions [2] [1]. Thus, these impose other design requirements to be considered.

Tilt test

The car is placed on a platform inclined at 45° to verify the absence of any type of leakage. Upon successfully passing this first step, the inclination is raised to 60° which represents a cornering force of 1.7g. To pass the test, all the wheels must remain in contact with the inclined platform.

Brake test procedure

The vehicle must perform a hard-braking maneuver after a straight-line acceleration. All the four wheels must be locked by using only the mechanical brakes. This is verified by turning the tractive system off at the end of the acceleration run. There are additional considerations regarding the tractive system but those are not directly related to this work.

1.2.2 Results from the preliminary analyses

1.2.2.1 Suspension geometry and loads

The Vehicle Dynamics division determined the suspension geometry for the SC18 car, specifying the locations of the *"hardpoints"*, i.e., the geometrical centers of all the spherical joints in the suspension mechanism. This determined the dimensions of the A-arms and the location of their attachments on the uprights.

Using a vehicle-centered reference system, the coordinates of the hardpoints were obtained and translated into a 3D sketch in Catia V5. This wireframe was used as base for all the other CAD models, including parts and assemblies, to ensure an accurate integration between the different vehicles systems of SC18. An image of the 3D wireframe with the Hardpoints is shown in Figure 25.

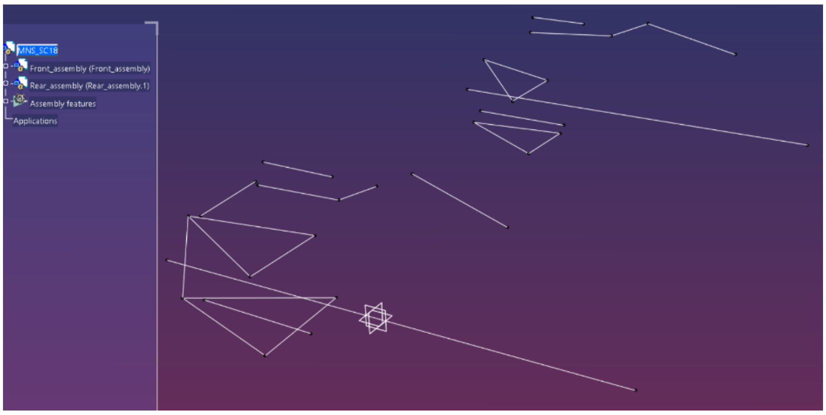

Figure 25: Screen capture of the hard points wireframe of the SC18 suspension used as reference geometry for developing the unsprung masses [28].

The Vehicle Dynamics division also determined the loads applied to each of the joints in the suspension system. Based on the longitudinal and lateral accelerations of the car center of gravity, the following load cases were defined:

- Hard Braking: straight-line hard braking maneuver at a deceleration rate of 1.75g.
- Turning: tight turn producing 2.2g of lateral acceleration.
- Brake in turn: a hypothetic situation in which the driver brakes while taking a turn, producing a longitudinal deceleration of 1g and a lateral acceleration of 1.5g.
- Acceleration in turn: longitudinal acceleration of 1g and lateral acceleration of 2g.

The forces at the outer ball joints are summarized in Table 9.

These maneuvers were considered the ones that would generate the highest loads through the suspension members and were used for dimensioning the unsprung components.

Table 9: Forces at the outer ball joints of the suspension members in the four load cases used for designing the unsprung components. X and Y directions are opposite to the reference frame shown in Figure 15.

Load case	Axle	Joint location	Force components [N]		
			X	Y	Z
Hard Braking 1.75g X	Front	LCAF	-2 582	-797	178
		UCAF	928	-697	125
		Tie rod	0	-468	30
	Rear	LCA	-1 042	-134	-48
		UCA	344	-205	14
		Tie rod	-11	-60	9
Turn 2.2g Y	Front	LCAF	184	2 889	-310
		UCAF	-182	-2 422	672
		Tie rod	-3	-696	62
	Rear	LCA	-49	3 497	-281
		UCA	26	-1 828	472
		Tie rod	22	129	-12
Brake in turn 1.0g X, 1.5g Y	Front	LCA	-1 892	1 008	-32
		UCA	529	-2 944	730
		Tie rod	-3	-761	70
	Rear	LCA	-1 041	1 377	-125
		UCA	353	-1 663	268
		Tie rod	-3	-19	11
Acceleration in turn 1.0g X, 2.0g Y	Front	LCA	734	2 866	-272
		UCA	124	-2 786	642
		Tie rod	1	304	-2
	Rear	LCA	450	4 102	-338
		UCA	727	-2 579	526
		Tie rod	-239	1 583	-184

1.2.2.2 Transmission envelope

The initial studies allowed the Powertrain division to determine the new gear train layout and obtain the outer envelope of the transmission, which is another constraint for the size of the wheel uprights. Figure 26 shows the transmission mechanism of SC17 which was the reference point for designing the SC18 gear train [12].

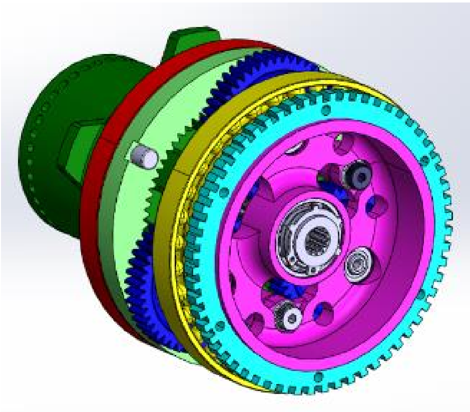

Figure 26 Transmission mechanism of the SC17 car.

To achieve the targets listed in Table 7, three key aspects were decided:

- The layout was changed: the sun gear was mounted on the motor shaft. This reduced the number of parts and the total length of the gear train.
- The spur gears module was reduced from 1.25 mm (on SC17) to 0.8 mm [12], obtaining a great reduction in the total size of the mechanism, compared to the previous year.
- The wheel bearings and shaft seal sizes were reduced accordingly.

Additionally, further studies showed that a transmission ratio of 14.5:1 was adequate for the SC18, instead of the initial estimate of 14.8:1 listed in Table 7.

Thanks to these measures, the new envelope was more compact than the SC17 one. A direct comparison can be seen in Figure 27. This geometry containing the features required to support the gear train elements (bearings, seals, ring gear, drain, fill and venting holes, motor attachment, etc.) was the baseline for designing the center of the wheel uprights.

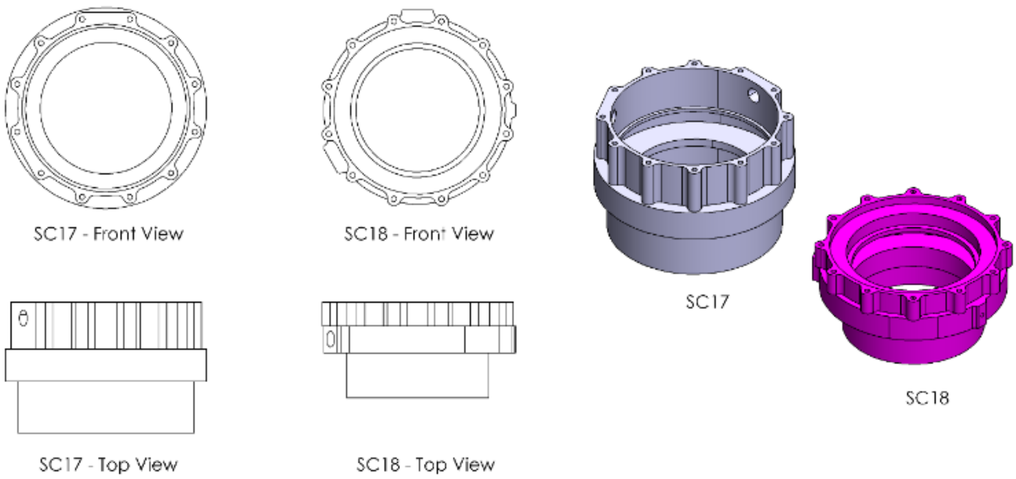

Figure 27 Preliminary SC18 transmission envelope [12] and comparison with SC17.

1.2.2.3 SC17 brakes performance

The performance of the SC17 brakes system was assessed in terms of the decelerations experienced during racing. This was done using the telemetry data from the 3-axis accelerometer [29] installed on the car, recorded through a Vector GL1000 Data Logger unit [30] connected to the vehicle's CAN network. It revealed that the maximum deceleration during most track events was in the range between 1.2g and 1.6g, with some peak values reaching 1.7g.

Figure 28 shows an extract of the longitudinal acceleration data collected during one of the runs of the Autocross event at the FSAE Italy 2017 competition. The top plot represents the decelerations in terms of g units and the second one the pressure applied to the front brakes. An evaluation of the filtered signals corresponding to the hardest braking maneuver from this sample dataset is shown in the third plot.

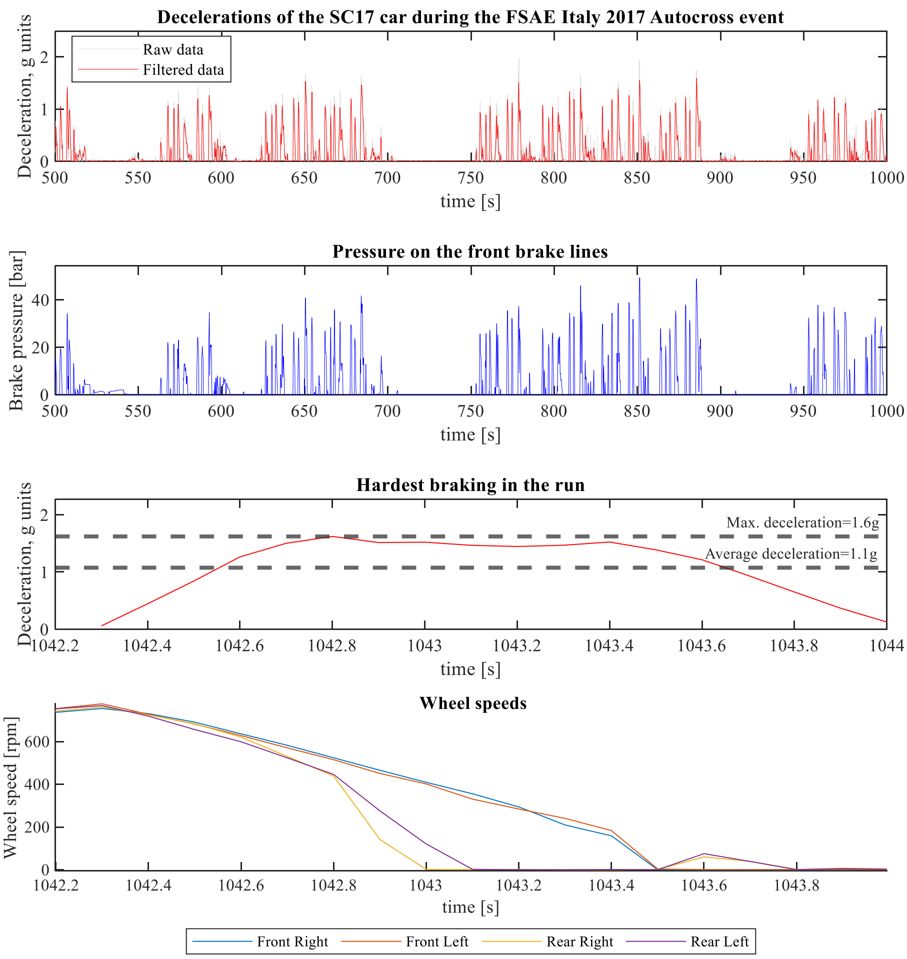

Figure 28: Decelerations and front brake circuit pressure during the FSAE Italy 2017 Autocross event.

This analysis was done in collaboration with the Vehicle Dynamics division of PoliTo Racing. They also performed several studies using the virtual simulation software *VI - grade* [31], finding that SC17 should be able to reach higher decelerations given its characteristics. The telemetry data also revealed an inadequate distribution of the braking loads, since early rear wheel lock up occurred during 7 and 25% of the braking maneuvers of the analyzed data logs.

A possible reason for the sub-optimal performance could be that the operating temperatures of the discs were below the ideal range for the brake pads, around 300°C. Figure 29 shows the variation of the friction coefficient of the Brembo Z04 brake pad compound used on the front brakes of SC17.

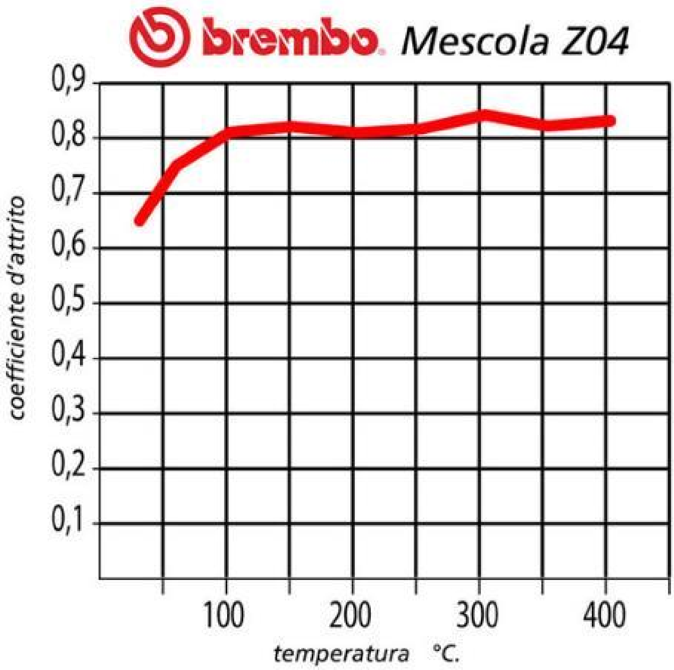

Figure 29: Friction coefficient of the brake pads compound used in the front brakes of SC17.

Unfortunately, there was no documented data available about the temperature measurements performed on the brake discs of SC17 during its development. The information collected from team members from previous years indicated that the temperatures were on the acceptable range between 100° and 400°C.

When aalyzing the weight-performance ratio, however, the SC17 brakes showed big opportunities for improvement. The outboard braking parts had the third biggest impact on the unsprung mass, as can be seen in Figure 30.

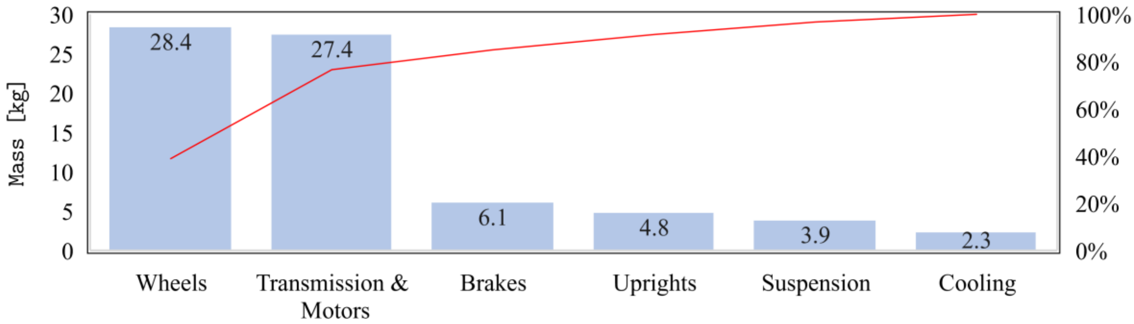

Figure 30: Distribution of the unsprung mass among the different systems of the SC17.

The SC17 braking system was based on commercially available parts provided by Brembo S.p.A. as part of a sponsorship agreement. The brake calipers and discs offered a consistent operation during the 2017 competitions, presenting no failures. The P4 30/34 brake calipers used on the front axle were CNC machined from a high strength aluminum alloy. They had 4 pistons in total and weighted 1030 g each one, including the brake pads. The rear brake calipers had a similar construction, but a much smaller size, weighting 262 g. Figure 31 shows the front and rear brake rotors and calipers of SC17.

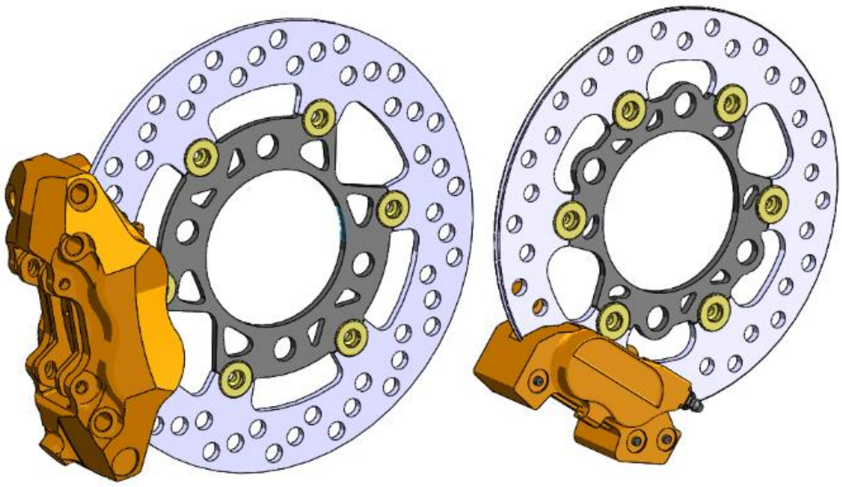

Figure 31: Front (left) and rear (right) outboard brakes of the SC17.

A benchmarking analysis indicated that the SC17 brakes were over-dimensioned compared to the Formula Student/SAE Electric competitors. In other words, they were excessively heavy for the loads developed by the formula car, especially the ones used in the front axle. Figure 32 shows some photos of brake discs and calipers used by other Formula Student teams.

Figure 32: Outboard brakes from some of the best competitors in previous years [32].

1.2.2.4 Steering system

The target steering parameters listed in Table 6 were decided to obtain a more direct steering response. This was accompanied by a change in the front caster angle from 5.57° to 6.87°. To prevent any type of interference between the suspension arms, the uprights and the wheels at large steering angles, a complete CAD assembly of SC18 was needed.

On the other hand, the steering system of the SC17 presented an excessive free play at the steering wheel. The cause was mainly the lack of stiffness in the upper steering column support. There was also too much radial clearance on the spherical joints at the ends of the tie rods due to inadequate tolerances in their attachment points on the steering rack and the uprights.

CHAPTER 2. DESIGN PHASE

This chapter summarizes the design process of the unsprung components, which began at the end of October 2017 (Figure 5). The first unsprung components to be designed were the ones belonging to the brakes system, since the definitive suspension hard points had not been decided yet. Next, the overall layout of the wheel assemblies was defined, and the design of the suspension elements and the wheel uprights started.

2.1 Brakes system design

At the start of the design phase, different possibilities for achieving the weight reduction targets listed in Table 8 were evaluated. This included a benchmarking analysis of the best competitors, and researching the different technical solutions that could be implemented for SC18.

The brake systems used by PoliTo Racing must comply with the regulations indicated in Table 8. A schematic diagram of the hydraulic layout of SC17 is shown in Figure 33. Each wheel is equipped with a brake caliper and a brake disc. As introduced in section 1.2.2.3, the front components were much heavier than the rear ones because of the different loads required during braking. The brake lines were routed directly from the two master cylinders to each wheel, and the force applied by the pedal was distributed between the front and rear circuits using a balance bar.

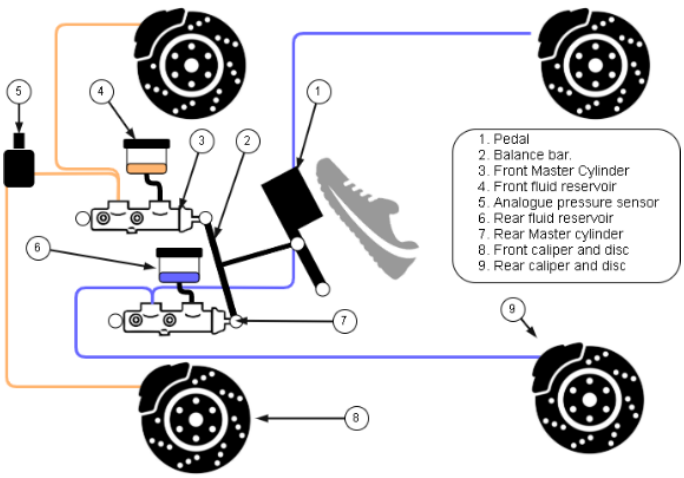

Figure 33: Layout of the SC17 brakes system.

In terms of unsprung components in the braking system, the calipers were the heaviest and most complex ones. For this reason, one of the first tasks was determining the best way to achieve the weight reduction target shown in Table 8 with focus on the brake calipers.

2.1.1 Possibilities for weight saving on the brake calipers

Usually, fixed-type calipers are used in Formula SAE cars because of their design simplicity and lightweight compared to floating-type calipers [33]. Standard motorcycle calipers are often used, although some teams choose to develop their own components. Figure 34 shows two different solutions adopted by some of the best competitors in the Formula SAE events.

Figure 34: Custom-made brake calipers and brake systems layouts adopted by two of the main competitors [83] [35].

The use of modern manufacturing technologies such as Selective Laser Sintering (SLS) or Selective Laser Melting (SLM) (Figure 34, left) allows creating complex geometries that would be impossible to obtain using traditional machining techniques. This widens the possibilities for weight optimization. Nevertheless, the components obtained by SLS often possess reduced surface quality and tolerances compared to machined ones, and additional *post-processing* operations are required [34]. The need for removing support materials as well as careful control of the possible distortions on the parts requires specific know-how that only an experienced technical partner could offer for developing critical parts such as the brake calipers.

The right side of Figure 34 shows a photo of the wheel assembly of the DUT14 car of the Technical University of Delft [35]. Both the brake calipers and rotors were designed and manufactured by the team to achieve optimal packaging. They used 10” wheels having a reduced space compared to the 13” ones used by the PoliTo Racing Team for the 2018 season.

The alternative to developing customized calipers is to adapt commercial parts, designed for other applications as in SC17. The drawback of this option is the limited weight optimization that can be achieved using existing parts. However, PoliTo Racing maintained a sponsorship agreement with Brembo S.p.A., and this meant that high-performance, reliable brake parts could be provided by them at no cost.

Considering the weight reduction targets as well as the available resources (time, budget, know-how), using Brembo calipers was a more viable option than developing custom ones. Table 10 shows a decision matrix with the different aspects considered in this decision.

Table 10: Matrix used for the Make vs Buy decision regarding the brake calipers.

Brake calipers choice	Weight	Performance	Reliability	Serviceability	Development time	Cost	Total
SC17	★	★★★★★	★★★★★	★★	★★★★★	★★★★★	23
Custom-made CNC machined	★★★★	★★★★	★★★★	★★★	★★	★★★	20
Custom-made Additive manufactured	★★★★★	★★★★	★★★	★★	★	★★	17
Commercially available (Brembo S.p.A.)	★★★	★★★★★	★★★★★	★★	★★★★	★★★★★	24

2.1.2 Brake caliper selection

To choose the particular caliper models to be used, the first step was to estimate the load distribution between the front and rear axles, considering the target maximum deceleration, and the overall vehicle dimensions. Figure 35 shows a schematic representation of the forces involved during braking.

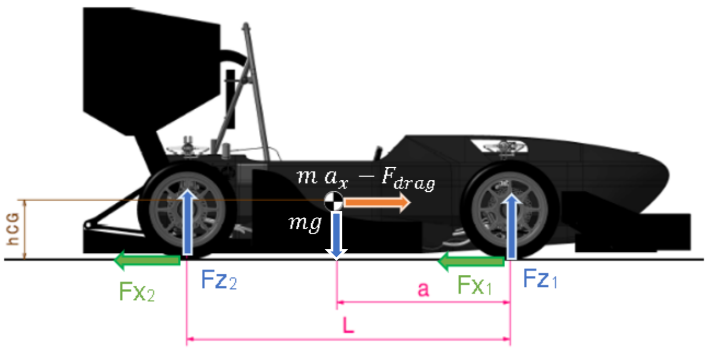

Figure 35: Schematic representation of the vehicle loads during braking.

The vertical tire loads during a braking maneuver can be obtained by [10]

$$Fz_{1_{braked}} = Fz_{1_{static}} + \Delta Fz \tag{15}$$

$$Fz_{2_{braked}} = Fz_{2_{static}} - \Delta Fz \tag{16}$$

where the subscripts 1 and 2 refer to the front and rear axles, respectively. The static axle loads correspond to the vertical forces present while the vehicle is travelling at a constant speed. Thus, these include the standing still load distribution and the aerodynamic downforces. The term ΔFz represents the longitudinal load transfer during braking, given by the expression [10]

$$\Delta Fz = ma_x \left(\frac{h_{CG}}{l}\right) \qquad (17),$$

in which a_x is the magnitude of the acceleration during the braking maneuver, h_{CG} is the center of gravity height with respect to the ground and l is the car wheelbase. Thus, using the information from the preliminary design, an initial estimate of the load distribution during a braking maneuver starting from 100 km/h was made. This speed value was chosen because it was the highest speed registered during the FSAE Italy 2017 autocross event. The data used is reported in Table 11.

Table 11: Assumed vehicle data for estimating axle loads during braking.

Vehicle Data	
Target mass (with 65 kg driver)	270 kg
a_x (target deceleration)	1.8g
a (X location CG)	838 mm
h_{CG} (CG to ground)	245 mm
Wheelbase	1525 mm
Front aero downforce[8] @ 100km/h	673 N
Rear aero downforce @ 100 km/h	759 N

Consequently, the vertical loads on the tires and the braking forces on each axle were estimated using (15) to (17) and (1), respectively. The results are summarized in Table 12.

[8] This data was provided by the Aerodynamics division of the PoliTo Racing team. Using separate lift coefficients for the front and rear axles accounts for the pitching moment generated by the drag force and the additional load change generated.

Table 12: Initial estimates of the axle loads during braking.

ΔF_z [N]	$F_{z1_{braked}}$ [N]	$F_{z2_{braked}}$ [N]	F_{x_1} [N]	F_{x_2} [N]
765	2630	1449	4735	2609

This represents an ideal case in which the numerical value of the longitudinal friction coefficient of the front and rear tires is equal to that of the target deceleration (1.8). It is used to simplify the calculations at the early stage. In reality, the maximum deceleration is limited by the tire adhesion coefficients and likely to be lower than the value used here. Moreover, the longitudinal friction coefficient of the rear wheels is usually higher than that of the front ones due to the load sensitivity of pneumatic tires [33].

From the braking force estimates, the brake torque required for a single wheel in the axle i can be obtained from

$$T_{brake_i} = \frac{F_{x_i}}{2} R_{l_i} \tag{18},$$

being R_l the loaded wheel radius. Lastly, to produce this torque, the pressure on the brake circuit acting on the axle of study must be

$$p_{line_i} = \frac{T_{brake_i}}{r_{pad_i}} \cdot \frac{1}{A_{c_i} \mu_{pads_i}} \tag{19},$$

where r_{pad} is the effective radius of the swept area or rubbing path where the pad enters in contact with the rotor [33]. This is approximated as the radius of the centroid of the pads contact area, as shown in Figure 36. For the initial estimates, r_{pad} was assumed to be equal to the values of the SC17 car, 94 mm for the front axle and 83 mm for the rear one. The symbol A_c represents the sum of the surface areas of the caliper pistons, and μ_{pads} is the friction coefficient between the brake pads lining and the rotor.

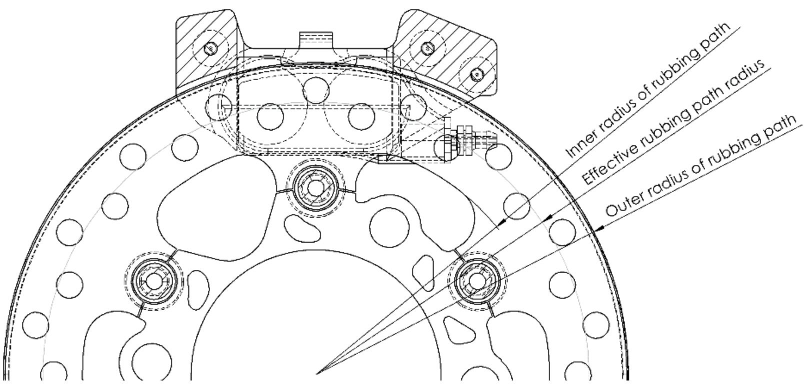

Figure 36: Effective rubbing path radius.

Using lighter (smaller) brake calipers usually requires higher pressure values in the brake circuit to achieve the required brake torque. Therefore, one of the main limitations for reducing the size of the calipers is the maximum pressure that can be applied on a brake line. This is mainly determined by the maximum pressure that the components used in the hydraulic circuit can withstand. Moreover, designing a hydraulic circuit that requires high pressures to provide the target decelerations means that the drivers will need to exert greater forces at the brake pedal. This can be compensated by changing the characteristics of the brake pedal, but the packaging constraints inside the cockpit limit the design possibilities. Figure 37 shows the different caliper models that were considered for the front and rear brake circuits. The weight of each one is contrasted with the hydraulic pressure that would be required in the circuit according to the initial estimates using (18) and (19).

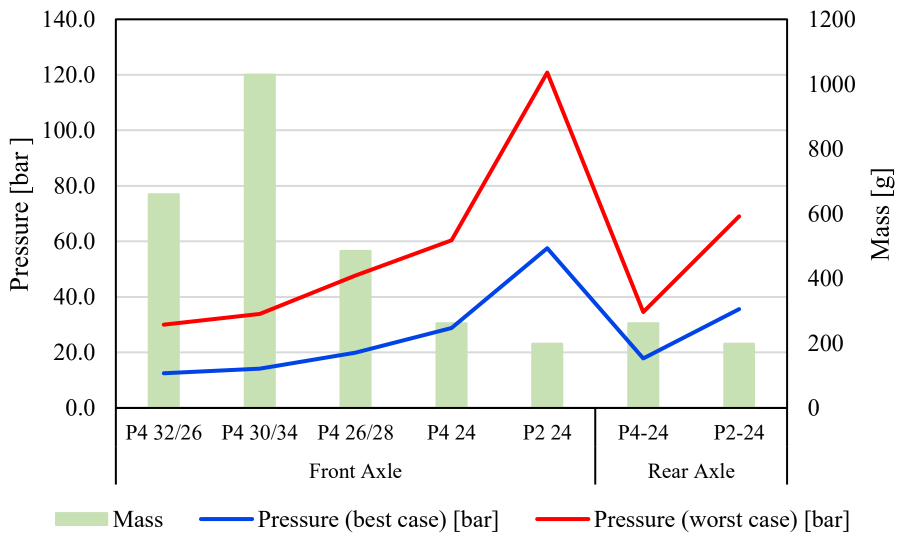

Figure 37: Caliper models considered for the SC18.

For the front circuit, the best candidate was the P4 24 model. This was the same model used in the rear axle of SC17. It offered an acceptable balance between weight and hydraulic pressure, considering that the maximum pressure values in the front circuit of SC17 were in the range between 15 to 35 bar. Peak values around 40 bar were registered by the data acquisition system in different events. On the other hand, this caliper model represents a 75% weight reduction compared to the P4 30/34.

For the rear circuit, the only suitable commercial option for reducing weight was the P2 24 model. It would require circuit pressures from 36 to 69 bar for the best and worst cases, respectively.

Both the P4 24 and the P2 24 calipers are commercialized by Brembo as rear calipers for motorcycles and their rated operating pressure is 40 bar, while the estimated pressure values for SC18 were higher. However, the maximum rated pressure indicated by Brembo is the one that guarantees an infinite mechanical life during a long-term operation. Since the Formula Student/SAE season lasts only one year, and the competitions take place for only 3 months, an infinite mechanical life was not necessary for SC18. Moreover, Brembo confirmed that the calipers would be able to withstand up to 250 bar as required by the homologation that they must comply with. For this reasons, using the P4/24 and P2/24 calipers on SC18 at the pressure ranges shown in Figure 37 was acceptable, knowing that they would have a reduced service life.

Besides the diameter of the caliper pistons, the hydraulic pressure required in the brake circuits depends also on the effective radius of the brake pads centroid. Larger radii result in lower pressure requirements, which is evident from (19). Nevertheless, increasing the effective radius of the brake caliper means incrementing the brake disc diameter and the size of the caliper brackets on the uprights. Considering the weight reduction and stiffness targets for the uprights (Table 5), the aim was to avoid increasing the effective caliper radius and accept higher pressures in the brake lines.

Nevertheless, the highest values of pressure reported in Figure 37 correspond to absolute worst cases and the actual operating pressures would be closer to the lower values. This is because the required brake torques were obtained using the ideal calculations for wheel adherence. Additionally, the hydraulic pressures shown in Figure 37 were obtained considering different values of the brake pads coefficient of friction as shown in Figure 38. The worst cases considered lower pad friction coefficients, this way, higher pressures are needed to produce the required brake torque.

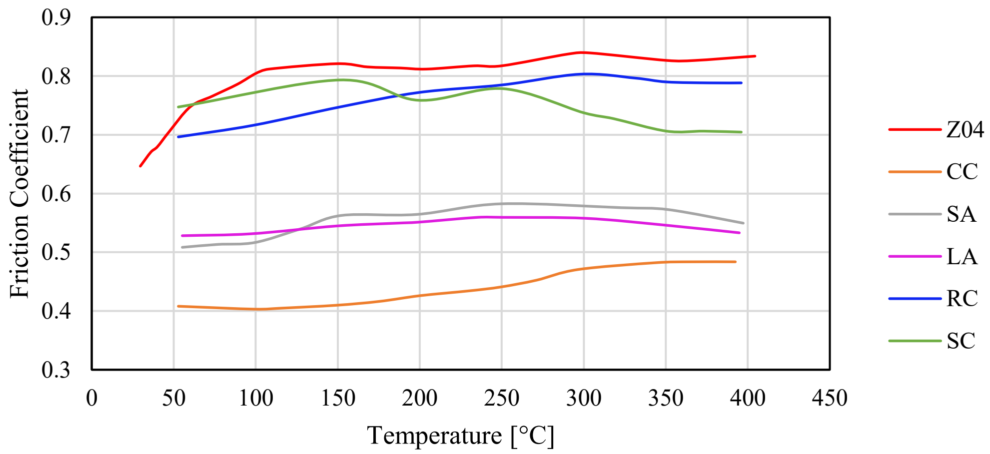

Figure 38: Friction coefficients for different brake pad compounds. Source: Brembo.

As introduced in section 1.2.2.3 the front calipers of SC17 featured brake pads having the Brembo high-performance Z04 compound [36]. For the P4 24 and P2 24 caliper models there were no brake pads based on the Z04 material. The best available option was the H38 sintered compound, which was claimed to be well suited for sports applications, with slightly lower performance characteristics that the Z04 one [36].

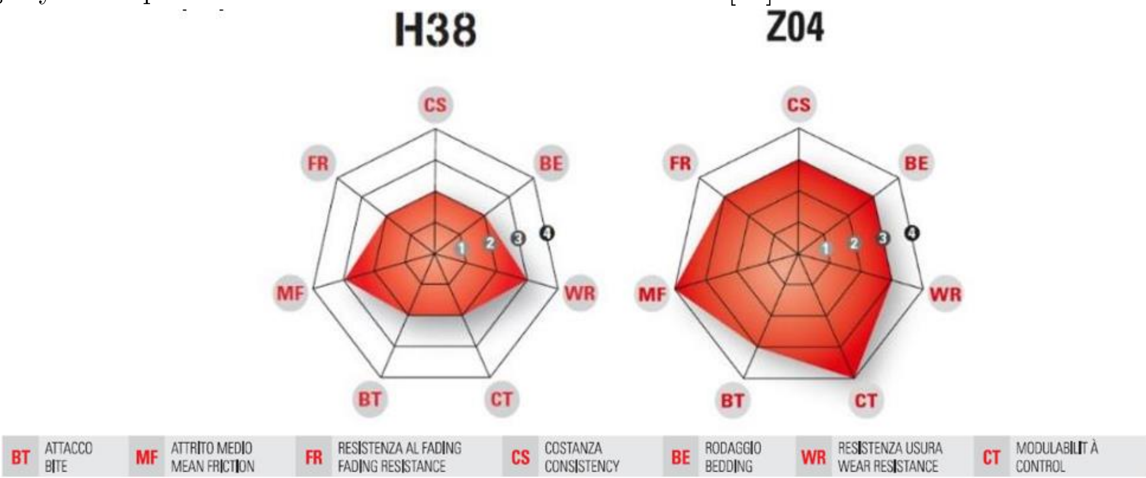

Figure 39 shows a qualitative comparison between the two materials.

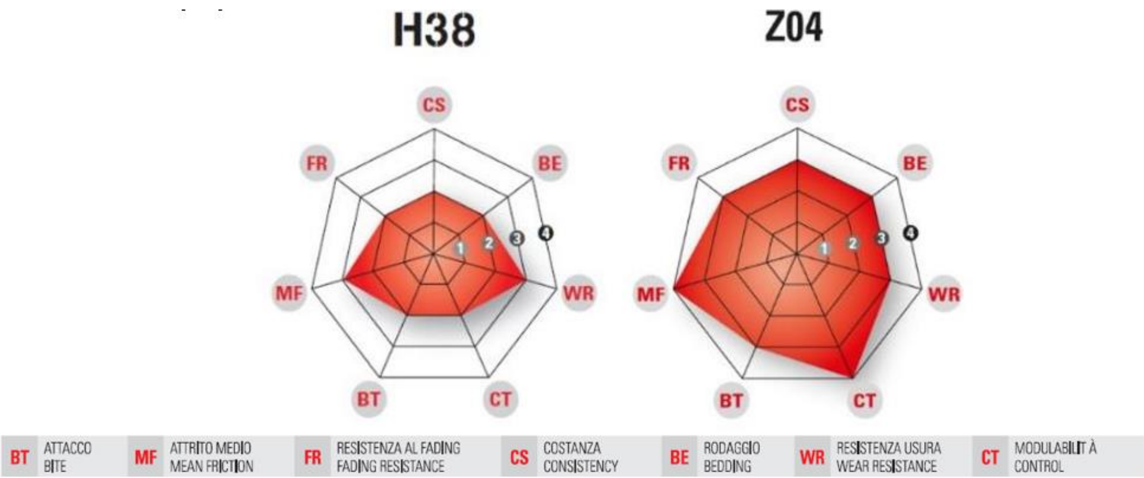

Figure 39: Qualitative comparison between the H38 and Z04 brake pad compound. Adapted from [36]

Since no specific data about the properties of the H38 compound was available, for the best case it was assumed to be similar to the RC lining (for sports use) shown in Figure 38, and for the worst case it was considered as the LA material (for road driving). The SAE J661 Brake Lining Quality Test Procedure specifies that the designation code H should be used for compounds providing a friction coefficient higher than 0.55 at 588 K [25]. However, it was unknown whether the commercial name H38 matched the SAE J661 designation.

2.1.3 Load distribution study

Having selected the brake calipers, it is necessary to define the rest of the hydraulic components to determine the distribution of the brake loads. This is essential for designing the brake discs later on. The master cylinders and brake pedal ratios were chosen based on the pedal effort required and the packaging constraints inside the cockpit. The calculations and methods used for doing so can be found in references [10] and [25]. For brevity, the characteristics of the chosen hydraulic components are summarized in Table 13.

Table 13: Characteristics of the hydraulic components selected for the SC18 brakes system.

	Front caliper	Rear caliper	Front Master Cylinder	Rear Master Cylinder	Pedal ratio
Pistons diameter [mm]	24	24	19	16	3
Number of pistons	4	2	-	-	
Total pistons area [mm^2]	1809.6	904.8	283.5	201	

Knowing the hydraulic characteristics of the braking system, the distribution of the braking loads can be studied. The starting point is defining a ratio between the braking torques in the front and rear axles [18]. For a given pedal force F_{pedal}, this ratio is

$$K_b = \frac{T_{\mathrm{brake}_1}}{T_{\mathrm{brake}_2}} = \frac{\frac{F_{\mathrm{pedal}}}{A_{\mathrm{MC}_1}} \times \frac{l_2}{L_{\mathrm{bar}}} \times r_{\mathrm{pad}_1} \times A_{C_1} \times \mu_{pad_i}}{\frac{F_{\mathrm{pedal}}}{A_{\mathrm{MC}_2}} \times \frac{l_1}{L_{\mathrm{bar}}} \times r_{\mathrm{pad}_2} \times A_{C_2} \times \mu_{pad_i}} \tag{20}$$

A_{MC_1} and A_{MC_2} are the areas of the master cylinder pistons in the front and rear circuits, respectively. L_{bar} is the effective length of the balance bar that connects the master cylinders with the brake pedal. The lengths l_1 and l_2 are the relative distances from the master cylinders to the balance bar pivot center, as shown in Figure 40.

Since both the front and rear calipers feature the same type of brake pad lining, it is possible to assume the same value of friction coefficient for both axles, and expression (20) is simplified as

$$K_b = \left(\frac{l_2}{l_1}\right) \left(\frac{A_{\mathrm{MC}_2} \times r_{\mathrm{pad}_1} \times A_{C_1}}{A_{\mathrm{MC}_1} \times r_{\mathrm{pad}_2} \times A_{C_2}}\right) \tag{21}$$

By defining the dimensions of the brake calipers and master cylinders, and the effective radius of the front and rear discs, the only variable that can be used to adjust this is the balance bar position. It is possible to define this adjustment as

$$\%Front\ Bias = \frac{l_2}{L_{bar}} \times 100 \tag{22},$$

which represents the percentage of the total pedal force that is transferred to the front master cylinder. Thus, for arbitrary values of Fx_1, the corresponding value of Fx_2 produced by the braking system can be obtained from

$$Fx_{2_{real}} = \frac{Fx_{1_{input}}}{K_b} \tag{23}$$

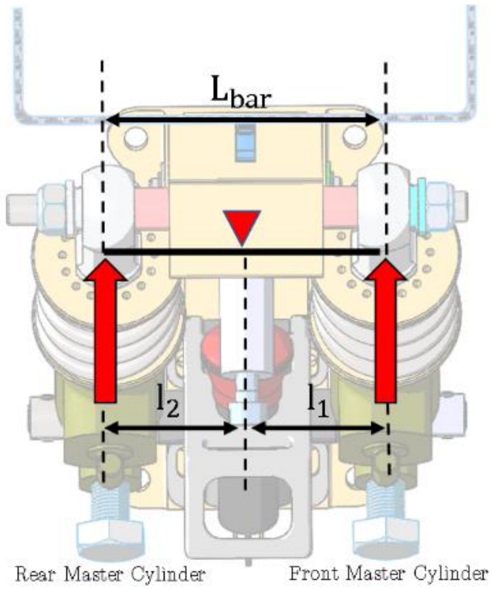

Figure 40: Brake balance bar of the SC18 car.

Expression (23) allows comparing the real system response for different front bias adjustments with the ideal brake force distribution that would be obtained if all tires had the same longitudinal friction coefficients. This ideal brake force distribution can be found from the relationship

$$\begin{aligned}\left(Fx_{1_{input}} - Fx_{2_{ideal}}\right) = \mu_x \Bigg(&\frac{m\,g}{l}\left(b - a + \mu_x\, 2\, h_{cg}\right) \\ &+ \left(Fz_{aero_1} - Fz_{aero_2}\right) - \frac{2\,F_{drag}\,h_{cg}}{l} + \frac{2\mu_x\left(Fz_{aero_1} + Fz_{aero_2}\right) h_{cg}}{l}\Bigg)\end{aligned} \tag{24}$$

where $\mu_x = \frac{Fx_{1_{input}} + Fx_{2_{ideal}}}{mg + Fz_{aero_1} + Fz_{aero_2}}$

and $Fz_{aero_i} = \frac{1}{2}\rho_{air} C_{z_i} S V^2$. The factors $C_{z_1}S$=1.504 and $C_{z_2}S = 1.696$ were provided by the Aerodynamics division of PoliTo Racing.

Solving (24) for $Fx_{2_{ideal}}$, the ideal brake force distribution is obtained for different values of vehicle speed at the start of a stopping maneuver. Figure 41 shows a comparison between the ideal braking curves and the system responses of the SC18 car (on the top plot) and those of the SC7 (bottom plot) for different balance bar settings.

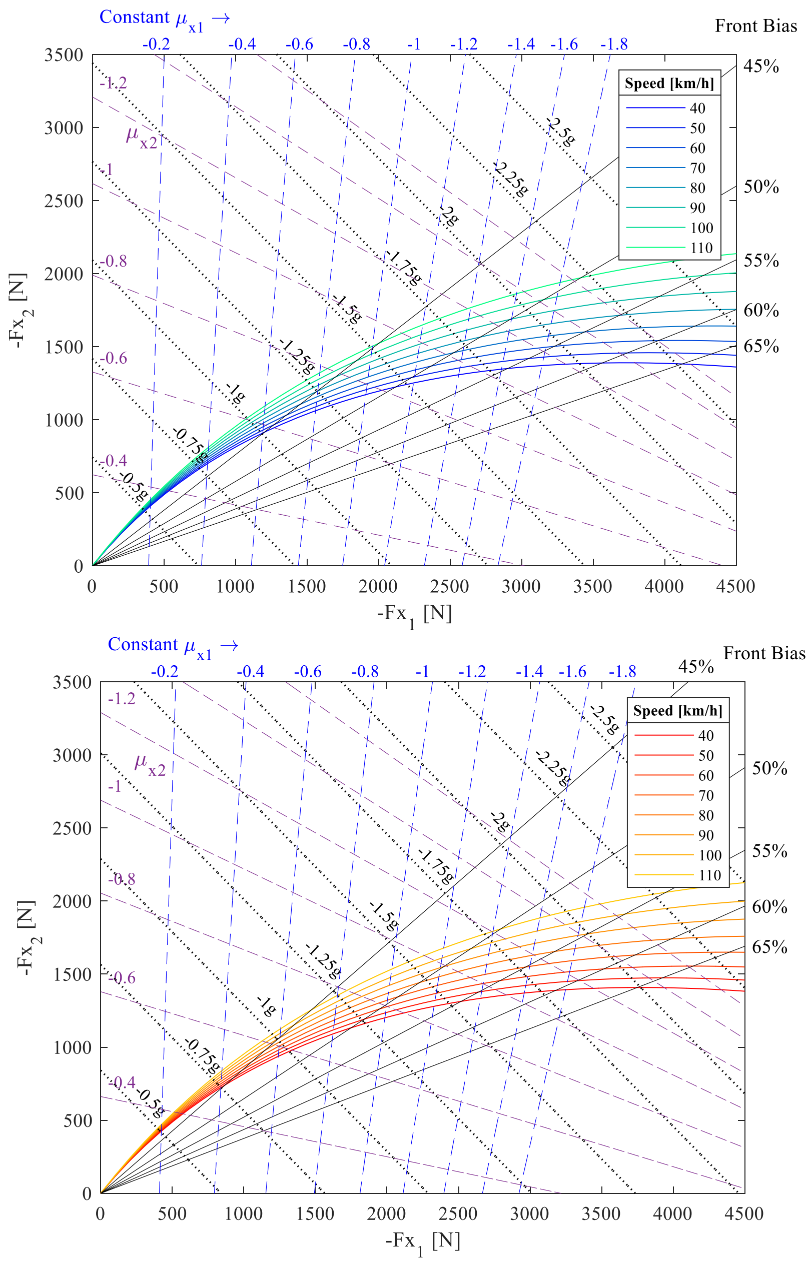

Figure 41: Ideal brake loads and actual system response of the SC18 (top) and SC17 (bottom).

As can be seen, the relationship between the ideal front and rear brake forces is parabolic. It is a function of the geometrical and inertial properties of the vehicle, and does not depend on the configuration of the brakes system [25].

Conversely, the real system response follows a straight line, with a slope equal to K_b. Different response lines are obtained by changing the front bias percentage; the more biased the system is towards the front axle, the less steep its response curve. This represents a greater difference between the force applied in the front and rear axles.

The information given by the curves of ideal brake loads is useful to gain insights during the design process to match the system response to the best configuration. In reality, the ideal (also known as "optimal" [25]) braking force distribution, occurs only under a very specific set of circumstances for a given vehicle.

The "*critical deceleration*" is the maximum rate at which the car can be braked maintaining the directional stability [25]. In the optimal braking forces plot, this value is represented by the point at which the system response intercepts the ideal force distribution curve [25]. Having different curves for different values of vehicle speed, there is a critical deceleration for each one. Since the target weight of the SC18 car is lower compared to the SC17, it could reach higher decelerations for a given operating speed range.

For instance, looking at the SC18 system response for 50% front bias, it intercepts the optimum curve corresponding to a vehicle speed of 70 km/h at a deceleration of approximately 1.7g. Conversely, for SC17, the 50% front biased system response shows a critical deceleration of 1.4g at the same speed. If a 55% front biased configuration was used in the SC17, the critical deceleration for the same speed would be almost exactly 1.75g. However, this would only occur provided that the longitudinal friction coefficient of the front wheels is close to -1.6, while in the case of the SC18, the required front friction coefficient is approximately -1.35. The SC18 is more likely to achieve a good performance because the estimated magnitude of the longitudinal friction coefficients seen in the past Formula SAE events were most of the time below 1.5.

From the optimal force distribution plot, it is possible to see that, for higher speeds, the amount of front brake bias required to match the ideal behavior is lower. Thus, to decide the adequate front bias setup range, it was necessary to determine the most frequent range of speeds at which the car would be driven. To this aim, the Vehicle Dynamics division of PoliTo Racing studied the percentage distribution of the speeds of SC17 during different track events in 2017. This was compared with the most frequent speed at which the braking maneuvers were started. Some of the results can be seen in Figure 42.

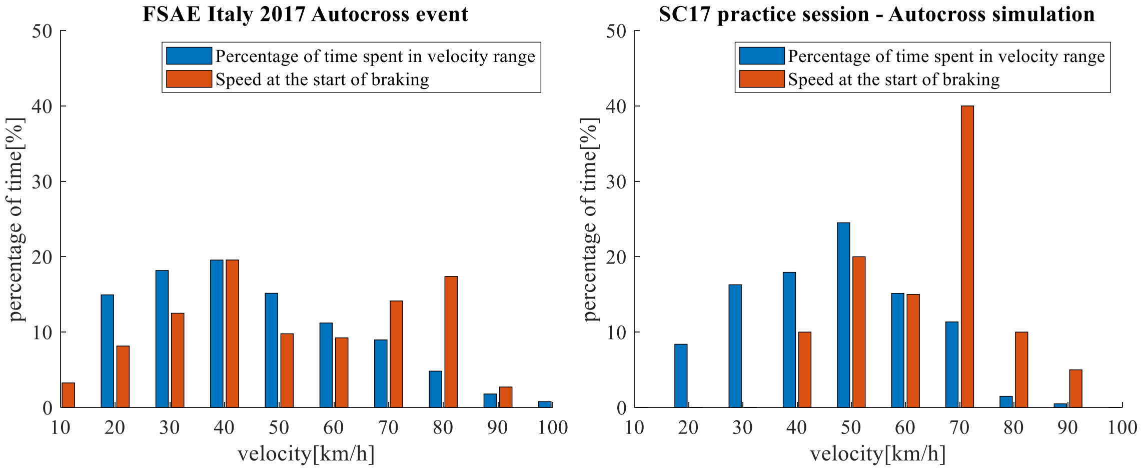

Figure 42: Analysis of the SC17 speed distribution.

Clearly, the conditions at which the braking maneuvers take place are very different for each circuit and vary from driver to driver. Nevertheless, the analysis showed that the most common speed range at which the drivers started to brake was between 50 and 80 km/h. Thus, a 50% front bias was chosen as baseline configuration for the SC18 car. This should offer the possibility of braking at rates between -1.5 and -1.7g for the speed range between 40 and 70 km/h, and the target deceleration of -1.8g for braking maneuvers initiated at 80 km/h. This theoretical setup would be adjusted based on different factors, such as the actual speeds reached in a given circuit, asphalt conditions and drivers preferences.

2.1.3.1 Proportional valve

Using a brake line pressure reducer valve [25] or fixed-setting pressure regulating valve [37] could allow adjusting the brake load distribution of the system by modifying the rate of pressure increase for the rear brakes above a defined change -over or “knee” point. Figure 43 shows the wide range of adjustments that could be achieved using a Tilton CP3550-14 proportional valve.

Despite the potential improvements in braking performance offered by the brake line pressure reducer valves, the inclusion of one of these in the SC18 system was discarded based in the following considerations:

- The weight of the commercially available and potentially suitable valves oscillated between 150 and 230 grams (180 for the Tilton CP3550-14 one). This was not in accordance with the weight reduction targets for the 2018 season.
- The pressure regulating valve would represent an additional cost that was not considered in the initial budget.

- To take full advantage of the characteristics of the valve, it would be necessary to have dedicated brakes tuning sessions, in different circuit layouts before the first competition, FSAE Italy in mid July 2018. The Team schedule did not have enough testing time prior to the competition to guarantee an effective use of the valve that would justify the additional weight and cost.

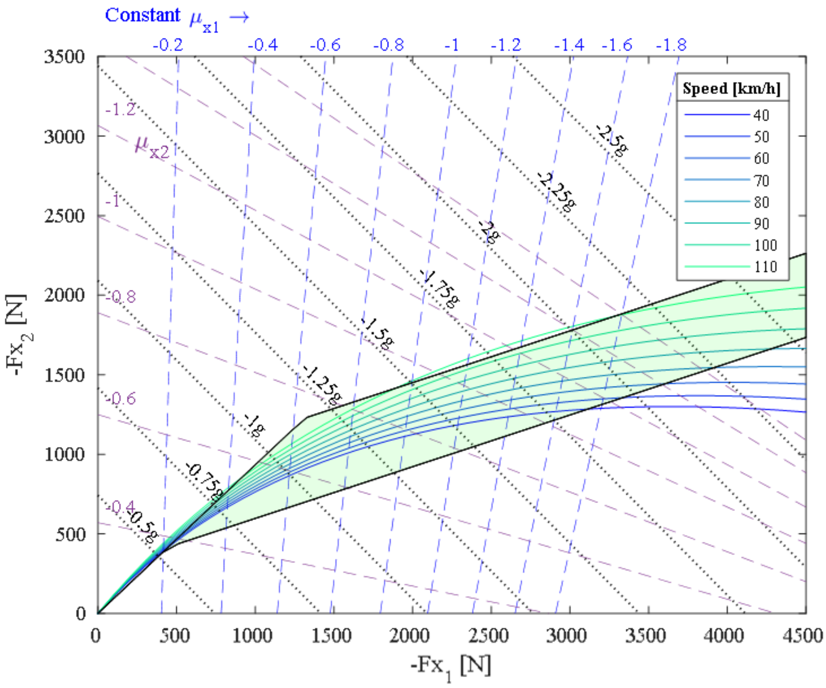

Figure 43: Regulation possibilities using a Tilton CP3550-14 proportional valve with a balance bar setup having a 40% front bias.

2.1.3.2 Effects of Regenerative Braking

The IWMs used in the SC18 were capable of producing a regenerative braking action during the Formula SAE Endurance events. Besides allowing recharging the battery pack during a race, the regenerative braking reduces the loads experienced by the mechanical braking components. This is because of the additional braking torque provided by the electric motors. The estimated electric braking torque contribution used for the SC18 was 200 Nm for the front wheels and 87 Nm for the rear wheels. This contribution can be active only during the first 90% of the brake pedal travel [1, 2]. However, since the mechanical brakes were designed to work under the worst use case with no regenerative braking, these considerations will not be discussed in detail in the following chapters, although they have a relevant effect on the control strategies and the brakes system design.

2.1.4 Brake rotors design

The first step for designing the brake rotors was to decide which type of outboard brakes would be used. Disc brakes are the default alternative for Formula SAE cars because they are lightweight and provide an effective braking action. Additionally, their simplicity of construction and packaging makes them a good choice for the formula car. The non-ventilated or "solid" type brake disc, commonly used in motorcycling [36], is widely adopted among the competitors (see Figure 32). The brake rotors used in the SC17 car were floating-type discs, constructed in two parts: a titanium center (the "disc carrier" or "mounting bell"), fixed to the wheel hub, and a stainless-steel outer part in which the rubbing surface of the pads is present. When the kinetic energy of the rotor is converted into heat in the friction surface, the disc is subjected to a thermal expansion. By allowing it to move freely, relative to the mounting face, it can expand and shrink without constraints, reducing undesirable effects such as warping or coning [33] [38]. This type of construction was also chosen for the SC18 brake rotors.

The next task was determining the maximum brake torques experienced by the rotors. Axle torques were determined in section 2.1.3 for assessing the maximum operating pressures required in the circuits to fully utilize the tire adhesion under ideal conditions. However, the longitudinal tire friction coefficient assumed when calculating the load distribution for the worst cases was -1.8, which was greater than the real values expected on the Formula SAE tracks. Additionally, the actual pressures on the brakes circuit is limited by the effective force exerted by the driver and the mechanical advantage of the brake pedal. Thus, the values of Fx_1 and Fx_2 reported in Table 12 are excessively conservative for designing the brake rotors in terms of mechanical resistance.

For this reason, the design loads for the brake rotors were defined using the information from the actual system response. Although the target deceleration rate during braking was -1.8g, the brake rotors were dimensioned considering the loads that would be required to brake at a rate of -2.2g. This deceleration rate was unlikely to be seen in reality, but this decision was made because the brakes represent a safety-critical system.

From Figure 41, we can see that the system response of the SC18 having a 55% front-biased setup intercepts ideal brake distribution curve for 80 km/h and the -2.25g constant deceleration line at approximately 4000 N of braking force for the front axle and 1800 N for the rear one. Using (18), the braking torques were computed, considering a loaded wheel radius of 237 mm for both axles. The tangential forces produced at the interface between the discs and the pads was obtained by dividing the applied torque by the effective pad radii. The results are reported in Table 14.

Table 14: Forces used for dimensioning the brake rotors in terms of mechanical resistance.

	Front Brakes	**Rear Brakes**
Longitudinal axle force [N]	4000	1800
Brake disc torque [Nm]	474	213
Effective pad rubbing path radius [mm]	94	83
Tangential disc force [N]	5043	2570
Compression force [N]	6303	3212
Circuit pressure [bar]	35	36
Deceleration rate	-2.25g	
Initial speed	80 km/h	

2.1.4.1 Determining the energy converted into heat by the brake rotors

Designing lighter brake rotors to reach the 30% weight reduction target for the brakes system required determining the thermal loads applied to the brake discs and calipers to size them accordingly.

The total amount of energy that must be converted into heat by the braking system is given by equation (10), presented in the introductory chapter. To develop the thermal design, it is necessary to determine the portion of this heat corresponding to a single brake. To do this, the so-called "brake force distribution" or "brake balance" factor [25] is defined by the ratio of the braking force on the rear axle to the total braking forces developed by the wheels:

$$\Phi = \frac{F_{x_2}}{F_{x_2}+F_{x_1}} \tag{25}$$

From it, we can obtain the total energy absorbed by one of the front brake discs when the vehicle is decelerated from and initial speed $V_{initial}$ to a final speed V_{final}

$$\Delta E_{b_1} = (1-\Phi)\left(\frac{m}{2}\left(V_{initial}^2 - V_{final}^2\right) - F_{drag} d_{brake}\right) + \frac{I_1}{2}\left(\omega_{initial}^2 - \omega_{final}^2\right) \tag{26}$$

And the energy absorbed by one of the rear discs:

$$\Delta E_{b_2} = \Phi\left(\frac{m}{2}\left(V_{initial}^2 - V_{final}^2\right) - F_{drag} d_{brake}\right) + \frac{I_1}{2}\left(\omega_{initial}^2 - \omega_{final}^2\right) \tag{27}$$

The distance d_{brake}can be determined by imposing a target average deceleration a_x,

$$d_{brake} = \frac{V_{final}^2 - V_{initial}^2}{2a_x} \tag{28}$$

The drag force is calculated at the mean speed during the braking maneuver:

$$F_{drag} = \frac{1}{2}\,\rho_{air}\,C_x\,S\,\left(\frac{V_{initial}+V_{final}}{2}\right)^2 \tag{29}$$

Using expressions (25) to (29), the energy converted into heat by each rotor was determined. This was done considering a hard-braking maneuver, in which the car is completely stopped from an initial speed of 110 km/h, representing an emergency brake during one of the FSAE events at the target maximum rate of 1.8g. The data used and the results obtained are summarized in Table 15.

Table 15: Energy converted into heat in the front and rear brake rotors.

Results		Data					
	E_b [J]	I [kg m^2]	Φ	a_x [m/s^2]	$V_{initial}$ [km/h]	V_{final} [km/h]	C_xS
Front axle	45596	0.354	0.31	-17.65	110	0	1.12
Rear Axle	22440	0.353					

Knowing the worst-case total energy dissipated at the rotors allows determining their Single Stop Temperature Rise (SSTR) [33], which is an indicator of the thermal capacity of a brake disc and can be used for comparison purposes at the early design stage. It can be determined using expression (11) discussed in the introductory section vi, assigning a partition coefficient p equal to 1. Thus, the SSTR assumes that the proportion of kinetic energy dissipated by the front or rear brake is entirely converted to heat and absorbed by the rotor neglecting all forms of surface heat loss. Table 16 shows different values of the SSTR for the front and rear brake rotors. The comparison was made using the characteristics of the SC17 brake discs as a baseline. The discs material was assumed to be a martensitic stainless-steel alloy with a constant heat capacity equal to 460 J/Kg K [39].

Table 16: SSTR comparison for different values of mass.

	Front Rotor				Rear Rotor			
% Mass reduction	**SC17**	-10%	-20%	-30%	**SC17**	-10%	-20%	-30%
Mass [kg]	**0.499**	0.449	0.399	0.349	**0.395**	0.355	0.316	0.276
SSTR [°C]	**198**	220	248	283	**123**	137	154	176

Hence, from this worst-case evaluation, a 30% weight reduction on the brake rotors would produce a 42% increase in the maximum temperature rise during a worst-case single stop, provided that only the mass of the rotor is changed, and the material properties are the same.

2.1.4.2 Thermal analysis of the brake rotors

Since the SSTR approach neglects all the heat transfer mechanisms taking place during the operation of the brakes, it cannot be used to design the brake discs. As mentioned before, it is just an indicator of how critical the temperature rise is during a worst-case hard-brake and the effect of changing the mass of the rotors.

In practice, three heat transfer mechanisms determine the total temperature increase [25]. During the operation of the brakes, part of the heat flows into the rotors and other portion is transferred to the brake pads and caliper by thermal conduction. The expression (11) takes this into account by including the coefficient that determines what "partition" of the braking energy is absorbed by the brake rotor. This factor depends on the material properties of the rotor and the brake pads, as well as the surface areas in which the rubbing action takes place. The heat partition coefficient is given by [33] [25]:

$$p = \frac{\sqrt{\left(k_{disc}\, C_{p_{disc}}\, \rho_{disc}\right)}\, S_{disc}}{\sqrt{\left(k_{disc}\, C_{p_{disc}}\, \rho_{disc}\right)}\, S_{disc} + \sqrt{\left(k_{pads}\, C_{p_{pads}}\, \rho_{pads}\right)}\, S_{pads}} \tag{30}$$

Where k, Cp and ρ are the thermal conductivity in W/ m K, the specific heat capacity in J/kg K and the material density in kg/m^3, respectively. S is the friction surface area in m^2. The subscripts $disc$ and $pads$ refer to the properties of the material of which the brake disc and the pads are constructed, respectively. Generally, for most material and geometry combinations, about 98% of the total heat flows into the brake discs, while only a 2% is transferred to the pads [33]. In addition to that, the cooling effects from radiation and convective heat transfer determine the temperature variations in time.

To consider the temporal effects, the braking power in a particular wheel can be considered as equal to the amount of energy that is converted into heat divided by the duration of the braking maneuver [25]:

$$P = \frac{d(E_{b_i})}{dt} \tag{31}$$

For a constant brake torque applied to the rotor, the instantaneous power can be obtained from the product

$$P_{i_{(t)}} = T_{brake} \cdot \omega_{i_{(t)}} \tag{32}$$

Thus, using equations (31) and (32), the temperature rise given by (11) can be computed more realistically for different instants of time using

$$\Delta T = \frac{(T_{brake} \cdot \omega_{i(t)} \cdot p - \dot{Q}_{conv_i} - \dot{Q}_{rad_i})\, t_i}{m_{disc} C_{p_{disc}}} \tag{33}$$

$\dot{Q}_{conv_i}$ and $\dot{Q}_{rad_i}$ are the heat losses per unit time due to the convection and radiation heat transfer mechanisms, respectively. The radiative heat transfer is given by [26]

$$\dot{Q}_{rad_i} = \epsilon \cdot \sigma \cdot A_{disc} \cdot T_{disc}^4 \tag{34}$$

A_{disc} is the total surface area of the brake disc in m^2, $\sigma = 5.670 \times 10^{-8}\ \frac{\mathrm{W}}{\mathrm{m^2\,K}}$ is the Stefan–Boltzmann constant and ϵ is the emissivity factor associated to the disc surface. Different values of the emissivity factor are found in the literature [26] for various materials and surface conditions.

Regarding the convective heat transfer, it is governed by the equation [26]

$$\dot{Q}_{conv} = \bar{h} \cdot A_{disc} \cdot (T_\infty - T_{disc}) \tag{35}$$

where h is the average heat transfer coefficient, in W/m^{2}K and T_∞ is the temperature of the air surrounding the brake disc, in K. The average heat transfer coefficient can be obtained from the average Nusselt number, which provides a measure of the convection heat transfer occurring at a surface, independently of the spatial variables in the problem of study [26]. The relationship between the average Nusselt number and the average heat transfer coefficient is given by [26]

$$\overline{Nu} = \frac{\bar{h}L}{k_{air}} \tag{36}$$

This number depends on several factors including the local temperatures and flow conditions, as well as the geometries involved in the thermal problem that is being solved [26]. Several empirical correlations have been found for simple geometrical shapes under determined types of flows, temperatures and turbulent or laminar regimes; these can be used in combination, to a certain extent, to estimate the thermal heat transfer coefficient for a more complex situation [26].

2.1.4.3 Analytical estimation of the average heat transfer coefficient

To determine a convection heat transfer coefficient that could be used for analyzing the thermal response of the brake rotors, the most realistic approach would be to perform an experimental study and obtain an empirical correlation applicable to the flow conditions in the wheels of the Formula SAE car. The next method was to use Computational Fluid Dynamics (CFD) to analyze the heat transfer between the disc brakes and the environment and determine the heat transfer coefficient based on the results from the numerical simulations. For the Unsprung Masses division, setting up a reliable CFD study was time-consuming, and would require additional time to learn how to properly utilize the computational tools. Thus, the initial estimates of the heat transfer coefficient were determined analytically. To use the empirical correlations available in the literature, the problem was decomposed in the following basic cases:

Cylindrical body

The outer edge of the brake discs was considered as a cylindrical body with length equal to the thickness of the rotor. The air was considered as flowing around the cylindrical edge at the vehicle speed and the average Nusselt number was obtained using the Hilpert correlation for flows over cylinders [26]. It is valid for Prandtl numbers greater or equal than 0.7.

$$\overline{h_{cyl}} = \frac{C\, Re_D^m Pr_f^{13} k_{air_f}}{2\, r_{disc}} \tag{37}$$

Planar body

The sides of the brake disc are considered a planar plate with a length much greater than the rotor thickness and the air flow at the vehicle speed is assumed to be parallel to the surface. For laminar flows, the plate is considered to be isothermal and the average heat transfer coefficient can be obtained from [26]

$$\overline{h_{plate}} = \frac{0.664\, Re_L^{1/2}\, Pr_f^{1/3}\, k_{air_f}}{2\, r_{disc}} \qquad Pr \geq 0.6 \tag{38}$$

For turbulent flows, the plate is assumed to have a constant heat flow and the average heat transfer coefficient is given by

$$\overline{h_{plate}} = \frac{0.680\, Re_L^{1/2}\, Pr_f^{1/3}\, k_{air_f}}{2\, r_{disc}} \tag{39}$$

Rotating thin disc

The thickness of the brake disc is neglected, and the heat transfer coefficient is found for the friction surface using the empirical correlation proposed by Latour, Bouvier and Harmand [40] for a rotating thing disc with transverse air crossflow:

$$\overline{h_{rot}} = \frac{\sqrt{\left(0.036\, Re_U^{0.8}\right)^2 + \left(0.556\, Re_\omega^{0.5}\right)^2}\, k_{air_f}}{2\, r_{disc}} \qquad \frac{Re_\omega}{Re_L} > 0.18 \tag{40}$$

The subscript f in expressions (37), (38), (39) and (40) means that the air properties and the flow conditions are evaluated at the so-called film temperature, which is the mean temperature between the solid body (the brake disc) and the surrounding air.

The combined contribution of the three heat transfer coefficients found for each vehicle speed was obtained considering the relative areas applicable for each one of the correlations used:

- The cylindrical body simplification was only associated with the small area around the edge of the rotor, $A_{edge} = 2\pi\, r_{outer} t_{disc}$, being t_{disc} the thickness of the disc.
- The coefficients obtained from the flat plate and the rotating thin disc assumptions were related to the side area of the discs, A_{side} considering the holes present on the SC17 car and including the surface area of the attachments between the rotor and the disc carrier. This last portion of the area was determined using a CAD model of the SC17 rotors in CATIA V5.

Hence, the equivalent heat transfer coefficient was defined as

$$\overline{h_{equiv}} = \left(\overline{h_{rot}} + 2\,\overline{h_{plate}}\right) R_{side} + \overline{h_{cyl}}\, R_{edge}$$

where $$R_{side} = \frac{A_{side}}{2\,A_{side} + A_{holes} + A_{edge}} \qquad R_{edge} = \frac{A_{edge}}{2\,A_{side} + A_{holes} + A_{edge}} \qquad (41)$$

Additionally, two experimental correlations for approximating the heat transfer coefficient of non-ventilated disc brakes mentioned in Brakes Design and Safety by Rudolf Limpert [25] were evaluated. These were obtained using experimental data collected from a light truck, meaning that the flow conditions were not the same as in the Formula SAE car. The heat transfer coefficients calculated using this correlation are shown in Figure 44. Figure 45 shows the results obtained for a disc temperature of 150°C.

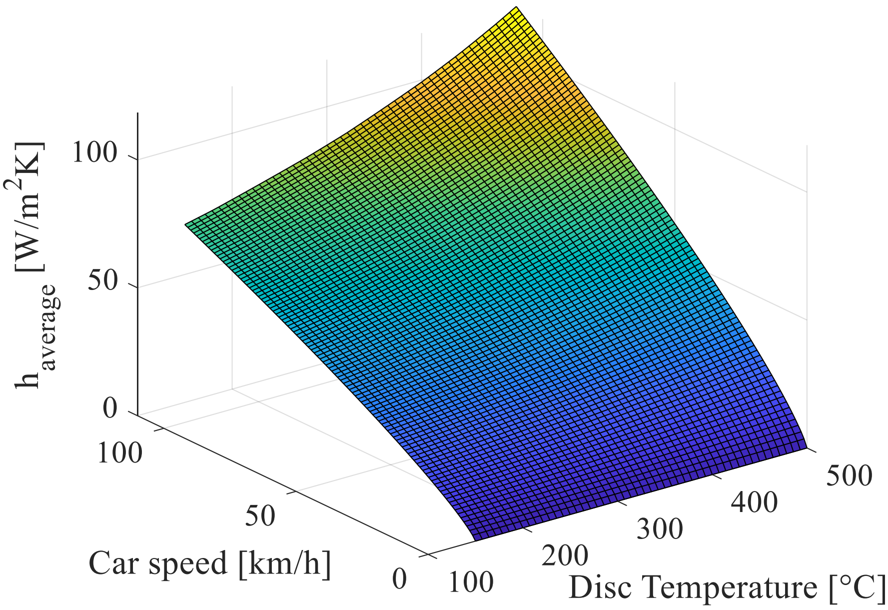

Figure 44: Heat transfer coefficients calculated using the correlation from R. Limpert [19].

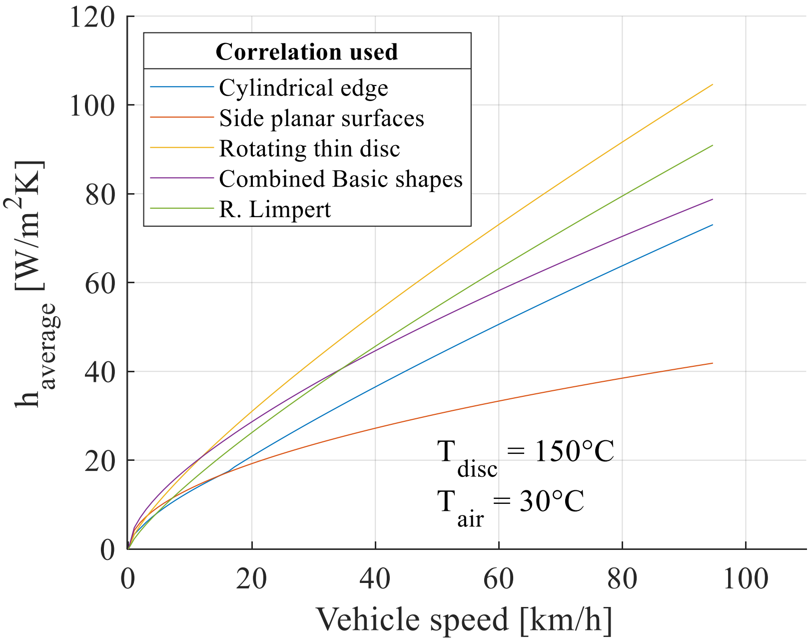

Figure 45: Average heat transfer coefficients of the SC17 front brake disc at varying vehicle speeds for a disc temperature of 150°C.

The calculations were done for brake rotors with the characteristics of the front and rear discs used in the SC17. The magnitude of the air velocity around the brake disc was considered as if it was equal to that of the vehicle speed, which was increased linearly from

0 to 110 km/h. Then, the Reynolds number $Re_L = Re_U = Re_D$ was calculated at each speed value. The *rotational* Reynolds number Re_ω was determined at the angular speed of the rotor corresponding to each vehicle speed.

At 60 km/h, the combined effect of the different correlations for basic shapes provided a value of 58 W/m^{2}K. From the combines correlations, the biggest contribution comes from the one that considers the rotation of the rotor.

Overall, the results indicated that the relationship between the heat transfer coefficient and the vehicle speed could be approximated as a straight line above 20 km/h. The values of the average convection coefficient were not very different from those obtained by the researchers Belhocine and a Bouchetara [41]. They performed a thermal analysis of a solid disc brake using Ansys CFX [42], although the characteristics of the rotor that they analyzed were different. Also, the results obtained by Lillo Harún [43] in his thesis work showed similar values using the decomposition approach to combine different empirical correlations, although the correlations that he used were different. The simulations performed by Tang, Bryant and Qi [44] produced similar results for the heat transfer coefficient in the external surfaces of a ventilated disc brake during a single brake application. On the other hand, the results from the CFD studies realized by Kothawade et. al. [45] were much higher. The brake rotors that they analyzed had similar characteristics to the ones used by the PoliTo Racing Team. Also, Vidiya and Singh [46] obtained an average heat transfer coefficient of 243.5 W/m^{2}K for a solid brake disc performing a full-vehicle simulation of a Formula SAE car travelling at 50 km/h. Thus, it was not clear to which extent the results could be applicable to the actual conditions in the PoliTo racing car.

Considering the uncertainty regarding the accuracy of the results, it was decided to analyze the thermal response of the SC17 rotors and use the results as a baseline to develop the new ones, aiming for a comparatively higher work temperature within a safe margin from the recommended range of 400°C. This would allow advancing the design process and obtaining a more rigorous validation at a later stage.

To consider the variation in time of the power transferred to the rotor, equation (33) was solved to obtain the temperature rise of a front brake rotor during a single stop. The initial conditions are the same reported in Table 15. The difference from the previous ones is that this new calculation is that it included the convection and radiation heat losses, as well as the heat partition coefficient given by (30), which was evaluated for different combinations of material properties, shown in Table 17.

Table 17: Thermophysical properties of the materials considered during the thermal study of the brake rotors.

Material	Thermophysical Properties		
	Thermal Conductivity [W/m K]	Density [kg/m³]	Specific Heat [J/kg K]
AISI 410 stainless steel [47]	24.9	7740	460
AISI 446 stainless steel [47]	21	7800	486
Aluminum-based MMC [48]	180	2760	950
Ti6Al4 titanium alloy [49]	6.7	4430	526
AISI 1060 carbon steel [49]	49.8	7850	502
ASTM 40 gray cast iron [49]	53.3	7150	490
Brake pads [50] [51]	12	2500	900

Although in reality the average heat transfer coefficient is influenced by on the temperature of the solid body, in this case it was only affected by the vehicle speed during the braking maneuver. The thermal power and the resulting temperature response can be seen in Figure 46.

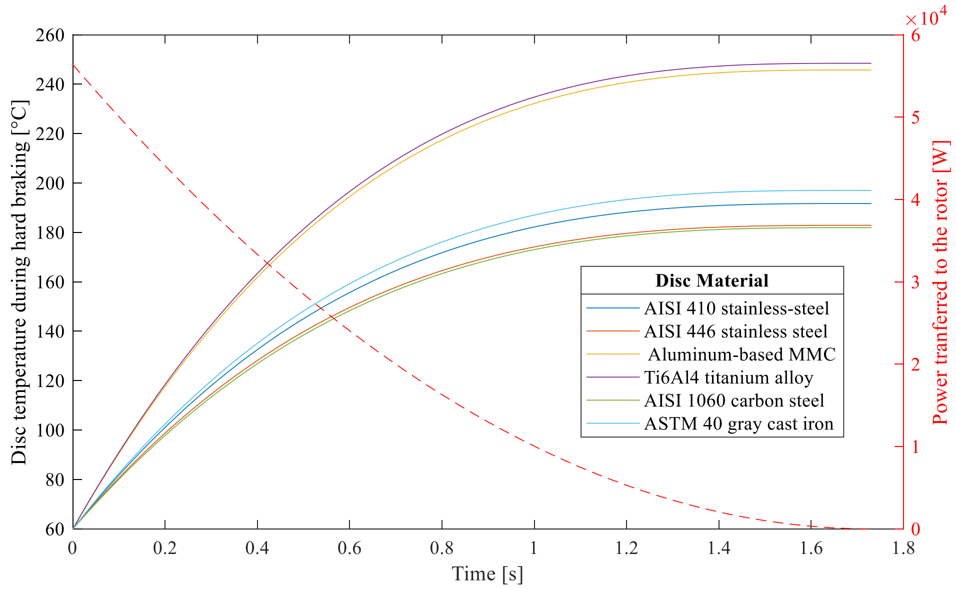

Figure 46: Thermal response of the front brake rotor during a single stop for different materials.

The Ti6Al4 alloy and the Aluminum-based MMC material exhibited a remarkably higher temperature rise compared to the other candidates.

During this type of maneuver, the effects of the material properties and the total mass dominate over the amounts of heat lost by convection and radiation [25] [52]. Despite the fact that the densities of the Aluminum-based MMC and the Ti6Al4 alloy are approximately 64% and 43% lower than those of the steel alloys, it would be necessary to add a considerable amount of mass to the brake discs to compensate for the excessive temperature rise during its operation. Nevertheless, the single-stop analysis is only indicative, and the real behavior of the brake rotors during a race can be better modelled considering the continuous operation of the brakes [25].

2.1.4.4 Simplified model: temperature response during continuous operation

The temperature of a brake rotor after the nth application of the brakes, can be obtained by combining (14) and (33), which results in the expression [25]

$$T_{disc(n)} = T_\infty + \frac{\left(1 - \mathrm{e}^{(-n\,Bi\,Fo)}\right)\Delta T_{disc(n-1)}}{1 - \mathrm{e}^{(-\,Bi\,Fo)}} \tag{42}$$

It allows estimating the response of the brakes during a continuous operation, which is more realistic. This approach is similar to the ones used by several some researchers [53] [54], although less accurate in terms of the temperature distribution across the brake rotor, since it is considered as a lumped body with uniform temperature distribution after verifying the condition (12).

Based on the information about the mean velocity of the SC17 car during the endurance events, and the most frequent speeds at which the braking maneuvers were initiated (see examples in Figure 42), the response of the front and rear SC17 brake rotors was modelled. A cooling time of 5 s was assumed between each application of the brakes, representing the time spent before reaching the next curve entry. The input data is summarized in Table 18 and the results for both rotors are shown in Figure 47.

Table 18: Data used for modelling the continuous operation of the brakes.

n	t_{cool} [s]	m [kg]	I [kg m^2]	Φ	a_x [m/s^2]	$V_{initial}$ [km/h]	V_{final} [km/h]	C_xS
100	5	270	0.354	0.31	-17.65	65	50	1.12

For the front discs made of steel alloys and gray cast iron, the stabilization temperatures were very close to the 400 °C limit, while the titanium alloy and the MMC surpassed it. Clearly, this is largely influenced by the initial and final speeds assumed, as well as the cooling time between maneuvers. Although the initial and final speeds used to simulate the continuous application of the brakes do not represent the maximum ones seen during the competitions, they simulate the average car speeds for most track events. The deceleration rate of 1.8g is the target maximum value for the SC18, while in reality, most braking maneuvers for the SC17 were performed at around 1g. Still, changing the simulated deceleration value from 1.8 to 1 had a little influence in the final stabilization temperatures. Instead, increasing the assumed cooling time between braking maneuvers produced an important reduction in the final temperatures. The value of 5 s was chosen based on the telemetry data from SC17, being the most representative of the actual conditions in the FSAE Italy 2017 endurance event.

Given the evidence from the 2017 season indicating that the discs did not work at the maximum desired temperatures, the results seen in Figure 47 were considered higher than the actual thermal conditions of the SC17 brakes.

However, for the rear rotor, since the stabilization temperatures were below 300 °C even under such a conservative analysis, this indicated that the opportunities for reducing its weight were much greater than those for the front discs.

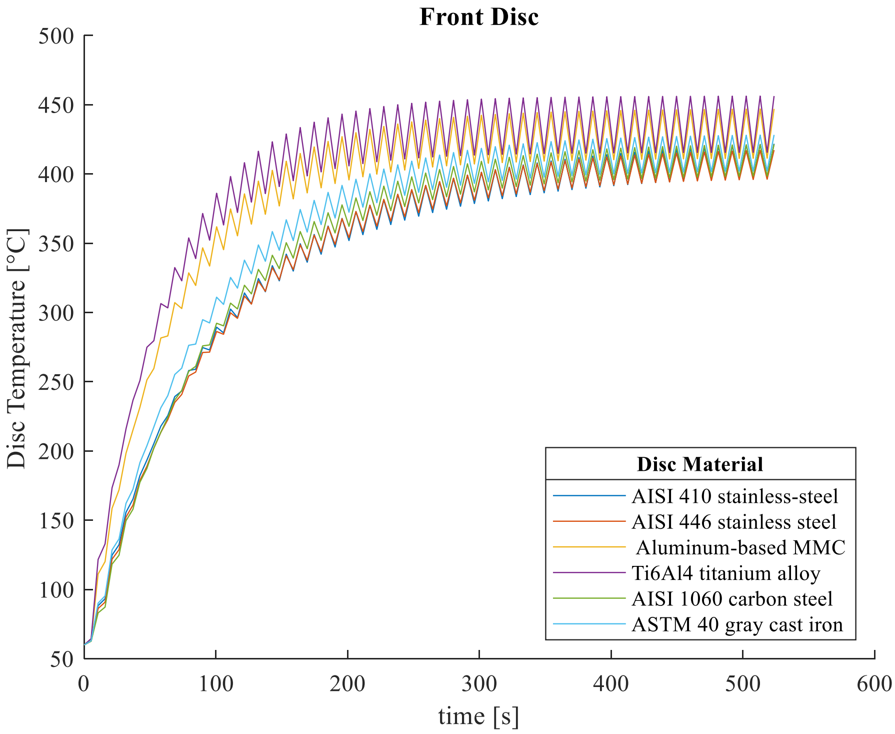

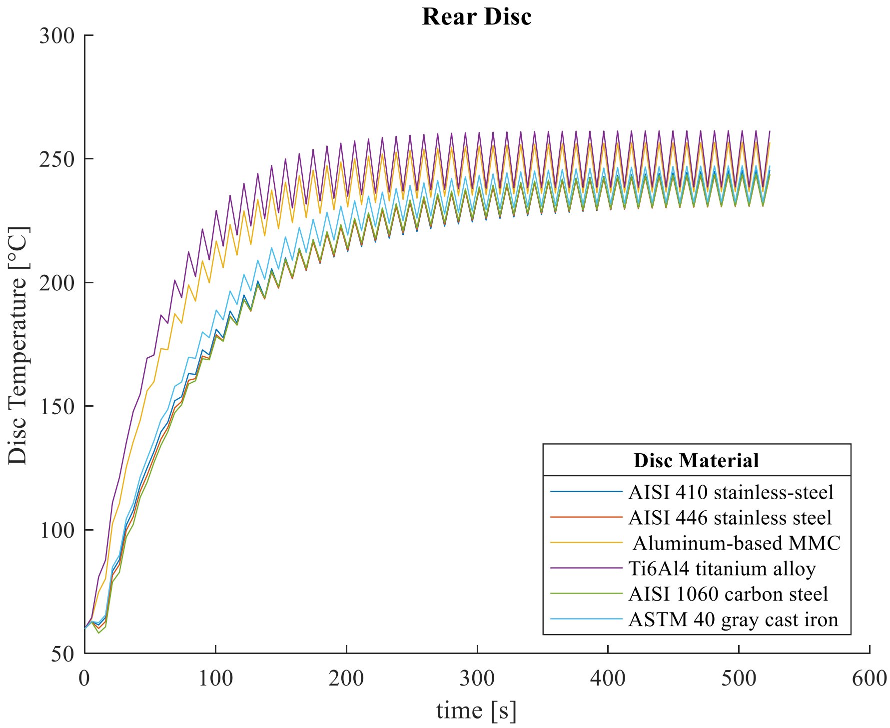

Figure 47: Analytical model of the temperatures of the SC17 brakes during continuous operation.

2.1.4.5 Calculation of disc temperatures using telemetry data from SC17

To overcome the limitation of the analytical model for the continuous operation of the brakes, in terms of dependency on the assumed velocities and cooling times, the temperatures of the brake rotors were estimated from the data recorded from the sensors installed in the SC17.

The car was equipped with pressure transducer (Honeywell PX3 Series model PX3AG1BS046BAAAX [55]) used for measuring the hydraulic pressure in the front circuit. Additionally, the speeds of the 4 in-wheel electric motors were recorded with the encoders built into the IWMs with a sampling frequency of 100 Hz.

Using (33), the temperature rise of the SC17 brake rotors was calculated for an Endurance event data log (FSAE Italy 2017). The expression (19) was used to calculate the brake torque applied to each disc using the pressure data and assuming a constant pad friction coefficient of 0.8. The hydraulic pressure of the rear circuit was determined from the front pressure values using

$$p_{rear} = p_{front}\left(\frac{100-\%Frontbias}{\%Frontbias}\right)\left(\frac{A_{\mathrm{MC}_1}}{A_{\mathrm{MC}_2}}\right) \tag{43}$$

assuming a balance bar front bias percentage of 60%.

The applied torque and power were calculated for each data point. Next, using an iterative script, the heat transfer coefficients were evaluated at the vehicle speed of the current iteration and used to solve (35) and (33)to determine the temperature change in the rotors. The temperature variation at each iteration was added to the disc temperature value from the previous iteration.

Three different correlations were used to determine the heat transfer coefficients at each vehicle speed. The first one was the one discussed in the previous section, based on the combination of empirical correlations for basic shapes. The second one was the experimental correlation for disc brakes of light trucks presented in the book from Rudolf Limpert. In third place, the average heat transfer coefficients mentioned by Vidiya and Singh [46] were used as reference.

The ambient air temperature was assumed to be 30°C and the initial temperature of the rotors 60°C. The heat partition coefficient was assumed as constant, equal to 0.83, and the radiation heat transfer was neglected, due to its small contribution to the thermal balance [25]. The resulting calculated temperature and brake power for the front and rear axles are shown in Figure 48. Only the results for the right wheels are shown.

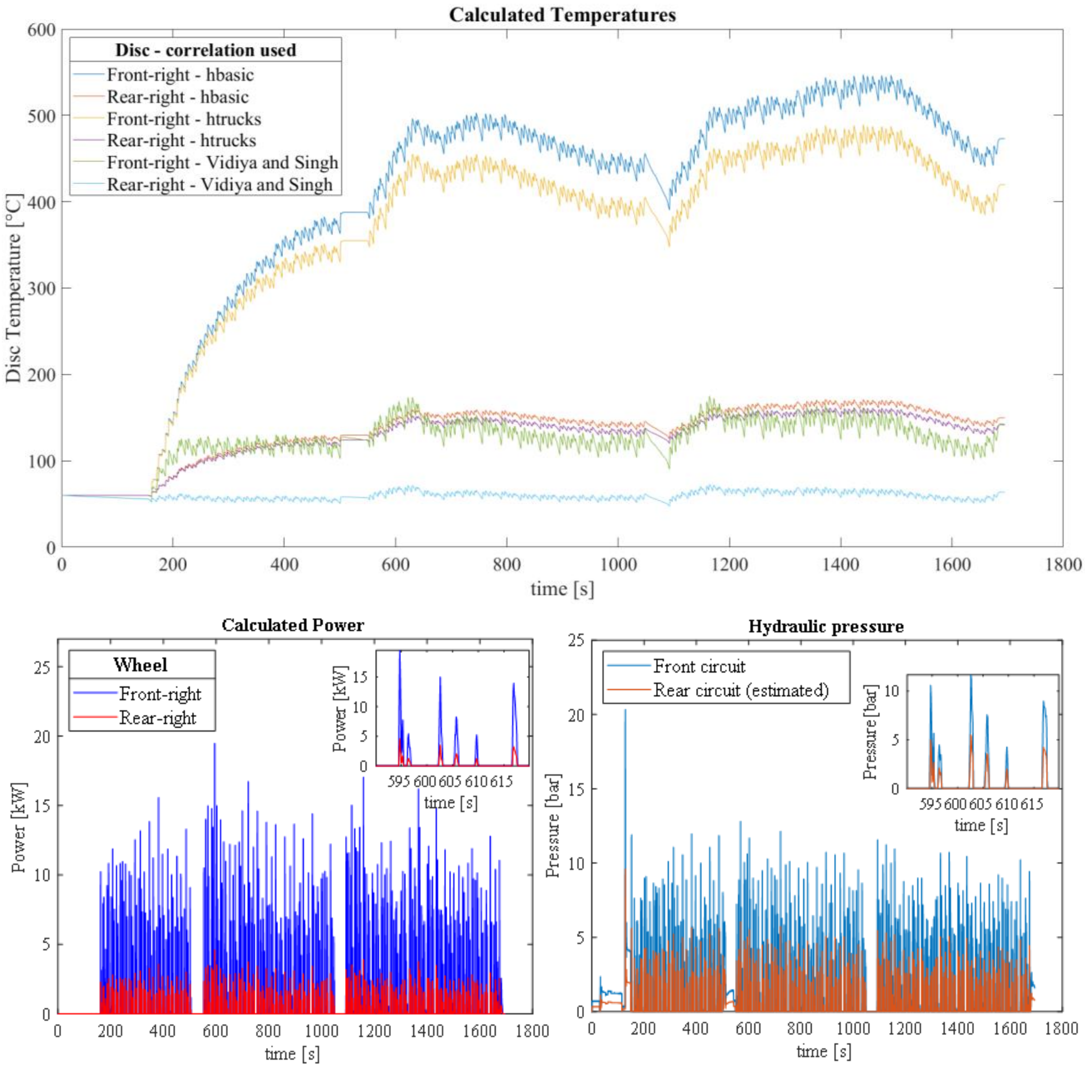

Figure 48: Estimation of the temperatures of the SC17 brake rotors during the FSAE Italy 2017 Endurance using the information from the motor speeds and brake pressure sensors.

The results from this analysis using the speed-dependent average heat transfer coefficients were similar to the ones obtained using the analytical model of the thermal response during repeated braking maneuvers (Figure 47). The temperatures obtained using the heat transfer coefficients from Vidiya and Singh were much lower than the other two cases. The temperatures predicted for the rear disc using such coefficients are quite unrealistic. The temperatures calculated using the heat transfer coefficients obtained using the correlations for basic shapes produced results similar to the ones obtained using the coefficients from the book of Rudolph Limpert. Nevertheless, since there was no existing data about the actual temperatures of the brake rotors during operation, the accuracy of the results could not be assessed.

2.1.4.6 CFD analysis of the SC17 front brake rotor

To obtain a more accurate evaluation of the heat transfer coefficient, the Aerodynamics division of the 2017 PoliTo Racing Team performed a steady state CFD study of the SC17 front brake rotor and the P4 24 caliper. The analysis was set considering the flow field around the rotating wheels obtained from a previous full-vehicle simulation with an air speed of 60 km/h. A constant surface temperature of 300°C was assigned to the brake disc and the caliper was assumed to be an adiabatic body. The results can be seen in

Figure 49. These images were provided by Matteo Allocco and Fabio Tosi, from the Aerodynamics division of the 2017 PoliTo Racing Team. Image (a) represents the heat flux contour plots on the side of the disc facing towards the vehicle center and image (b) shows the opposite side, closer to the spokes of the wheel rim. Considering that the total surface area of the brake disc was 0.0437 m^2 and the total power exchanged with the fluid was approximately 678 W, they estimated an average heat transfer coefficient of 60 W/m^2K.

Although the result matched the value obtained analytically using empirical correlations, the velocity magnitude contour plot (d) indicated that the air speeds in the vicinity of the brake rotor were much lower than those assumed in the analytical computations. Thus, it was not clear whether the calculated variation of the heat transfer coefficient with the vehicle speed was reliable. Moreover, during a race, the constant changes in direction make very difficult to predict the actual value of the heat transfer coefficient, despite the fact that the biggest contribution seen in Figure 45 comes from the rotation of the disc.

From these analyses, the conclusion was that the operating temperature of the SC17 front brakes was much higher than that of the rear ones, although the actual values were not known.

Considering the vicinity to the 400°C limit for the worst case in the front brakes, the decision was to design the SC18 front rotors reducing the mass and rotating moment of inertia compared to SC17 ones, while avoiding increasing the temperature more than 100°C. For the rear brake discs instead, the weight reduction target of at least 30% was maintained.

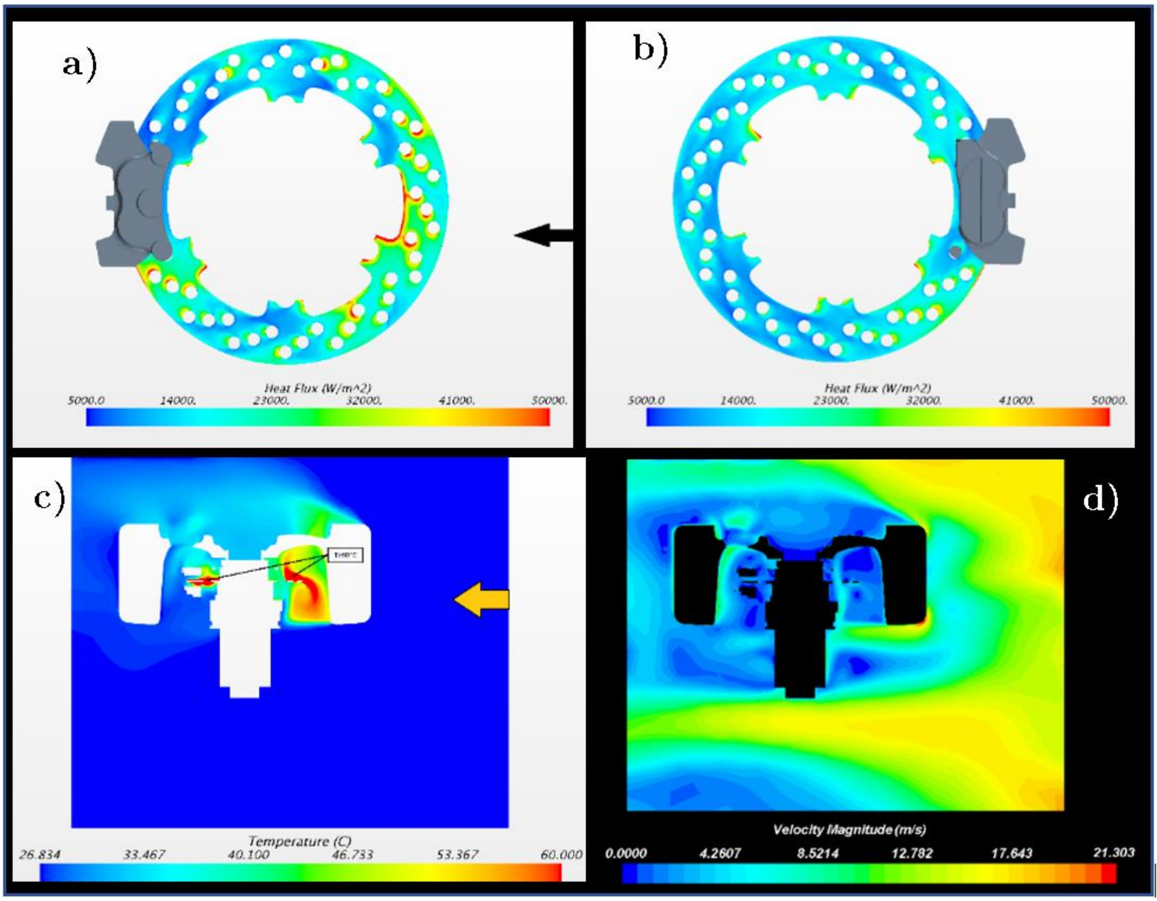

Figure 49: CFD analysis of the SC17 front brake disc and the P4 24 caliper.

2.1.4.7 Material selection and design exploration

In this section, the selection of the material used for the brake rotors is addressed, followed by the analysis of the geometric characteristics of the discs, using a Design of Experiments approach. Most of the considerations regarding the material choice for brake discs and the problems to be solved when designing them have been obtained from reference literature [25] [33].

Several geometric parameters affect the mechanical and thermal response of a brake disc, in addition to the material used. These parameters must be defined according to the loads to which the rotor is subjected during operation, which often present opposing requisites.

The rotor thickness and diameter, as well as the presence of holes, determine the total thermal mass of the disc, its structural stability and rotational inertia. The holes or slots through the disc rubbing band are implemented to prevent the pseudo-hydrodynamic sliding conditions between the rotor and the brake pads known as “fading” caused by the formation of pressurized organic vapors at the friction interface [33]. In addition to that, the holes pattern can influence the temperature distribution on the friction surface and help reducing the weight and inertia.

Non-uniform temperature distributions are the cause of thermal stresses, and thicker rotors are more prone to exhibit thermal gradients [25]. However, the repeated effect of the clamping forces and the surface friction from the brake calipers induces thermomechanical deformations that may lead to fatigue failures, and this has a greater impact on thin discs. Additionally, the constant heating and cooling cycles can produce thermo-elasto-plastic, permanent deformations resulting in residual stresses that can distort or modify the shape of the rotors and increase the risk of cracking [33].

In the case of the Formula SAE cars, during the competitions, the vehicles are subjected to consecutive highly intense stops, and then rapidly accelerated. This represents a rather unfavorable thermal cycle for a brake disc.

Surface cracks are formed when the residual or thermal stresses are greater than the material strength. On the other hand, for a given rotor material characterized by a certain strength, some of the factors that reduce the predisposition to crack formation are a reduced thermal expansion coefficient and elastic modulus, and the possibility to have an unconstrained thermal expansion (as in the case of the floating discs). The material thermal conductivity defines the temperature difference between two points in the rotor body while the rate of temperature variation in a given area of the rotor is limited if the specific heat and material density are increased [25].

Based on these considerations and the thermal analyses so far discussed, the selection matrix shown in Table 19 was obtained. It weighs up the different thermophysical and mechanical properties of each one of the materials considered for making the rotors and the feasibility for the Team to source it and process it. Regarding the brake discs used in the SC17 car, they were made of stainless steel, although the exact alloy was not known. For the SC18 ones, the decision was to use a martensitic stainless-steel alloy. Although it was extremely hard, this type of material presented the best combination of properties for the application in terms of thermal response and mechanical resistance.

Table 19: Decision matrix for choosing the material type for the brake discs.

Brake discs material choice	Density	Tensile Strength	Hardness	Machinability	**Predicted temperature rise**	Thermal Conductivity	Cost	Thermal expansion	Total
Martensitic stainless steel	★	★★★★★	★★★★★	★★	★★★	★★	★★★★	★★★	25
Ferritic stainless steel	★	★★★★	★★★★	★★	★★★	★★	★★★	★★★	22
Aluminum-based MMC	★★★★★	★★	?	★★★★★	★	★★★★★	★	★★	21
Titanium alloy	★★★	★★★★★	★★★★★	★	★	★★★★	★	★★★★	24
Carbon steel	★	★★	★★★	★★★	★★★★	★★★	★★★★	★★★	23
HSLA steel	★	★★★	★★★★	★★	★★★	★★	★★★	★★★	21
Grey Cast Iron	★	★	★★	★★★★★	★★★	★★	★★★★★	★★★	22

The material properties of AISI 410 were used for the thermal and mechanical simulations of the rotors. These are reported in Table 20.

Table 20: Material properties of AISI 410 steel (Quenched at 950°C, water-tempered at 730°C).

Tensile Yield Strength [MPa]	Ultimate Tensile Strength [MPa]	Coefficient of Thermal Expansion [µm/m/°C]	Thermal Conductivity (W/m K)	Specific Heat 0-100 °C (J/kg K)
598	798	0.99 (0 to 100°C), 1.05 (T> 300°C)	24.9 at 100 °C	460

Design Exploration study

The simulation software package used for assessing the stress and temperature response of the brake rotors was ANSYS Workbench [56]. The ANSYS Academic Teaching License offered the possibility for solving structural physics problems having a mesh with a maximum of 32 000 nodes or elements. This represents a limitation regarding the level of accuracy that could be obtained from the simulations. However, this software package was preferred for developing the brake rotors because the documentation available was easily accessible and the learning curve was less steep than other options. This was important because the design of the brake rotors needed to be completed between November and mid-December 2017, to continue the development of other components of the unsprung masses.

To study the influence of different geometric parameters in the rotor's response in terms of mechanical stresses and temperature distribution, a Design Exploration study [56] [57] was performed for the front brake rotor. The aim was to determine a combination of thickness and number of holes that would result in a more uniform temperature distribution and reduced weight, for a limited temperature increase and mechanical stress. This study was only used as a first approximation, and the resulting disc model was further developed with more accurate analyses.

A simplified disc model, based in the SC17 front one, was analyzed. The shape and size of the interface with the carrier bell was maintained and separated from the outer ring, which was remodeled with the same inner and outer diameters, with three independent hole patterns at different radial distances. The geometric features related to the number of the holes in each pattern and the rotor thickness were parametrized considering manufacturable values, using Space Claim [56].

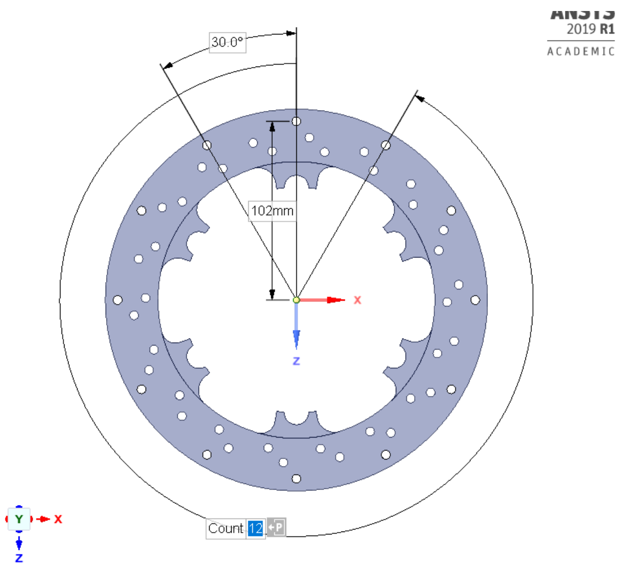

Figure 50: Basic geometry used for parametric analysis.

The number of holes and their diameters were modified independently for each pattern. The baseline thickness was 2.5 mm. Table 21 contains the values used for the design exploration study.

Table 21: Parameters used during design exploration study.

Design Parameter	Level
Number of holes in the patterns	6 9 12 15 18
Added thickness from baseline [mm]	0 0.5 1 1.5

A coupled thermal and mechanical stress analysis was set within Ansys Workbench. Figure 51 shows the interaction scheme between the simulations and the design exploration. The software generated 125 design points, each one corresponding to an updated geometry featuring the different levels of the design variables. The results allowed creating a response surface that could be used to determine the most appropriate combination of parameters.

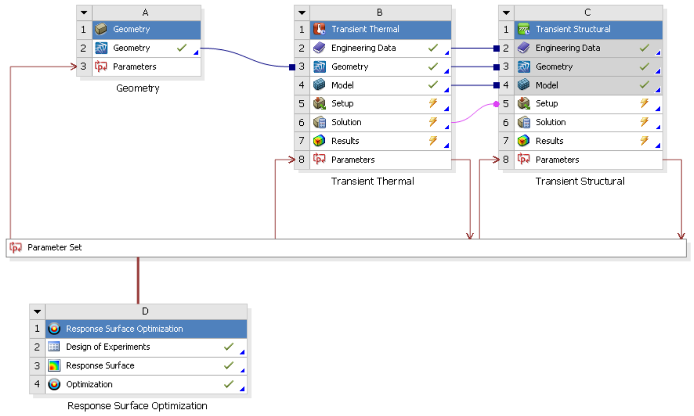

Figure 51: Configuration of the coupled transient thermal and structural analyses used for design exploration on Ansys Workbench

Boundary conditions

Regarding the transient thermal and mechanical analyses used during each design point iteration, they simulated a hard stop maneuver as the one listed in Table 14.

A heat flow was applied to the friction surfaces of the disc, and a variable heat transfer coefficient was applied to all the surfaces. The values are shown in Figure 52. The ambient temperature was set to a constant value of 30°C.

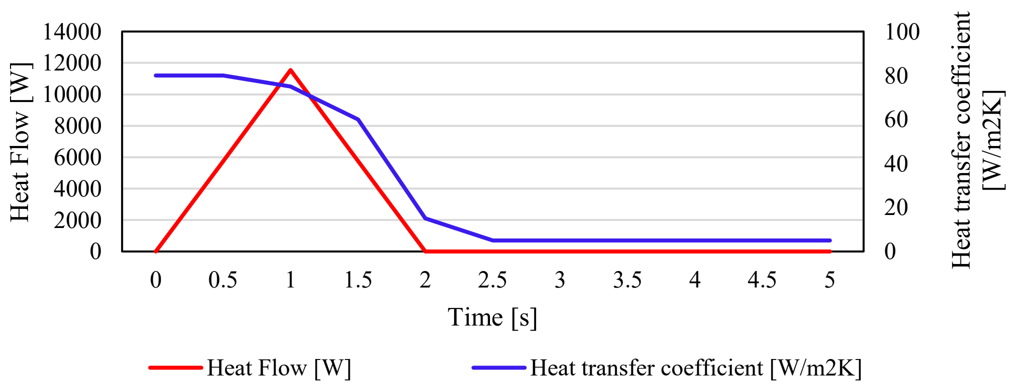

Figure 52: Thermal inputs used for the design exploration analyses.

In terms of the transient mechanical stress analysis, the boundary conditions applied to the interfaces between the brake disc and the floating buttons (shown in the detail in Figure 53) allowed a tangential displacement about the cylinder axis, while constraining the motions in the axial and radial directions. This type of constraint was not an accurate simulation of the "floating" characteristic of the disc. Nevertheless, it allowed to prevent rigid body motions and assess the performance on a worst case of thermal expansion constraints for the design exploration that was being performed as initial approximation.

A constant brake torque of 470 Nm was applied to the rotor. Since the parametrization study would update the disc geometry for each design point, it was not possible to associate a tangential force to a zone representing the contact face of the brake pads. To overcome this, the torque was applied to both sides of the friction ring. This is not a realistic representation of the actual loading conditions on the rotor, but it allowed to assess the mechanical properties associated to each design point. During the following stages of the rotor design, the loads were modeled more appropriately.

The transient mechanical simulation received the temperatures distributions results from the thermal analysis

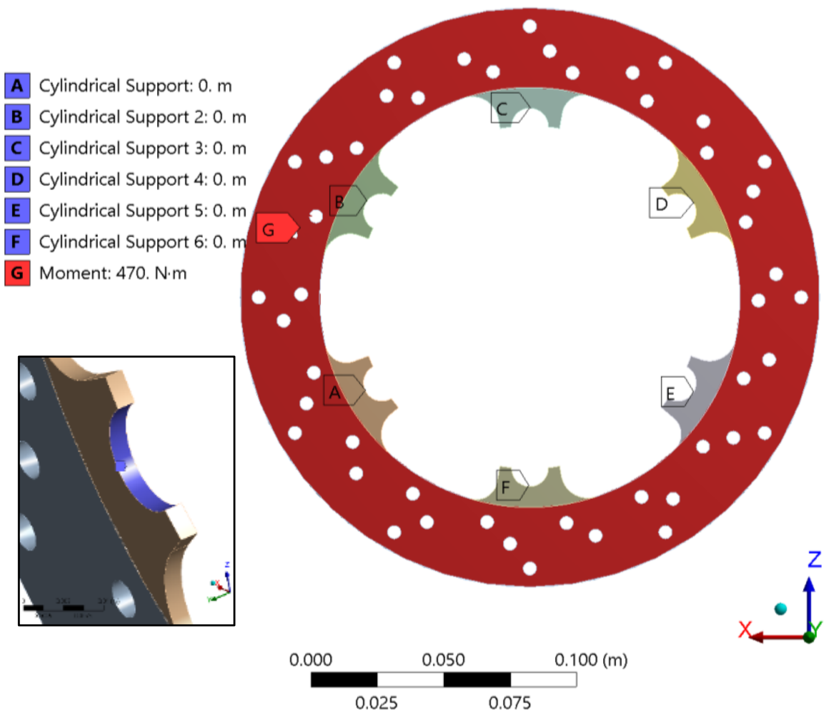

Figure 53: Boundary conditions for mechanical stress analysis used for design exploration.

Mesh used for the design exploration study

Given the large number of design points to be solved, the discretization of the geometry was done considering the time required by the solver to evaluate each one of the simulations and update the model geometry before proceeding to the next one. As a result, the mesh used had 5475 elements, which is a rough discretization of the disc volume. The mesh was automatically updated from one design point to another, as the geometry was changed by the optimization software. Hexagonal elements were used in the friction ring, and tetrahedral elements were used in the supports of the brake rotor. The mesh quality report indicated that more than 75% of the elements were within the recommended range of quality index, within 0.5 and 1. Clearly, the results would not be completely accurate in terms of local values of temperatures and stresses, but the design exploration study was only aimed at determining a suitable geometry to be optimized through further analyses. The mesh for an arbitrary design point can be seen in Figure 54.

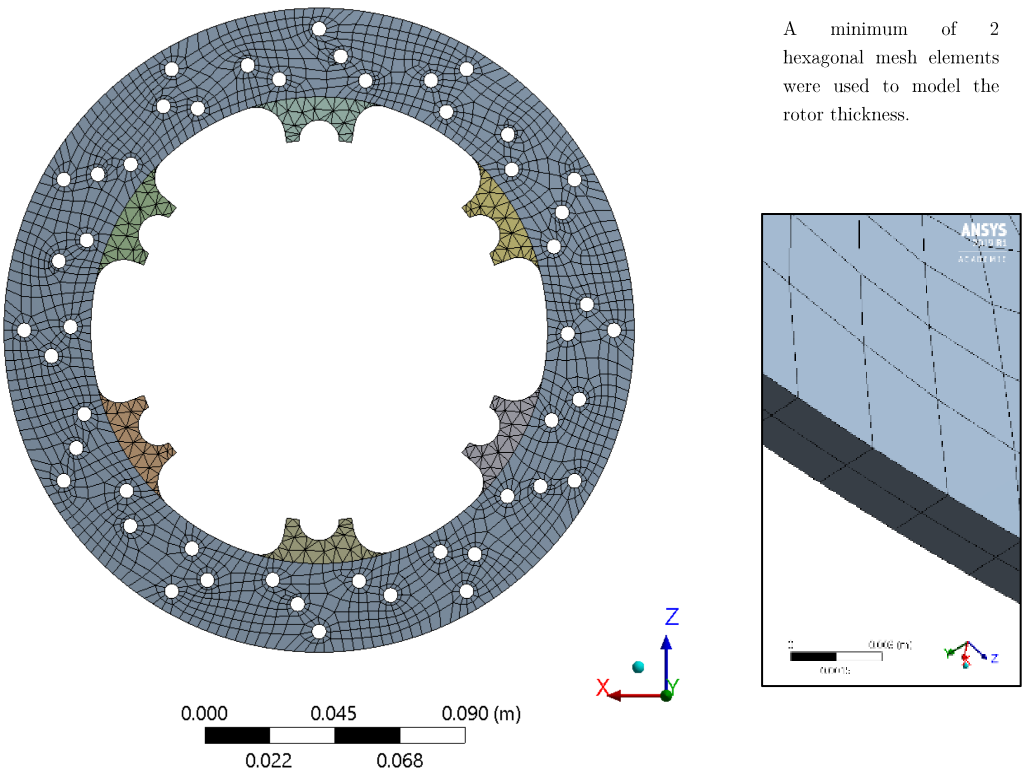

Figure 54: Example of the mesh used during the design exploration study.

Response surface

The design exploration study produced a response surface that allowed to see the trends in temperature rise depending on the variation of the geometric features to find a suitable compromise. A 3-axis representation of the temperature results versus the added rotor thickness (from the baseline of 2.5 mm) and number of holes in the external pattern is shown in Figure 55

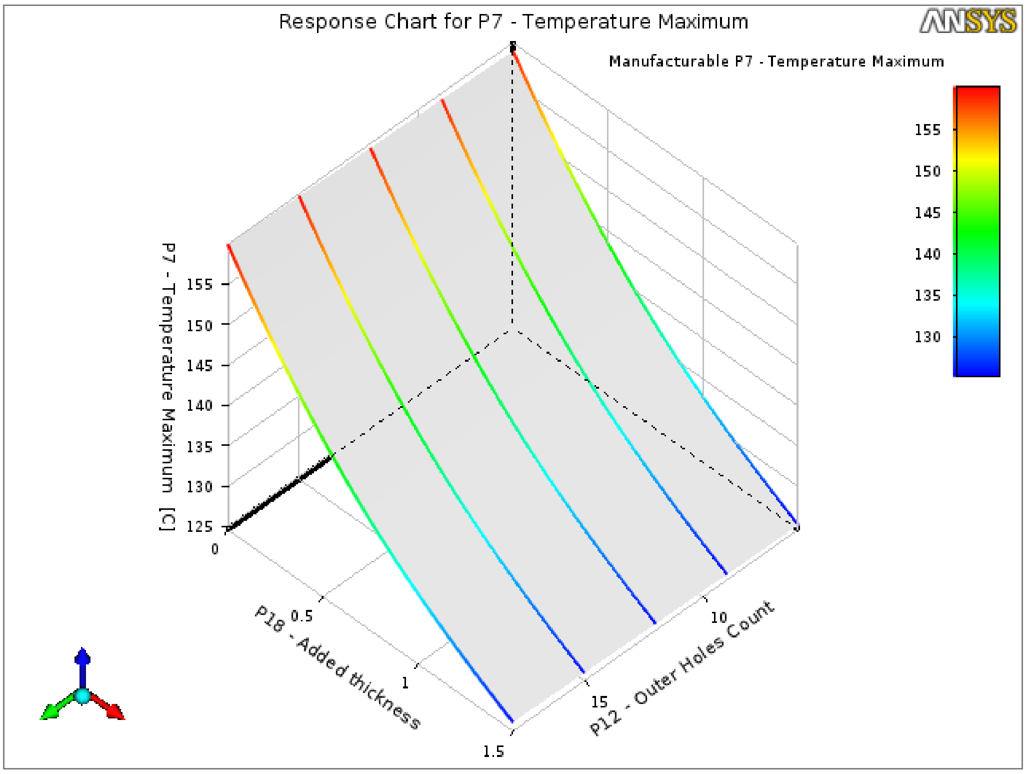

Figure 55: Temperature response surface from design exploration.

The results showed that, for a given rotor thickness, the greater the number of holes, the greater the maximum temperature, but the temperature gradient across the friction ring was lower. Increasing the thickness from the baseline value had a greater impact on the total mass than reducing the number of holes in the patterns. However, lower thicknesses also resulted on higher temperatures than an equivalent increase in the number of holes, in terms of the amount of material subtracted from the baseline design. Another important aspect is that, the more holes were present, the faster the rotor was cooled after the application of the heat flow, considering the same heat transfer coefficients represented in Figure 52 for all the design points.

2.1.4.8 Detailed design of the rotors

Based on the insights from the response surface, six final candidate versions were analyzed with further detail to determine the most adequate design for the front brake rotor. For brevity, only the last version of this refinement process will be discussed, comparing the results obtained with the SC17 front brakes and previous iterations of the

SC18 design, when relevant. For the rear brake rotor, instead, the process followed to arrive to a final solution was more straightforward because of the greater room for increasing the operating temperature with respect to the SC17.

For the front rotor, the number of holes was increased from 54, on the SC17 rotors, to 69, and the thickness was reduced from 4 to 3 mm. This produced an increased operating temperature, especially during the autocross event, and a slightly higher temperature during an endurance race, according to the predictions from the analytical models and the finite element thermal analyses. Figure 56 shows three different stages of the front brake rotor design. The left one was the starting geometry, having the same hole pattern as the SC17 front disc, but a reduced thickness (3 mm). After performing further analyses, the holes pattern was modified to obtain a more uniform temperature distribution in the surface, resulting in the version shown in the center of Figure 56. In the last step, the outer edge and the radii of the attachment interfaces were redesigned, as shown in the right side of the figure.

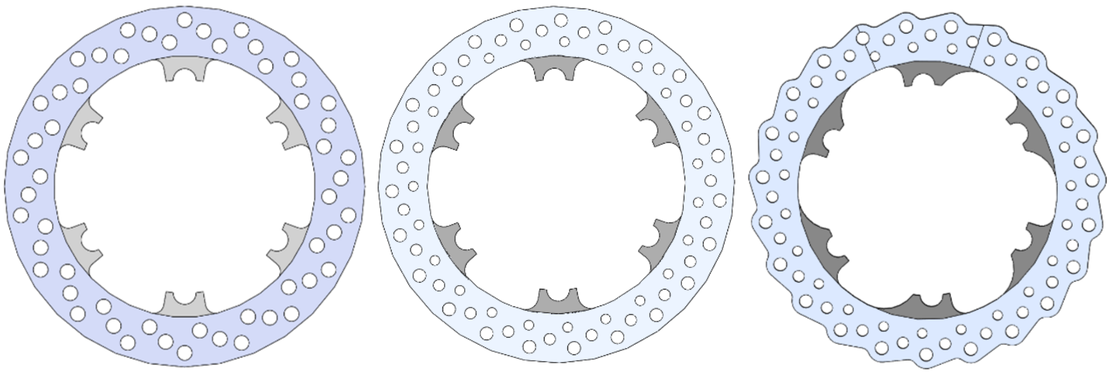

Figure 56: Different iteration stages of the front brake rotor design.

Regarding the hole pattern on the front disc, the design was driven by the need for reducing the temperature gradient on the friction ring, while improving the cooling rate.

Assuming that the pressure distribution of the brake pads is uniform in the radial direction, the frictional work rate, equal to $\mu p v$, is proportional to the applied pressure p and the tangential or relative "sliding" speed v between the pad and the rotor surface [33]. Since the tangential speed is given by ωr, it increases towards the outer edge of the rotor. Thus, the temperature rise, and the pad compound wear rate will be higher close to the outer diameter of the disc [33]. To compensate this effect, the relative surface area of the friction ring was reduced along the radial direction of the rotor by increasing the diameter of the holes in the outer side of the pattern. This allowed improving the temperature gradient between the external edge and the inner one. Additionally, having larger holes in towards the outer border allowed a further reduction in the rotational inertia of the disc. Although the design specification for the brakes system did not include a target value for the rotational inertia of the brake rotors, it is one of the main considerations when designing a race car, and any possible reduction is beneficial.

For the rear rotor, the thickness was reduced, and the holes were replaced by slots to further reduce the mass and increase the work temperature. This also had a beneficial effect because of the reduced rotational inertia. The minimum thickness providing an acceptable structural integrity according to the simulations was 2.5 mm. However, it was discarded because in real conditions such a small thickness could be prone to cracking due to an extremely fast cooling, and the type of simulations performed were not able to predict this. In addition to that, 2.5 mm was below the recommended minimum thickness by Brembo for the P2 24 calipers, and represented a manufacturing difficulty, since none of the stainless-steel sheets available in the market had a suitable thickness, slightly greater than 2.5 mm that could be grinded to the desired thickness without requiring an extensive material removal. Thus, the final thickness was 3 mm.

Final analyses

This phase took place between the end of November 2017 and mid-December of the same year. The final version of the front brake rotor design was released on December 18th. To simulate the structural response, the tangential and compressive forces associated to the contact of the pads were applied to the geometries in a static structural analysis, in which the body temperatures history was imported from a transient thermal analysis simulating an Autocross lap.

A more realistic approach would have been implementing a multi-body simulation, including the brake pads and the floating buttons to analyze the non-linear contacts occurring at the center of the rotor and the friction effects on the rotor surface. Performing such type of analysis would have allowed a more realistic computation of the surface stresses and the actual distribution of the temperatures in the rotor [33] [38]. However, this was computationally more expensive and time consuming. Considering that the design phase needed to be completed by December 31st, 2017 (Figure 5) and some components, such as uprights needed to be approached as well, a simplified analysis was considered enough to assess the mechanical stresses. Nevertheless, the structural and thermal responses of the final versions of the rotors were assessed through more realistic finite-elements analyses (FEA) than the ones used for the design exploration study.

Constraints

To constrain the remote points connected to cylindrical interface of the floating brake buttons were created, as depicted in the detail in Figure 57. These are unidimensional elements that transfer the loads and boundary conditions applied to the master node (central element) to the slave ones, located in the associated surface or mesh elements [58]. The displacement constraints were applied to the master nodes of the remote points, to restrict the displacements in the three coordinate directions (X,Y and Z), while allowing the rotations along each coordinate axis. As in the case of the design exploration analyses, this type of boundary condition does not represent the clearance existing between brake disc and floating buttons, that allows an unconstrained thermal expansion and axial self-alignment of the disc.

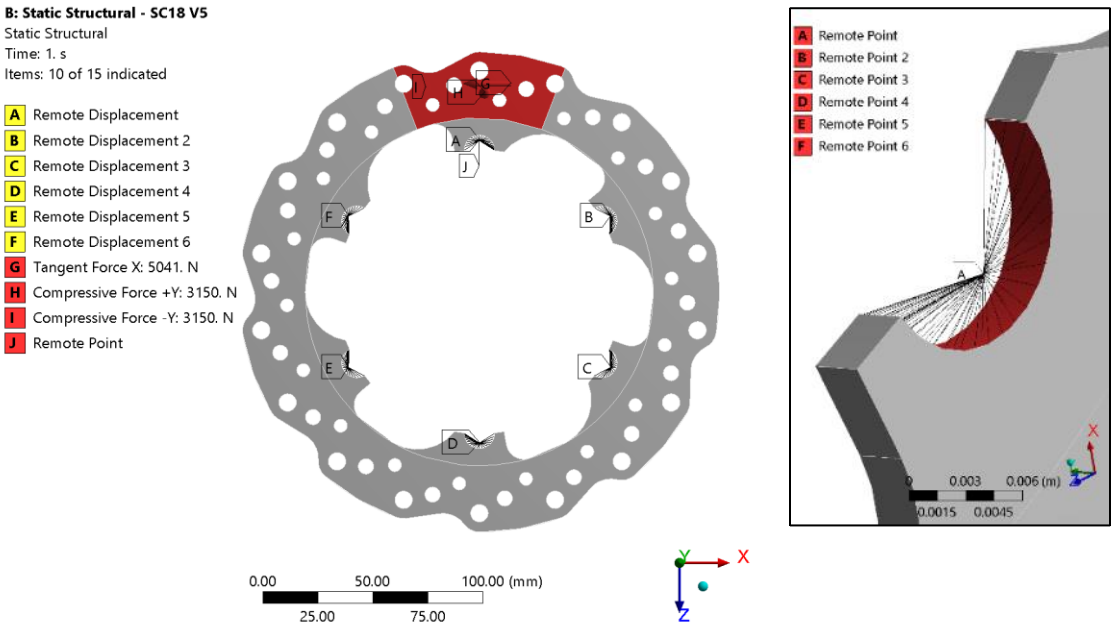

Figure 57: Constraints for the final analyses of the brake rotors.

Applied loads

The magnitudes of the forces applied to the front and rear rotors in the static structural analyses were calculated in section 2.1.4 and listed in Table 14 (page 60). To implement these, the friction surfaces of the CAD models were split, as shown in Figure 57 (read area on the top of the disc), to represent the interface with the brake linings. Then, the tangential and compressive forces were associated to both sides of the discs, simulating a symmetric contact of the brake pads.

To estimate the fatigue life, a normalized load history was implemented in the *Fatigue Tool* of Ansys Mechanical. This was obtained from the brake pressure data recorded during the Formula SAE Italy 2017 Autocross event. Since the applied load corresponded to a deceleration rate of 2.2g as a design worst case, the pressure values were normalized so that the highest peaks corresponded to a scaling factor of 0.8. This way the fatigue life was calculated considering load blocks analogue to an Autocross run, in which the maximum loads applied were equivalent to a deceleration rate of 1.8g.

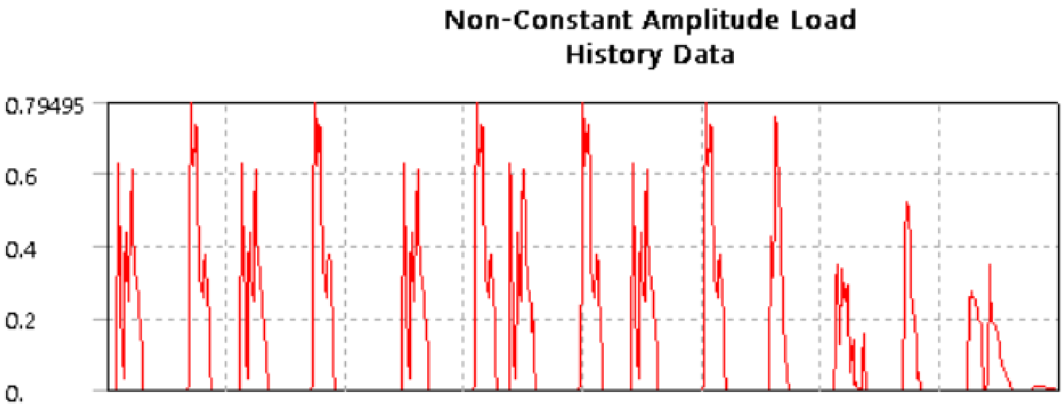

Figure 58: Normalized load history applied used to calculate the fatigue life of the rotors.

This load history was defined as a block of cycles, and the design life and fatigue damage were calculated assuming infinite life as 500 000 blocks. To account for possible material and production imperfections, a fatigue strength factor of 0.6 was introduced, using the Soderberg criterion to determine the expected life [59]. This is a conservative theory, but it was preferred given the simplicity of the simulation.

Additionally, the fatigue life was also assessed using the Strain-Life criterion, using the Morrow theory [60]. The material properties of the AISI 410 steel were obtained from reference [61] and [62]. The Stress-Life (S-N) and Cyclic Stress-Strain curves for the material under the conditions reported in Table 20 are shown in Figure 59.

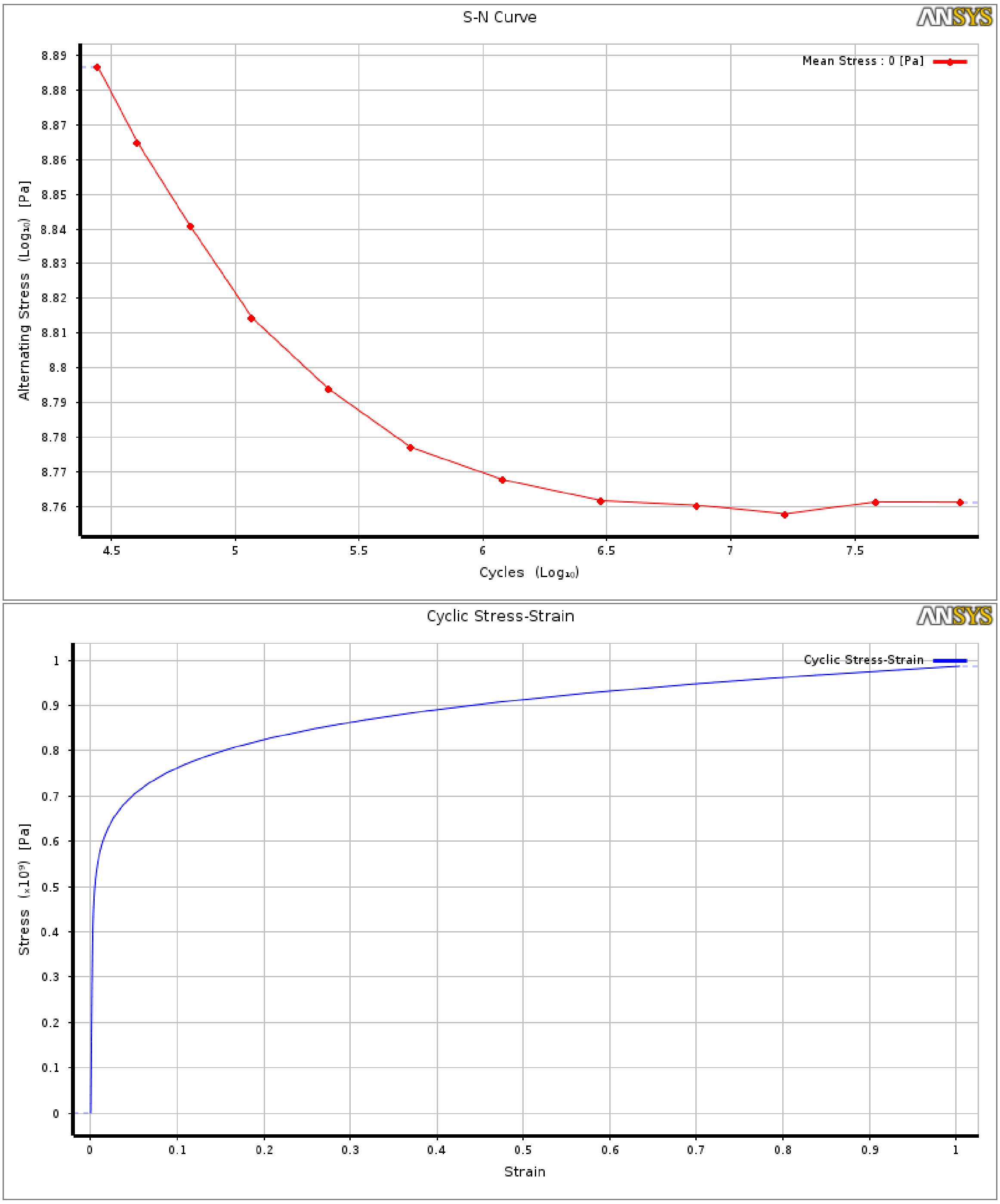

Figure 59: Fatigue properties of AISI 410 steel used for the structural analyses [61] [62].

Regarding the thermal loads, the calculated history of heat flux (brake power) corresponding to the same Autocross run used for the fatigue life estimation was applied to both sides of the friction ring. This was calculated from the sensor data of the SC17 car, similarly to calculations shown in Figure 48. Since the calculation of the power was done assuming a brake pad friction coefficient equal to 0.8 for both the front and rear brakes, the applied loads were conservative, with respect to the actual conditions. The real friction coefficient for the brake pads compound used was unknown, but the information from Brembo indicated that the value would be lower than the one assumed (see Figure 38 in page 51).

In terms of heat transfer coefficient, two different cases were evaluated, given the uncertainties from the previous analyses. The worst-case assumed extrapolated values from the analytical calculations shown in section 2.1.4.2, which were considered low based on the temperatures obtained from the analytic models. The best-case considered the experimental values presented by Vidiya and Singh [46], which were much higher. The time history of the thermal loads used for the front brake rotors are shown in Figure 60.

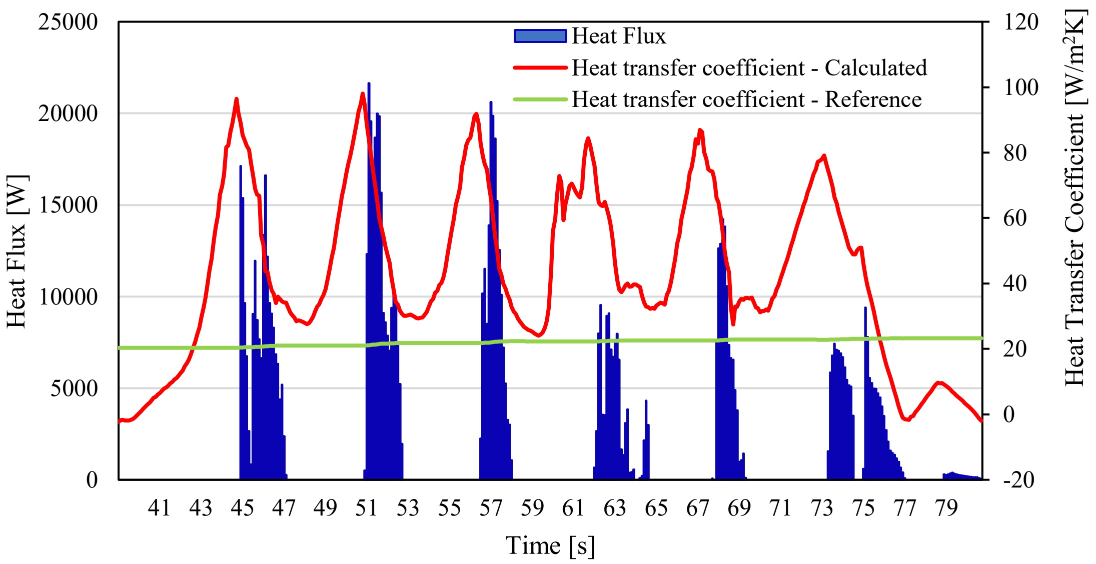

Figure 60: Thermal loads and heat transfer coefficients implemented to determine the fatigue life of the front rotors.

Meshing

Given the maximum number of cells and elements permitted by the ANSYS Academic License, meshes used for the simulations had 23 225 nodes and 2 936 elements for the front disc, and 31 635 nodes with 19 070 for the rear one. In both cases, more than 75% of the elements had a quality index above 0.7. The mesh used for the front disc is shown in Figure 61.

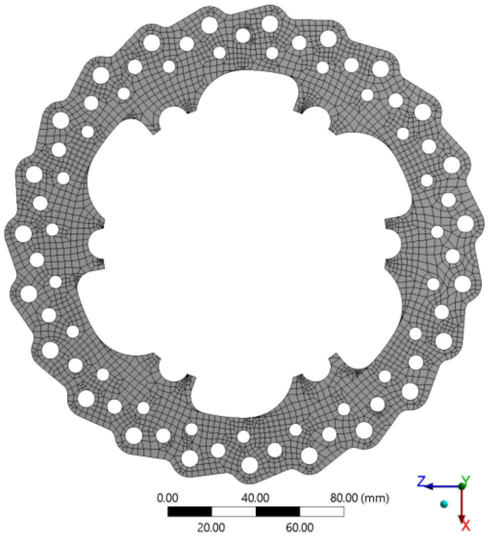

Figure 61: Mesh used for the simulations of the front disc.

2.1.4.9 Simulations results

Temperature distributions

The temperature distributions presented a remarkable difference between the best and worst cases. Some of the resulting temperature contour plots are shown in Figure 62. The top-left image corresponds to the worst-case results for the front SC18 brake rotor and the left one corresponds to the worst-case SC17 front brake disc. These were obtained using the input loads shown in Figure 60. The second row shows the temperature plots for the temperature distributions during an Endurance race, obtained using the heat transfer coefficients from [46].

As can be seen, the temperature gradient in the SC18 disc was lower than that of the SC17 one, regardless of the assumption made for the average heat transfer coefficient. Nevertheless, since the simulations did not account for the relative displacement between the brake pads and the rotor and the heat flux was applied uniformly, the results were only indicative. The actual temperature distributions would be more similar to the heat transfer coefficient contour plots shown in Figure 49.

The worst and best cases for the rear brake disc are shown in the left and right side of the bottom row of Figure 62, respectively. As expected, the obtained temperatures were lower than those of the front rotors. The contours plot on the right was obtained from one of the intermediate design iterations in which the rotor thickness was 2.5 mm.

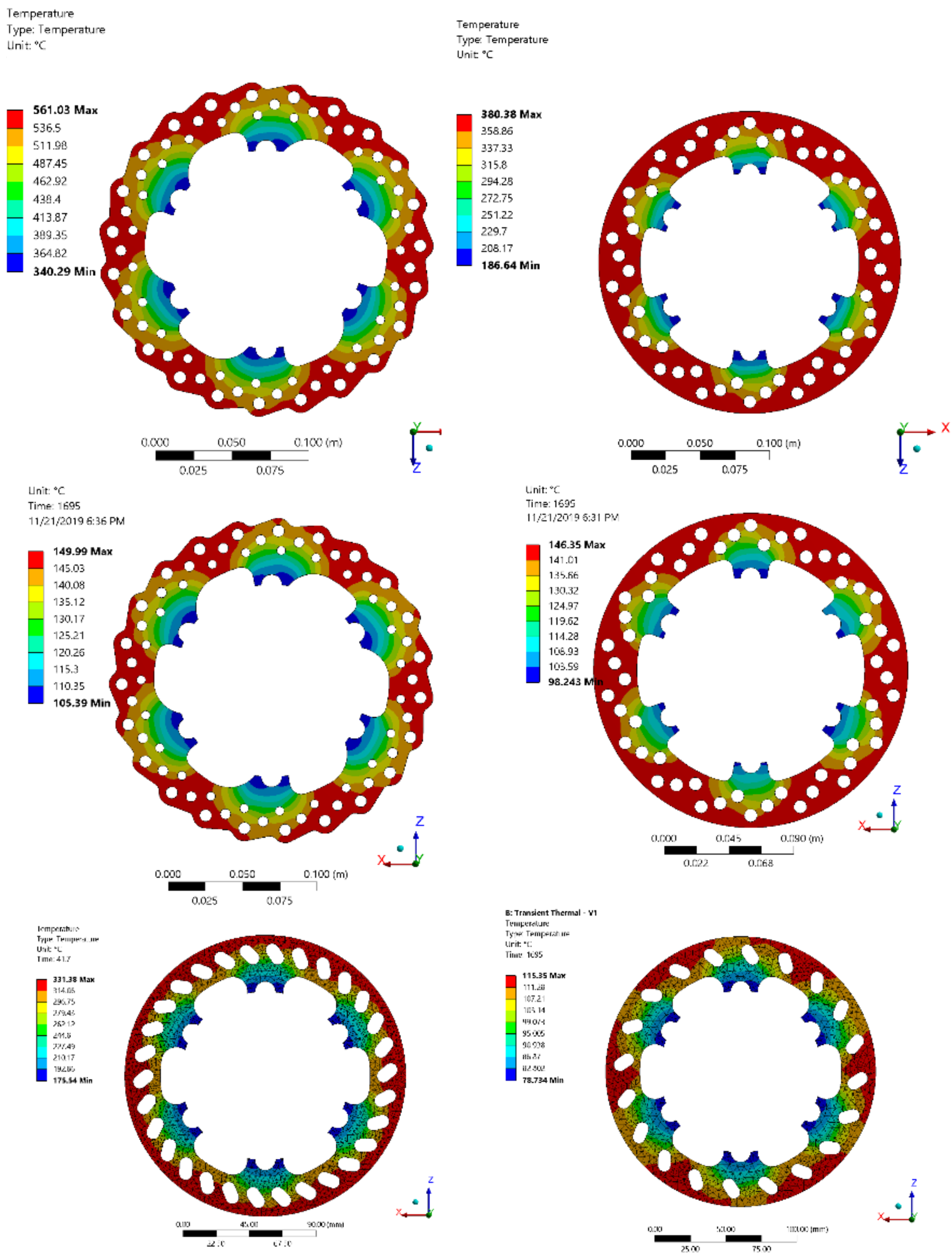

Figure 62: Temperatures contours plots.

Thermo-mechanical stresses and predicted fatigue life

The stress analyses for the front brake rotor were the most critical ones, given the magnitude of the forces involved (Table 14). The Von-Mises equivalent stress [59] contour plots were used to modify the shape of the inner brackets that are used to fix the rotor to the disc bell. As can be seen in Figure 63, the most stressed areas in the SC17 disc were the surfaces were the brackets join the outer ring. To consent the reduction in thickness and compensate the stress values in that region, the radii were changed for the SC18 disc. This incremented the safety factor against pure-mechanical loads from 3.43 (SC17) to 3.73 (SC18).

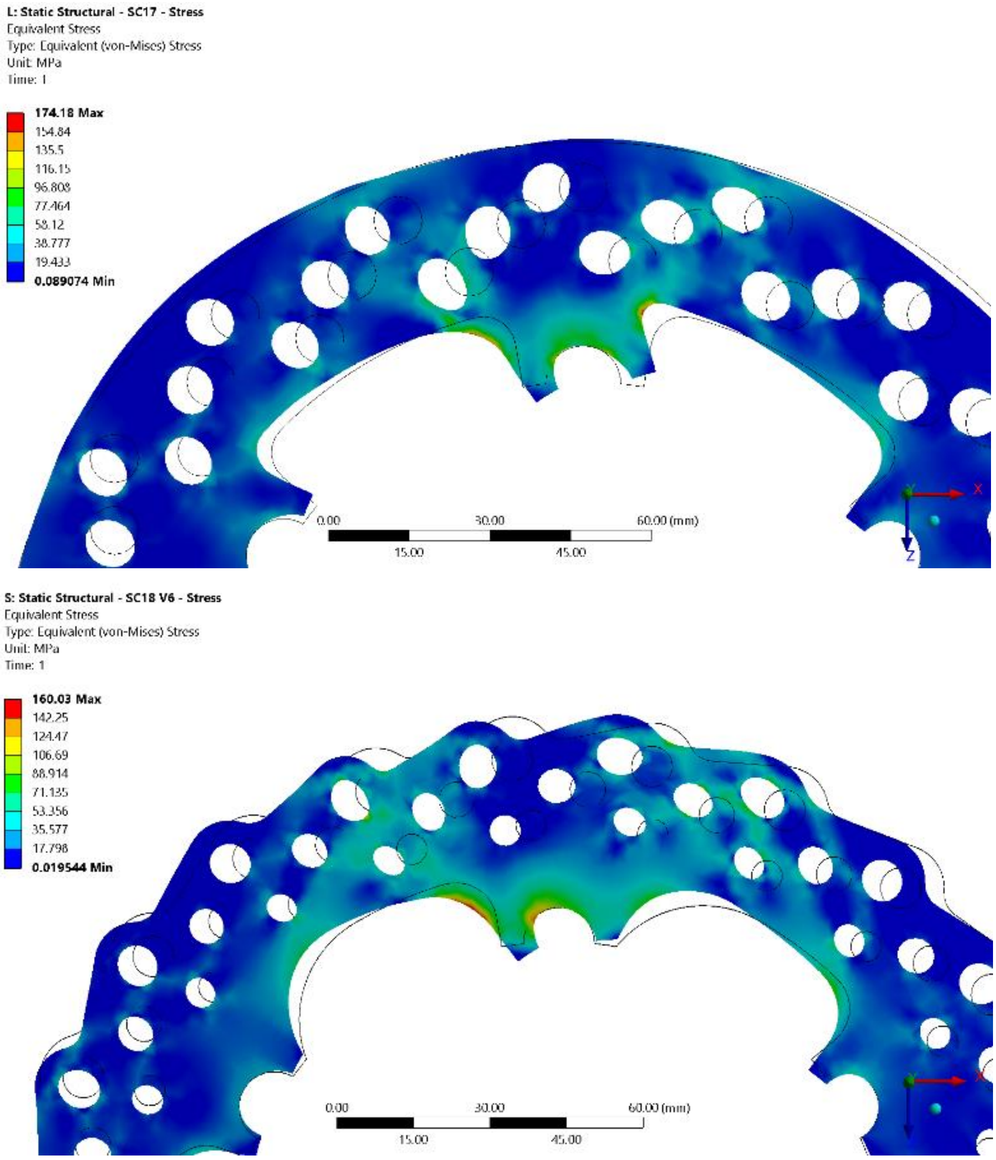

Figure 63: Von-Mises Stress contour plots for the SC17(top) and SC18 (bottom) front discs.

To analyze the contribution of the thermal strains the worst-case temperature distributions obtained from the transient thermal simulations were imported into the static structural analyses. From the imported results, the thermal strains were calculated and used to solve the von-Mises equivalent stresses across the geometry of the rotors.

The inclusion of the thermal loads had a huge impact on the results of the structural simulations. The equivalent von-Mises stress contour plots for the front SC18 and SC17 rotors obtained using the best-case temperatures (endurance race) can be seen in Figure 64. In the case of the SC18 front brake disc, the maximum stresses were increased to 617 MPa, while the SC17 one showed a maximum von-Mises stress value of 254 MPa under the same conditions. The fatigue life results obtained using the strain-life theory indicated that the minimum duration predicted was 4081 blocks, considering each block as an Autocross lap, as explained previously. This was a 50% reduction compared to the SC17 front rotor, which showed an expected minimum life of 9081 blocks. In both cases, the minimum expected life was located in the edges of the anti-fade holes.

This meant that the front brake rotor could withstand a maximum of 4081 autocross laps, in which the magnitude of the maximum tangential forces applied from the brake pads was 0.8 times the applied load of 5 041 N that represented a deceleration rate of 2.2g. in other words, the duration was defined based on the continuous application tangential forces of 4 032 N, corresponding to a deceleration rate of 1.8g (design target).

In reality, for the SC17 car, such deceleration rates were registered only during some autocross events. Moreover, the actual values of braking torque depend largely on the effective longitudinal friction coefficient between the tires and the asphalt. The calculated values assumed an optimal friction coefficient of 1.8 and this value was greater than the ones seen during the competitions.

Additionally, the fatigue life was calculated based on the material properties used for the simulation (Table 20 and Figure 59), while the AISI 410 steel present improved properties in different heat treatment conditions. Besides, other existing martensitic steel alloys offer even better mechanical properties in terms of strength and fatigue resistance [49] [61] [62].

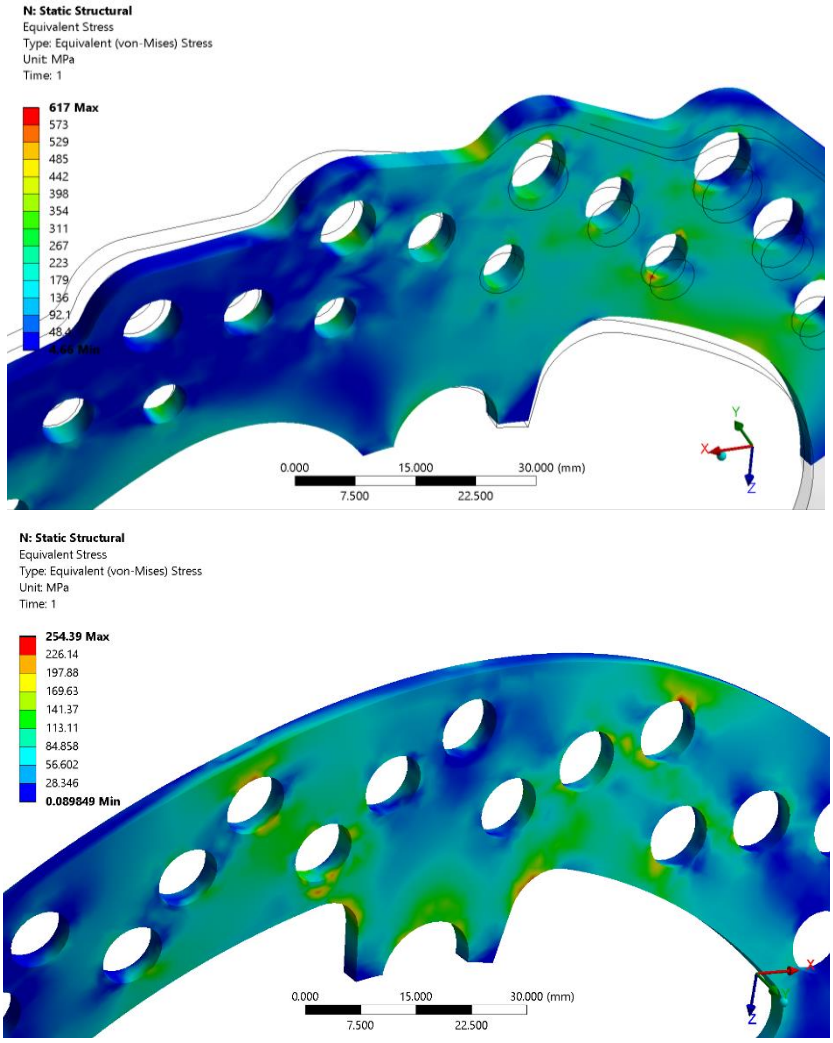

Figure 64: Equivalent von-Mises stresses in the SC18 (top) and SC17 (bottom) front rotors, using the best-case temperature distributions.

For the worst-case temperatures, the predicted fatigue life was further reduced. In the case of the SC18 front disc, the minimum predicted life using the strain-life failure criterion was 400 blocks (Figure 65, top). Interestingly, the worst case for the SC17 front rotor with the thickness reduced by 1 mm showed a minimum predicted life of 187 blocks. This could be related to the greater thermal gradient on the SC17 front rotor, as has been shown in Figure 62. Under the worst-case thermal conditions, the maximum temperature difference between the coldest and hottest points in the rotors was 221°C and 194°C for the SC18 and SC17 discs, respectively. However, the transition from the highest value to the lowest one occurred across a wider area in the case of the SC18 disc, while the temperature gradient in the SC17 one was limited to a smaller zone. In any case, the fatigue life prediction was extremely conservative in both cases, because of the high temperatures considered in the computation of the thermal strains. Moreover, it is important to note that the applied constraints did not simulate the “flotation” characteristic of the discs under real operation, which allows the thermal expansion of the rotor, reducing the thermal stresses.

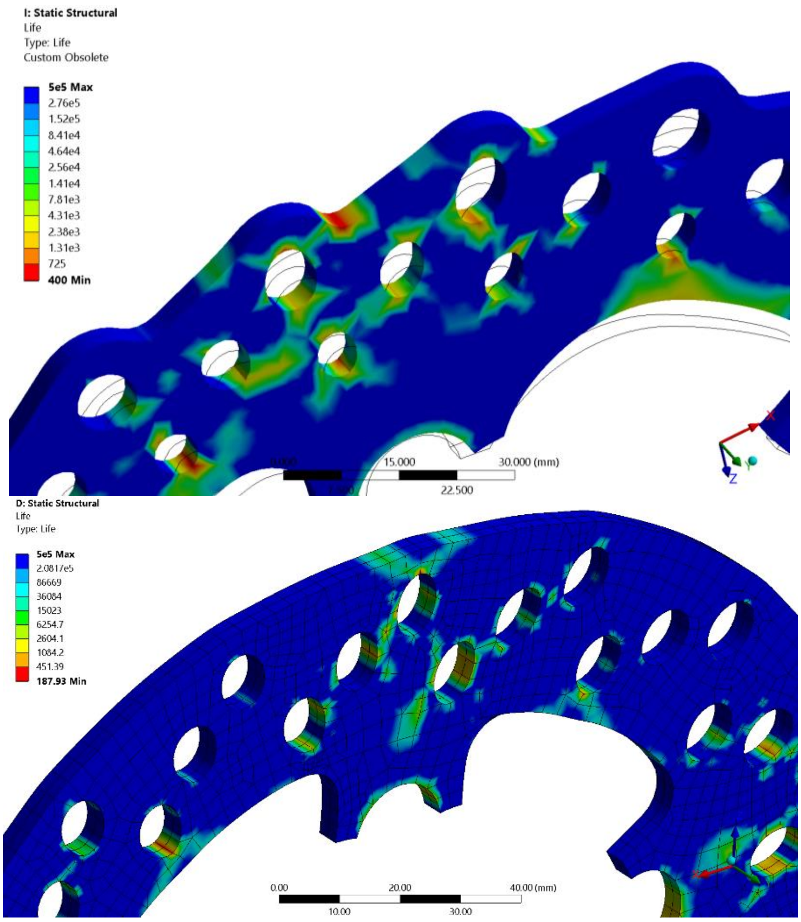

Figure 65: Predicted fatigue life of the SC18 (top) and SC17 (bottom) front brake rotors for the worst-case loads.

In the case of the rear brake rotor, the pure mechanical stresses contour plots showed that the maximum von-Mises stresses in the SC18 disc were largely below the tensile yield strength of the AISI 410, with a safety factor of 7. The SC17 rear rotor exhibited a safety factor of 10 under the same conditions. Thus, despite the reduction in thickness from the SC17 disc to the SC18 model, and the addition of the anti-fading slots, the rotor seemed to be largely oversized for the applied forces. The von-Mises stress contour plots can be seen in Figure 66.

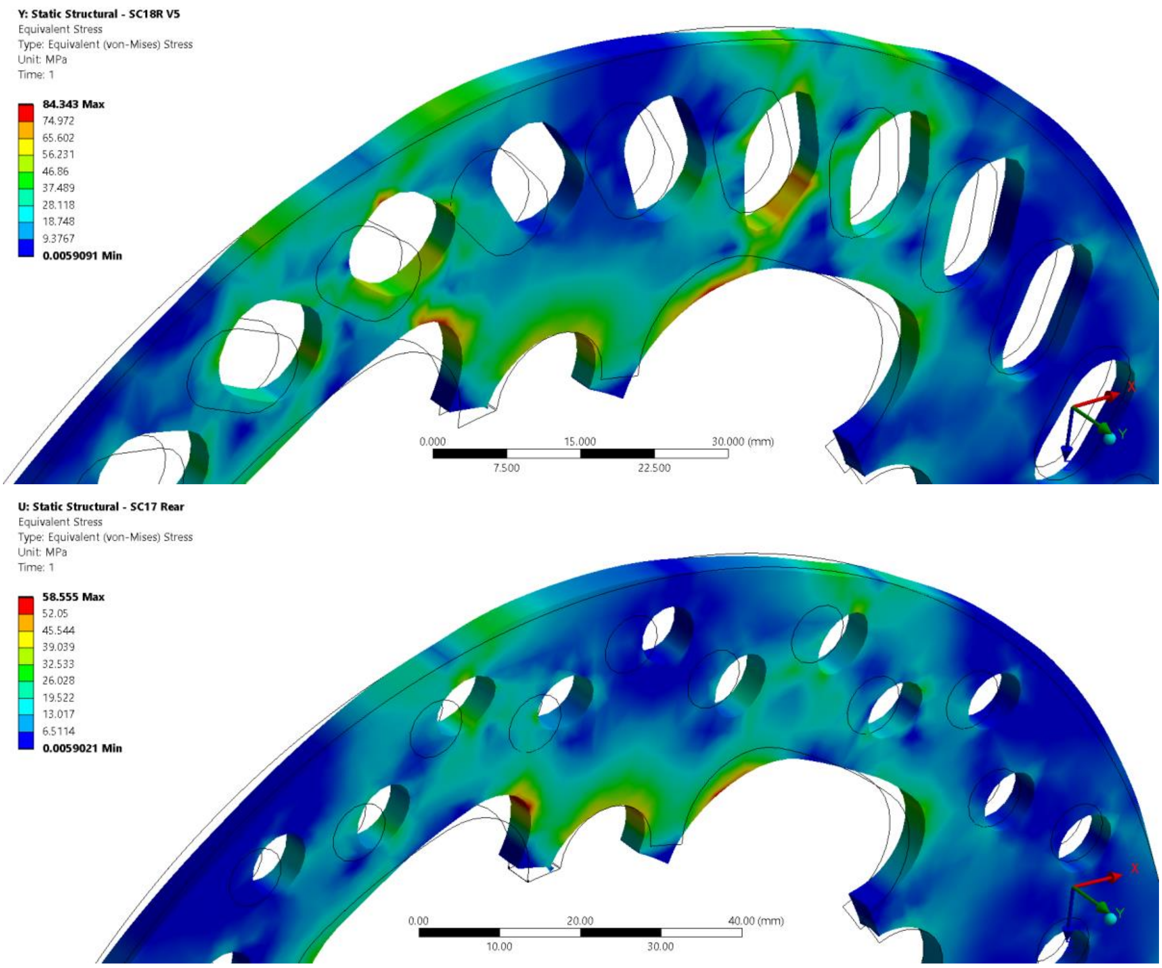

Figure 66: Von-Mises stress contour plots of the SC18 and SC17 rear brake rotors.

Despite the pure mechanical stress results suggested that the design was over-sized, the inclusion of the temperature distributions obtained from the worst-case transient thermal analyses resulted in much higher stress values. The fatigue life calculation using the strain-life approach indicated that the minimum duration of the disc would be 700 autocross laps, under the thermal conditions assumed and the maximum tangential forces applied. The resulting contour plot can be seen in Figure 67.

As in the case of the front brake rotors, this was a conservative estimate, since the applied tangential force of 2 654 N was calculated for a maximum tire adhesion condition, for a deceleration rate of 2.2g.

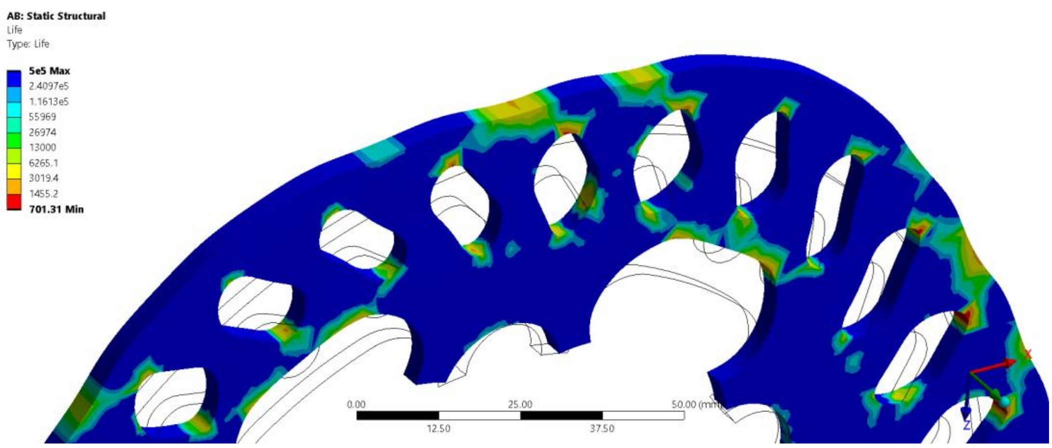

Figure 67: Fatigue life contour plot for the worst-case loading condition of the rear brake rotor.

2.1.4.10 Summary of the brake rotors design

The results from the thermo-mechanical simulations and the final characteristics of the SC18 brake rotors are summarized in Table 22. The best and worst-cases of thermal loading were used to define an estimated temperature range for the brake discs, based on the comparison with the results for the SC17 ones under the same loading conditions.

Table 22: Results from the final thermo-mechanical analyses of the SC18 brake rotors.

Rotor	Thermal case	Max. Von-Mises Stress [MPa]	Max. Temperature [°C]	Fatigue life [N° Autocross loading blocks]	Mass [kg]	I_{yy} [g/mm^2]
Front	Best	617	196	4081	0.370	3047883
	Worst	971	561	400		
Rear	Best	-	152	50000	0.254	1678204
	Worst	700	338	700		

The worst-case analyses of the front brake rotor yielded elevated values of stress caused by the high temperature gradients. Since the assumed loads (Table 14 and Figure 60) were already conservative, the resulting minimum values of fatigue life were considered acceptable.

It is important to note that these numerical simulations were rather simplified and did not account for several factors that determine the actual stresses present in the brake discs. For instance, the frictional loads that cause further surface stresses and temperature distributions different from the simulated ones. Moreover, the numerical limits of the ANSYS Academic License prevented implementing a more refined mesh for the complete geometry of the discs. This could have been overcome, for instance, by taking advantage of the symmetries in the studied problems. On the other hand, the uncertainties about the thermal conditions could only be overcome by having real data to compare with.

Overall, the design was considered satisfactory and coherent with the targets presented in Table 8. To provide an insight about the differences with respect to the SC17 brake discs, a comparison between the characteristics of the new and old brake rotors is shown in Figure 68. The different magnitudes have been normalized, to allow a rapid visual comparison and appreciate the magnitude of the variations.

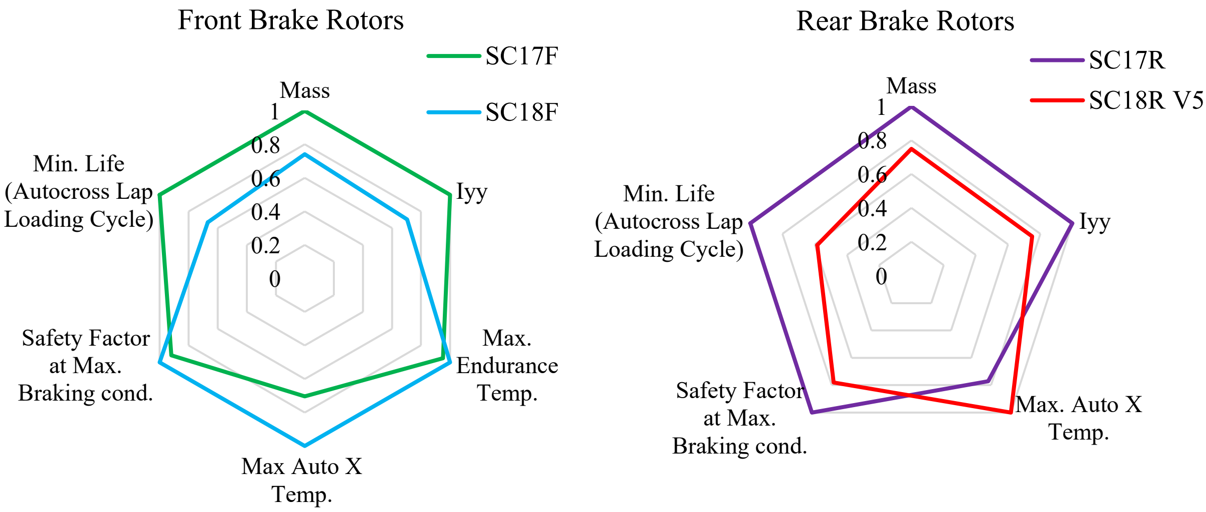

Figure 68: Comparison between the characteristics of the SC18 brake rotors and the SC17 ones, according to the simulations.

For both the front and rear discs, the maximum operating temperatures during an autocross event were increased, while the Endurance ones were kept almost unchanged. As indicated before, the modifications in the geometry of the front brake disc resulted in a slight increase of the von-Mises stress safety factor against pure-mechanical loads. This was not done for the rear one because it was already over-designed for the tangential forces applied (the new design has a safety factor of 7, considering only the equivalent von-Mises stresses resulting from the application of the tangential and compressive loads from the pads).

Brake carriers and floating buttons

As already mentioned, the brake rotors used for the SC18 car were floating type solid discs. So far, the design of the outer friction rings has been discussed. These are the main load-bearing components, since the thermal and frictional forces are applied to them.

However, the transmission of the braking torque to the wheel hub occurs through the central part of the rotors, i.e., the brake disc carrier or mounting bell, and the floating buttons. Figure 69 shows a representation of the SC18 front and rear brake rotors, on the right and left side, respectively.

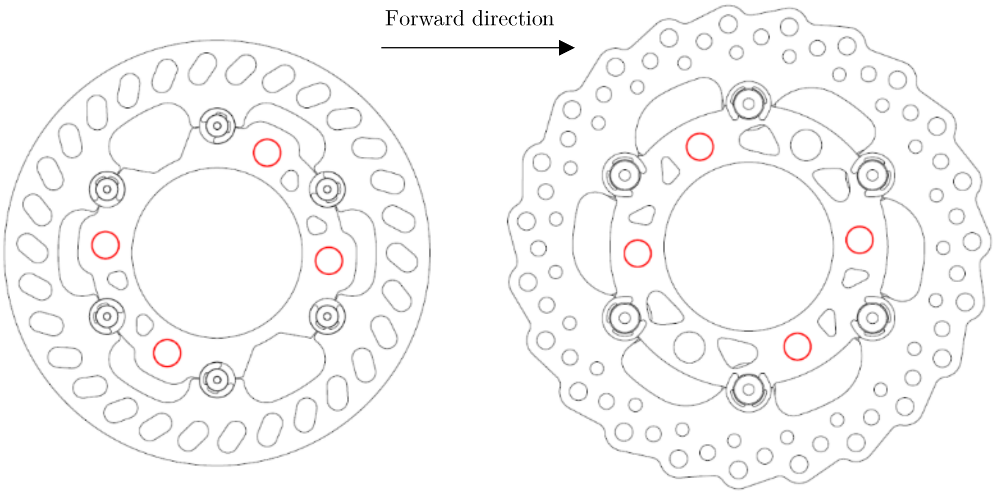

Figure 69: SC18 brake rotors.

Both the front and rear brake carriers were designed using the geometry of the SC17 ones as the starting point. Regarding the floating buttons, only the ones in the front axle were designed, since the dimensions of the front brake disc attachments were the same as in the SC17 versions, allowing to use the standard brake buttons provided by Brembo. The detailed design and analysis of these components will not be discussed in this work. Instead, an overview of their functions and the considerations that drove the development process is included.

Considerations for the brake carriers

The loads transferred through the brake carriers derive from the brake torque applied on the outer friction ring and the resistance opposed to it by the wheel due to the longitudinal friction force between the tires and the road, and the inertia of the rotating components. These loads are reacted on the mating surfaces of the floating buttons and the holes used for transmitting the braking torque to the wheel through the center pins; these connect the wheel hub to the rim, passing through the brake mounting bells. The holes highlighted in red color in Figure 69 serve as mating surfaces for the center pins. To appreciate this more clearly, Figure 70 depicts a cross section of the SC18 rear wheel assembly, showing the interface between the wheel hub and the rim.

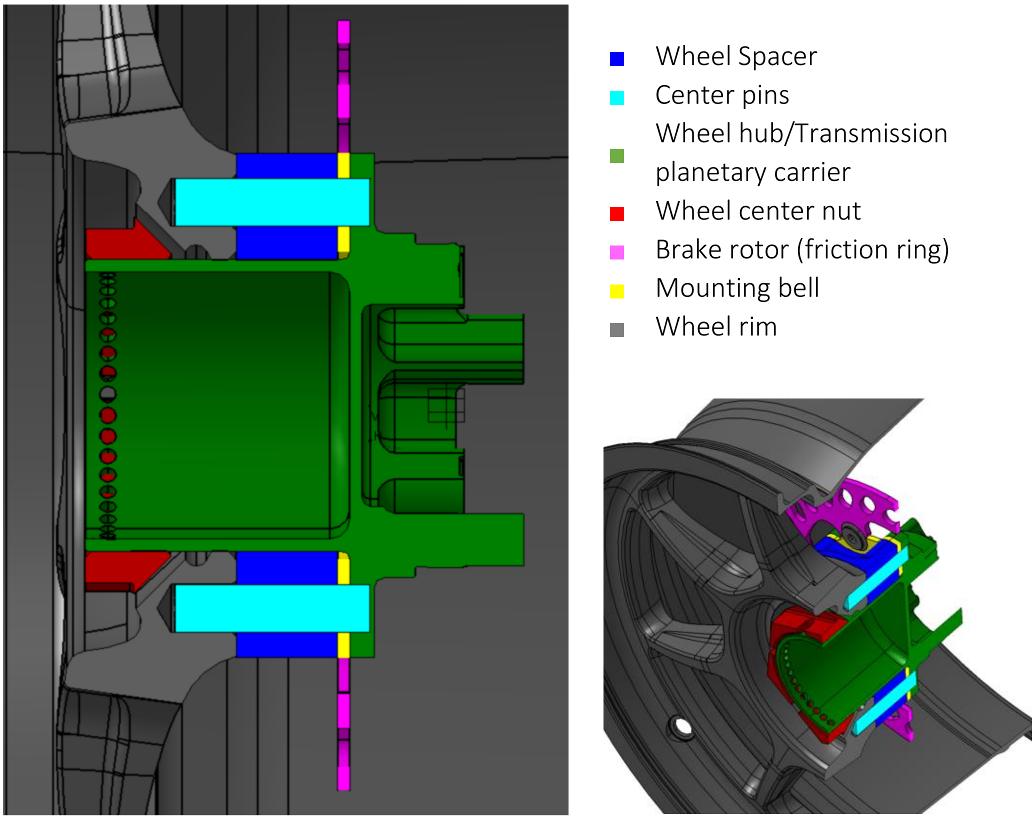

Figure 70: Interfaces between the wheel hub and the wheel rim.

As can be appreciated, apart from the reactions deriving from the brake torque transmitted, the brake bell is also loaded axially by the compression forces generated from the tightening of the wheel center nut. It also reacts to the wheel loads transferred from the rim to the wheel hub. Moreover, several times during the 2017 season the wheel center pins were not used for practical reasons: not having them allowed faster wheel mounting and dismounting operations during the track test sessions and the races. Thus, in those occasions, the driving power was transferred from the hub to the wheel rim by means of the high frictional forces created from the tightening torque magnitude of approximately 300 Nm. This was translated into a compression force of nearly 27 000 N between the wheel rim and the hub, affecting also the brake carrier.

To lower the solicitations deriving from the huge compressive forces on the wheel hubs in 2018, the new design by the Powertrain division featured a 12% increase in the contact area of the outer face of the hub. The difference can be seen in Figure 71.

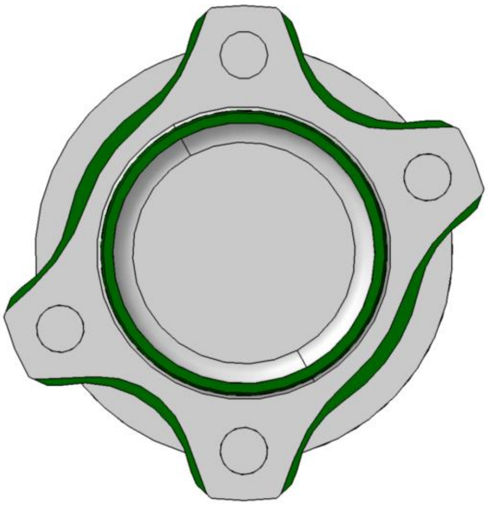

Figure 71: Increased contact area of the outer face of the wheel hubs. The green color represents the SC18 design.

This was a geometric constraint for the design of the brake carriers, which were adjusted to match the increased mating surface. The result can be seen in Figure 72.

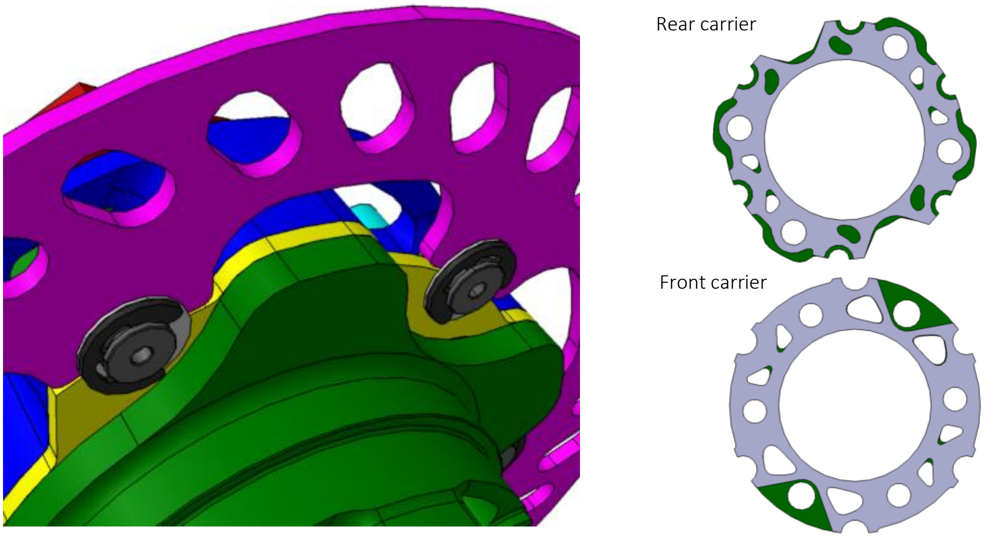

Figure 72: SC18 brake carriers modified to match the contact surface of the brake hubs. On the right side, the green contours represent the SC18 versions of the mounting bells.

The finite elements analyses (FEA) to validate the structural integrity of the mounting bells were performed using the Altair Hyperworks simulation platform [58], evaluating different cases (as discussed in section 1.2.2.1), with different intensities of brake torque and compressive loads for each one. The magnitude of the torques considered for the worst-case braking condition were the same as the ones used for dimensioning the brake rotors, listed previously in Table 14. Based on the results from the simulations, some of the weight-saving pockets that were present in the SC17 versions were eliminated or reduced. The reason was that, to reach the weight reduction targets of the season, the material used was changed, from Ti6Al4 titanium alloy to 7075-T6 aluminum, which offered lower mechanical properties. In addition to that, the higher stresses associated with the reduction in thickness, from 4 to 3 mm to match the design of the brake rotors.

Floating buttons

The rear floating buttons were modified from the SC17 design to eliminate the geometrical interference with the wheel spacer, caused by the modified cross section of the wheel hub discussed in the previous section. The problem is shown on the left side of Figure 73. The right side shows the new version of the brake button with the axial preload spring. The nominal diameter of the loaded section was reduced from 13.9 to 10 mm.

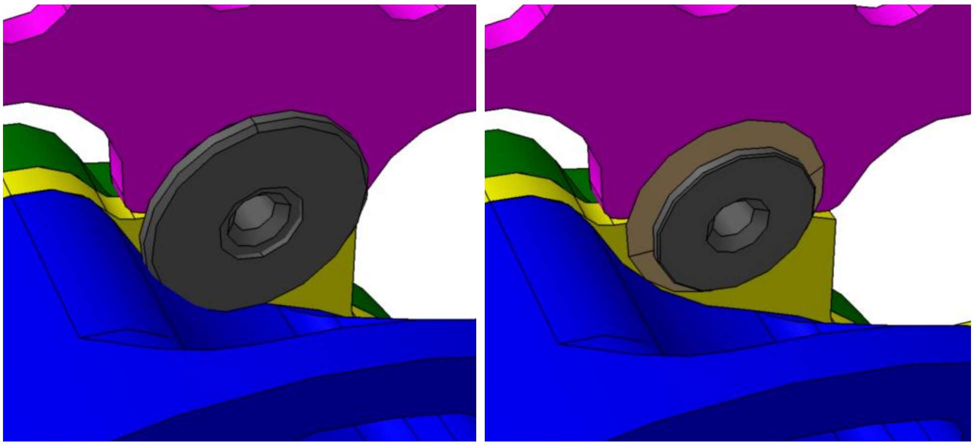

Figure 73: Comparison between the SC17 rear brake floating button and the SC18 one.

To assess the resistance of the new design, the Hertzian contact stress between a brake button and the brake disc was calculated, considering the mating surface on the brake rotor as an inner cylinder [59]. The contact force applied to a single button was given by

$$F_{button} = \frac{T_{brake_{rear}}}{3\, r_{button}} \tag{44}$$

were the braking torque for the rear axle is the one considered in Table 14, and r_{button} was 57 mm. The computation assumes that the total load is resisted by only three of the 6 buttons present on each brake, and was repeated for the contact between the buttons and the brake carriers. Additionally, the maximum shear stress on the brake buttons was computed, assuming the same value of forces given by (44). The results from the calculations are shown in Table 23.

Table 23: Contact and shear stress computations for the rear brake buttons.

	Diameter[9] [mm]	Elastic Modulus [GPa]	Poisson's ratio	Force [N]	Contact length [mm]	Maximum Hertzian Contact Pressure [MPa]	Max. Shear Stress [MPa]
Button	10	70	0.35			212	64
Disc	10.3	200	0.3	1250	3	212	64
Carrier	10.3	70	0.35			176	53

2.1.5 Manufacturing specification

The manufacturing specification of the brake rotors started at the end of February 2018. The only critical aspects from the design process that needed to be verified were the clearances between the different parts of the brake rotors (disc, carrier and buttons) to provide the desired "floating" characteristics. Since the standard Brembo brake buttons would be used for the front axle, the necessary clearances for the discs and the bells were determined from the SC17 brake rotors.

Thanks to the partnership with FCA Prototypes, it was possible to measure the six mounting holes of an SC17 brake disc that had been kept as a replacement part and never mounted on the car. A picture of the rotor is shown in Figure 74.

Figure 74: SC17 front brake disc used to determine the mounting clearance for the floating buttons.

The FCA Prototypes metrology laboratory verified the geometrical features of the disc, providing a report with the measurements of the mounting holes and the innermost diameter of the disc (highlighted in red in Figure 74). The reported dimensions are summarized in Table 24.

[9] These diameters were assumed as a worst-case condition for the rotor and the carrier.

Table 24: Results from the metrology inspection of the SC17 front brake disc.

Measurement	**Diameter [mm]**
Fixing hole 1	13.959
Fixing hole 2	13.932
Fixing hole 3	13.926
Fixing hole 4	13.924
Fixing hole 5	13.922
Fixing hole 6	13.928
Central circumference	128.929

Based on the measurements, the tolerances for the brake rotors and the rear floating buttons were defined as indicated in Table 25.

Table 25: Specified tolerances for the fixing holes of the brake rotors.

	Fixing hole nominal diameter [mm]	Max. deviation [mm]	Min. deviation [mm]
Front disc	13.9	+0.03	+0.02
Front carrier	13.9	+0.02	0.00
Rear disc	10.1	+0.02	+0.01
Rear carrier	10.1	+0.02	0.00

In terms of the materials used for the brake rotors, the three main options considered among the martensitic stainless steels [61] are listed in Table 26. Both the front and rear rotors would be made of the same material to simplify the production process.

Table 26: Martensitic stainless-steel alloys considered for the brake rotors.

<table>
<tr><th>EN 10088-3:
2005
Steel number</th><th>UNI 6900:
71</th><th>AISI/SAE</th><th>Preferred
Condition</th><th>Minimum Acceptable
Tensile
Yield Strength [MPa]</th></tr>
<tr><td>1.4006
1.4024</td><td>X12Cr13
X15Cr13</td><td>410</td><td>Q+T 316 °C</td><td rowspan="2">650</td></tr>
<tr><td>1.4028
1.4031</td><td>X30Cr13
X39Cr13</td><td>420</td><td>Q+T 427 °C</td></tr>
</table>

The aluminum alloys for the brake carriers and buttons are listed in Table 27.

Table 27: Aluminum alloys specified for the brake carriers and rear brake floating buttons.

	Aluminum Alloy	Preferred conditions	Minimum acceptable Tensile Yield Strength [MPa]	HBW min.
Mounting bells	7075	T6, T651	500	-
	7068	T6, T6511		-
Rear floating buttons	7068	T6511	500	150

The 7068-aluminum alloy was chosen for the brake buttons because of its ability to maintain good fatigue resistance at greater temperatures than the 7075 alloy [62]. Moreover, it offers a much greater surface hardness when treated with a hard-anodizing process. This was important because of the contact between buttons and the steel brake rotors.

Regarding the unsprung hardware components of the brake system, the parts required to assembly the rear floating buttons are shown in Figure 75 and the technical specifications are listed in Table 28.

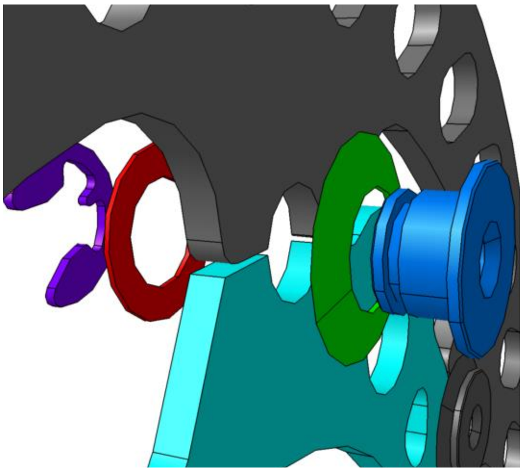

Figure 75: Rear brake buttons assembly.

Table 28: Hardware components required for the rear brake rotors.

Component	Specification
■ Belleville washer	Type K disc spring di=11 mm
■ Shim Washer	DIN 988 PS 10x16x0.5
■ RA 08 Type	DIN 6799 Di=8mm Do= 15.75 mm

The unsprung mass of the brakes system was further reduced by adopting braided stainless-steel brake hoses that did not have the plastic cover that was present in SC17. This represented approximately a 30% weight reduction in the brake lines (almost 200 grams). Additionally, banjo-type AN-03 fittings made of aluminum were chosen instead of the stainless-steel ones used in SC17. The density of aluminum is about 2 700 kg/m^3 and that of steel 7 800 km/m^3. This represents another 60% weight reduction, or effectively 20 grams per wheel. Figure 76 shows the brake fittings and hoses used for the SC17 and the SC18 on the left and right side, respectively.

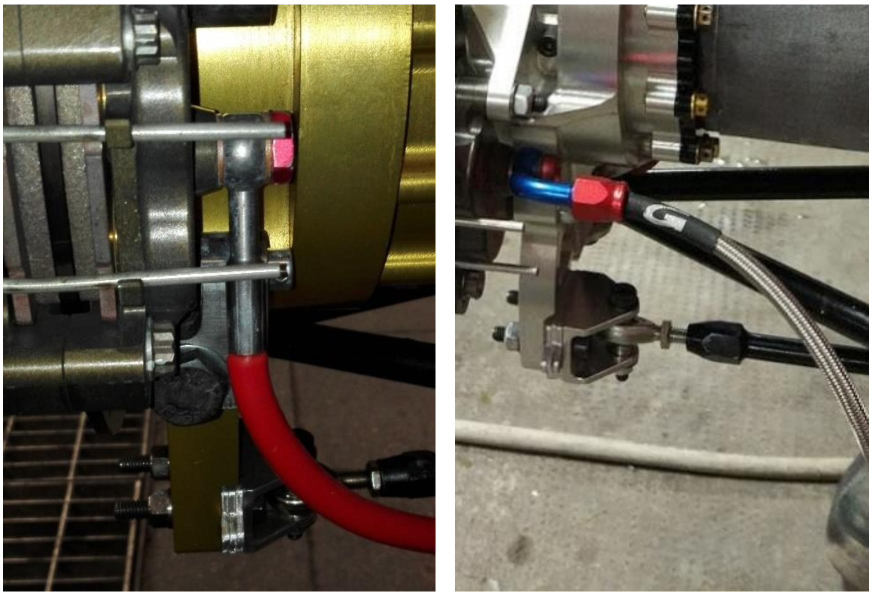

Figure 76: Brake fittings and hoses connected to the unsprung mass.

2.2 Unsprung components of the suspension system

Until now, the design of the brakes system was briefly discussed, with a focus on the design of the unsprung elements that make part of it. In this section, the development process for the suspension components that contribute to the unsprung mass will be addressed. The starting point was the definition of the wheels size, by the Vehicle Dynamics division, and the definition of the suspension hardpoints introduced in section 1.2.2.1.

The design of the uprights proceeded in parallel with the rest of the suspension components. The suspension arms were developed by Danesin [28]. His bachelor's degree final project documents the design and experimental verification of the CFRP suspension arms to be implemented on the SC18 car. Unfortunately, due to a series of issues related to the available resources during the 2018, a set of A-arms made of welded steel tubes was fabricated as a second and cost effective-effective solution. Thus, most of the stress analyses discussed in this chapter correspond to the original design of the suspension arms and a verification of the substitute solution is addressed at the end.

Wheels

As introduced above, the wheel size was selected by the Vehicle Dynamics division at the beginning of the 2018 season in the fall of 2017. The definitive tire model, instead, was determined based on track tests performed during the development process of the SC18 car. The chosen wheel size was 13" for all the four wheels. The 7 x 13 inches magnesium wheels with center lock, model OZ Formula Student, were selected. One of these is depicted in Figure 77.

Figure 77: Wheels used in the SC18 car.

These were a lightweight and reliable option that had been also used in the 2017 car. Developing customized wheels was discarded considering the available resources (people, time, budget).

Having determined the wheel model, the spacers were designed to match the geometry of the wheel center and the brake carriers described in the previous section (see Figure 70 and Figure 72). This was done by the Powertrain division.

2.2.1 Uprights

We have introduced the function of the uprights (also referred to as "knuckles" [10]) as integration point between the suspension components, the wheel brake system, the wheel hub and, in the case of the Squadra Corse prototype, the electric motors and planetary geartrain, as can be seen in Figure 78. The uprights transfer the loads from the wheel to the suspension and steering members, so they are necessarily robust and rigid components. Additionally, they must guarantee the following functions:

1. Provide radial and axial support for the wheel bearings, and insertion surfaces for the radial seals of the wheel transmission mechanism.
2. Define the location of the outboard ball joints of the suspension arms.
3. Serve as attachment bracket for the brake caliper.
4. Allow the steering actuation on the front wheels, by providing a spherical joint connection to the tie rods.
5. Offer a fixing flange for the electric motor and cooling jacket.
6. Integrate the planetary gearbox, holding the ring gear and providing lubrication and ventilation holes for maintenance.

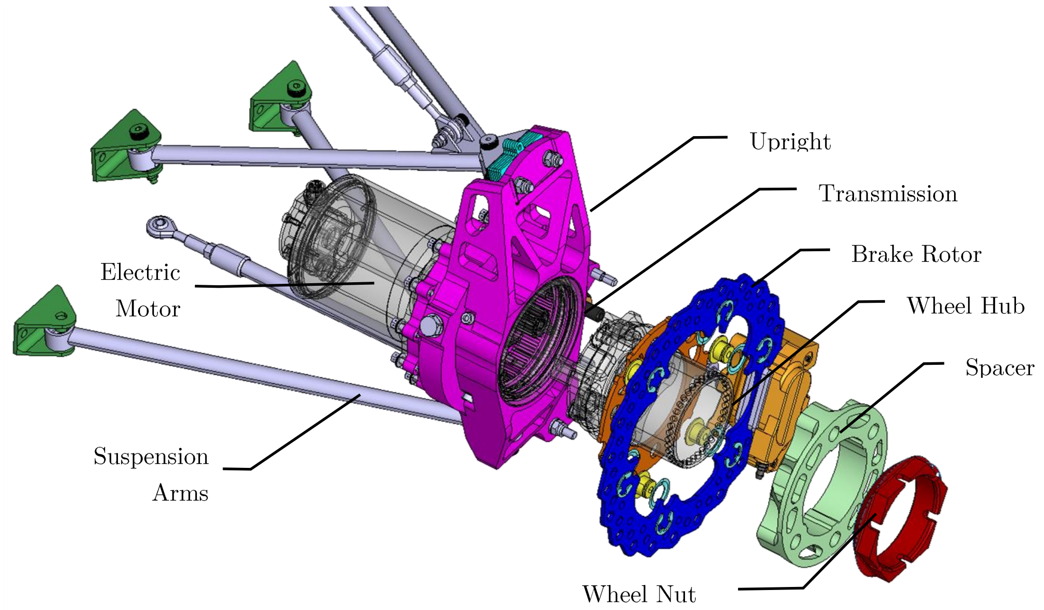

Figure 78 Front Unsprung Masses Assembly (the wheel is not shown).

2.2.1.1 Constraints

The integration between the gear train and the wheel upright is determined by several geometrical constraints related to the correct functioning of the transmission, brakes and suspension systems. This type of arrangement requires a complex upright design that needs to provide dimensional accuracy and great rigidity at the interface with all other components to guarantee the functions discussed above. Figure 79 shows a section view of the front wheel assembly of the SC17 car, allowing to appreciate this.

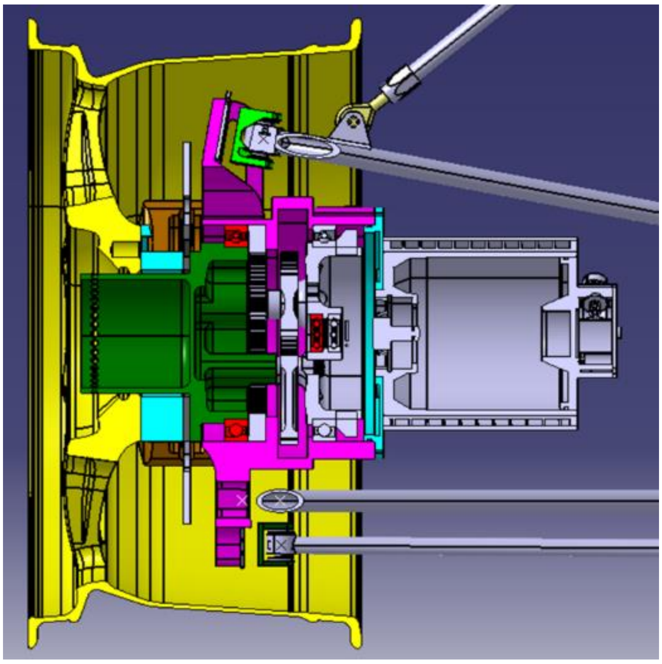

Figure 79: Section view of the front wheel assembly of the

Significant deflections of the A-arms attachment points would produce an undesirable variation of the suspension parameters, like the camber and toe angles, that would be detrimental for the drivability of the car. Thus, the maximum deflection targets listed in Table 5 must be verified considering the combined contribution of the suspension arms and the uprights.

The internal surfaces of the upright serve as the seat for the wheel bearings and geartrain components. Any important deformations would compromise the functioning of the epicyclic transmission, not only reducing its performance but also potentially damaging the wheel bearings or the gears. The same applies to the flange to which the electric motors are attached. It must ensure an accurate positioning of the motor relative to the transmission and must be rigid to provide a good alignment in all loading conditions.

Another important aspect is that the brake calipers should be rigidly fixed to the upright to prevent them from moving under the effect the friction drag loads [33]. The Brembo P4 24 and P2 24 calipers selected in section 2.1 require axial mounting holes to be installed. Since the attachment points are offset from the midplane of the discs, there is a moment arm to the tangential force between the brake pads and the rotor that tends to twist the calipers in the direction of the wheel rotation [33].

All these constraints are opposed to the need for the lightest components possible, so the optimal compromise must be found.

The front uprights are also connected to the steering tie rods, that transfer the control action from the steering rack. This attachment point must be stiff enough to produce the desired steering response, with minimum toe angle variations (Table 6). In the case of the rear upright, the toe angle variations are associated with the car cornering stability [10] [16].

An additional consideration that limits the possible design choices is the feasibility of producing the components, which depend on several factors, such as availability of production facilities or technical partnerships, available materials, budget and manufacturing times that should be compatible with the Team's schedule.

2.2.1.2 Material and process selection

The concurrent engineering method [13] implies that the materials and manufacturing processes must be considered during the design phase to develop parts that can be produced with the available resources. Thus, the design of a given component is driven by how it will be fabricated. Considering this, different combinations of materials and fabrication methods were studied to determine the most convenient one for the uprights.

Being complex components with several geometrical constraints and subjected to different loads, the uprights are often made by other Formula SAE teams using additive manufacturing techniques, as shown in Figure 80. This allows implementing complex and organic shapes that are highly efficient in terms of stiffness and mass. These are generally designed using CAE techniques such as Topology Optimization.

The Polito Racing Team had implemented additive-manufactured titanium wheel uprights in previous seasons, resulting in a reduction of the mass compared to traditionally machined uprights. Although this would be beneficial for reaching the SC18 targets, the implementation of additive-manufactured parts happened several years before the adoption of the in-wheel electric motors scheme. In 2018, the more complex geometries needed to integrate the planetary transmission would require further post-processing operations [34] to obtain the desired results. To achieve an adequate level of reliability using additive-manufactured parts, those must be produced by a specialized technical partner.

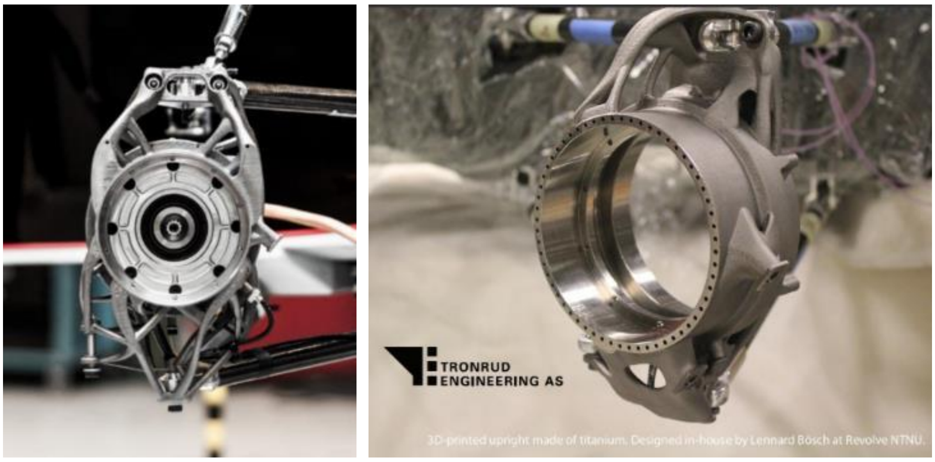

Figure 80: Additive-manufactured uprights by Revolve NTNU [63]

Other solutions adopted by some Formula Student teams are based on compound or hybrid construction methods, such as the ones shown in Figure 81.

Figure 81: Hybrid upright construction methods used by TUW Racing [64] and TU Graz Racing [65].

These offer the possibility of utilizing different material properties for different features based on their functions and loading conditions. These are highly innovative approaches, but they require great development times, including prototyping ans physical validation.

On the other hand, the SC17 uprights were made of 7075-T6 aluminum using a 5-axis CNC milling machine. The major advantage of these was their mechanical reliability. Another positive aspect was the existing collaboration with a specialized manufacturing partner (Officina Meccanica Massola Giuseppe [66]) that offered a close collaboration during the development process of the mechanical parts in 2017 and the previous years.

They provided precise results and adjusted their manufacturing schedule to match the necessities of the Team.

Considering the advantages and disadvantages of the different alternatives the decision was to develop the uprights to be CNC-machined from 7075 aluminum. The matrix shown in Table 29.

Table 29: Decision matrix for selecting the material and production process for the uprights.

Manufacturing technique	Weight-reduction opportunities	Reliability	Manufacturing complexity	Development time	Cost	Total
CNC-machined aluminum	★★	★★★★★	★★★★	★★★	★★★★	18
CNC-machined titanium	★★★	★★★★★	★★	★★★	★★	15
Additive-manufactured aluminum	★★★★	★★★	★★	★★	★	12
Additive-manufactured titanium	★★★★	★★★★	★	★★	★	12
Hybrid production (casting, composites, etc.)	★★★★	★	★	★	★★★	10

The material properties of 7075 aluminum in two different heat treatment conditions are listed in Table 30 and the S-N (Wöhler) curves for un-notched specimens are shown in Figure 82.

Table 30: Properties of 7075 aluminum [62].

	Yield strength [MPa]	Tensile strength [MPa]	Young Modulus [GPa]
7075-T651	516	573	71.7
7075-T6	488	567	

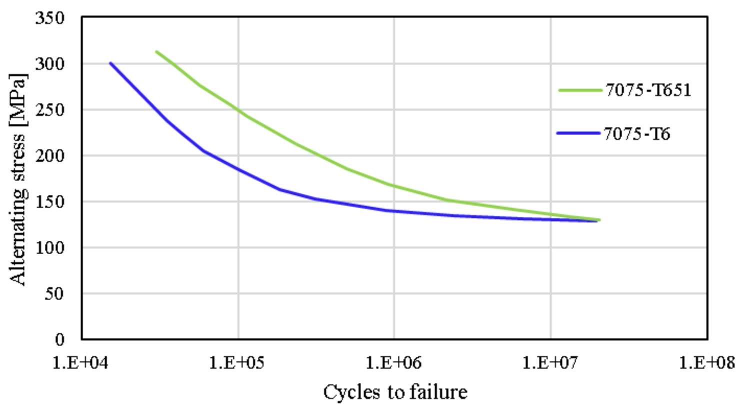

Figure 82: Wöhler curves for un-notched specimens of 7075 aluminum [62].

2.2.1.3 Geometry definition

As already introduced, the primary geometric constraints for the design of the uprights were determined by the suspension hardpoints and the planetary transmission envelope.

Once the brake calipers were selected, and their positions defined (based on the results from the CFD analyses shown in Figure 49) the initial geometries of the uprights were defined.

Considering the manufacturing process to be used, an initial rectangular aluminum billet was considered for both the front and rear uprights. Then, the features required to integrate the different systems were added to define the zones to be respected during the development. After that, the design was refined through a series of iterations, using Altair Optistruct [58] to perform stress analyses and verify the stiffness targets while minimizing the mass. Since all the transmission assemblies were equal, both the front and rear uprights had the same central geometry.

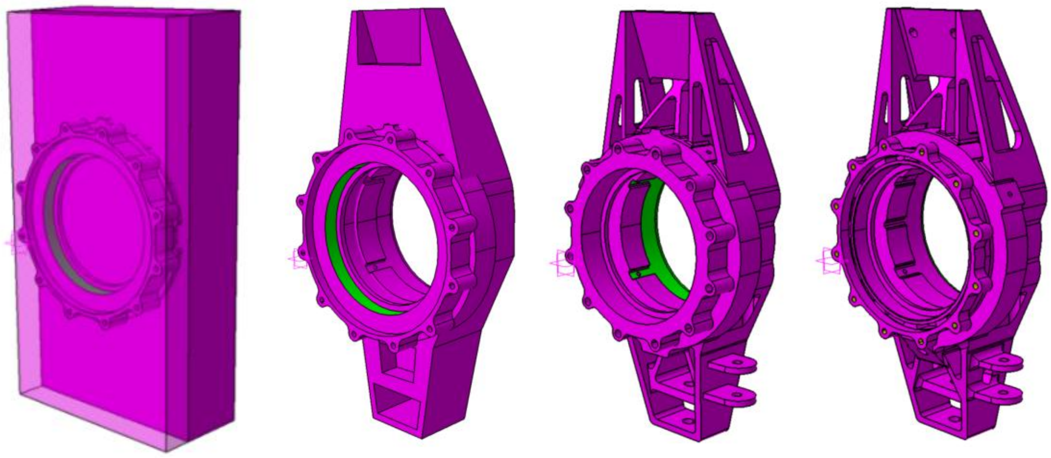

Figure 83: Different stages of the development process of the rear uprights.

To facilitate the machining operations, the pockets implemented for weight reduction were added considering the minimum lengths and radii required to remove the material, as well as avoiding any geometries difficult to make from milling operations.

For brevity, not all the decisions taken for moving from one iteration to another will be discussed. Instead, a summary of the functional features of the uprights is presented.

Figure 84 shows a cross-section view of the SC18 rear wheel assembly. The critical components integrated in the inner part are highlighted.

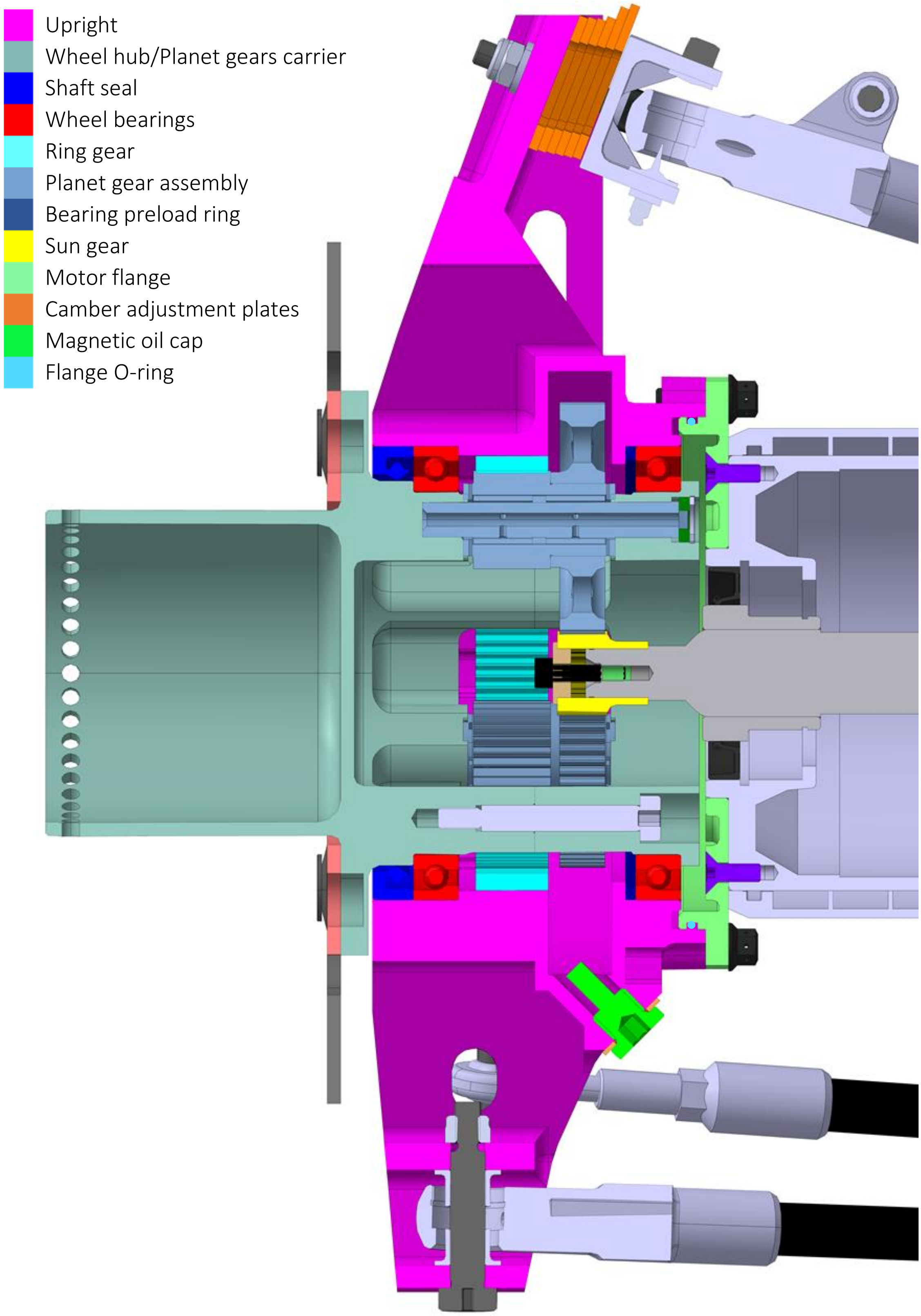

Figure 84: Cross-section of the SC18 rear wheel assembly.

Integration with the planetary geartrain

The detailed design of the SC18 planetary gear train is documented in the Master of Science Thesis work by Marco Cova [12]. The calculations and analyses performed for defining the gear train specifications are thouroughly described in his work. Here, we only summarize the relevant features for integrating the transmission system and the electric motors on the uprights. Most of these can be seen in Figure 84.

The upright must provide installation seats for the wheel bearings. These were SKF angular contact ball bearings, designation 71816 ACD/P4 [12] [67].

In the outer end of the central cylinder (i.e., the one facing the brake rotor), an additional seat is required for the shaft seal that contains the transmission oil. In the inner end instead, the electric motor is fixed to a flange that is bolted on the upright. To seal the transmission oil, the flange has an O-ring gland on its external surface, so that the elastomeric seal is squeezed when installed on the upright. These installation surfaces, common between the front and rear uprights, must have an adequate surface finish (roughness) and precise tolerances to guarantee the correct operation of the seals.

Considering the serviceability, the uprights have three different threaded holes used for changing the transmission oil. A bottom hole, used for draining, is sealed by a magnetic oil cap, that collects the steel particles produced by the gears wear. On the top side of the upright center, above the liquid level, there is a hole to facilitate filling new oil into the housing. There is also a smaller hole, also above the oil level, that serves for venting during the oil change operations. Because of the different positions of the lower ball joints between the front and rear suspension, the position of the draining holes is not the same in both axles. The difference can be seen in Figure 85.

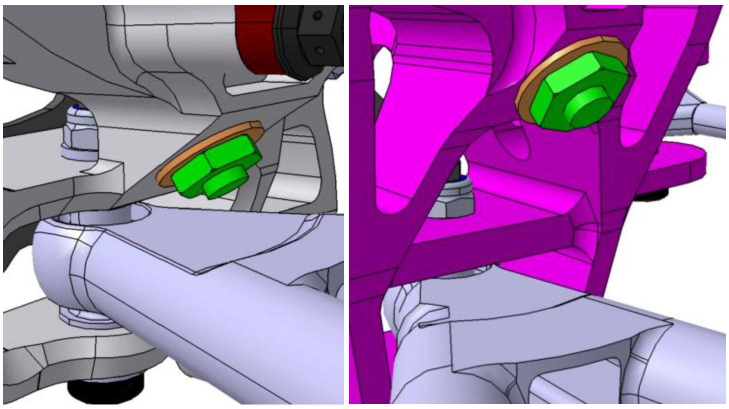

Figure 85: Location of the oil draining hole in the front and rear uprights (left and right side, respectively).

In Figure 84 the ring gear is highlighted in cyan color. Six installation grooves guarantee its correct positioning on the upright and provide a rotational constraint, reacting to the moment transferred by the planet gears. The axial constraint is provided by three positioning pins, threaded into the upright, that prevent the axial displacement of the ring gear once installed. All these mating surfaces are equal in both the front and rear uprights and were designed in collaboration with the Powertrain division. Figure 86 shows a section view of the rear upright in which these features can be appreciated.

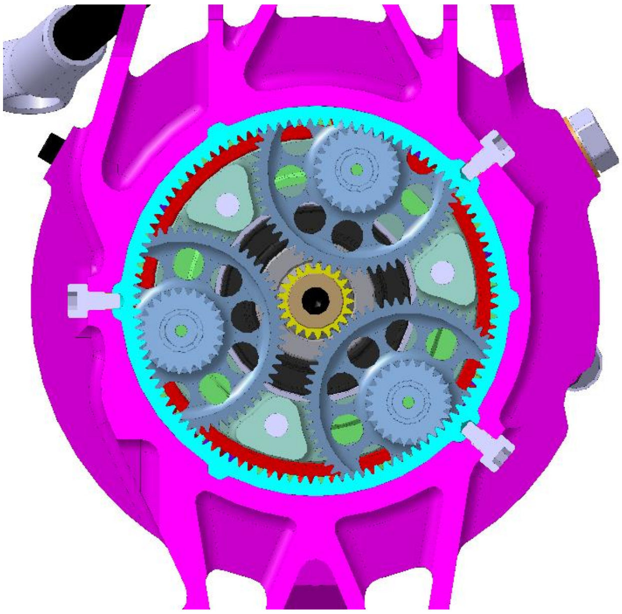

Figure 86: Integration between the ring gear and the upright.

Suspension and steering joints

Among the specifications indicated in Table 5 and Table 6, the regulation possibilities for the static camber angle was required. To achieve this, the attachments of the upper control arms were separate brackets, bolted into the uprights. Between them, a series of aluminum camber adjustment plates or "*camber shims*" were placed, as can be seen in Figure 84. This solution was already adopted in 2017 and proved to be effective and easy to implement. For the SC18 car, each camber shim had a thickness of 2 mm. Thus, each shim added produced a positive camber variation of approximately 0.5 degrees. The same type of camber plates was used for the front and rear axle. Similarly, to adjust the Ackerman ratio [10] in the front axle, the attachment of the steering tie rod was separated from the upright by smaller aluminum shims of the same thickness. The geometry of the shims is shown in Figure 87.

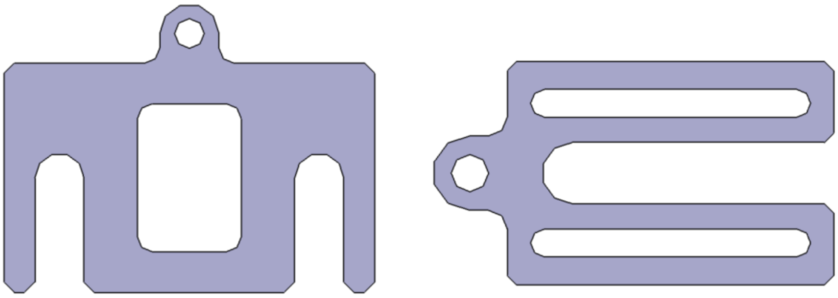

Figure 87: Aluminum shim used to regulate the static camber angle (left) and the Ackerman ratio.

To minimize the free play in all the connections with the suspension and steering systems, shoulder screws (similar to ISO 7379) were used in all the joints. To comply with the regulations introduced in section 1.2.1 regarding the critical fasteners, the screws were made of a steel alloy with a mechanical resistance equivalent to ISO 12.9 grade. They were secured with nylon lock nuts in all the low temperature zones, and their length was selected so that a minimum of 3 threads protruded from the nuts. All the joints between the uprights and the suspension and steering system were designed to have the fasteners loaded in double shear. An example can be seen in Figure 88.

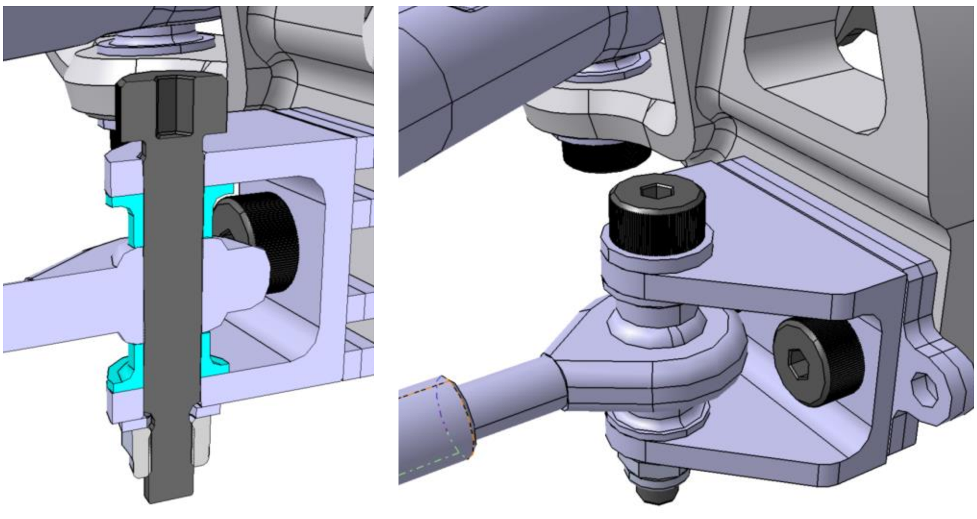

Figure 88: Steering tie rod attachment in the front upright.

To verify the absence of interferences during the operation of the steering mechanism, the detailed CAD model of the front suspension assembly was used to simulate the maximum steering angles, as shown in Figure 89.

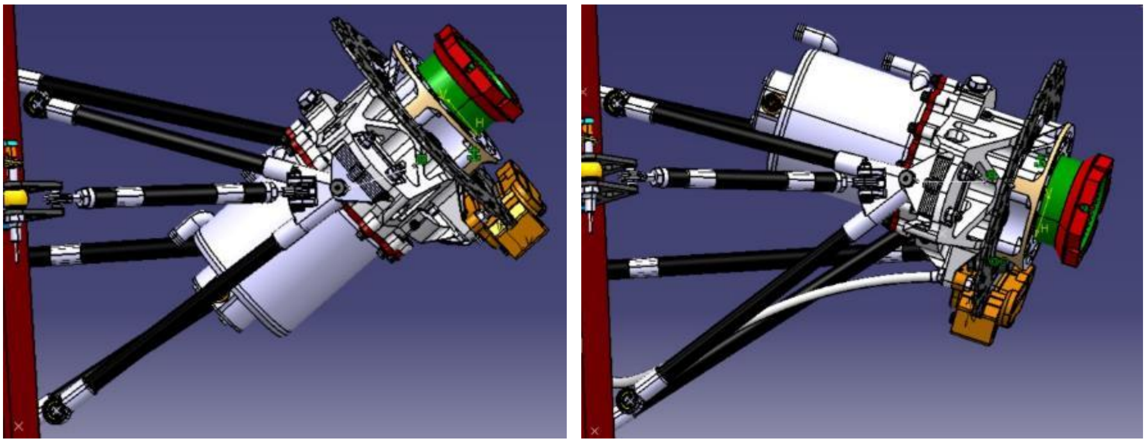

Figure 89: Verification of the correct operation at the maximum steering angles.

Brake Caliper attachments

As introduced, the correct and rigid positioning of the brake calipers on the uprights is critical to obtain a reliable operation of the brakes. The mounting brackets on the front and rear uprights were designed considering the effects of caliper twisting [33] using suitable loading conditions on the stress analyses of the uprights, as will be discussed later. During the design process the assembly clearances necessary for the fasteners and hydraulic fittings was considered allowing to achieve a god packaging as shown in Figure 90.

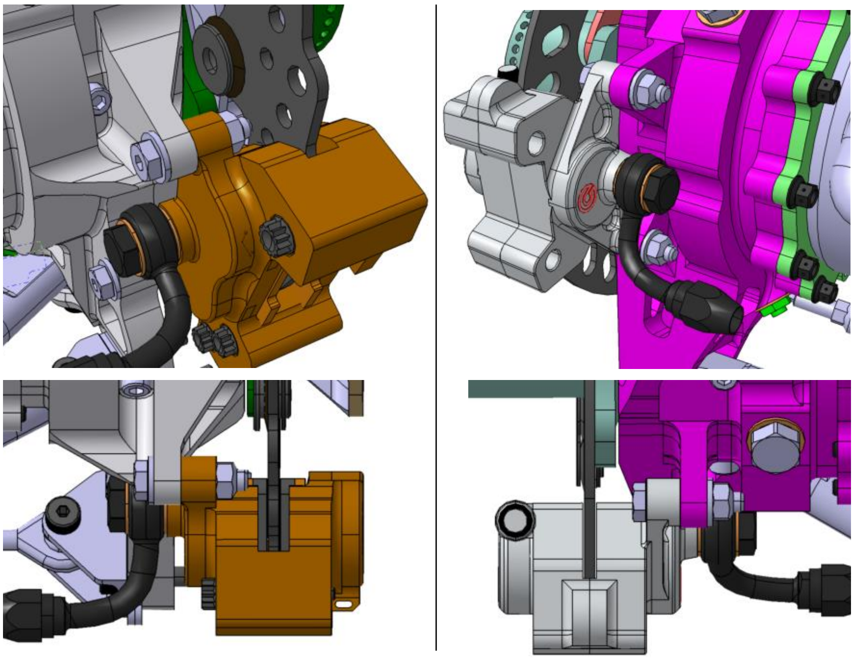

Figure 90: Brake caliper attachments in the front (left side) and rear (right side) uprights.

To secure the calipers in position accurately, custom shoulder screws were designed to fit their installation holes. Since the P4 24 and P2 24 brake calipers are commercial products, they are designed to fit attachment brackets with a wide range of tolerances. Thus, their fixing holes have a nominal diameter of 7.2 mm which does not match precisely any existing metric bolt size. The purpose of this is to provide enough clearance so that the radial position of the calipers can be adjusted during the installation process, to achieve the correct alignment with the friction ring even in case of small deviations from the nominal dimensions of the motorcycles in which they are installed [36]. On the other hand, the position of the calipers in the SC18 uprights with respect to the brake rotors was determined by the manufacturing tolerances of all the parts that make up the wheel assembly. Since the components of the 2018 Formula Student car would be produced using rather precise specifications, securing the calipers with bolts having a precise fit was a way to ensure that their location matched the one determined by design.

The bolted connection was analyzed considering the loading conditions indicated in Table 14. Figure 91 shows a scheme of the forces and dimensions used in the calculations (the reference system does not correspond to the vehicle-centered one).

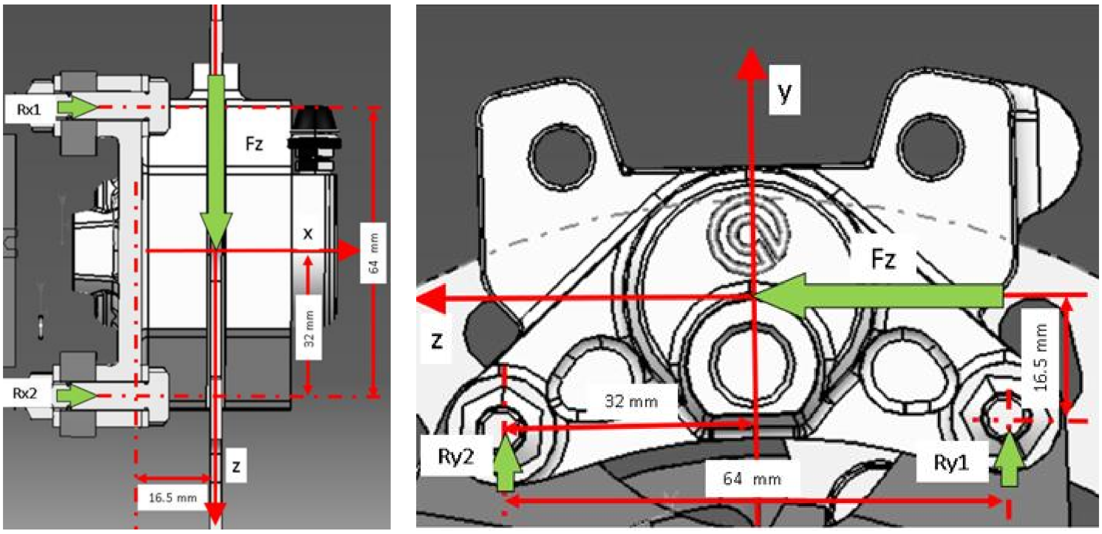

Figure 91: Schematic representation of the forces considered for dimensioning the caliper bolts.

The results from the computations for the most stressed bolts in the front and the rear axles (R1 in Figure 91) are summarized in Table 31 and Figure 92 shows the drawing of the bolts used for the rear calipers. The analysis method can be found in references [59] and [9].

Table 31: Static stress and fatigue life computations for the caliper bolts.

	Tensile load [N]	Tangential load [N]	Joint separation factor	Von Mises Stress [MPa]	σ_m (mid-range stress) [MPa]	Fatigue safety factor (Gerber)
Rear bolt	1098	2740	2.43	147	148	2.50
Front bolt	2070	5163	1.29	248	198	1.48

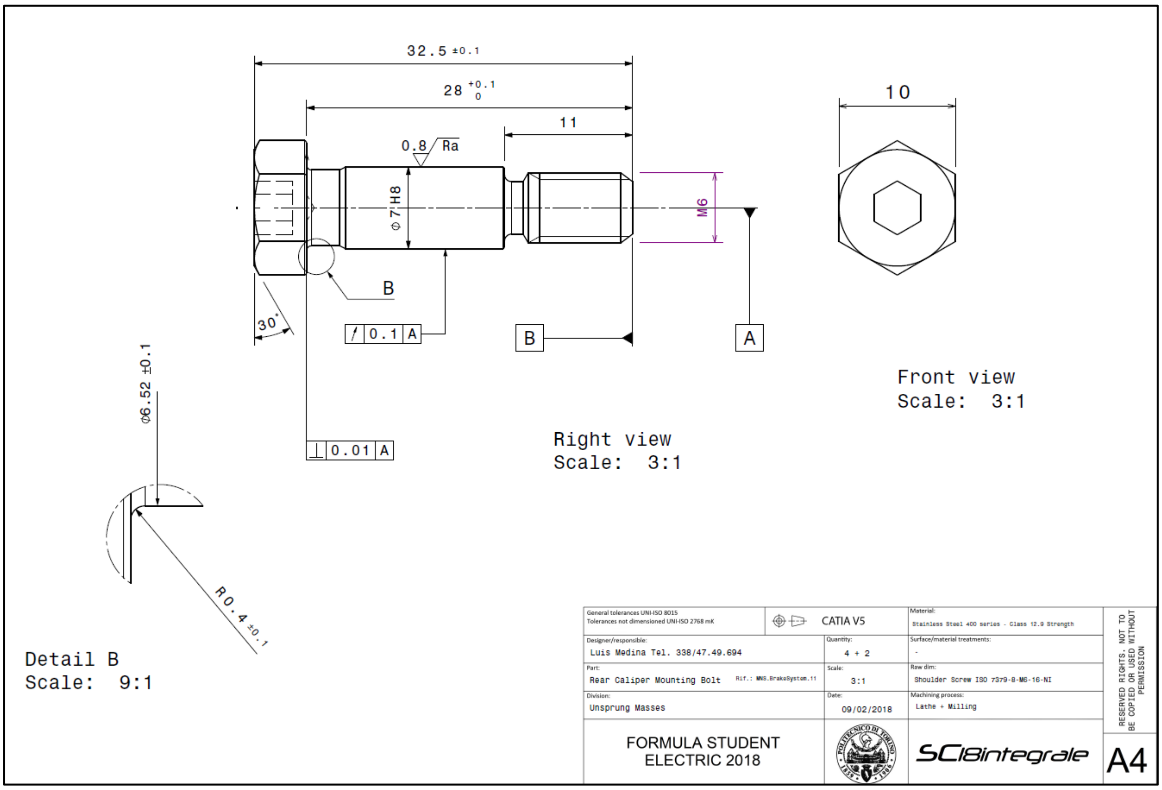

Figure 92: Rear brake caliper shoulder screw (not to scale).

2.2.2 Structural analyses

Two different types of static stress analyses were performed using Altair OptiStruct to verify the characteristics of the uprights. The first type was implemented during the early stages of the development process to assess the mechanical response of the uprights considering the input loads listed in Table 9. This type of analysis will be referred to as "single component analysis" in the following. When the design was already more advanced, a second type of simulation was performed to verify the response of the suspension assembly (A-arms and uprights) to the loads transferred from the tire contact patch. In this section, both types of analysis are described, starting from the single-component type.

Before addressing the details of the simulations, the type of mesh used for both types of analysis will be briefly reviewed.

Mesh and types of elements used

The 3D meshes were based on TETRA4 elements [58]. The element size was changed in different stages of the development process. For the first simulations, the it was set to 1.5 mm. This resulted in a mesh size of approximately 300 000 elements, which was enough for the initial assessments. To verify the final geometries at the end of the design process, the mesh size was reduced to 0.1 mm, in order to obtain greater accuracy in the critical areas that had stress concentration features such as small radii or sharp edges. For this reason, the number of elements was about 8 millions. The meshing method started from a semi-automatic generation of a 2D mesh based on a quality index optimization for the target element size [58]. The surface geometries used as input for generating the 2D mesh were manually modified to create "washers", surface partitions around holes and circles, in which the mesh density or the distribution of the elements can be refined to obtain a more accurate discretization of the curved shapes. Two examples of this can be seen in Figure 93.

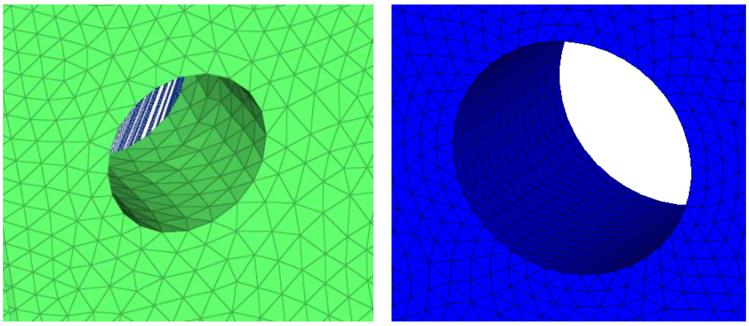

Figure 93: Mesh washers around small features.

2.2.2.1 Single-component analysis: compliant boundary conditions based on bearing stiffness data

This type of analysis assumed that all the loads transferred through the suspension geometry would be reacted by the uprights, without considering the stiffness of the suspension arms. Both the front and rear upright were analyzed considering the four load cases and the forces listed in Table 9. The configuration of the analyses is shown in Figure 94.

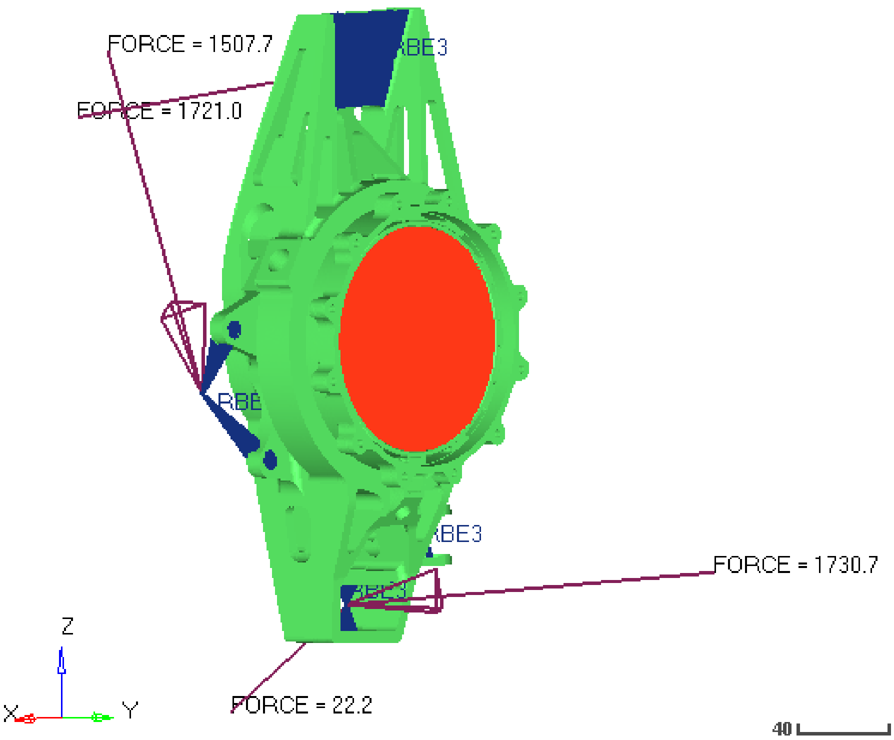

Figure 94: Loads applied for a single component analysis of the rear upright (Brake in turn load case)

As can be seen, the forces were applied through RBE3 elements [58]. This type of unidimensional elements is used to associate a dependent node to a group of mesh nodes. The displacement of the dependent node is calculated as the weighted average of the motion of the associated nodes. Thus, they can be used to apply load without adding an artificial stiffness to the mesh [55]. The dependent nodes were located at the center of the spherical joints of the upper and lower control arms, the center of the rod-end at the outer end of the tie rod, and the projection of the brake pads centroids in the midplane of the brake rotor. The independent nodes were associated to the elements on fixing holes for the fasteners, as can be seen in Figure 95. In the case of the upper control arm, the load was distributed on the contact area of the camber plates.

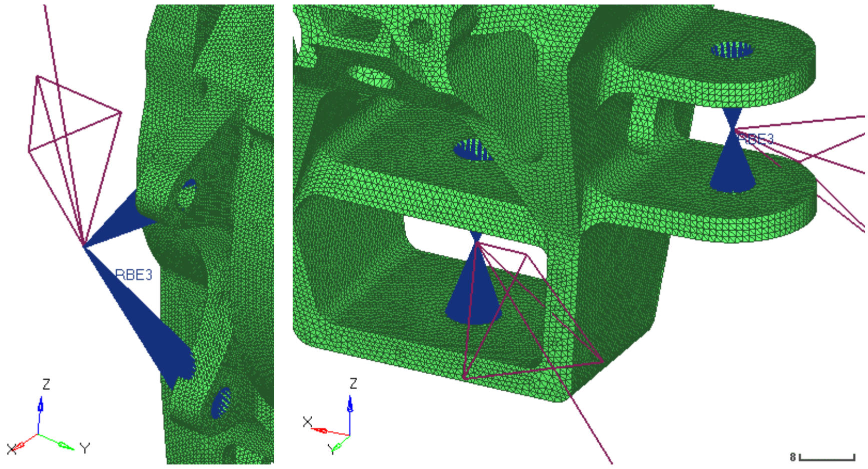

Figure 95: Detail of the RBE3 elements used to apply the loads in the single component analyses.

Since the application point of the caliper force is offset from the attachment points, this simulation considers the caliper twisting effect [33].

Regarding the motion constraints, the displacements of the elements located at the surfaces of the bearing seats were restricted using a combination of RBE3 and CBUSH elements [58]. The latter are unidimensional elements composed by two nodes, normally used to model compliant fasteners or springs.

One RBE3 element was created for each wheel bearing. The dependent node was located at the center of the bearings and the independent ones were the mesh elements located on the corresponding bearing seat.

To simulate the wheel bearings, two CBUSH elements were created with an arbitrary length. For each bushing, one end was associated to the dependent node of an RBE3 element and the displacement of the other one was limited by a single point constraint restricting the 6 degrees of freedom of the bushing end. Finally, the constrained ends of the CBUSH elements were shifted to obtain zero-length bushings, as shown in Figure 96.

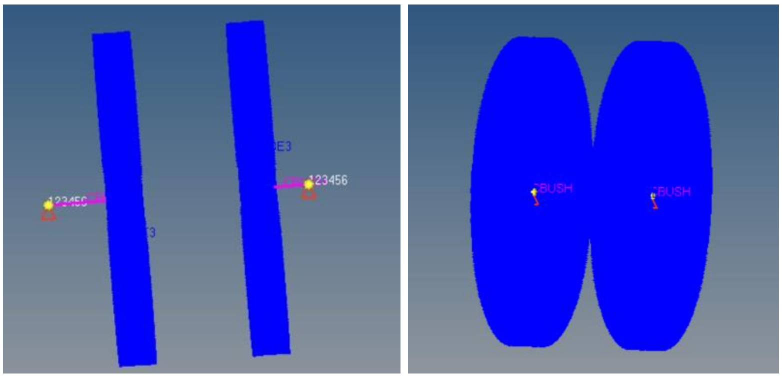

Figure 96: Compound elements used to simulate the wheel bearings.

Since the CBUSH elements are compliant, the motion restriction was not directly applied to the upright's geometry, avoiding the addition of artificial stiffness.

The stiffness of each CBUSH elements was defined using the properties of the SKF 71816 ACD/P4 bearings [67]. The axial and radial stiffness values used are listed in Table 32.

Table 32: Bearing stiffness values used for the FEA.

Axial stiffness [N/µm]	Radial stiffness [N/µm]
171	115

Results

The simulations were used to determine the stresses and displacements on the uprights. The results of the analyses done on the SC18 uprights were compared to those performed on the SC17 ones using the same type of boundary conditions. This provided a better idea about what could be considered acceptable in terms of stresses and deformations, given the fact that the material used for producing the new components would be the same used in 2017. A comparison of the resulting displacement contour plots for the rear SC17 and SC18 uprights is shown in Figure 97.

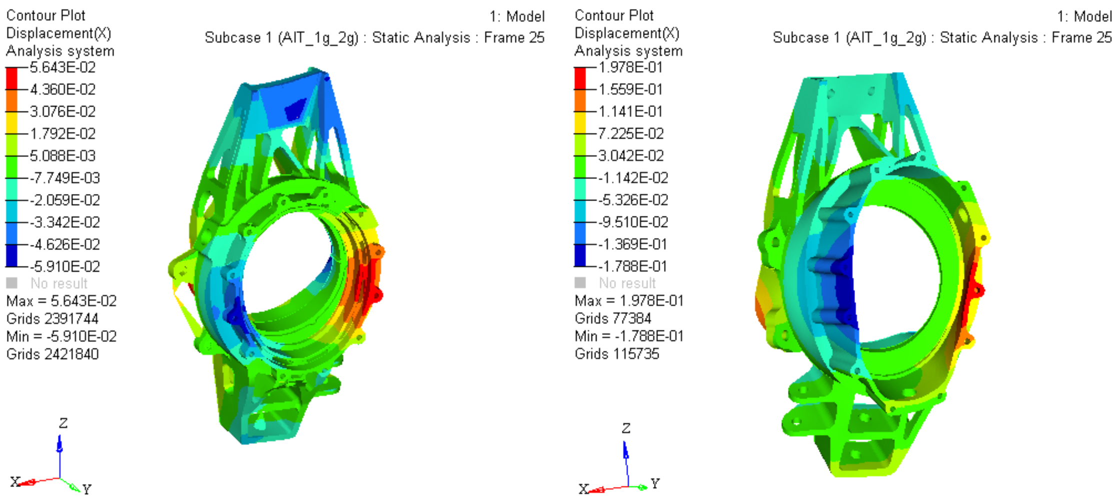

Figure 97: Comparison between the contour plots of the displacements (in mm) along the X axis for the rear SC18 and SC17 uprights.

The displacements along the X direction provided an insight on the deformations of the bearing seats under loads. The SC18 version (left) presented a much greater stiffness in this area, compared to the SC17 one (right). The Maximum bearing deformation for the new upright was only about 30% of the SC17 value. Although the 2017 uprights were optimized for maximum stiffness, the use of rigid constraints in the bearing surfaces added artificial rigidity to the bearing supports, preventing the optimization from reducing the deformations in that zone. Thus, using the compliant constraints in 2018 allowed improving the accuracy of the stress analysis. The deformation of the bearing seats was also lower because of the reduced size of the transmission envelope, which resulted in a much shorter length of the transmission housing. Thus, the structure was intrinsecaly more rigid than the SC17 version.

The signed von-Mises stress contour plots were used to analyze the distribution of the tension and compression stresses in the uprigths. The aim was to verify that the maximum tension stresses were below the fatigue limit of the component. Based on the properties of 7075-T6 aluminum shown in Figure 82 the fatigue limit for the uprights was 140 MPa, considering a duration of 100 000 cycles and a fatigue stress correction coefficient of 0.8. This was a conservative assumption, since the loading conditions studied correspond to absolute worst-case scenarios, and the Formula SAE car is designed to compete during only one season. Thus, the possibilities of loading the uprights under those conditions such a high number of times was very low. Additionally, the maximum stresses found in the SC17 uprights analyzed under the same conditions were much higher, as shown in Figure 98, although the actual components did not exhibit any type of failure. Further analyses can be done in this area for the following years.

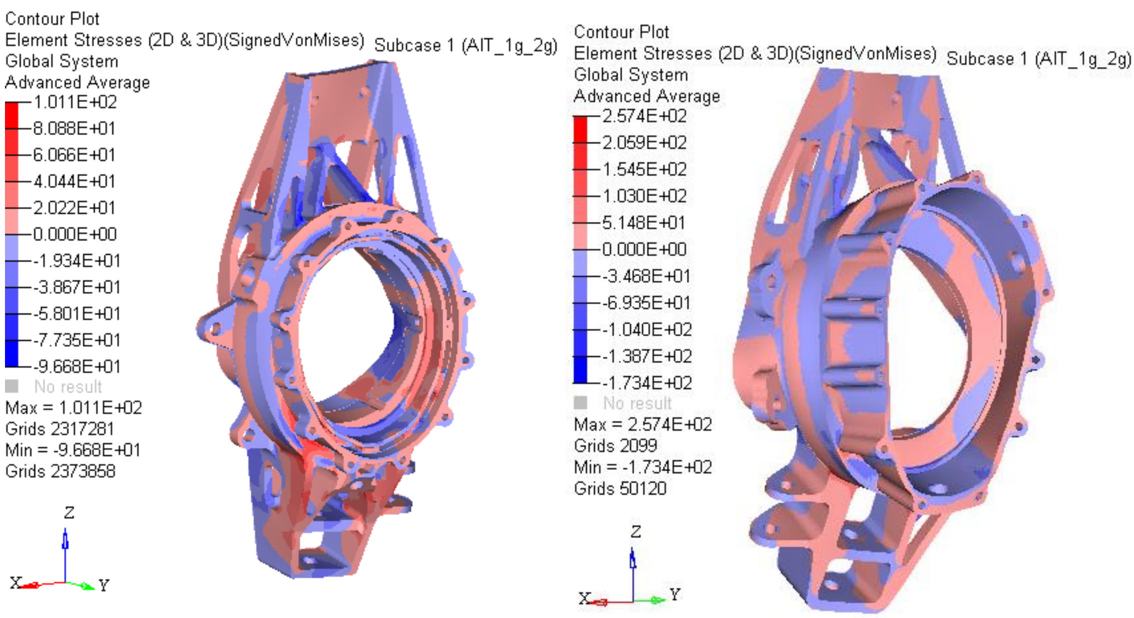

Figure 98: Comparison of the signed von-Mises stress contour plots (MPa) of the rear SC18 and SC17 uprights.

The worst-case loading condition for the rear uprights was the acceleration in turn (AIT) load case, while for the front ones the greatest stresses resulted from the brake in turn maneuver. Figure 99 shows the overall results for the von-Mises stresses in both uprights under those loading conditions.

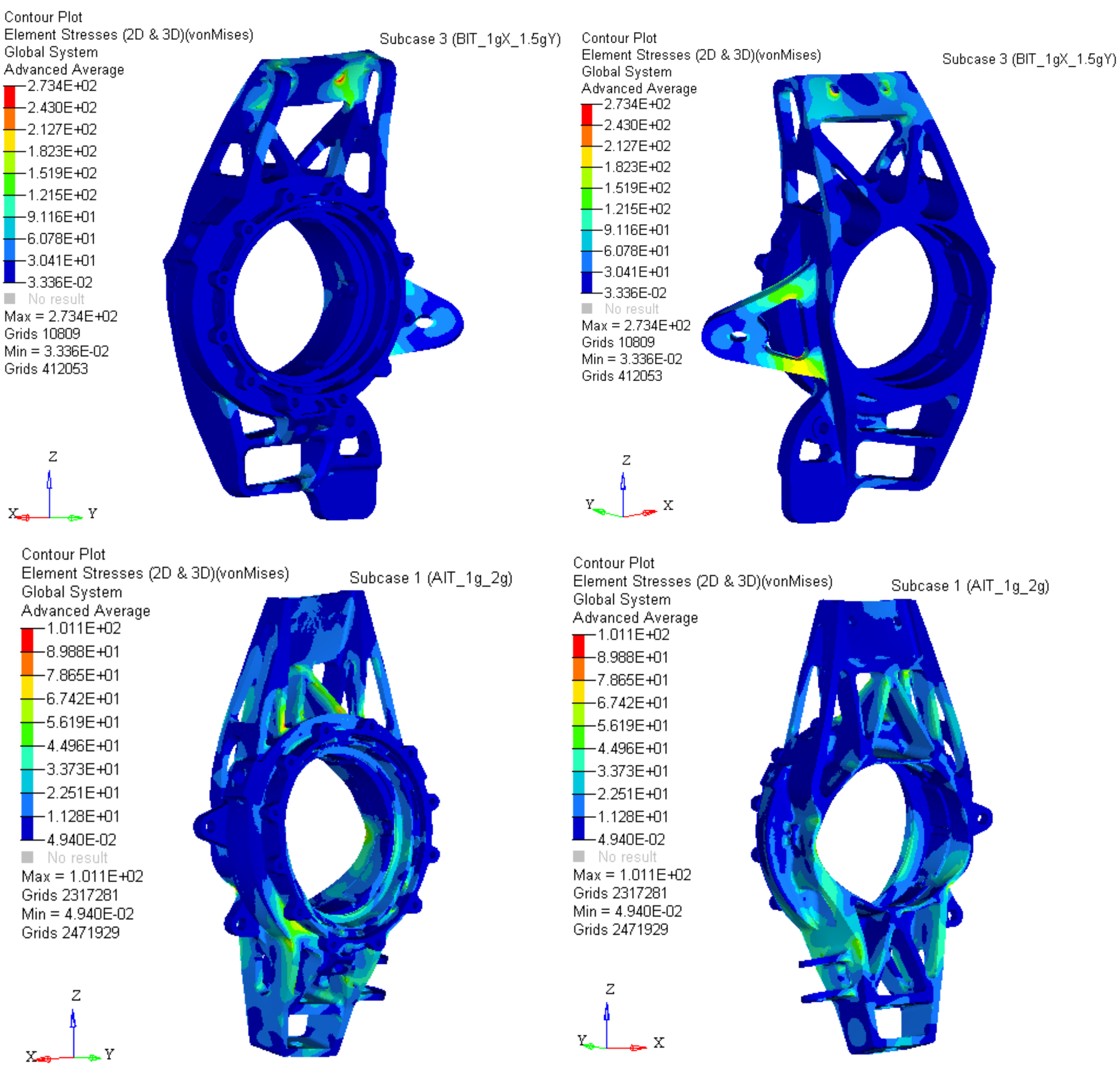

Figure 99: Von-Mises stress [MPa] contour plots of the front and rear uprights under the worst loading conditions (top and bottom images, respectively).

As can be seen, the rear upright was uniformly stressed across all the geometry, and the maximum stress value of 101 MPa was within the acceptable values for fatigue life. Figure 100 displays the von-Mises stress contour plots of the critical areas for the rear upright.

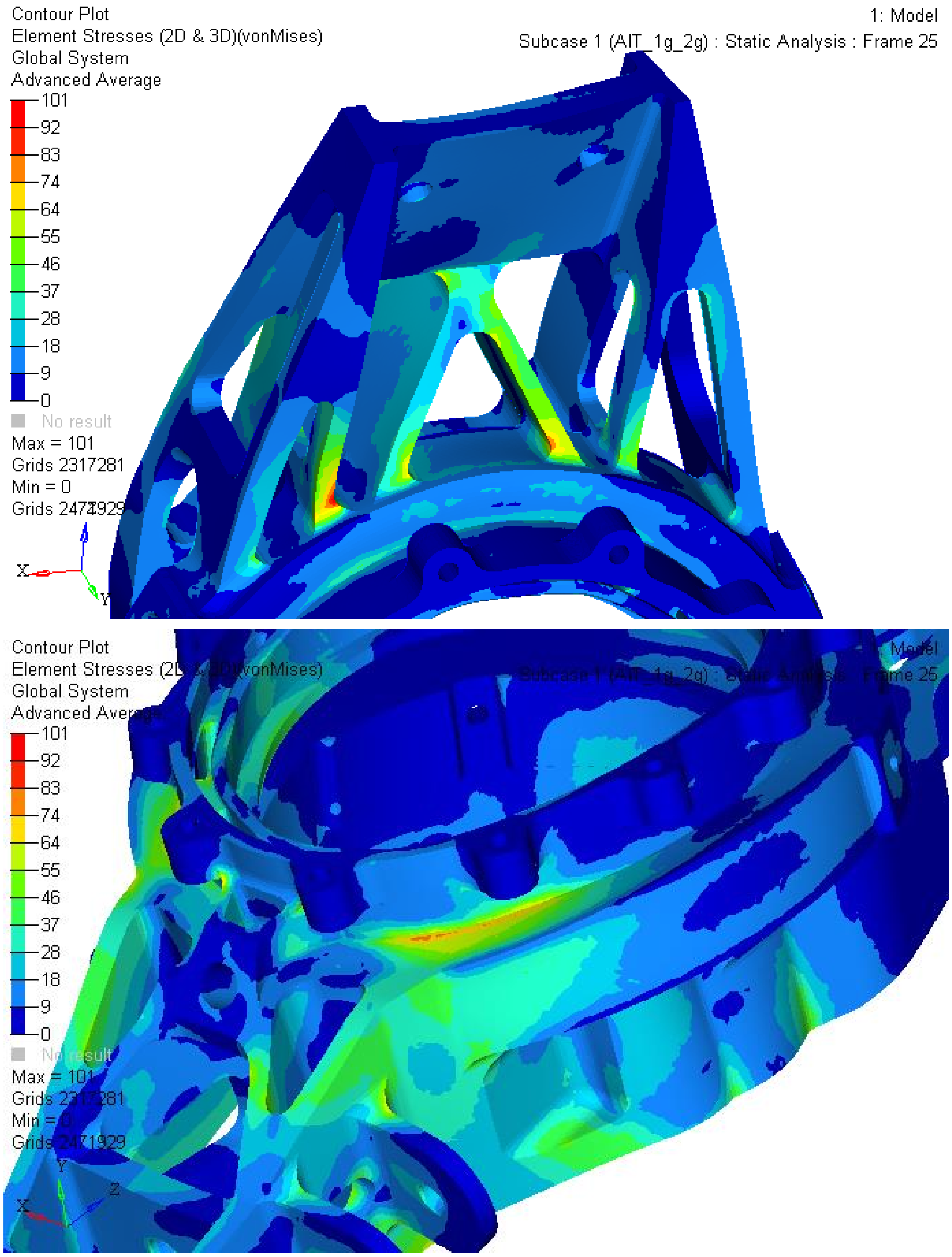

Figure 100: Von-Mises stress contour plots of the critical areas in the rear uprights [MPa].

On the other hand, the front upright showed much larger stresses localized in the caliper bracket.

The maximum displacement of the caliper upper caliper attachment point was 1.6 mm due to the effect of the caliper friction drag force. Although the simulations were done using very conservative load cases, this result was considered excessively high. Thus, the geometry of the caliper braket was modified and verified for the hard braking load case. The new design produced a maximum deflection of 0.1 mm. The results can be seen in Figure 101.

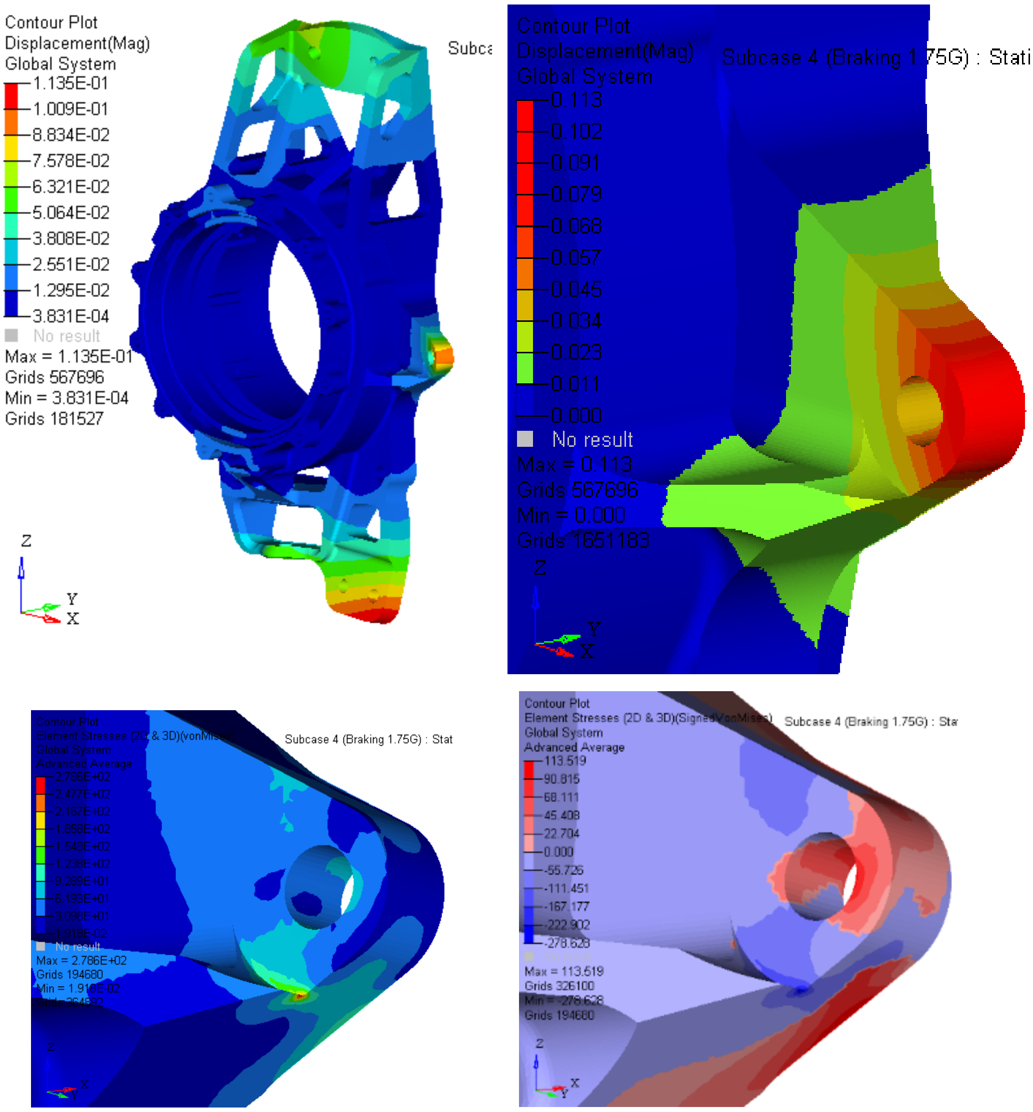

Figure 101: Contour plots of the stress analyses of the modified front caliper bracket under hard braking loads. Top: displacements, in mm. Bottom left: von-Mises stress (in MPa). Bottom right: signed von-Mises stress (in MPa).

The maximum von-Mises stress value was 278 MPa, which was beyond the accetable range for fatigue life of 7075 aluminum loaded in tension. However, the results were acceptad based in two considerations:

1. The peak stress was in compression state, as shown in the signed von-Mises contour plot. The available literature [62] indicates that, when loaded in compression, 7075 aluminum exhibits a greater fatigue resistance.
2. The high value seemed to be caused by the sharp edge on the lower side of the braket, that would probably generate a discontinuity on the mesh, resulting in higher stresses.

The results from the single-component analyses are summarized in Table 33. Overall the new uprights achieved a reasonable improvement with respect to the SC17 ones in terms of weight reduction. The implementation of the compliant constraints resulted in much lower values of deformation on the bearing seats, according to the simulation results.

Table 33: Characteristics of the SC18 uprights and results from the simulations.

Upright model	Mass [kg]	Material Efficiency	Peak von-Mises Stress at max Load [MPa]	Max. Bearing seat deformation [mm]	Fatigue limit for 100 000 cycles [MPa]
SC18R	0.959	10%	119	0.059	150
SC18F	1.094	9%	138	0.039	

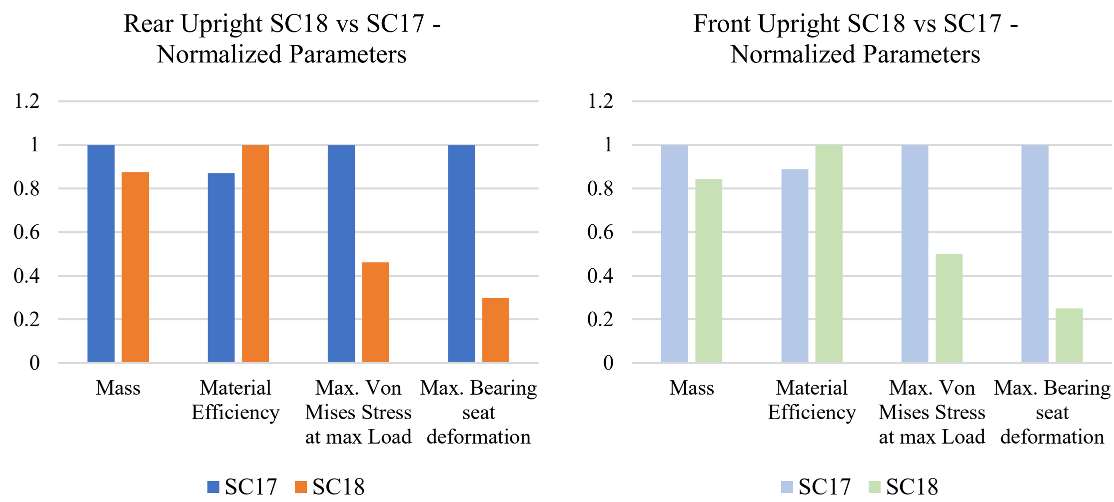

Figure 102: Comparison between the SC18 and SC17 uprights.

2.2.2.2 Suspension assembly analysis

This type of analysis was performed to analyze the response of the front and rear suspension assemblies. Particularly, the variations in camber and toe angles were evaluated. The simulation models use the tire loads as input, constraining the displacements of the on-board attachment points of the suspension elements. These analyses included the loads from the brake calipers as well. Those were applied using RBE3 elements as discussed previously. The tire forces used for the different load cases are listed in Table 34

Table 34: Tire contact patch forces used for simulating the response of the suspension assemblies.

Load case	Axle	Force components [N]		
		X	Y	Z
Hard Braking 1.75g X	Front	-4335.37	0	4134.144
	Rear	-1430.16	0	-493.854
Turn 2.2g Y	Front	0	-2545.93	1394.656
	Rear	-10.	2663.345	1490.146
Brake in turn 1.0g X, 1.5g Y	Front	-3282.87	-1650.22	3549.049
	Rear	-1311.08	1333.171	-644.405
Acceleration in turn 1.0g X, 2.0g Y	Front	-1506.42	-2460.06	1566.177
	Rear	1528.451	2854.417	1529.167

The wheel loads were applied through RBE3 elements in which the dependent node was located on the theoretical center of the tire contact patch. The dependent nodes were associated to the wheel bearing seats in the upright. This can be seen in Figure 103.

Most of the simulations were done considering the CFRP suspension arms (shown in Figure 103), as introduced at the beginning of section 2.2. and the carbon steel suspension arms were validated at the end of the design process. To simulate the CFRP tubes, these were modeled as an isotropic, linear material, implementing an equivalent Young modulus of 150 GPa. The steel tubes, instead, were modeled using the properties of 25CrMo4 steel, with a Young modulus of 210 GPa. The material properties of the aluminum components, such as ball joint housings (in the case of the CFRP a-arms), the upper control arm brackets and the uprights are listed in Table 30.

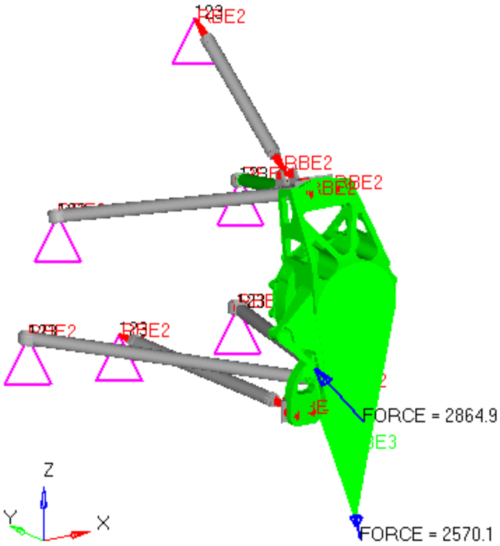

Figure 103: Boundary conditions for simulating the response of the front suspension assembly.

All the fasteners were modeled as rigid elements RBE2. In contrast with the RBE3 type, RBE2 elements add stiffness between the nodes connected by them [58]. In this case, there is one independent node, also known as "master node" that transfers its displacement to the dependent ones ("slaves"). However, since the stiffness of the fasteners was considered much greater than that of the suspension arms and the upright, using RBE2 elements should not have a great influence in the displacement results.

To restrict the free body displacements, the independent nodes of the RBE2 elements simulating the inner ball joints were constrained, blocking the displacements in the X, Y and Z directions, while leaving the other three degrees of freedom free. This ensured that no moments would be transmitted through the joints, as in the real spherical ones. Some examples of the RBE2 elements can be seen in Figure 104.

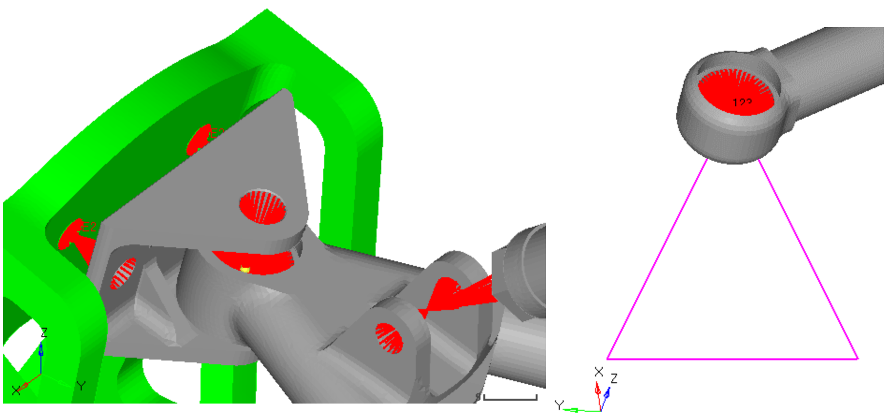

Figure 104: Rigid elements used to simulate the steel fasteners.

Results of the assembly simulations

The four load cases listed in Table 34 were evaluated for both the front and rear suspension assemblies. We will start analyzing the results for the rear axle. The displacement and signed von-Mises stress contour plots are shown in Figure 105:

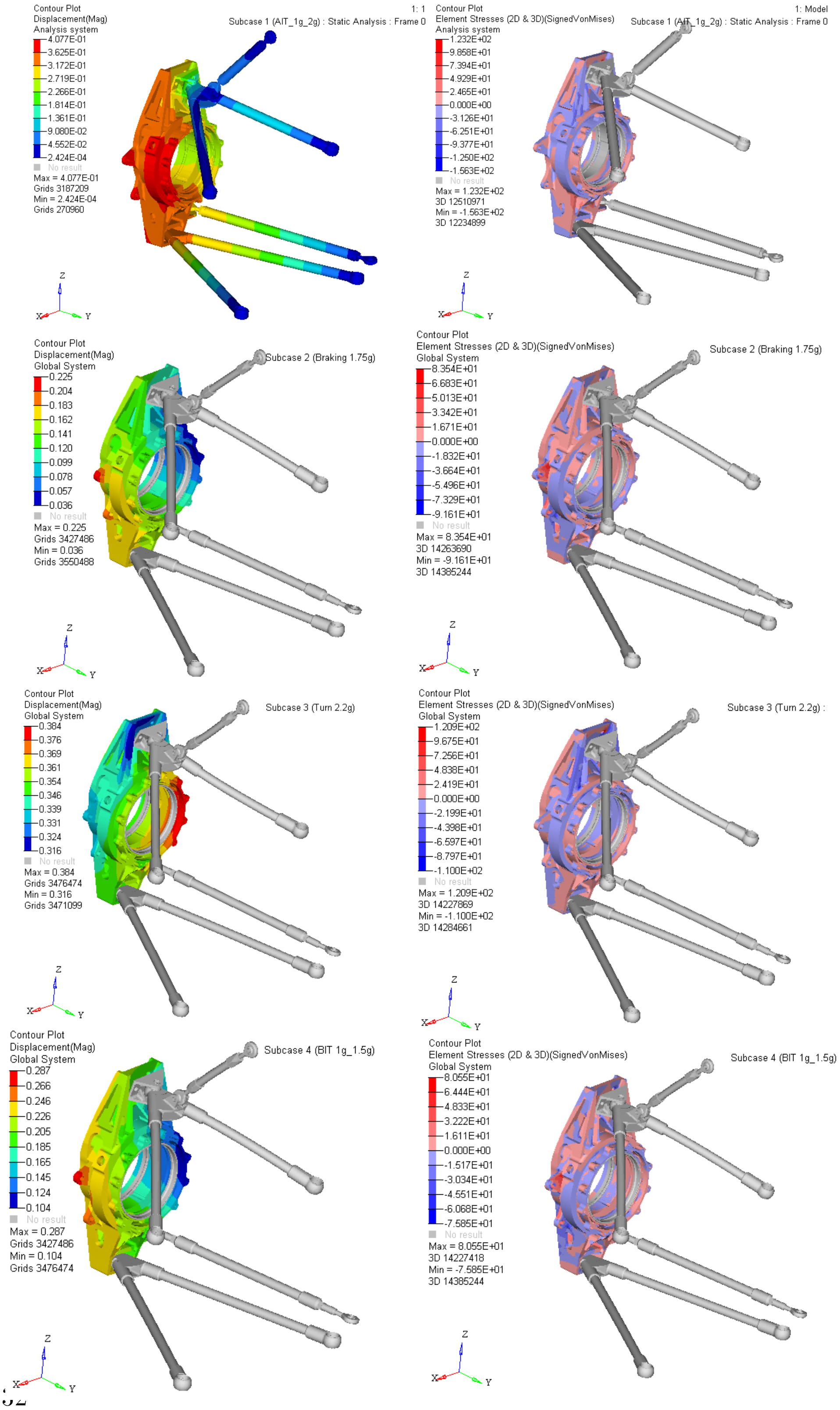

Figure 105: Displacement (in mm, left) and signed von-Mises stress (in MPa, right) results of the rear suspension analyses.

The FE models of the suspension assemblies exhibited higher values of von-Mises stresses on the rear upright. The attachment of the upper control arm presented a stress peak of 154 MPa in compression state, as shown in Figure 106.

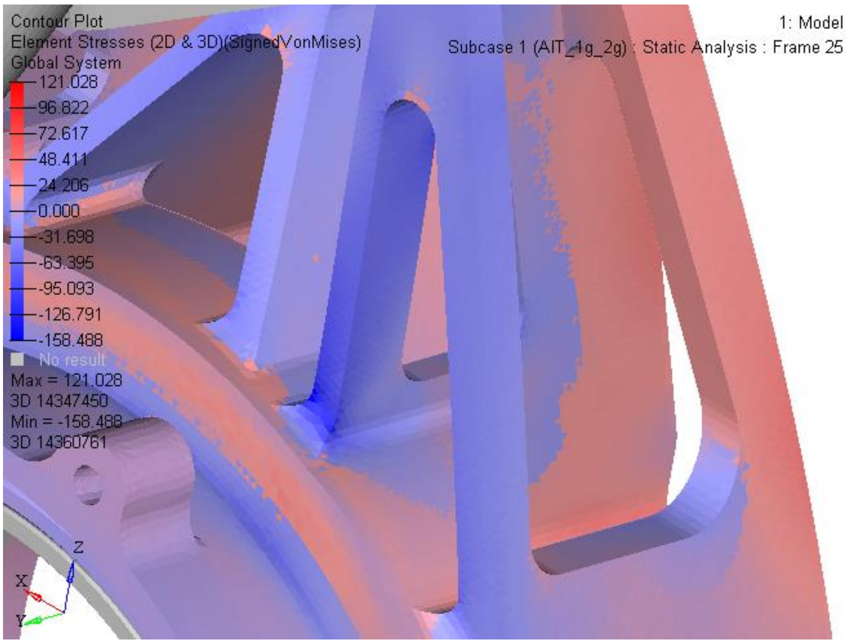

Figure 106: Highest von-Mises stress values on the rear upright [MPa].

This stress value is greater than the fatigue limit established for the uprights (Table 33) based on the properties of 7075-Al (Figure 82). However, taking as reference the maximum stresses found on the SC17 model (Figure 98), it was not considered critical for the fatigue life during a Formula SAE season.
The resulting variations in the suspension angles are listed in Table 35.

Table 35: Rear suspension angle variations.

	AIT 1g X 2g Y	**BIT 1g X 1.5g Y**	**Turn 2.2g Y**	**Braking 1.75 g**
ΔCamber [deg]	-0.001	-0.013	-0.0021	-0.0055
ΔToe [deg]	0.026	-0.036	0.0010	-0.0327
ΔCaster [deg]	0.045	-0.040	-0.0073	-0.0438

The results for the front suspension are shown in Figure 107.

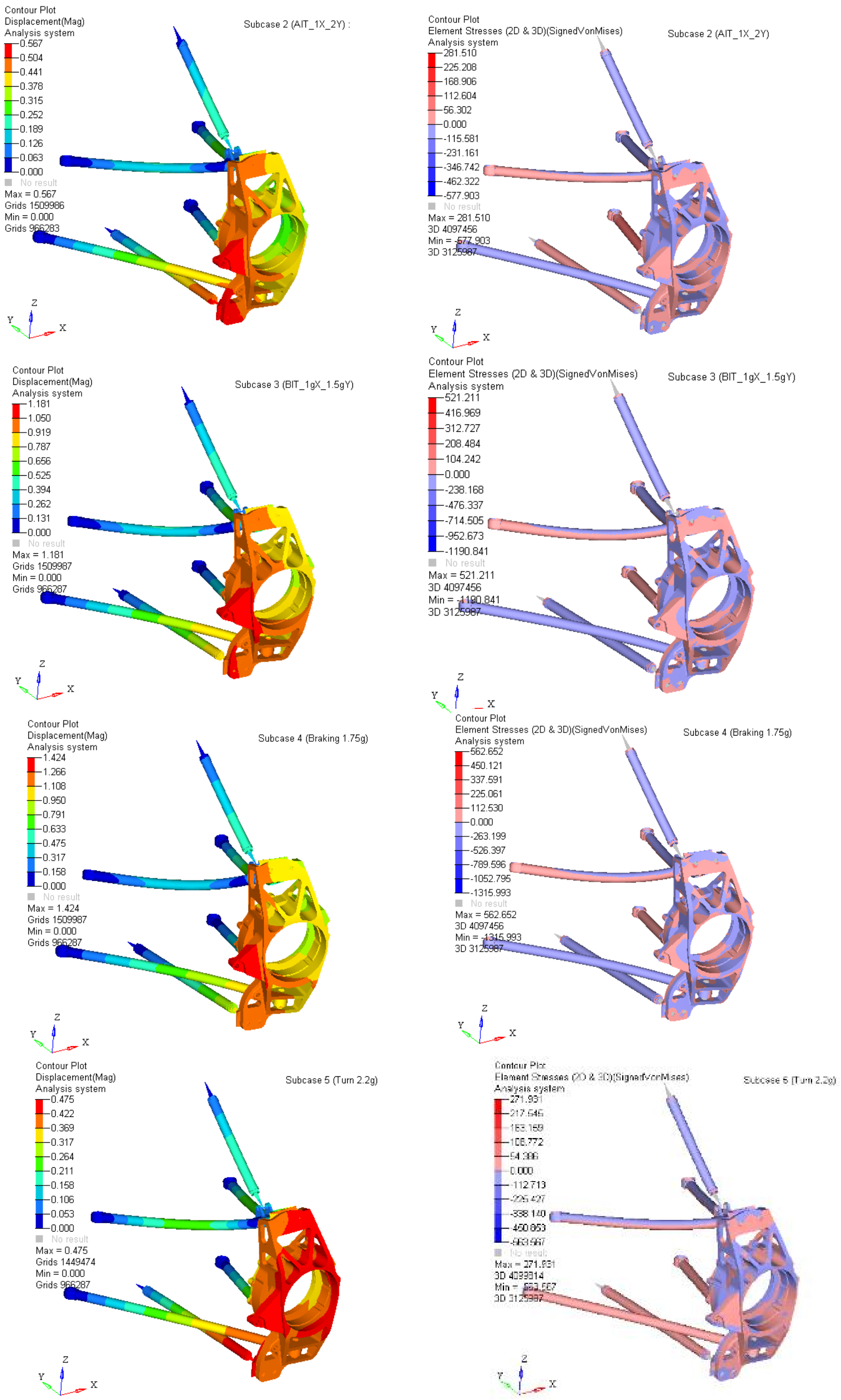

Figure 107: Displacement (in mm, left) and signed von-Mises stress [in MPa, right] results of the front suspension analyses

As can be seen, much higher stresses that the ones obtained with the single component analyses were found. However, these were concentrated in very few mesh elements, close to the attachments of the upper control arm bracket. They were caused by the increased stiffness of the RBE2 elements. Filtering the results showed that the peaks occurred on the sharp edges of the holes that were connected through RBE2 elements as can be seen in Figure 108. Thus, the results were considered safe.

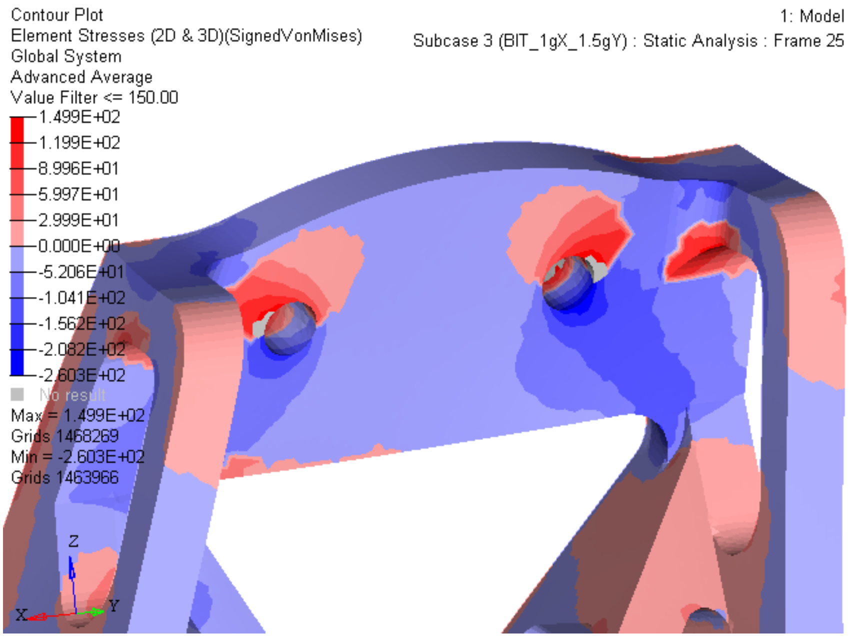

Figure 108: Highest Von-Mises stress values on the front upright [MPa].

The resulting variations in the suspension angles are listed in Table 36:

Table 36: Front suspension angle variations.

	AIT 1g X 2g Y	**BIT 1g X 1.5g Y**	**Turn 2.2g Y**	**Braking 1.75 g**
ΔCamber [deg]	0.0318	-0.0056	0.0264	0.0071
ΔToe [deg]	0.0696	0.1200	0.0383	0.0971
ΔCaster [deg]	-0.0732	-0.0949	0.0029	-0.1181

Overall, the design of the uprights was considered satisfactory, reaching the design targets listed in section 1.2.1. The Toe angle variation during a hard-braking maneuver with a deceleration of 1.75 g was slightly above the target maximum value of 0.1 degrees. However, since the analyses were based on conservative assumptions about the loads applied, this result was accepted.

2.2.2.3 Manufacturing specification

To comply with the requirements from section 1.2.1, detailed geometrical and dimensional tolerances were specified for the functional features of the uprights.

The locating grooves on the upright, shown in Figure 86, must facilitate the correct installation of the ring gear allowing it to slide in position without effort. At the same time, the interface between the outer face of the ring and the grooves must guarantee the contact between them in all loading conditions. Thus, tight tolerances are required to manufacture these features and care must be taken during the design process to verify that the deformations in the upright do not compromise the transmission mechanism. Figure 109 shows an extract from the manufacturing drawing of the rear upright. The specified tolerances for the ring gear grooves can be seen.

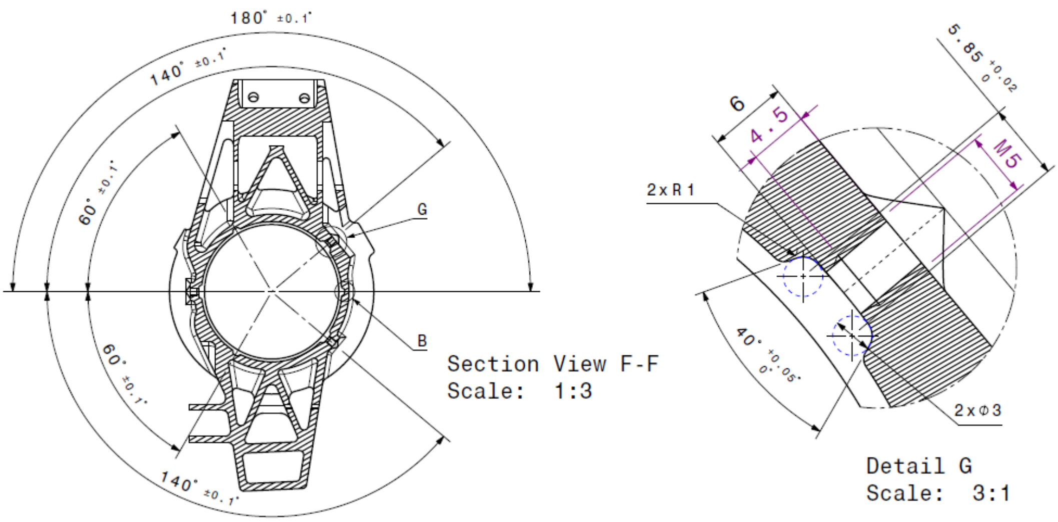

Figure 109: Extract from the manufacturing drawing of the rear upright. Tolerances for the ring gear locating grooves. The dimensions are in millimeters and the image is not to scale.

The blue circles on the detail view represent calibrated pins used to verify the radii of the grooves. This solution was adopted because the grooves were located in a zone with difficult access, on the internal faces of the upright.

Additionally, adequate geometrical tolerances must be specified to achieve excellent concentricity and parallelism between the bearings and the installation surfaces of the transmission and the electric motor. Figure 110 shows another extract from the manufacturing drawings in which the tolerances were specified.

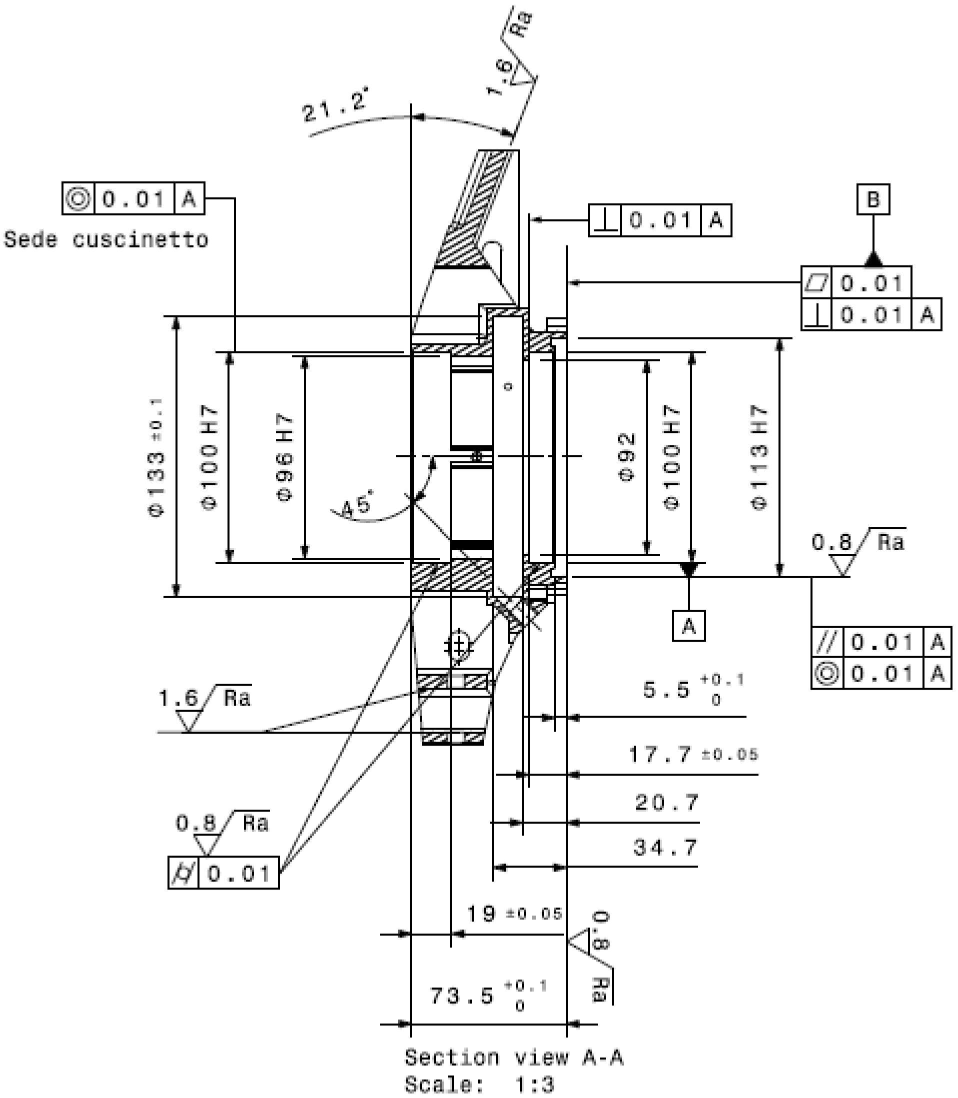

Figure 110: Geometrical and dimensional tolerances for the internal features of the uprights (the rear one is shown). The dimensions are in millimeters and this figure is not to scale.

CHAPTER 3. MANUFACTURING AND ASSEMBLY

This chapter contains a brief overview of the manufacturing and assembly processes of the SC18 unsprung components. The fabrication of most of the machined parts requiring complex operations was done by the Team's technical partner, Officine Meccaniche Massola Giuseppe [66]. For this reason, only the fabrication of the components made in collaboration with FCA Prototypes is discussed, as they required several prototyping steps that are worth documenting.

3.1 Brake discs and mounting bells

In Table 26 and Table 27, the specified materials for the brake rotors and the disc carriers were listed. For the mounting bells, a 3 mm thick 7075-T6 aluminum sheet was sourced to fabricate them. For the brake discs, instead, only a 3 mm AISI 420B steel sheet was available, in annealed conditions. Thus, the material properties were similar to the worst-case material used for the simulations, listed in Table 20. Since the simulations also considered worst-case loads, this material was used for fabricating the rotors.

Thanks to the partnership with FCA Prototypes, the brake rotors and bells were fabricated using their equipment with support from the specialized personnel. Given the tight tolerances in the contact surfaces of the brake discs and carriers, these features were produced using an Electronic Discharge Wire Cutting Machine (W-EDM). The process of cutting complicated shapes with such type of equipment is very time consuming. One estimate showed that the time required for producing all the holes of the front brake rotors with such technique would require approximately 3 days of operation. Thus, it was unfeasible to fabricate all the features in the discs and the mounting bells using that equipment.

Since a laser cutting machine was also available, a hybrid fabrication process was implemented, using the W-EDM to create the surfaces requiring tight tolerances, and the laser-cutting machine to complete the parts. The advantage of the laser-cutting machine was that it could cut complex geometrical features quickly. The W-EDM, instead, could be used to cut simultaneously several stacked parts with tighter tolerances.

To make use of the capabilities of both fabrication methods, the blank metal sheets for the rotors and bells were cut in smaller pieces and stacked together, held in place by screws and nuts. Small through-holes for inserting the cutting wire of the W-EDM were drilled in stacked plates, as shown on the left side of Figure 111. This allowed cutting central contour and three positioning holes, that would be used as reference for the laser-cutting machine in the next fabrication step. This can be seen in Figure 111 on the right.

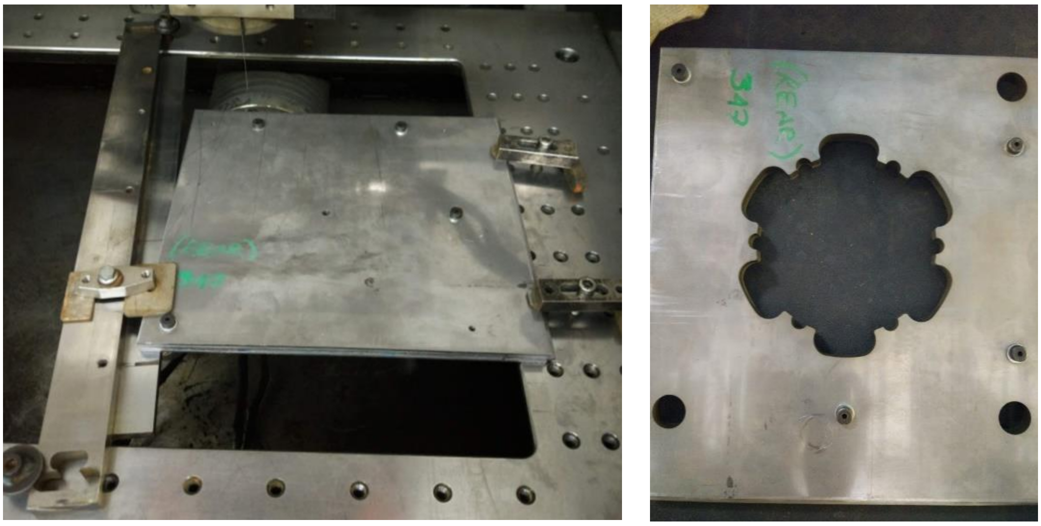

Figure 111: First two steps of the manufacturing of the brake discs.

Then, using the positioning holes to place the parts in the laser-cutting machine, the outer contour and the anti-fading holes of the rotors were cut, placing one sheet at the time on the machine's work plane. The first prototype of the rear brake discs can be seen in Figure 112.

Figure 112: First prototype of the rear brake discs.

One of the anti-fading holes was not completed by the laser cutting process because it required a more accurate setting of the working parameters. The machine was normally used to cut thinner steel panels from body components, and the 3 mm AISI 420B steel plates represented a technical challenge. Thus, several iterations were necessary to achieve the desired results for the brake discs. After each prototyping batch, the results were verified by the metrology laboratory of FCA Prototypes. They used a coordinate-measuring machine (CMM) to verify the dimensions of the features and the concentricity between the rotor attachment points and the external contour (Figure 113)

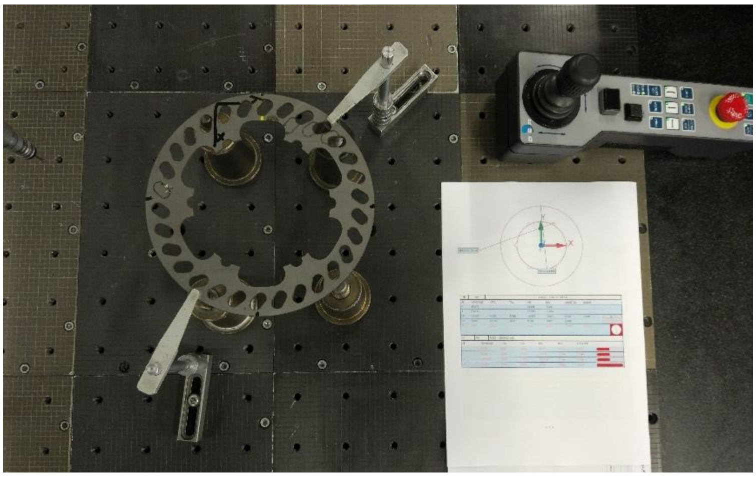

Figure 113: Measurement of one of the prototypes of the rear brake rotors.

The measurements showed that this process did not produce acceptable results in terms of geometric and dimensional accuracy. The outer contour of the rotors was not concentric with the central pattern made with the W-EDM; the offset between their geometrical centers was as large as 1.02 mm in the case of the front rotor and 0.70 mm for the rear one. Additionally, the diameter of the semi-circumferential mating surfaces in the central pattern of the discs were not within the required tolerances. The W-EDM produced features smaller than specified, with a deviation between -0.02 and -0.05 mm.

For these reasons the fabrication steps were modified to achieve an acceptable concentricity between the features produced with the W-EDM and the laser cutting machine. The new method consisted in using the laser-cutting machine first to produce the anti-fading holes, four positioning holes to align the parts stack for the W-EDM, and a center hole, smaller than the central pattern of the discs, that would be used as reference by the W-EDM. A stack of laser-cut plates with the hole pattern of the rear rotors, ready for the W-EDM process is shown in Figure 114.

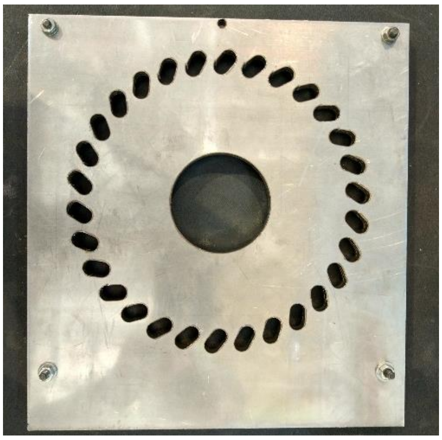

Figure 114: Stack of AISI 420B pre-cut plates with the hole pattern of the rear brake rotor. The center hole was used as centering reference for the W-EDM process.

To obtain the desired dimensional tolerances, the CAD models used to generate the G-code for the W-EDM were modified to compensate for the deviation of the machine. Once the desired tolerances were achieved, the final brake rotors were grinded to obtain an adequate surface finish.

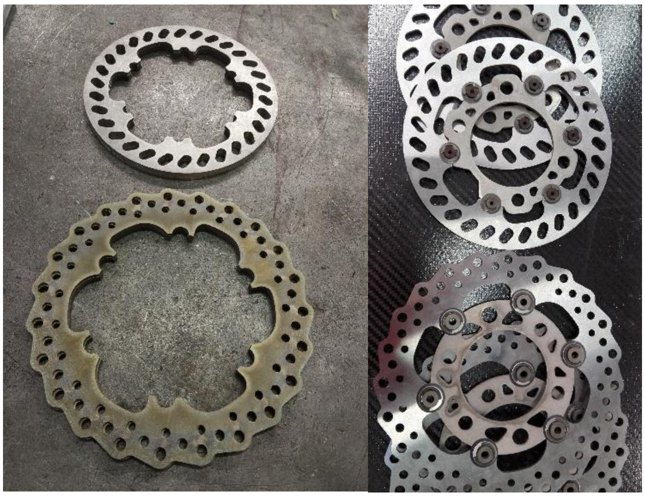

Figure 115: Brake rotors before and after grinding (left and right, respectively).

In the case of the brake disc carriers, all the fabrication was done using the W-EDM machine. However, several iterations were required as well, to obtain the desired dimensions of the contact surfaces with the floating buttons and the wheel center pins.

3.2 Suspension arms and tie rods

The production method used for manufacturing the steel control arms was based on the one presented by Carboneri in 2018 [19]. Thus, for brevity, it will not be described in detail. The steel tubes were turned to the required thickness and then cut to length and notched using a milling machine. The spherical joint housings were turned as well. Then, the A-arms were then TIG-welded using a set of custom aluminum fixtures as shown in Figure 116. Further details about this process can be found in the MSc thesis work by Carboneri.

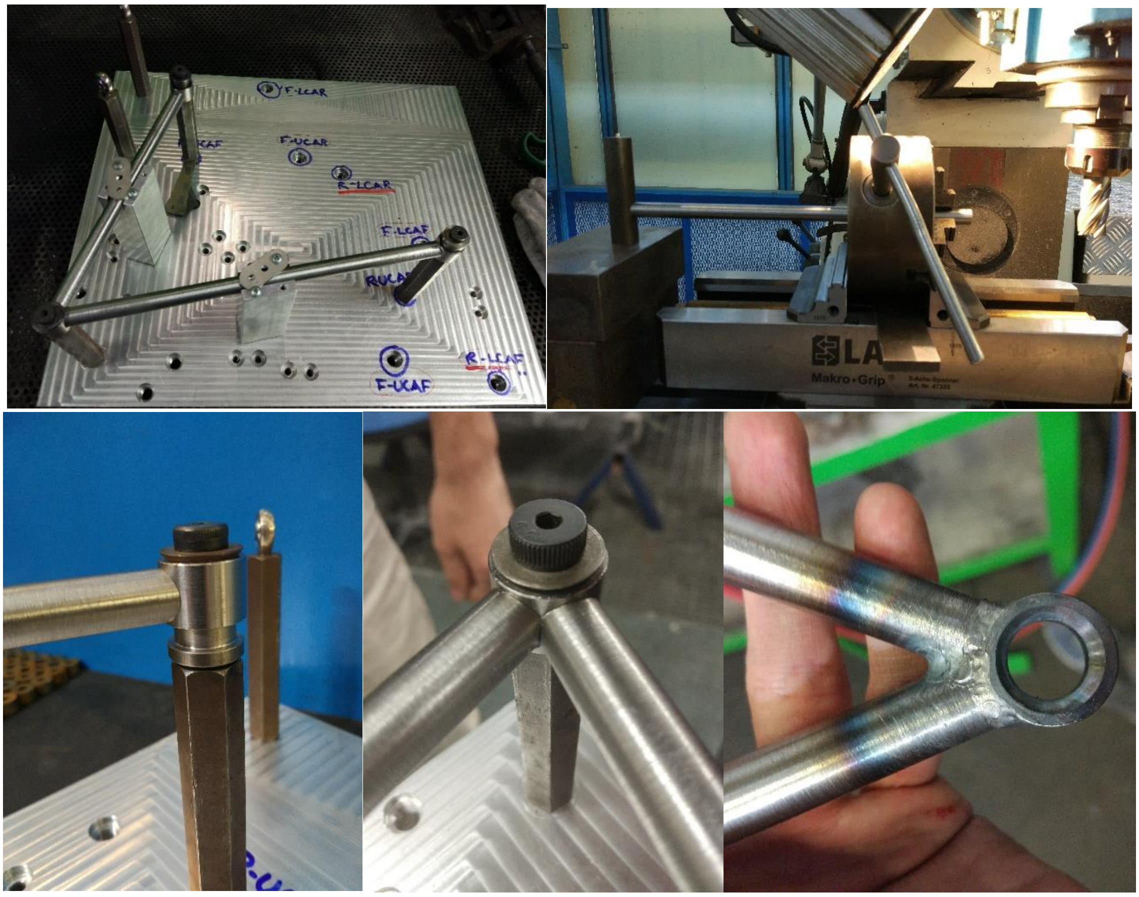

Figure 116: Fabrication of the steel control arms.

Once the welding operations were completed, the spherical joints were press-fitted in place and covered with masking tape to paint the steel tubes to prevent any type of rust formation.

Once the monocoque was painted, the A-arms were installed, along with the suspension mechanism (shock absorbers, bell cranks, anti-roll bars). Some of the A-arms were difficult to fit in place. This was because of the tolerance stack-up of the production processes for the a-arms and the monocoque itself. After the welding process, the A-arms were slightly deformed due to the thermal gradients. Additionally, the fixing holes on the monocoque were not located precisely according to the CAD geometry, even though they were produced using a CNC machine. Hence, the rear A-arms were difficult to install on the car, but fortunately, the suspension geometry was not significantly changed, which would have required producing a new set of A-arms to compensate for the deviation.

All the attachment point to the monocoque consisted of an aluminum bracket bolted to the composite panel and supported by a backing plate on the inside of the cockpit, as shown in Figure 117. The 6 mm screws used to fix them were tightened to a torque of 10 Nm and secured using all-metal lock nuts as required by the competition rules [1]. The position of the screws was marked to identify any kind of rotation later on.

Figure 117 A-arms fixing points on the monocoque.

3.3 Uprights

Being complex parts, the uprights were manufactured by PoliTo Racing's technical partner, Officine Meccaniche Massola Giuseppe [66]. They used a 5-axis CNC milling machine to fabricate the four uprights. A picture of the left front and rear uprights is shown in Figure 118.

Figure 118: Freshly machined left front and rear uprights of the SC18 car.

The finished parts were verified using precise CMMs. The internal surfaces of the uprights, destined to accommodate the transmission bearings and ring gears, were checked against the CAD geometry and the actual shape of the fabricated gears. Based on the measurements, each transmission set was assembled with the best-matching upright in terms of geometrical and dimensional tolerances [12], as seen in Figure 119.

Figure 119: Assembly of the planetary transmissions. This was done by the Powertrain division of the PoliTo Racing team.

The final step of the fabrication of the uprights involved adding a transparent anodizing coat to the external surfaces for aesthetic purposes.

3.4 Integration on SC18

The assembly process of SC18's suspension system and unsprung masses was simpler with respect to the assembly process of SC17. The main reason was the thorough documentation of all the components of the car and the availability of the complete CAD models and vehicle mock-up done during the design phase. Considering the installation space and tolerances of all fasteners of the suspension attachments when designing the SC18 demonstrated to give meaningful advantages in terms of organization and assembly time. Additionally, including all fasteners in a complete CAD model allowed finding critical areas before the start of the production process.

CHAPTER 4. TESTING AND VALIDATION

In this chapter, the tests performed with the SC18 unsprung components are summarized with a special focus om the outboard brakes (calipers and discs). The data collected is used to assess the validity of the analytical models used for estimating the working temperature of the SC18 brakes. Short analyses and discussions about the problems found during testing are also included.

4.1 Track tests on the SC17 car

On 15, 16 and 17 May of 2018, a series of track test sessions were performed using the SC17. We will refer to those as test sessions 1, 2 and 3, respectively. Their main goal was to evaluate the control strategies developed by the Vehicle Dynamics division and collect data for choosing the definitive tire compound to be used for SC18. They also served as training for the new drivers of PoliTo Racing. Sessions 1 and 2 also allowed assessing the performance of the new brake calipers and obtaining data about the working temperature of the rotors.

4.1.1 Tested components and instruments used

Table 37 summarizes the components installed in the braking system of SC17 during the test sessions. The brake calipers of SC17 were replaced by the ones to be used in SC18. This allowed having a good approximation of the response of SC18 since the size of the master cylinders and the brake discs effective radius were the same. To install the P4 24 calipers in the SC17 front uprights, a set of custom adapters was made. These are shown in Figure 120. The P2 24 calipers, instead, had the same mounting geometry of the P4 24 ones used in the rear axle of the SC17. Thus, the substitution did not require any type of adapter.

Table 37: Brake system components installed on SC17 during test sessions 1 and 2.

Component	**Model** [36]	**Technical Specs.**	**Comments**
Front calipers.	Brembo P4-24	4 pistons, Ø 24 mm each	Rear calipers used in SC17.
Rear calipers	Brembo P2-24	2 pistons, Ø 24 mm each	Calipers used in a previous formula car (2012)
Front brake pads	Brembo 07934040	H38 sintered compound. 30 x 49.75 x 7.5 mm	-
Rear brake pads	Brembo 07934080	H38 sintered compound. 24 x 35.75 x 7.6 mm	-

Table 37: Brake system components installed on SC17 during the test sessions 1 and 2 (continued)

Front Master Cylinder	Brembo A6.S2.13	Piston Ø19 mm	Used in SC17
Rear Master Cylinder	Brembo A6.S2.11	Piston Ø16 mm	Used in SC17
Front brake rotors	Brembo 8670186	Ø 218 mm, 4 mm thick. Stainless steel	Used in SC17
Rear brake rotors	Brembo 8670190	Ø 190 mm, 4 mm thick. Stainless steel	Used in SC17

Figure 120: P4 24 calipers mounted on the SC17 front uprights.

The instruments used for recording the temperatures and measuring the hydraulic pressure on the brake circuit are listed in Table 38. The thermal adhesives were attached to the brake calipers as shown in Figure 120 to register the maximum temperature reached during operation. The temperature of the brake rotors, instead, was recorded using a thermal camera and contact thermocouple at the end of each test. Only the pressure on the front brake circuit was measured using the pressure transducer.

The deceleration of the car was recorded by the accelerometer installed in the SC17's electronic control system, and the encoders built into the IWMs provided the data to determine the wheel speeds.

Table 38: Instruments used during the test sessions 1 and 2.

Instrument	Model	Measuring range	Accuracy
Thermal camera	RS Pro TG-301 Thermal Camera 918-1085 [68]	-30 to 650°C	±1.5%
Thermal adhesives	Brembo 02.5168.20 [36]	88 to 127°C 132 to 210°C	-
Contact thermocouple	-	Up to 800°C	-
Accelerometer	Bosch Sensortec BNO055 [29]	±4g	±4%
Pressure Transducer	Honeywell PX3AG1BH046BAAAX [55]	Up to 46 bar	±0.25 %FSS[10]

4.1.2 Location of the tests

The tests were performed in a karting track, at Cerrina, near the city of Turin, Italy [69]. An aerial photography of the circuit is shown in Figure 121.

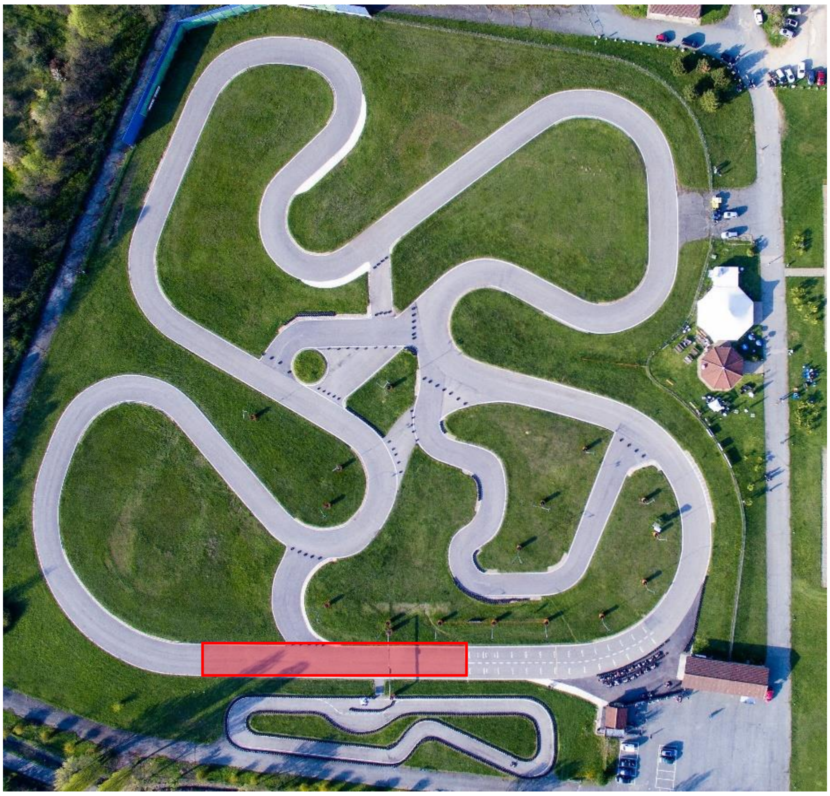

Figure 121: Cerrina Race track. Source: Google Maps.

[10] Full Scale Span [85]

4.1.3 Data collection procedure and tests performed

To register the temperatures of the brake rotors and calipers, the drivers were requested to stop the car in the red area highlighted in Figure 121 after each one of the test runs performed to validate the control systems. On some occasions, acceleration stints followed by hard braking maneuvers were done to evaluate the response of the braking system. The temperatures were measured by two people using the instruments listed in Table 38 and written in test sheets. The CAN sensors data was stored in an SD card inserted in the Data Logger unit [26]. The weather conditions were considered good for the test sessions, with ambient temperatures between 20 and 25°C and asphalt temperatures between 31 and 41°C at the start of the tests. The tires used were Pirelli P-Zero 130/530-13.

Table 39 summarizes the tests performed and the measured temperatures. The temperature readings from the thermal camera were affected by rapid and continuous oscillations when pointed directly at the brake discs. Since there was no way to store those values to perform a proper statistical analysis, the considered values are the ones more frequently seen on the device's screen during a 5 seconds period for each disc. Thermal images of the discs were also captured and stored in the camera's SD card, but because of the variability in the readings, many of them do not match the reported temperatures. Images captured after the runs 8 and 9 of test session 2 are shown in Figure 122. As indicated in the top right corner of each image, the emissivity value configured for measuring the temperatures of the discs was 0.75, as recommended by different sources [68] [70] for measuring worn stainless steel surfaces with infrared instruments producing a wavelength of 8-14 μm.

The discs temperatures reported in Table 39 correspond to the average between the readings from the TG-301 thermal camera and the contact thermocouple when the difference between them was within 20% of the maximum value. When the difference between the temperature readings was greater than that, the highest value was annotated. This was done to reduce the effect of cooling during the time between the stopping of the car and the measuring of the temperatures (between 5 and 30 seconds).

In the case of the calipers, the maximum temperatures indicated by the thermal adhesives were registered when they were available as indications of the maximum temperature reached. Due to the limited availability of thermal adhesives during these test sessions, some test runs were done keeping the thermal adhesives used in previous stints. In those cases, the temperature marked by the adhesives was reported only when it was increased from the value indicated at the start of the run. Otherwise, the caliper temperatures were reported as in the case of the brake discs. Pictures of the thermal adhesives after some tests during test session 2 are shown in Figure 123.

Table 39: Summary of the tests performed with the SC17 car.

Test Session	**Run**	**Test type**	**Balance bar front bias [%]**	**Mean. Decel. [g]**	**Max. Avg. Decel. [g]**	**Max. Peak Decel. [g]**	**Caliper Temp. [°C] FL/FR/RL/RR**	**Disc Temp. [°C] FR/FL/RR/RL**	**Weighted avg. speed at start of braking [km/h]**	**Comments**
1	1	AutoX 1	50	0.25	0.64	1.2	140/140/ 100/100	-	52.9	Rear wheels locked 34% of the time
1	2	AutoX 1	60	-	-	-	160/160/ 100/100	250/255/ 144/109	-	Corrupted telemetry data log. Positive driver feedback.
2	1	AutoX 2	60	0.3	0.74	1.5	>210/>210/ >127/>127	411/250/ 270/230	58.2	7 laps + hard brake. Rear wheels locked 6% of the time
2	2	Accel. + Hard Brake	60	-	0.91	1.5	76/75/ 40/43	113/105/-/-	93	Stopping distance 30 m.
2	-	Accel.	70	-	-	-	30/26/32/29	60/50/50/49	-	Launch control SC17. Hard braking not performed
2	-	Accel. + Hard Brake	70	-	1.1	1.8	36/28/30/32	62/58/60/59	119	Launch control SC18. Positive driver feedback.
2	6	AutoX 2 (inverted)	60	-	-	-	76/-/-/-	142/165/ 118/128	-	CAN communication error.
2	8	AutoX 2	60	0.29	0.91	1.5	-	154/187/ 142/160	50	Rear wheels locked 10% of the time
2	9	AutoX 2	60	-	-	-	177/199/-/-	300/309/160/177	-	5 laps. Telemetry data log not available

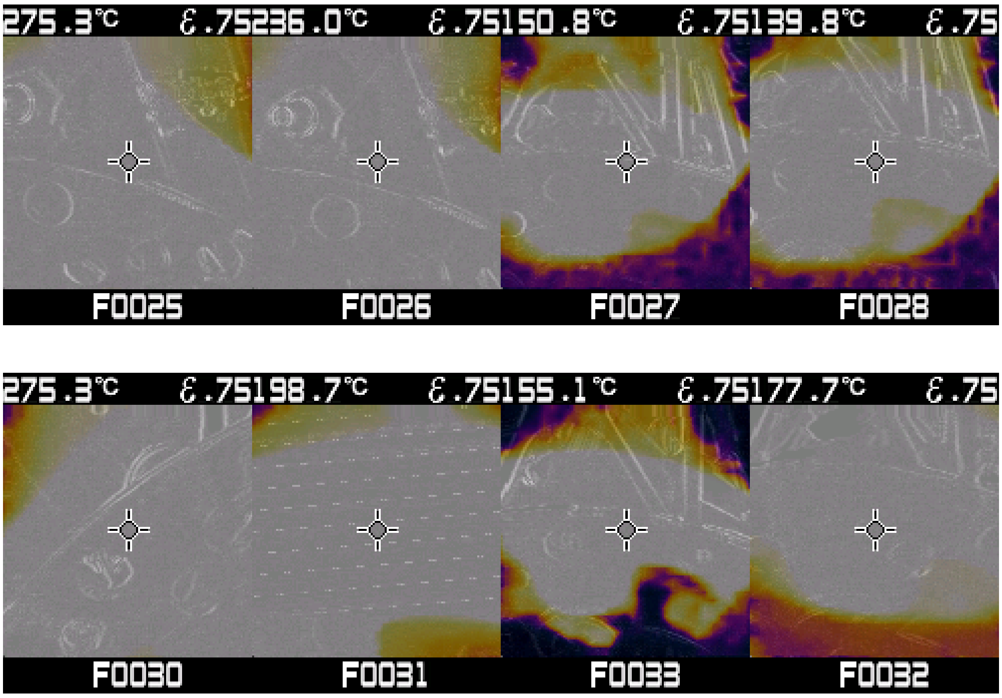

Figure 122: Thermal images of the brake rotors after the test runs 8 (top) and 9 (bottom) of test session 2. From left to right: Front left, front right, rear left and rear right rotors.

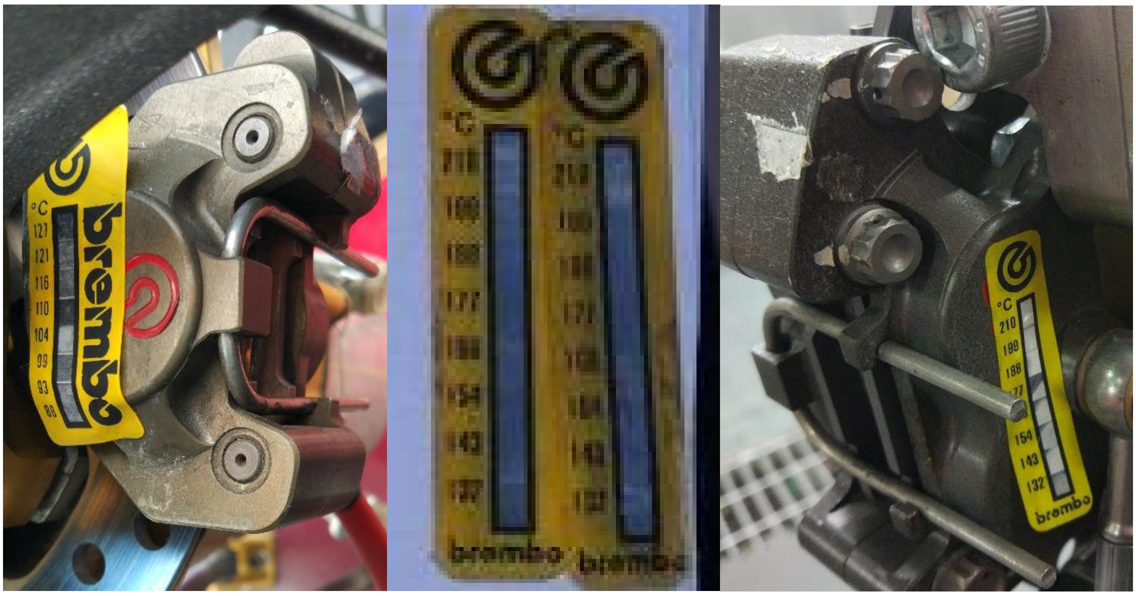

Figure 123: Caliper temperatures indicated by thermal adhesives during test session 2. From left to right: rear right caliper (run 1), front calipers (run 1), front left caliper (run 9).

4.1.4 Analysis of collected data

4.1.4.1 Brake load balance

Test sessions 1 and 2 allowed to assess experimentally the benefits of the balance bar for obtaining an adequate brake force distribution. Incrementing the front brake bias from a 50% baseline reduced the tendency of the rear wheels to lock and increased the working temperature of the front calipers, as expected. Taking as an example the hardest braking maneuver during run 1 of test session 1, shown in Figure 124, we can see that the rear right wheel locks when the rear circuit pressure was 16.5 bar. This represents a rear axle braking force of 482 N. Although this force value is lower than the one indicated by the system response curves shown in Figure 41 for a deceleration between 0.5 and 0.75g, the rear right wheel locked earlier than the rest. One of the main reasons for this is the uneven tire load distribution while the car was braked. As shown in Figure 124, the car was taking a right-hand curve while braking. However, similar situations exhibiting rear axle lock occurred for 34% of the braking maneuvers performed with a 50% front bias configuration, demonstrating that this configuration produces a negative impact on the brake force distribution.

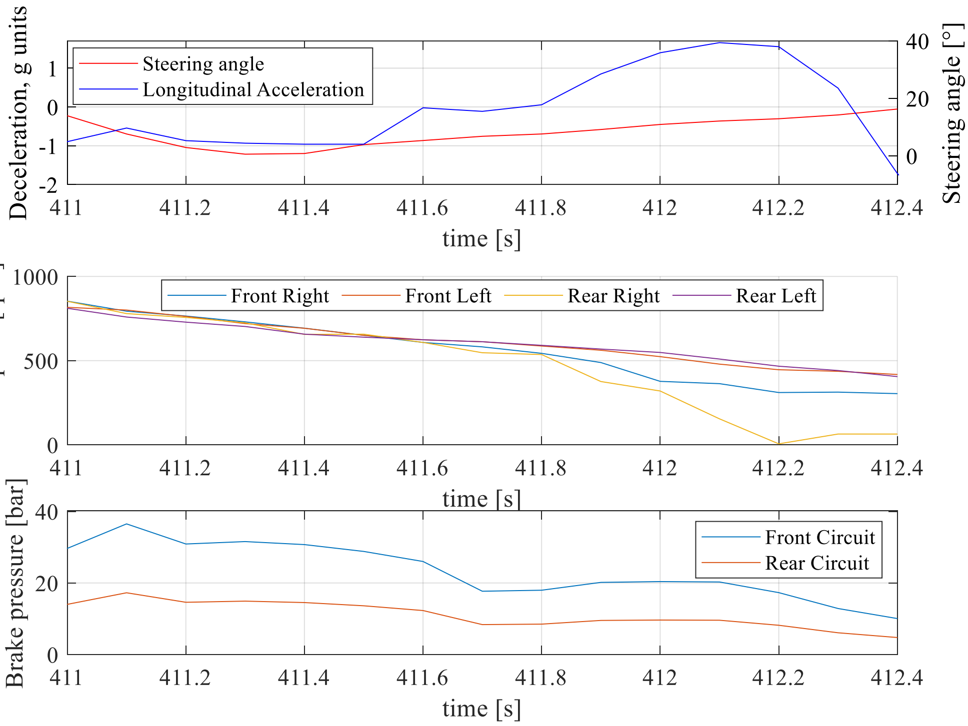

Figure 124: Data corresponding to the hardest braking maneuver during run 1 of test session 1.

The hard-braking maneuvers performed during test session 2 while testing the SC17 and SC18 launch control algorithms showed the potential increase in straight-line braking with a 70% front bias distribution based on the achieved decelerations. However, in those cases, excessive front axle lock was seen from the telemetry data. The general feedback from the drivers favored a front bias around 60% during the autocross simulations. With that configuration, early rear wheel locking occurred between 6 and 10%, which represents an improvement compared to the 25% seen on some competition events during 2017. Thus, that set up was kept as the baseline for SC18.

4.1.4.2 Deceleration capability

The hard-braking maneuvers were used to assess the straight-line deceleration capability of the car. Figure 125 shows a comparison between run2 and the SC18 launch control test run during test session 2. In these two runs, the front brake bias was adjusted to 60% and 70%, respectively. In the first case, the maximum peak deceleration reached was 1.5g with an average of only 0.91 g, despite that the maximum pressure in the front brake lines surpassed 46 bar (the maximum readable value by the pressure transducer listed in Table 38). This was considered sub-optimal for the targets for the SC18 car (Table 8).

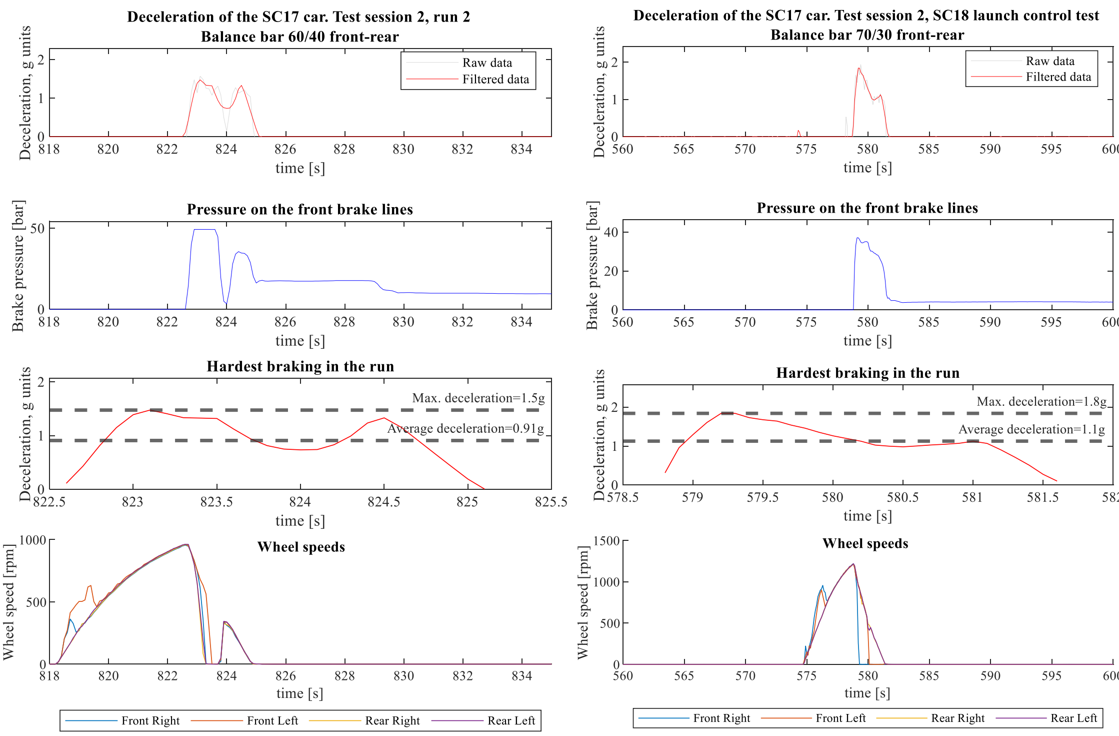

Figure 125: Comparison between the hard-brake tests performed in test session 2.

One of the reasons could have been the need for more thorough bleeding of the brake circuits before the tests. The presence of air bubbles in the circuit limits the hydraulic pressure rise when the master cylinders are compressed. This could have required the drivers to exert an excessive force to achieve the desired deceleration. As a consequence, they were not capable of maintaining a constant circuit pressure, as evidenced by the pressure drop while braking shown on the left plots of Figure 125. It should be noted also that the new drivers were not familiar with the force required to operate the SC17 brakes when performing the first tests.

During the hard-braking maneuvers performed while testing the SC18 launch control algorithm, the maximum decelerations were higher. Despite that, the car showed a less balanced brake force distribution.

4.1.4.3 Brake discs temperatures

The tests performed with the SC17 car were useful to gather reference data about the working temperature of the brake discs. The test runs simulating autocross laps represent worst-case use scenarios since the regenerative braking was not enabled. Moreover, the autocross event during the Formula SAE Electric competitions consists of a single lap, while, during the test runs, several laps were done consecutively.

Simplified continuous braking model

The temperatures calculated using the continuous braking model used in section 2.1.4.4 were compared to the measured values. The autocross test runs were simulated as a continuous sequence of identical braking maneuvers. The average speeds at the start and the end of the braking maneuvers, and the mean time interval between consecutive applications of the brakes were determined from the telemetry data logs and used as input for the model.

Figure 126 shows the results for test runs 1 and 8 of test session 2.

As can be seen, the continuous braking model can either over or under-estimate the temperature of the discs. In the first case, the predicted temperatures match the lower measured values for the front discs and are close for the rear ones. However, the maximum readings were much higher than the predictions for both the front and rear discs. It should be noted that run 1 concluded with a hard-braking maneuver, which could have offset the temperatures with respect to the ones seen during operation. In the case of run 8 of test session 2, calculated temperatures exceed the maximum readings reported in Table 39. One factor to consider is that the temperatures were measured after the car was stopped.

Hence, the reported values are likely to be lower than the ones experienced by the rotors during the tests.

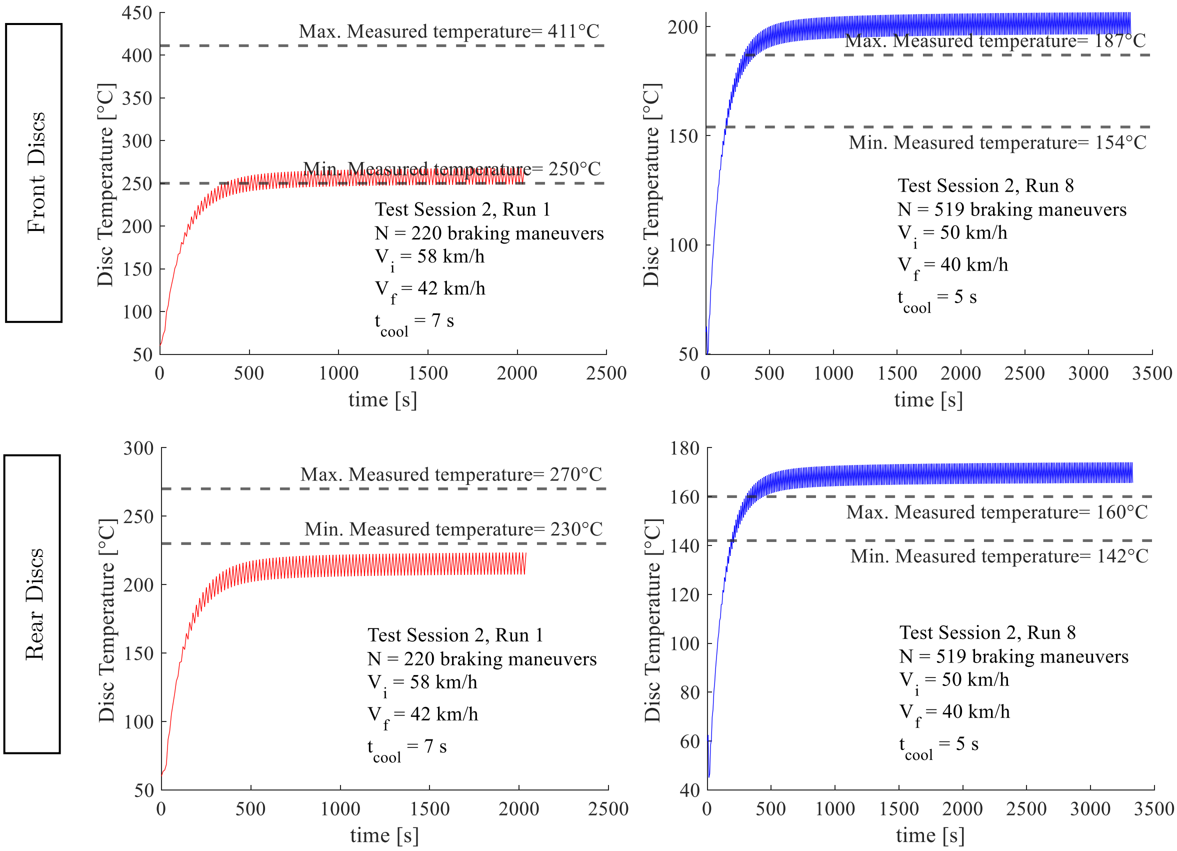

Figure 126: Brake rotors temperature predictions from the continuous braking model for runs 1 and 8 of test session 2.

Calculation of brake disc temperature from telemetry data

The telemetry data was also used to calculate the disc temperatures using the model presented in section 2.1.4.5 and compare the results with the ones reported in Table 39. Different values of the brake pad friction coefficient μ_F were used. This parameter functions as a scaling factor, determining the amount of energy converted into heat, which defines the temperature rise. Figure 127 shows the temperatures of the right-side discs calculated from the data of run 1, test session 2, using three different correlations for the heat transfer coefficient and different values of μ_F.

The heat transfer coefficients from the work of Vidiya and Singh provided temperatures much lower than the ones shown in Table 39, despite of the values of μ_F used. When using the other two correlations, assuming μ_F equal to 0.8 resulted in much higher temperatures for the front right disc than the ones reported in Table 39. Assuming μ_F equal to 0.4, the temperatures predicted using the empirical correlations are close to the value measured on the front right disc. However, it should be noted that the real working temperature is likely to be higher than the one measured on the disc at the end of the test. Hence, a value of μ_F between 0.4 and 0.6 would provide a better match.

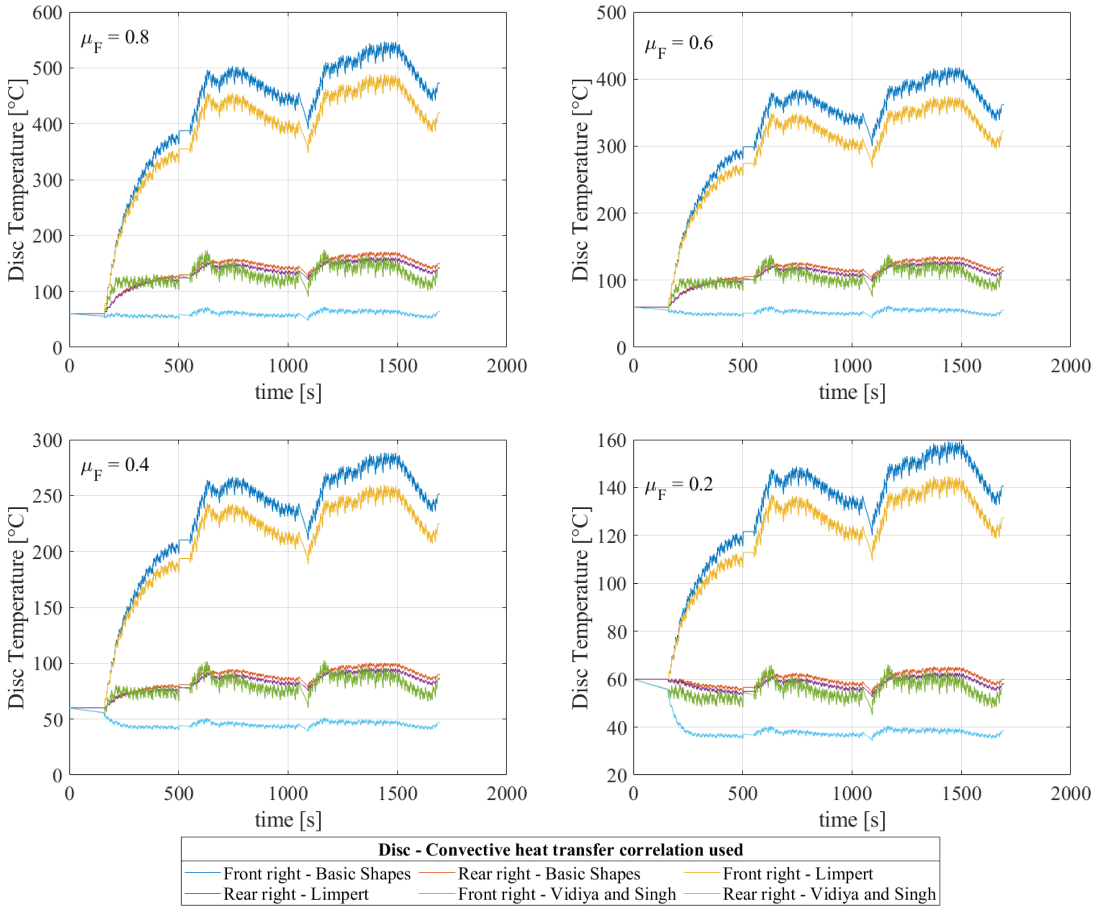

Figure 127: Disc temperatures calculated from the data obtained in run 1, test session 2.

Regarding the rear disc, all temperature predictions were lower than the values reported in Table 39, regardless of the correlations used for calculating the heat transfer coefficient or the values assumed for μ_F. A hypothesis is that the heat transfer coefficients on the rear brake discs are lower than in the front ones because of the unfavorable airflow conditions. Hence, the rear rotors reach higher temperatures than predicted even when assuming the optimal value of μ_F (0.8).

Single stop temperature rise

The data from run 2 of test session 2 was used to evaluate the accuracy of the analytical calculations of the temperature rise on the brake discs during a single stop. In addition to the information provided in Table 39, the details of the most relevant maneuver performed are indicated in Table 40.

Table 40: Details of the hard-braking maneuver performed during run 2, test session 2.

Wheel	Disc temperature [°C]	Caliper temperature [°C]	Initial car speed [m/s]	Time to stop [s]	Stopping distance [m]
Front Left	113	76	26.3	2.5	~30
Front Right	105	76			
Rear Left	40	-			
Rear Right	43	-			

Using equations (19) and (33) with the parameters listed above, the temperature response of the brake rotors was calculated. The results are shown in Figure 128.

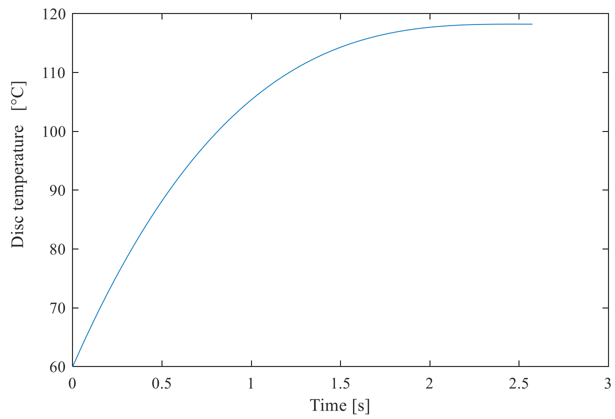

Figure 128: Calculated temperature trend of a front SC17 brake rotor during the hard-braking maneuver (run 2, test session 2).

As can be seen, the calculated temperature trend resulted in a final temperature value close to the measured ones, with a maximum relative error of 0.11%.

4.2 FSAE Italy – 11th to 16th July 2018

Before the FSAE Italy 2018 competition, the outer edge of the front and rear brake discs of the SC18 car were marked with a thermal paint (Brembo 02571120 [36]) to monitor the maximum temperatures reached during the race. Figure 129 shows a picture of the brake rotor before and after the endurance race, on the left and right side, respectively.

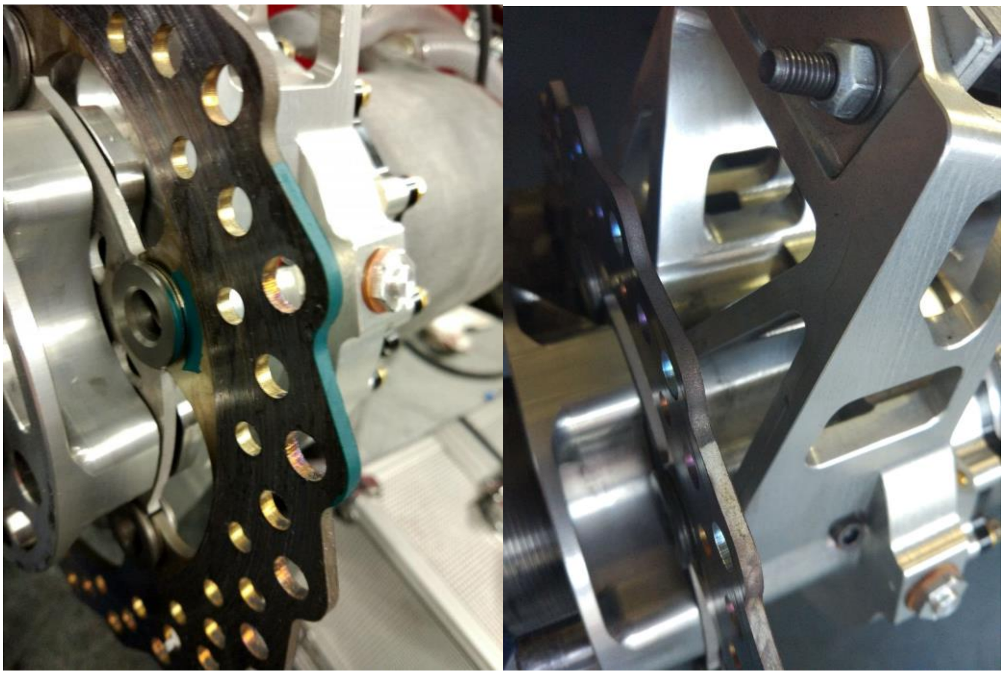

Figure 129: Front right SC18 brake disc before (left) and after (right) the FSAE Italy 2018 Endurance event.

The change in color from green to white indicates that the maximum temperature that the discs surpassed 430°C [36] during the Endurance event. This did not occur during the test sessions prior to the competition.

The brake calipers were equipped with thermal adhesive (RS components, part N° 555-437 [71]). After the Endurance event, the adhesives did not register any change. This indicates that the calipers did not reach temperatures beyond 204 °C during operation, which would be detrimental for the EPDM piston seals. Since the brake fluid used in SC18 (Brembo HTC64T [36]) had a boiling temperature of 335°C, there were no concerns about evaporation of the brake fluid.

Unfortunately, the measured temperatures could not be compared with the values predicted by the calculation models because the data log was not available after the competition.

4.3 Front brake calipers failure

After the FSAE Italy 2018 competition, the Team continued to perform practice and tuning sessions on the SC18 car. In July 27th, there was a failure in one of the front brake calipers. The inner caliper pistons were consistently sliding farther than the outer ones, causing an asymmetric clamping of the disc, as can be seen in Figure 130.

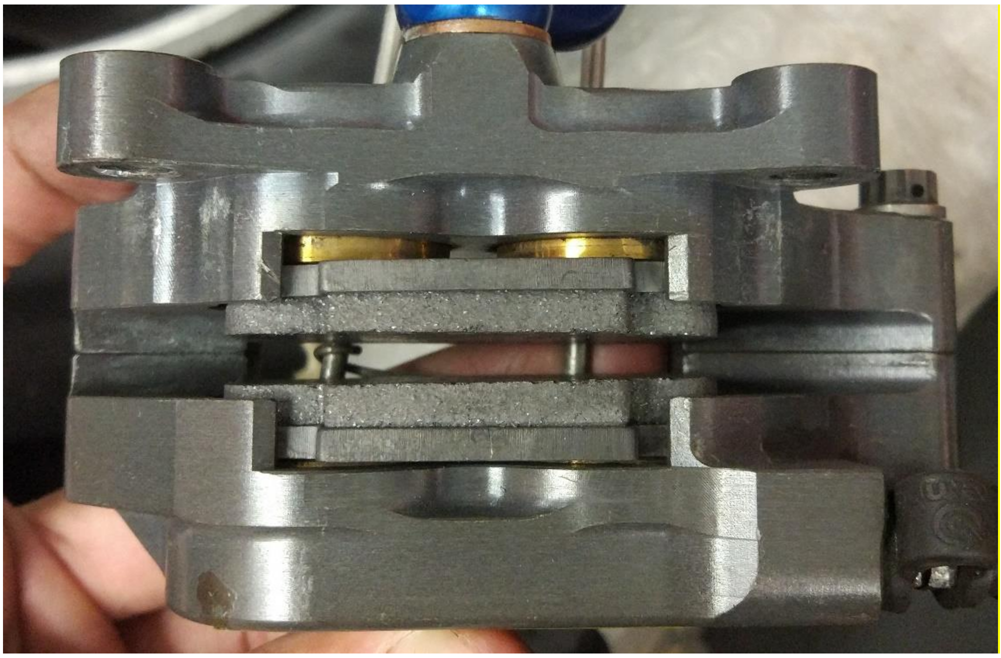

Figure 130: Asymmetric front caliper pistons closure.

This was noticed by the drivers, who felt a constant “brake dragging” effect coming from the affected wheel. Manually pushing the pads to obtain a symmetric closure did not solve the problem. Hence, the caliper was dismounted from the car to examine the pads and pistons.

As can be seen in Figure 131, the pads did not show significant wear nor signs of a prolonged non-uniform contact. This was an indicator that the problem had not been present for a long time before it was noticed. The inspection of the pads also showed a slightly vitrified rubbing surface on both pads. This could have been caused by the high disc temperatures marked by the thermal paints during the FSAE Italy competition, as indicated in section 4.2.

The caliper pistons and seals showed signs of degradation of the seal’s material, as shown in Figure 132. The pistons from the inner side had rubber marks distributed across their length. The pistons from the outer side of the caliper, instead, showed more evident rubber marks close to their outer edge, with small portions of melted rubber attached to them.

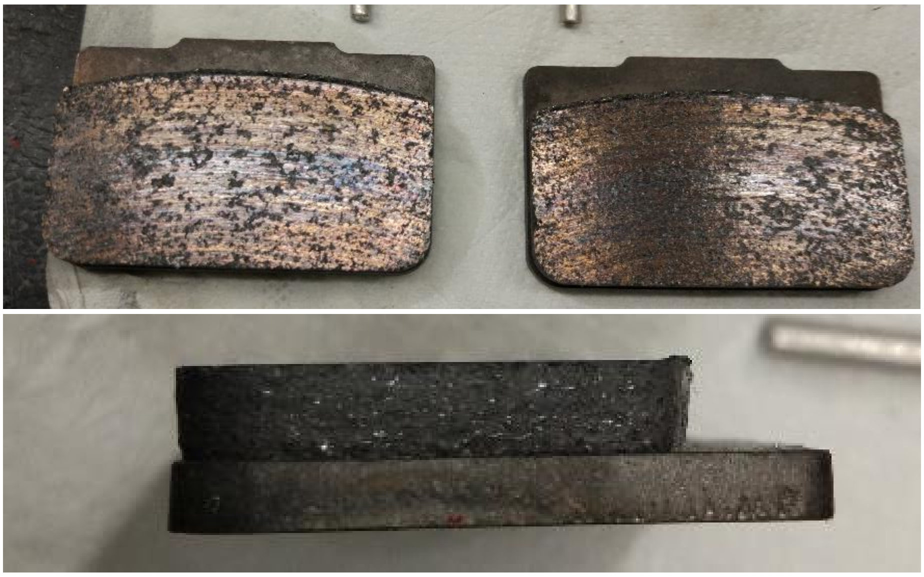

Figure 131: Front brake pads examined after the caliper failure.

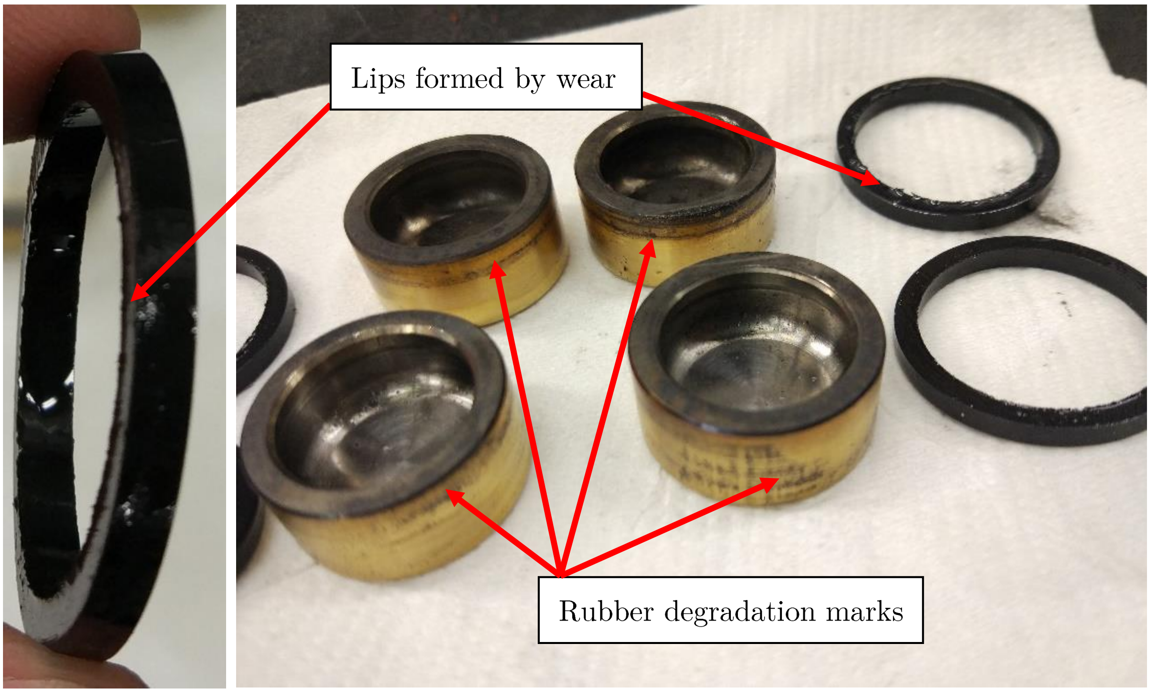

Figure 132: Front brake caliper pistons and seals showing signs of degradation of the rubber seals.

Unfortunately, a detailed log of the tests performed is not available, and the telemetry data acquisition was not working properly when the failure occurred. Hence, the causes can only be inferred. The caliper seemed to have surpassed the operating temperature range of the EPDM rubber used for the piston seals for a prolonged period, causing their degradation. The deformed rubber may have caused the outer caliper pistons to seize in their seats, producing the asymmetric clamping.

After examining the parts, the caliper was overhauled, installing new seals and cleaning the pistons before assembling. Coarse-grit sandpaper was used to eliminate the vitrified layer of the pads.

4.4 Front brake discs failure

On August 12th, 2018, the front left brake disc of the SC18 car failed due to “coning”. This phenomenon is caused when the discs are subjected to high thermal gradients that generate high thermal stresses. When the axial thermal deflection at the disc outer radius is different to that at the inner one, the disc is deformed, adopting a conical shape [33]. This results in an abnormal contact between the brake pads and the disc, generating substantial drag torque and further increasing the rotor temperature.

Figure 133 shows some pictures of the coned disc. The thermal paints on the edge of the disc indicates that it reached temperatures higher than 430°C (green paint, turned white), but below 560°C (orange paint). There is no telemetry data log available to estimate the work temperatures using the predictive models.

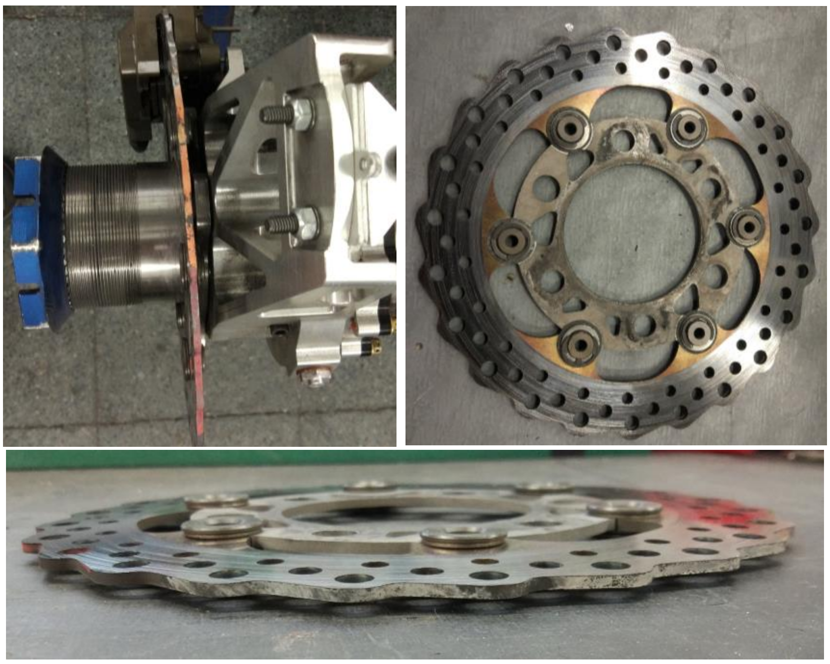

Figure 133: "Coned" front left SC18 brake disc.

4.5 Test session of August 16th, 2018

Before the Formula Student Spain 2018 event, several tests sessions were performed with the SC18 to improve the tuning of the controls systems and as practice for the drivers. The test session of August 16th, 2018 was especially relevant for measuring the temperature of the brakes after a series of Endurance and Autocross simulations.

4.5.1 Instruments used

A high precision thermal camera was used to measure the temperature after each test run. The characteristics of the camera are listed in Table 41.

Table 41: Characteristics of the high-standard thermal camera [72]

Brand	Model	Measuring range	Accuracy
Fluke	Fluke Ti110	-20 °C to +250 °C	± 2 °C or 2 % (at 25 °C nominal, whichever is greater)

The Brembo 02571120 thermal paints were also applied to the rotors to monitor the maximum temperatures reached in exercise.

4.5.2 Location of the tests

The tests were performed in a karting track, at Moncalieri, near the city of Turin, Italy [73]. An aerial photography of the circuit is shown in Figure 134.

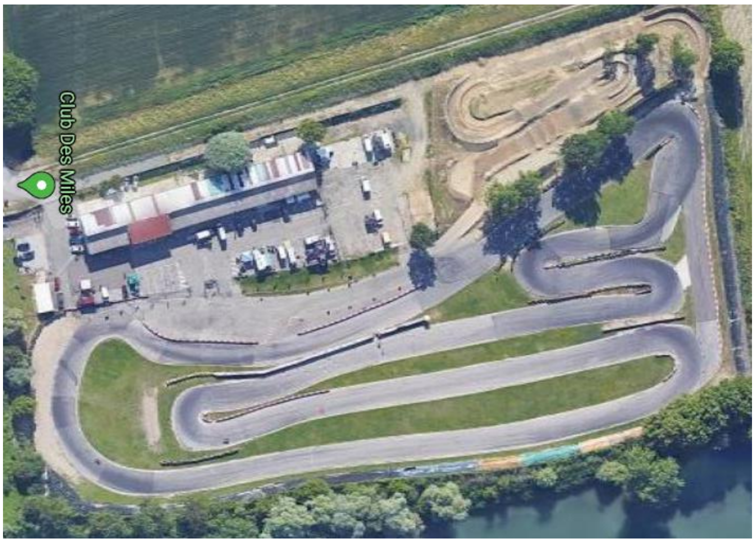

Figure 134: Karting circuit used during the test session of August 16th, 2018.

4.5.3 Tests performed and data collection procedure

Table 42 summarizes the most relevant tests performed during this test session. The procedure followed to collect the data was similar to the one discussed in section 4.1.3. However, the high-grade thermal camera provided more consistent results compared to the instruments used in previous test sessions.

Table 42: Tests performed on August 16th

Run	Test Type	Balance bar front bias [%]	Mean. Decel. [g]	Max. Avg. Decel. [g]	Max. Peak Decel. [g]	Caliper Temp. [°C] FL/FR/RL/RR	Disc Temp. [°C] FR/FL/RR/RL	Weighted avg. speed at start of braking [km/h]	Comments
1	Endurance	60	0.36	0.73	1.3	93/104/ 78/86	94/148/80 /83	72.2	Regenerative Braking
2	Endurance	60	0.2	0.51	0.93	54/57/ 51/55	37/54/43/ 44	65.2	No regenerative braking. Slow pace
1	Autocross	60	-	-	-	-/150/ -/110	-/275/ -/150	-	No regenerative braking.
2	Autocross	60	-	-	-	-/150/ -/113	-/250/ -/148	-	No regenerative braking.
3	Autocross	60	-	-	-	-/140/ -/110	-/250/ -/146	-	No regenerative braking.

4.5.4 Analysis of collected data

Some examples of the images obtained with the thermal camera can be seen in Figure 135. They show a remarkable temperature gradient (represented in Fahrenheit degrees) across the brake rotors. The maximum temperature, towards the outer edge, was higher than the maximum value readable by the instrument (275°C), while the innermost surfaces (the mating tabs for the brake buttons) show temperatures around 130°C.

This large temperature difference explains the coning failure experienced during the previous test sessions. Despite the better precision of the Fluke Ti110 thermal camera compared to the RS Pro TG-301, the limitation of the measurements being taken only when the car has been stopped remains. Because of this, the real trend of the temperatures during operation is unknown.

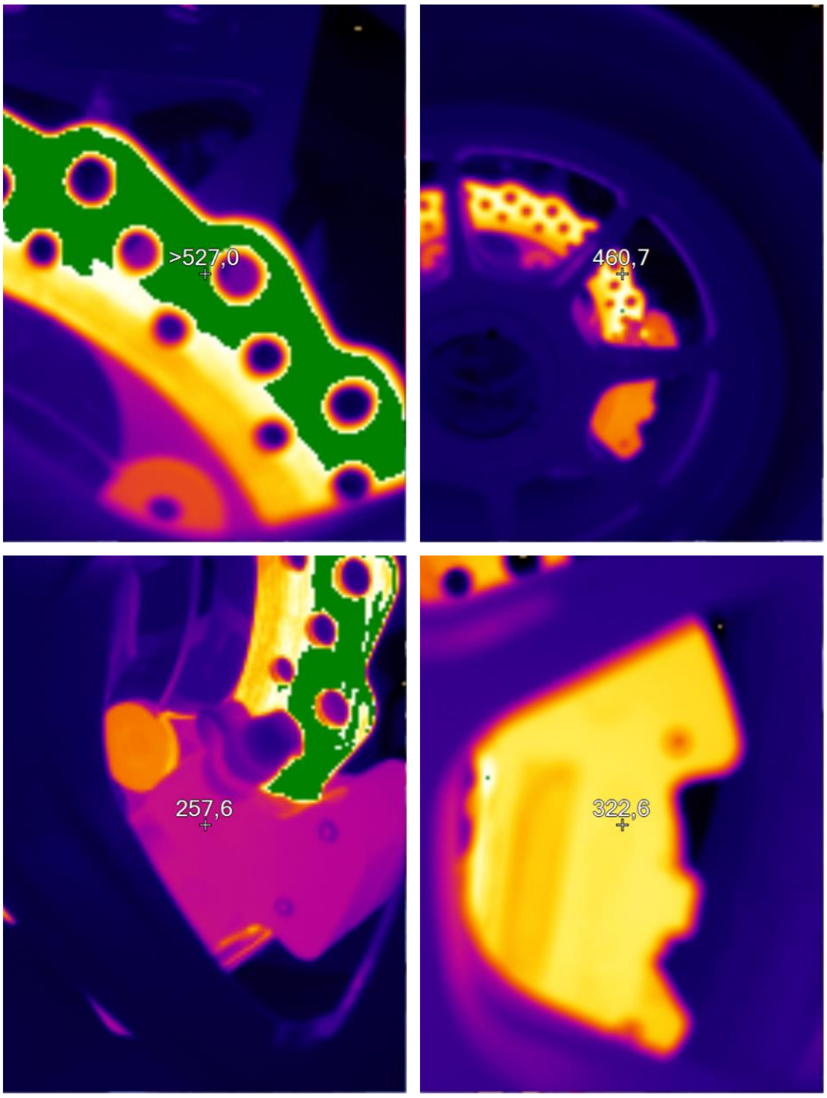

Figure 135: Images obtained with Fluke Ti110 thermal camera. Temperature readings in Fahrenheit degrees.

The thermal paint applied to the brake discs showed that the temperatures did not exceed 560°C. Conversely, the temperatures predicted using the telemetry data of the endurance runs are unrealistically higher, as shown in Figure 136.

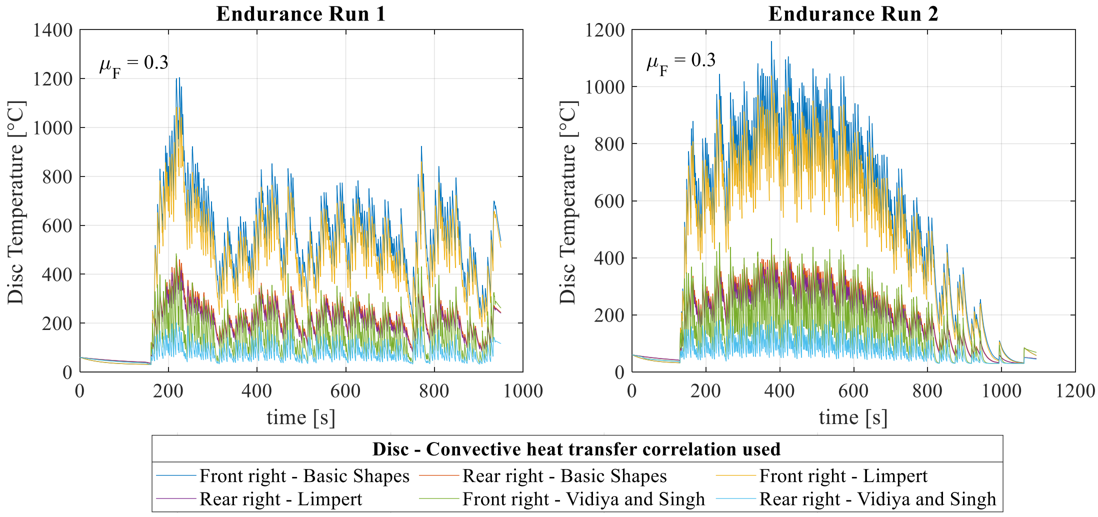

Figure 136: Temperatures predicted using the telemetry data of the endurance runs of the test session of August 16th, 2018.

As discussed in sections 2.1.4.5 and 4.1.4.3, the calculation model is quite sensitive to the assumed value of the brake pad friction coefficient. The results shown in Figure 136 indicate that a scaling factor could be used to adjust the accuracy of the predicted temperature values to match the actual operating temperatures. Figure 137 shows that using a scaling factor of 2 the predicted temperatures are within the measured range except for some peak values.

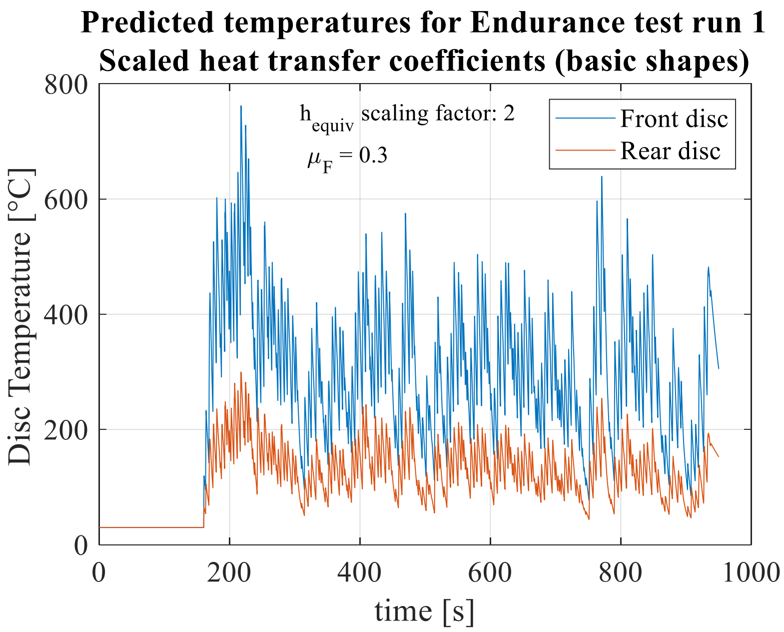

Figure 137: Brake disc temperatures predicted using the telemetry data of the Endurance run 1 of August 16th, 2018 and the average heat transfer coefficients found from the combination of empirical correlations for basic shapes discussed in section 2.1.4.3.

4.6 Brake rotors failure during Formula Student Spain 2018

The Formula Student Spain 2018 competition took place between the 21st and the 26th of August, at the “Circuito de Cataluña”. At the end of the Endurance race, one of the front brake rotors presented a crack in the rubbing surface, as shown in Figure 138.

Figure 138: Crack on the SC18 front brake rotor after the Formula Student Spain 2018 Endurance race.

The crack originated in one of the critical areas indicated by the fatigue life FEM simulation results contour plot (Figure 65, page 94). Despite the conservative approach used for modeling the load history of the rotors (page 85), the actual operating conditions caused greater temperature gradients across the rotors than predicted. This induced higher thermal stresses. Additionally, the anti-fading holes created by the laser-cutting machine presented a rough surface finish. These constitute severe stress raisers and are detrimental for the fatigue resistance of the rotors [25]. The surface defects on the edges of the holes can be seen in Figure 139.

Figure 139: Surface defects on the laser-cut anti-fading holes of the SC18 front brake rotors.

There were no direct temperature readings of the brake discs at the end of the Formula Student Spain Endurance event. The temperature predictions based on the telemetry data log are shown in Figure 140. These were obtained using the same scaling factor found in the previous section, but the predicted temperatures are unrealistically high compared to the thermal measurements showed in previous tests. Hence, the model parameters (μ_f, heat transfer coefficient correlation and scaling factor) found for the tests performed before the race do not apply to this case. Because of this strong dependence of the calculated temperatures on the assumed input values, this model cannot be used reliably to predict the temperatures of the brake discs.

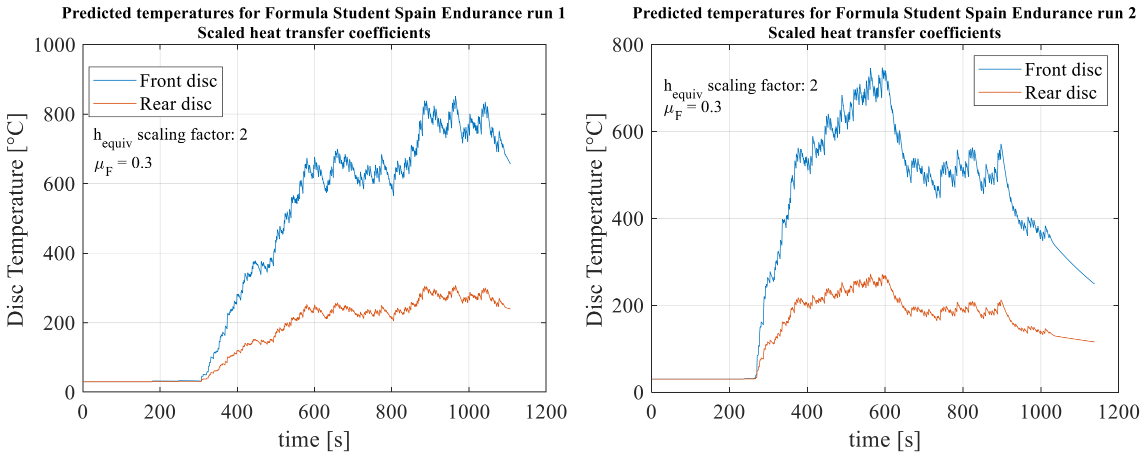

Figure 140: Brake disc temperatures predicted using the telemetry data of the Formula Student Spain 2018 Endurance test. The average heat transfer coefficients used were found from the combination of empirical correlations for basic shapes discussed in section 2.1.4.3 and scaled.

Although no data about the structural response of the uprights and the A-Arms was collected, at the end of the 2018 Formula Student Electric season they did not exhibit any signs of structural damage, such as cracks or deformations.

DISCUSSION

The development process of SC18's unsprung components has been described in detail. The methods and criteria applied for designing the main elements (uprights, brake discs) were less conservative than the ones used in 2017. The 2018 Formula Student/SAE Electric season was a suitable context for testing the capabilities of SC18, and the results obtained using the new design approaches.

The use of boundary conditions based on the stiffness of the wheel bearings when simulating the structural response of the wheel uprights (discussed section 2.2.2.1) is a new technique in the context of the PoliTo Racing team. The FEM structural analyses performed using them resulted in von-Mises stress values higher than the conventional limit for fatigue resistance used by PoliTo Racing in previous seasons. On the other hand, the analyses of SC17's uprights using this new type of boundary conditions showed deformations and von-Mises stresses greater than the ones obtained in 2017 using rigid constraints (Figure 98 and Figure 102). Although no physical data about the mechanical response of SC18's uprights was collected, the fact that they were in integral conditions at the end of the season demonstrates that the criteria used for determining the acceptable stress levels is safe, if not conservative. The 16% and 13% weight reduction of the front and rear SC18's uprights compared to the SC17 ones come mainly from the fact that the new gear train was much smaller than the previous design and thus required a smaller housing. However, using realistic boundary conditions during the FEM simulations allowed designing more lightweight components that are stiffer (in theory) than their heavier predecessors. To verify this, experimental measurements of the deformations experienced by the uprights are needed.

In terms of the brake discs and calipers, the temperature measurements obtained during the test sessions allowed evaluating the calculation models used during the design process to estimate the work cycle of the discs. The temperature predictions calculated using telemetry data (wheel speeds and brake circuit pressures) and average heat transfer coefficients obtained from different empirical correlations and steady-state CFD analyses were compared to experimental values. The results varied among the different track tests analyzed. The assumptions used for parameters like the brake pads friction coefficients and the average heat transfer coefficients have a large impact on how well the predicted disc temperatures match the measured ones. The fact that different scaling factors were required to find a good correspondence between the calculation results and the measurements makes this method unsuitable for predicting the temperatures of the discs if no reference data is available for scaling the results.

For faster circuits, such as the autocross runs, the models presented in section 2.1.4.2 tend to produce greater discrepancies with respect to the measured values. However, measuring the disc and caliper's temperatures at the end of each test session using a thermal camera provides only an approximated reference value of their exercise temperatures. The thermal paints and adhesives are useful for determining whether they exceeded a threshold value which depends on the type of paints and adhesives used. For this reason, it was not possible to find a correlation coefficient between the real rotor temperatures and the predicted ones.

Knowing the spatial and temporal temperature variations on the brake discs is important because they determine the thermal stresses that may cause fatigue failure or deformations [25, 33]. Both of these failure modes occurred on the SC18 front brake disc. Hence, the design cannot be considered satisfactory in terms of reliability. This result was caused by a combination of factors:

1. Manufacturing method

   Using a two-step manufacturing process allowed using the available resources to produce the brake rotors and bell carriers relatively fast. The in-house fabrication gave the possibility of following the production process closely. However, several trials and prototypes were required to reach the desired dimensional tolerance on the brake rotors, which reduced the time advantage gained. Additionally, the laser-cutting machine available was not suitable for producing complex hole-patters. The poor surface finishes of the anti-fading holes of the discs (Figure 139) propitiated the initiation of the crack found at the end of the season.
2. Simulation methods and input data

   Inaccurate predictions of the temperature variations were used for simulating the thermal stresses of the discs through FEA. The temperature images captured during track tests showed greater thermal gradients than the ones obtained with the FEM analyses. Additionally, the thermal and mechanical stress FEM simulations performed were based on simplified assumptions about the load application and did not account for the rubbing contact stresses on the surface of the discs.

The failure of the brake caliper seals could have been a consequence of the high temperatures reached on the brake rotors and their "coning". A deformed disc will enter in contact with one of the brake pads even in when they are in a retracted position. Another hypothesis is that the calipers worked at high temperatures for a prolonged time, causing the degradation of the piston seals. Since one of the functions of caliper piston seals is to aid the retraction of the caliper pistons [33], a degraded seal can cause the piston to seize in the compressed position. In this case, the continuous contact of the brake pad with the disc produced disc and caliper temperatures higher than under normal operation.

Despite the unsatisfactory reliability of the brake discs, they fulfilled the design target number 1 for the brakes system (Table 8), mainly because of the downsizing of the front brake calipers.

Additionally, the telemetry data demonstrated the impact of brake balance setup for achieving optimal decelerations during braking. Using an improved brake load distribution provided a greater contribution for improving the braking performance than the modifications in the components.

The telemetry data also revealed that the hydraulic pressure in the brake circuits was consistently below 40 bar, while higher pressures would allow better exploitation of the braking capabilities of SC18. This could be because the forces required to the drivers at the brake pedal were too high. Another possibility is that the brake pedal was not designed in an ergonomically optimized way, which would prevent the drivers from exerting the required force.

CONCLUSIONS

This thesis addressed the development process of the unsprung components of the SC18 Formula Student Electric vehicle. The work was structured according to the V model to organize the required tasks in a logical sequence progressing from the design of macro-areas and systems to the design of individual components.

The mechanical integrity of the unsprung components was verified through FEM structural analyses. The methods used for assessing the mechanical resistance of SC18's parts were more realistic than the ones used for SC17. In particular, boundary conditions based on the stiffness of the wheel bearings were applied when simulating the mechanical response of the uprights. Additionally, less-conservative criteria were used when evaluating the von-Mises stress values considered safe for obtaining an acceptable fatigue life of the parts. This allowed reaching the weight reduction targets for SC18's uprights while achieving the required stiffness of the suspension attachment points, at least in terms of simulation results. When compared against SC17's uprights under the same type of boundary conditions, the predicted deformation of the wheel bearing seats was reduced 70% and the stiffness of the suspension hardpoints was increased 20% overall.

In terms of the unsprung components of the braking system, the process of determining the characteristics of the brake calipers and discs used has been described, including considerations about brake load distribution. Then, track tests allowed determining the brake load distribution setup (via a balance bar) that provided the best results.

The brake calipers and discs used on SC18 reached the weight reduction targets of Polito Racing for 2018.

The brake rotors were designed using the telemetry data of SC17 to calculate the amount of energy converted into heat during an Endurance race and the load history of the applied torques. FEM analyses were used to assess the thermo-mechanical response of the brake discs. To do this, average heat transfer coefficients were calculated for different vehicle speeds to simulate the thermal response of the brakes and predict their fatigue life under combined mechanical and thermal stresses.

The temperature measurements collected from the brake discs and calipers during track test sessions were used for assessing the validity of the temperature calculations performed when designing the brakes. The results showed that the working temperature of the brake discs cannot be accurately predicted using wheel speed and brake circuit pressure data, and calculated speed-dependent average heat transfer coefficients. The main reason is the large number of simplifications and assumptions required to do so.

The failures found on the brake calipers and rotors were analyzed in this work, highlighting the possibilities for future development to design improved components learning from the lessons of 2018.

Further analyses of the temperature gradients of the brake discs during operation and the working temperatures of the brake calipers are required to improve their reliability. In the following seasons, bench tests could be done to measure the brake discs and pads temperatures more accurately and verify the heat transfer coefficients experimentally. Also, the brake pads friction coefficients could be determined; this information would allow analyzing the brake discs in more detail considering contact stresses and frictional heat.

Overall, the design of the 2018 unsprung components covered several aspects that had not been fully addressed in previous years, setting an encouraging baseline for the following competition seasons.

Polito Racing competed with the SC18 car in the 2018 Formula SAE Italy and Formula Student Spain events, achieving the 2^{nd} and 13^{th} places, respectively. Thanks to this, the team was placed in the 24^{th} position of the worldwide Formula Student Electric Ranking at the end of 2018. This fact demonstrates that the components designed for SC18 were capable of fulfilling their functions at a competitive level, which is an overall positive result.


Squadra Corse PoliTO
E146
ECV
FCA


oerlikon
oerlikon
oerlikon
brembo
brembo
dallara
dallara
E146
ECV

REFERENCES

[1] Formula Student Germany, *Formula Student Rules 2018,* Formula Student Germany, 2018.

[2] SAE International, *2017-18 Formula SAE® Rules,* 2017.

[3] Mazur - events, "Formula Student Electric - World Ranking List," 10 October 2018. [Online]. Available: https://mazur-events.de/fs-world/E/#. [Accessed 08 11 2018].

[4] "KA-RaceIng e.V. - Formula Student Team Karlsruhe," [Online]. Available: https://www.ka-raceing.de/. [Accessed 19 October 2019].

[5] "Formula Student Team Delft," [Online]. Available: https://www.fsteamdelft.nl/. [Accessed 19 October 2019].

[6] "Greenteam Uni Stuttgart Site - Formula Student Electric & Driverless Team Universität Stuttgart," Greenteam Uni Stuttgart English, 2019. [Online]. Available: https://www.greenteam-stuttgart.de/en/. [Accessed 19 October 2019].

[7] "RMIT Electric Racing," RMIT Electric Racing, 2018. [Online]. Available: http://rmitelectricracing.com/. [Accessed 19 October 2019].

[8] "Penn Electric Racing," [Online]. Available: http://www.pennelectricracing.com. [Accessed 19 October 2019].

[9] R. . C. Juvinall and K. M. Marshek, Fundamentals of Machine components design, 4th edition., Wiley, 2011.

[10] W. F. &. M. D. L. Milliken, Race Car Vehicle Dynamics, Warrendale, USA: SAE International, Inc., 1997.

[11] G. Genta, Motor Vehicle Dynamics: Modeling and Simulation - Series on Advances in Mathematics for Applied Sciences - Vol. 43, Toh Tuck Link, Singapore: World Science Publishing Co. Pte. Ltd., 1997.

[12] M. Cova, "Design of an epicycloidal geartrain for a four-wheel drive Formula Student electric vehicle," Turin, Italy, 2020.

[13] K. Forsberg and H. Mooz, *System Engineering for Faster, Cheaper, Better,* Center for Systems Management, Inc., 1998.

[14] Defense Acquisition University Press, Systems Engineering Fundamentals, Fort Belvoir, 2001.

[15] K. Forsberg and H. Mooz, "The Relationship of System Engineering to the Project Cycle," in *Proceedings of The 12th INTERNET World Congress on Project Management*, Oslo, 1994.

[16] C. Smith, Tune to win: The art and science of race car development and tuning, Aero Publishers, Inc., 1978.

[17] G. Genta and L. Morello, The Automotive Chassis Vol. 1 Component Design, Springer, 2009.

[18] G. Genta and L. Morello, The Automotive Chassis Vol. 2 System Design, Springer, 2009.

[19] E. Carboneri, "Progettazione e produzione di Sospensioni e Masse non Sospese per una vettura di formula SAE," Politecnico di Torino, Turin, 2018.

[20] Watts, A. et al, "Integrating In-Wheel Motors into Vehicles - Real-World Experiences," *SAE International Journal of Alternative Powertrains,* vol. 1, no. 1, pp. 289-307, 2012.

[21] M. Anderson and D. Harty, "Unsprung Mass with In-Wheel Motors - Myths and Realities," in *10th International Symposium on Advanced Vehicle Control*, Loughborough, UK, 2010.

[22] H. &. C. F. &. C.-D. F. Yu, "Optimal Design and Control of 4-IWD Electric Vehicles based on a 14-DOF Vehicle Model," *IEEE Transactions on Vehicular Technology,* 2018.

[23] C. Rouelle, "Getting to gips with your yaw moments," OptimumG, May 2017. [Online]. Available: http://downloads.optimumg.com/Technical_Papers/RCE1.pdf. [Accessed 19 October 2019].

[24] Mechanical Simulation Corporation, "CarSim Overview," [Online]. Available: https://www.carsim.com/products/carsim/index.php. [Accessed 19 October 2019].

[25] R. Limpert, Brake Design and Safety, Warrendale, PA.: Society of Automotive Engineers, Inc., 1999.

[26] F. P. Incropera, D. P. Dewitt, T. L. Bergman and A. S. Lavine, Fundamentals of Heat and Mass Transfer, 6th Edition, John Wiley & Sons, Inc., 2007.

[27] K. Maxey, "Engineering.com," 29 November 2019. [Online]. Available: https://www.engineering.com/DesignerEdge/DesignerEdgeArticles/ArticleID/5023/Top-Down-and-Bottom-Up-Design.aspx. [Accessed 19 October 2019].

[28] P. M. Danesin, "Progettazione e calcolo strutturale di un sistema sospensivo in materiale composito," Politecnico di Torino, Turin, 2018.

[29] Bosch Sensortec GmbH, "Smart sensor BNO055," 2020. [Online]. Available: https://www.bosch-sensortec.com/products/smart-sensors/bno055.html. [Accessed 12 October 2019].

[30] Vector Informatik GmbH, "GL Logger - Flexible, Robust and Reliable Data Logging | Vector," 2019. [Online]. Available: https://www.vector.com/int/en/products/products-a-z/hardware/gl-logger/#c91033. [Accessed 19 October 2019].

[31] VI-grade engineering software & services, "Driving Simulation | Dynamic driving simulation | VI-Grade," 2017. [Online]. Available: https://www.vi-grade.com/. [Accessed 19 October 2019].

[32] Stahlbus® GmbH, "Photos and Videos - Formula Student - Bleeding Brakes," 2019. [Online]. Available: https://www.stahlbus.com/info/de/galerie/category/11-formula-student. [Accessed 19 October 2019].

[33] A. Day, Braking of Road Vehicles, Elsevier Inc., 2014.

[34] I. Gibson, D. Rosen and B. Stucker, Additive Manufacturing Technologies - 3D Printing, Rapid Prototyping, and Direct Digital Manufacturing, 2nd edition., New York: Springer, 2015.

[35] Racecar Engineering, "TU Delft - DUT14 - Racecar Engineering," Chelsea Magazine Company, 2019. [Online]. Available: https://www.racecar-engineering.com/cars/delft-4/. [Accessed 19 October 2019].

[36] Brembo S.p.A., *Brembo Racing - High Performance Motorcycle catalogue,* 2013.

[37] Robert Bosch GmbH, Brakes, Brake Control and Driver Assistance Systems - Function, Regulation and Components, K. Reif, Ed., Springer Vieweg, 2014.

[38] A. Rashid, "Overview of Disc Brakes and Related Phenomena - a review," *International Journal of Vehicle Noise and Vibration,* vol. 10, no. 4, pp. 257-301, 2014.

[39] The MathWorks, Inc., "MATLAB - Mathworks - MATLAB & Simulink," 2019. [Online]. Available: https://www.mathworks.com/products/matlab.html. [Accessed 19 October 2019].

[40] B. Latour, P. Bouvier and S. Harmand, "Convective Heat Transfer on a Rotating Disk With Transverse Air Crossflow," *Journal of Heat Transfer,* vol. 133, pp. 021702-1 -10, 2011.

[41] A. Belhocine and M. Bouchetara, "Thermal analysis of a solid brake disc," *Applied Thermal Engineering,* vol. 32, pp. 59-67, 2011.

[42] ANSYS, Inc., "ANSYS CFX: CFD SOFTWARE," 2019. [Online]. Available: https://www.ansys.com/products/fluids/ansys-cfx. [Accessed 19 October 2019].

[43] S. P. Lillo Harún, ""Comportamiento mecánico de un disco de freno macizo y uno auto-ventilado" - Mechanical behavior of a solid brake disc and a ventilated one," Universidad Austral de Chile, Valdivia, 2006.

[44] J. Tang, D. Bryant and H. Qi, "Coupled CFD and Mechanicla Simulation of a Disc Brake," in *EuroBrake 2014 Conference Proceedings*, Lille, France, 2014.

[45] S. Kothawade, A. Patankar, R. Kulkarni and S. Ingale, "Determination of the heat transfer coefficient of a brake rotor using CFD simulation," *International Journal of Mechanical Engineering and Technology,* vol. 7, no. 3, pp. 276-284, 2016.

[46] M. Vidiya and B. Singh, "Experimental and Numerical Thermal Analysis of Formula Student Racing Car Disc," *Journal of Engineering Science and Technology Review,* vol. 10, no. 1, pp. 138-147, 2017.

[47] S. M. Sheiton, "THERMAL CONDUCTIVITY OF SOME IRONS AND STEELS OVER THE TEMPERATURE RANGE 100 TO 500 C," *Bureau of Standards Journal of Research,* vol. 12, pp. 441-450, 1934.

[48] Sinter Ljubljana d.o.o., "Sinter - Power of Control," 2017. [Online]. Available: www.sinter.si. [Accessed 30 October 2017].

[49] Automation Creations, Inc., "Online Materials Information Resource - MatWeb," MatWeb, LLC., 2019. [Online]. Available: http://www.matweb.com/. [Accessed 30 October 2017].

[50] P. Thiyagarajan, R. B. Mathur and T. L. Dhami, "Thermomechanical Properties of Carbon Fibres and Graphite Powder Reinforced Asbestos Free Brake Pad Composite Material," *Carbon Science,* vol. 4, no. 3, pp. 117-120, 2003.

[51] F. Talati and S. Jalalifar, "Analysis of heat conduction in a disk brake system," *Heat and Mass Transfer,* vol. 45, p. 1047–1059, 2009.

[52] A. Adamowicz and . P. Grzes, "CONVECTIVE COOLING OF A DISC BRAKE DURING SINGLE BRAKING," *Acta mechanica et automatica,* vol. 6, no. 2, pp. 5-10, 2012.

[53] P. Grzes, "Maximum temperature of the disc during repeated braking applications," *Advances in Mechanical Engineering,* vol. 11, no. 3, 2019.

[54] A. Adamowicz and P. Grzes, "Influence of Convective Cooling on a Disc Brake Temperature Distribution During Repetitive Braking," *Applied Thermal Engineering,* vol. 31, no. 14, 2011.

[55] HONEYWELL INTERNATIONAL INC., "PX3 Series Heavy Duty Pressure Transducer - Honeywell," 2019. [Online]. Available: https://sensing.honeywell.com/sensors/heavy-duty-pressure-sensors-and-transducers/PX3-series. [Accessed 19 October 2019].

[56] ANSYS, Inc., "Simulation Capabilities | Ansys Design Xplorer," 2019. [Online]. Available: https://www.ansys.com/products/platform/ansys-designxplorer/designxplorer-capabilities#cap1. [Accessed 19 October 2019].

[57] D. Montgomery, Design and Analysis of Experiments, Wiley, 2012.

[58] Altair University, Practical Aspects of Finite Element Simulation - A Study Guide (3rd edition), Altair Engineering, Inc., 2015.

[59] R. G. Budynas and J. K. Nisbett, Shigley's Mechanical Engineering Design 8th Edition, McGraw—Hill Primis, 2006.

[60] R. I. Stephens, A. Fatemi and R. R. Stephens, Metal Fatigue in Engineering, 2nd Edition, Wiley, 2000.

[61] C. Boller and T. Seeger, Materials data for cyclic loading - Part C: Hihgh-Alloy Steels, Amsterdam: ELSEVIER SCIENCE PUBLISHING COMPANY INC., 1987.

[62] ASM International, Atlas of Fatigue Curves, ASM International, 1986.

[63] REVOLVE NTNU, "NTNU | Revolve," 2019. [Online]. Available: https://www.revolve.no/. [Accessed 19 October 2019].

[64] TUW Racing, "TUW Racing," 2019. [Online]. Available: http://racing.tuwien.ac.at/. [Accessed 19 October 2019].

[65] TU Graz Racing Team, "TU Graz Racing Team," [Online]. Available: https://racing.tugraz.at/. [Accessed 19 October 2019].

[66] Officina Meccanica Massola Giuseppe, "Officina Meccanica Massola Giuseppe - Special Components," [Online]. Available: http://www.officinamassola.it/. [Accessed 19 October 2019].

[67] © SKF Group 2016, "SKF Super-precision bearings catalogue," 2016. [Online]. Available: https://www.skf.com/binary/30-129877/0901d19680495562-Super-precision-bearings-catalogue---13383_2-EN.pdf. [Accessed November 2017].

[68] RS Components, "Termometro a infrarossi RS PRO," 2018. [Online]. Available: https://it.rs-online.com/web/p/termometri-a-infrarossi/9181085/. [Accessed 12 October 2018].

[69] Cerrina Race Track , "Cerrina Race Track," 2017. [Online]. Available: https://www.cerrinaracetrack.com/. [Accessed 20 10 2019].

[70] Fluke Process Instruments, "Emissivity - Metals," 2020. [Online]. Available: https://www.flukeprocessinstruments.com/en-us/service-and-support/knowledge-center/infrared-technology/emissivity-metals. [Accessed 11 October 2019].

[71] RS Components, "Etichetta termosensibile RS PRO," RS Components S.r.l. , 2018. [Online]. Available: https://it.rs-online.com. [Accessed 24 10 2018].

[72] Fluke Corporation, "Ti125, Ti110, Ti105, Ti100, Ti95, Ti90, TiR125, TiR110 and TiR105 Infrared Cameras Technical Data," Fluke, 2020. [Online]. Available: https://www.fluke.com. [Accessed 10 February 2020].

[73] Club des Miles s.r.l., "CLUB DES MILES," [Online]. Available: http://www.clubdesmiles.com. [Accessed 10 February 2020].

[74] P. Pandy, "Transient thermal analysis of a brake disc in regenerative braking system using finite element analysis," in *Proceedings of the ASME 2015 International Design Engineering Technical Conferences & Computers and Information in Engineering Conference*, Boston, Massachusetts, USA, 2015.

[75] R. L. C. D. M. M. William Kucinski, "ME 351 - Formula Electric In-Hub Motor System for Formula SAE Electric," University of Wisconsin - Madison, Madison, Wisconsin, USA, 2017.

[76] M. Ortiz, "Pedal of honour: the big brake out - All you need to know to sort brake pedal pressure for FSAE," *Race car engineering,* pp. 18, 19, 2015.

[77] J. P. Almeida Vianna, "Torque Vectoring in Electric Vehicles with In-wheel Motors," Politecnico di Torino, Turin, 2018.

[78] "AMZ Racing - Electric," AMZ Racing, 2019. [Online]. Available: http://electric.amzracing.ch/. [Accessed 19 October 2019].

[79] "DHBW Engineering Stuttgart eV," DHBW Engineering Stuttgart eV, 2019. [Online]. Available: https://dhbw-engineering.de. [Accessed 19 October 2019].

[80] "Formula Student Team Tallinn," FS Team Tallinn, 2019. [Online]. Available: https://formulastudent.ee. [Accessed 19 October 2019].

[81] "UPC ecoracing," 2019. [Online]. Available: http://www.ecoracing.es. [Accessed 19 October 2019].

[82] Continental AG, *Continental Formula Student Tire - Competition Tire 2016 (C16) - Documentation,* Continental Reifen Deutschland GmbH, 2016.

[83] AMZ Racing, "@amzracing," [Online]. Available: https://www.instagram.com/amzracing/?hl=es. [Accessed 19 October 2019].

[84] Siemens Industry Software Inc., "STAR-CCM+," 2019. [Online]. Available: https://www.plm.automation.siemens.com/global/en/products/simcenter/STAR-CCM.html. [Accessed 19 October 2019].

[85] Honeywell International Inc. , "Pressure Sensor Glossary of Terms," 2011. [Online]. Available: https://sensing.honeywell.com/pressure-sensor-glossary-of-terms-tn-008200-2-en-final-08jul11.pdf. [Accessed 12 October 2018].